

PhotoMechanics & iDICs conference



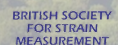
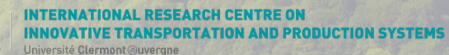
Book of abstracts

Clermont-Ferrand, France
October 29-31, 2024

Event organized by:



Event supported by:





The latest release from Correlated Solutions - VIC-3D 10 - is an unparalleled DIC workspace with features designed specifically to facilitate 3D data analysis and visualization. Building on *iris*, the data visualization engine introduced in the previous version, VIC-3D 10 features a significant increase in processing speed, and it delivers a range of new capabilities that broaden DIC's scope for FFT projects, FEA validation, and integrated stress analysis. In addition, the *iris* workspace has been updated to provide even more flexibility and functionality to display your DIC analysis clearly and professionally. We invite you to visit our booth at iDICs or contact one of our engineers to explore the ways digital image correlation with VIC-3D 10 can improve your efficiency and results.

Continuous innovation for more than 25 years from the inventors of Digital Image Correlation

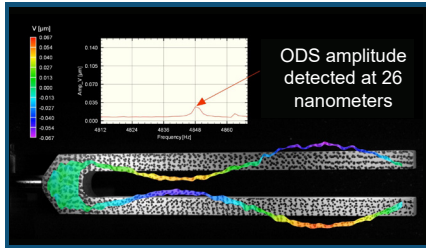
VIC-3D 10 New Features



VIC-3D QX System
(12 MP @ 335 fps)

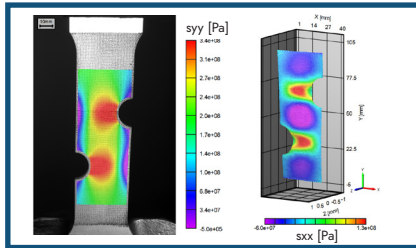


VIC Trigger Boxes &
DAQ systems



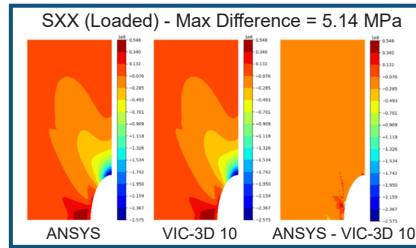
FFT Vibration Visualization

New FFT vibration visualization in *iris* allows for in-plane & out-of-plane ODS to be displayed in stunning, high-resolution graphics.



Integrated Stress Analysis

Integrated stress analyzer converts strain history to stress with models defined through a dialog or through JSON files.



Expanded FEA Validation

In conjunction with FE simulations in Abaqus™ & Ansys™, users can now more effectively and efficiently validate FEA results.



VIC-3D Calibration
Gimbal



3D-Micro-DIC +
"Blue Falcon" - 24 MP



Correlated Solutions welcomes you to join a walking tour of Clermont-Ferrand followed by a wine & cheese reception on Tuesday, October 29th at 18:00.

correlatedsolutions.com



Contact our Sales Team to explore the range of industry-leading digital image correlation systems from Correlated Solutions.
sales@correlatedsolutions.com

Sponsors

Gold support



Since the establishment of the International DIC Society in 2015, **Correlated Solutions** has continued its steadfast support of iDICs through scholarship and sponsorship. We are proud to be here in France with our partners from Correlated Solutions Europe to share the latest hardware and software developments that are designed to increase efficiency and broaden the scope of DIC. Our flagship software VIC-3D 10 is now available and features a significant increase in processing speed. This is matched with an unparalleled DIC workspace designed specifically to facilitate 3D data analysis and visualization. In addition, VIC-3D 10 delivers a range of new capabilities for FFT projects, FEA validation, and integrated stress analysis. We invite you to visit our booth at iDICs to explore the ways digital image correlation with VIC-3D 10 can improve your productivity and results.

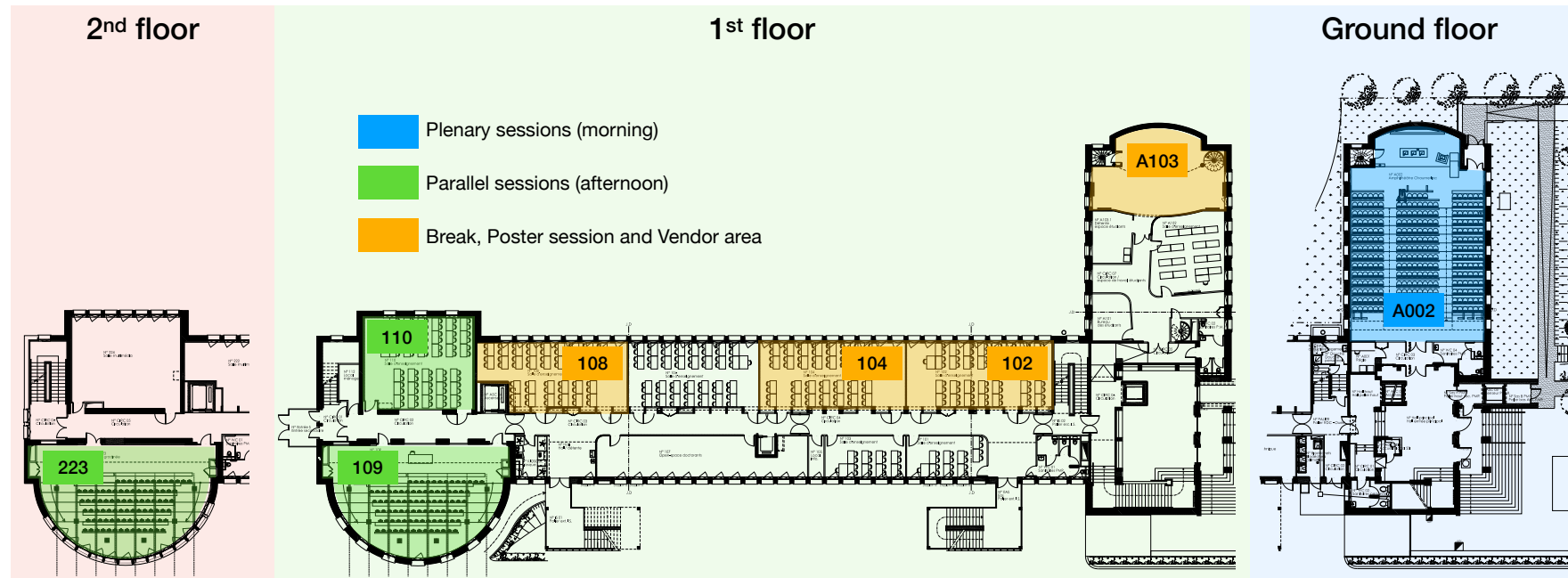
Bronze support



Vision Research is dedicated to the development of Phantom high-speed cameras which lead the industry in frame rate, resolution, and image quality. The combination of revolutionary sensor technology and engineers with a deep understanding of the research and development needs has resulted in the creation of a broad range of high-speed cameras suitable for nearly all applications.



Conference building layout



Social events

Tuesday 29

- **18:00 - City tour**

Enjoy a one-hour stroll through the heart of Clermont-Ferrand, led by local guides who will showcase the city's main sights and share fascinating insights into its rich history. This event is generously sponsored by **Correlated Solutions, Inc.**

- **19:00 - Town Hall reception**

Join us for a welcome drink and cheese tasting at the Town Hall of Clermont-Ferrand. This event is generously sponsored by **Correlated Solutions, Inc.**

Wednesday 30

- **15:30 - Bus Departures to Lemptégy Volcano**

The buses will depart in front of the Océania Hotel “82 Bd François Mitterrand, Clermont-Ferrand” (4-minute walk from the conference building).

- **16:45 - 17:45 - Visit of Lemptégy Volcano**

Discover the heart of an authentic volcano! Situated in the center of the tectonic hotspot known as the “Chaîne des Puys – Faille de Limagne”, a UNESCO World Heritage Site. We invite you to experience a unique and rare exploration of the interior of a completely natural volcano. The tour can be enjoyed either on foot or aboard a little train.

- **18:10 - 19:00 - Keynote by João Quinta da Fonseca**

Keynote by João Quinta da Fonseca in a conference room of Lemptégy site. The lecture is entitled “Measuring and modelling the elastoplastic transition in engineering alloys at the microstructure scale”.

- **19:30 - Conference dinner**

- **22:00 - Bus Returns to Clermont-Ferrand**

Tuesday October 29, 2024

Morning

09:30	<p>Keynote Room A0002</p> <p style="text-align: right;">Chair: Benoit Blaysat</p>
	<p>Chasing anticracks - How PTV and DIC revolutionized snow avalanche research <i>Alec Van Herwijnen, WSL Institute for Snow and Avalanche Research SLF</i> p.22</p>
10:50	<p>Extrem Room A0002</p> <p style="text-align: right;">Chair: Marco Rossi</p>
10:50	<p>X-ray digital image correlation for deformation measurements in extreme environments <i>Elizabeth Jones, Sandia National Laboratories</i> p. 24</p>
11:10	<p>Deformation of CANDU Pressure Tube under Biaxial Stress State at High Temperatures <i>Chukwudi Azih, Canadian Nuclear Laboratories</i> p. 25</p>
11:30	<p>A SHPB digital twin for the optimization of specimens dedicated to heterogeneous high strain rate tests <i>Thomas Fourest, DMAS, ONERA, 59000, Lille, France</i> p. 26</p>

Tuesday October 29, 2024

Afternoon

13:50	Volume measurements Room 109 Chair: Clément Jailin	Inverse and identification methods Room 110 Chair: Fabrice Pierron	DIC Room 223 Chair: Iniyan Thiruselvam N.
13:50	Universal Tomographic Calibration: Achieving 1/100th Voxel Digital Volume Correlation (DVC) Displacement Precision <i>Alex Arzoumanidis, Psylotech, Inc. - Brian Bay, Oregon State University; School of Mechanical, Industrial, and Manufacturing Engineering - André Phillion, McMaster University [Hamilton, Ontario]</i> p. 27	Boundary conditions and constitutive parameter identification <i>Antoine Vintache, EikoSim, Laboratoire de Mécanique Paris-Saclay</i> p. 28	Deformation Behavior Analysis of Honeycomb Structure Under In-plane Compression Using Global DIC <i>Yamaguchi Yuki, Aoyama Gakuin University</i> p. 29
14:10	Dual X-ray and Neutron tomography to observe hydro-mechanics in porous media <i>Hilario Gregg, 3SR Lab</i> p. 30	Characterization of anisotropic hyperelastic behavior with a data-driven approach <i>Annie Morch, Institut de Recherche en Génie Civil et Mécanique Nantes université</i> p. 31	Full-Field Mechanical Deformation Behaviour of Different Metallic Laser Welded Joints under Tensile Loadings <i>Patricio Carrion, Sandia National Laboratories [Albuquerque]</i> p. 32
14:30	Optical Scanning Tomography to measure harmonic displacement fields and to identify visco-elastic parameters distributions <i>Bertrand Wattrisse, Laboratoire de Mécanique et Génie Civil</i> p. 33	Image-based B-Spline beam models of architected materials using Virtual Image Correlation with variable cross-section <i>Jean-Charles Passieux, Institut Clément Ader</i> p. 34	DIC for Detection of Embedded Structures <i>Izabela Nowakowska, Heriot-Watt University</i> p. 35
14:50	Towards color X-ray tomography: Detection of small quartz grains via contrast-enhanced 3D images of carbonate rocks using a CdTe Photon Counting Detector <i>Franck Decroos, Laboratoire Navier</i> p. 36	Material testing 2.0 for viscoelasticity : characteristic time sensitivity vs experiment duration <i>Margot Leclercq, Université Paris Saclay, ENS Paris-Saclay, CentraleSupélec, CNRS, LMPS, 91190, Gif-sur-Yvette, France</i> p. 37	Application of digital image correlation in the characterization of metal powder spreadability for additive manufacturing <i>Lukas Daut, Oregon State University; School of Mechanical, Industrial, and Manufacturing Engineering</i> p. 38
15:10	Measuring residual stresses in 3D woven composite fan blades via DVC <i>Yannick YASOTHAN, Laboratoire de Mécanique Paris-Saclay</i> p. 39	Optimising test sequences for robust material identification using a data assimilation approach <i>Marie Guerder, Institut Clément Ader</i> p. 40	Development of a digital image correlation system for in-situ epoxy cure shrinkage, thermal expansion, and wafer warpage measurements <i>Alexander Landauer, National Institute of Standards and Technology</i> p. 41

16:00	Volume measurements Room 109 Chair: Brian Bay	Inverse and identification methods Room 110 Chair: Elizabeth Jones	Softwares Room 223 Chair: Mark Iadicola
16:00	Using DVC to measure manufacturing differences in 3D woven composite parts <i>Arturo Mendoza, Safran Tech, Laboratoire de Mécanique Paris-Saclay</i> p. 42	Constitutive model validity evaluation for MT 2.0 applications <i>Amar Peshave, MatchID NV</i> p. 43	The Stereo-DIC Challenge 2.0: DIC Strain Comparisons Using Common Images <i>Phillip Reu, Sandia National Laboratories [Albuquerque]</i> p. 44
16:20	Debonding quantification via Digital Volume Correlation. Application to a mortar reinforcement pull-out. <i>Sylvain Langlois, Laboratoire de Mécanique Paris-Saclay</i> p. 45	Identification of heterogeneous elastic parameters with the Equilibrium Gap Method <i>Rémi Haustrate, LMPS - Laboratoire de Mécanique Paris-Saclay, 91190, Gif-sur-Yvette, France.</i> p. 46	R3XA: Toward a metadata standard for experimental (photo)mechanics datasets <i>Jean-Charles Passieux, Institut Clément Ader</i> p. 47
16:40	Projection enhanced DVC to analyze relaxation and crack propagation until failure on architected aluminum alloy <i>Viktor Kosin, Ecole Normale Supérieure Paris-Saclay, Leibniz University Hannover</i> p. 48	Spatial mapping of plastic properties in welds with the VFM <i>Robert Hamill, University of Southampton</i> p. 49	iDVC - Open-Source Interactive Software for Digital Volume Correlation <i>Danica Sugic, STFC Rutherford Appleton Laboratory</i> p. 50
17:00	3D virtual image correlation (3D-VIC) for lattice structures metrology using x-ray radiographs <i>Julien Réthoré, Nantes Université, Ecole Centrale Nantes, CNRS, GeM, UMR 6183, 1 rue de la Noë, France</i> p. 51	A crystal plasticity-based intragranular stress fields identification framework: application to commercially pure aluminium <i>Raphaël Langlois, Nantes Université, Ecole Centrale Nantes, CNRS, GeM, UMR 6183, 1 rue de la Noë, F-44321 Nantes, France</i> p. 52	uCheckMate : An open-source python library for research and development of Finite element stereo digital image correlation <i>Houssein MATAR, Institut Pascal</i> p. 53

Wednesday October 30, 2024

Morning

08:30	Small scale Room A0002 Chair: João Quinta da Fonseca
08:30	Automated, quantitative identification of slip system, twinning & boundary sliding activity maps from EBSD-SEM-DIC data <i>Johan Hoefnagels, Eindhoven University of Technology</i> p. 54
08:50	High resolution 3D stereo DIC for small FOV using the Scheimpflug principle <i>Hendrik Pulju, isi-sys GmbH</i> p. 55
09:10	Study of strain localization and crystal reorientation at the early stage of plastic deformation using LSCM, HR-EBSD and DCT-6D <i>Damien TEXIER, Institut Clément Ader</i> p. 56
09:30	Elevated temperature High Resolution Digital Image Correlation in a Scanning Electron Microscope <i>Allan Harte, UK Atomic Energy Authority</i> p. 57
09:50	Micro-computed topography from SEM backscattered electron multidetector images <i>Stéphane Roux, Laboratoire de Mécanique Paris-Saclay (LMPS)</i> p. 58

Poster session 10h10 → 11h40			
Room A103	Room 102	Room 104	Room 108
<p>Identification of heterogeneous elastic limits in polycrystalline 316L austenitic stainless steel during tensile loading <i>Qi HU, Laboratoire de Mécanique, Multiphysique, Multiéchelle - UMR 9013</i> p. 59</p>	<p>Statistical study of intermittent calorific phenomena associated to the Portevin-Le Chatelier effect in an aluminum alloy <i>Antoine JURY, Université Clermont Auvergne, Clermont Auvergne INP, CNRS, Institut Pascal</i> p. 60</p>	<p>Identifying forces in 2D granular materials using the Virtual Fields Method from strains measured by Localized Spectrum Analysis <i>Kunanon Jongchansitto, Chiang Mai University</i> p. 61</p>	<p>An imaging technique for the strain-engineering of deformable electrodes <i>Fabien Amiot, Franche-Comté Électronique Mécanique, Thermique et Optique - Sciences et Technologies (UMR 6174)</i> p. 62</p>
<p>High Throughput Tensile Testing for Characterization of Static Strain Aging <i>Ville Björklund, Aalto University School of Engineering, Department of Mechanical Engineering, PO Box 14200, FI-00076 Aalto, Finland</i> p. 63</p>	<p>Simultaneous thermal and kinematic full-field measurements on optimal patterns based on thermography and spectral analysis <i>Thomas Jailin, Université Clermont Auvergne, CNRS, Clermont Auvergne INP, Institut Pascal, BP 10448, 63000</i> p. 64</p>	<p>Characterization of the effect of roughness on dynamic ruptures along frictional interfaces <i>Saba Robinary, NANTES UNIVERSITÉ - École Centrale de Nantes</i> p. 65</p>	<p>Developing a new optical strain gage for full-field measurements <i>Adrien Vinel, Université Clermont Auvergne, Clermont Auvergne INP, CNRS, Institut Pascal</i> p. 66</p>
<p>Using full-fields measurements to determine the influence of crack velocity and non-singular terms on KIC of an epoxy resin <i>Bastien Lammens, DMAS, ONERA, F-59014 Lille, France</i> p. 67</p>	<p>Quantifying thermo-elastic cooling and heating during tensile strength testing of solid engineering alloys with a highly sensitive cooled infrared camera <i>STEPHANE BOUBANGA TOMBET, Telops</i> p. 68</p>	<p>Digital Image Correlation Study of Surface Defects on Plastic Bonded Explosives <i>John Graham, Lawrence Livermore National Laboratory</i> p. 69</p>	<p>Elimination of Interpolation Error in Digital Volume Correlation <i>Samuel Wantz, Institut Pprime, Centre Technique des Industries Mécaniques</i> p. 70</p>
<p>Measuring the displacement of masonry stones by motion capture <i>Julien Archez, Laboratoire Navier</i> p. 71</p>	<p>Michelin's Talk for PM-iDICs 2024 abstracts <i>UMRANI Florian, Michelin - Sophie Charpin, Michelin</i> p. 72</p>	<p>Analyses of grain-scale strain heterogeneities to provide input for polycrystalline models <i>Jean-Patrick Goulmy, Mechanics surfaces and materials processing (MSMP)</i> p. 73</p>	<p>DIC data filtering proposal for complex environments <i>Gweni Alonso Aruffo, IMT Mines Albi, Centre ICA-A, Albi - Rébecca Bonnaire, IMT Mines Albi, Centre ICA-A, Albi</i> p. 74</p>

Poster session 10h10 → 11h40			
Room A103	Room 102	Room 104	Room 108
Residual stress measurement in tire cables by FIB hole drilling <i>Raphaël Engel, Laboratoire de Mécanique Paris-Saclay</i> p. 75	Overview of Digital Image Correlation in Aerospace Engineering in India <i>Abhishek Gurudutt, Pyrodynamics</i> p. 76	Microstructural study of additively manufactured ALF357 alloy: Effect of tensile loading and build orientations <i>Avinash Mohan, Indian Institute of Technology Madras</i> p. 77	Evaluation of Influences on Results of Digital Image Correlation by Window of Constant Temperature Bath <i>Ayano Seki, Aoyama Gakuin University</i> p. 78
Real-time measurement of surface strain for understanding creep behavior in bending polymer films <i>JIAYI YU, Department of Chemical Science and Engineering, School of Materials and Chemical Technology, Tokyo Institute of Technology [Tokyo], Laboratory for Chemistry and Life Science, Institute of Innovative Research, Tokyo Institute of Technology [Tokyo]</i> p. 79		Strain signature of solid-solid phase transitions within a diamond anvil cell <i>Nicolas Bruzy, CEA DAM Bruyères le Châtel</i> p. 80	
		Understanding Anisotropy of Carbon-reinforced PEEK Using Stereo DIC <i>Vipin Gupta, Birla Institute of Technology and Science</i> p. 81	

11:40	Keynote Room A0002 Chair: Brian Bay & Phil Reu
	From random speckles to checkerboard patterns <i>Michel Grédiac, Université Clermont Auvergne</i> p.82
13:15	iDICs meeting - DIC Challenge Room 109 Chair: Benoît Blaysat

Wednesday October 30, 2024

Afternoon

14:00	Materials Room 109 Chair: Michel Coret	Aerospace Room 110 Chair: Phil Reu	Thermography Room 223 Chair: Janice Barton
14:00	Understanding the behaviour of a Cu-CuAl functionally-graded alloy using DIC <i>Filipa Cunha, Faculdade de Ciências e Tecnologia = School of Science & Technology</i> p. 83	Building simulation models credibility: the role of DIC in a complex structural testing environment <i>Pierre Baudoïn, EikoSim</i> p. 84	Investigation of the dissipative mechanisms in 3D layer-to-layer woven composite under cyclic loading <i>Vincent Le Saux, Institut de Recherche Dupuy de Lôme (IRDL)</i> p. 85
14:20	Localized Deformation and Band Formation in Superelastic Nitinol Wires <i>Dinc Erdeniz, University of Cincinnati</i> p. 86	DIC data integration to achieve multi-measurement system on full-scale wing tests <i>Emily Rolfe, AIRBUS Operations Ltd.</i> p. 87	Investigating heterogeneous strain-induced crystallization in natural rubber with infrared thermography based micro-surface calorimetry <i>Jean-Benoît LE CAM, Institut de Physique, Université de Rennes 1</i> p. 88
14:40	Strength characterisation of Nicrofer–Stellite joint using Digital Image Correlation <i>N. Iniyyan Thiruseelvam, BITS Pilani K. K. Birla Goa campus, Goa 403726</i> p. 89	Full Field Imaging and Data Fusion for Substructural Testing <i>Riccardo Cappello, University of Bristol</i> p. 90	Infrared Thermography Applied to In-Situ Crack Growth Assessment <i>Lorenzo Bercelli, Institut de Recherche Dupuy de Lôme</i> p. 91
15:00	Experimental Quantification of Ultraslow Slip Rate of Shear Interfaces Using Digital Image Correlation <i>Vito Rubino, NANTES UNIVERSITÉ - École Centrale de Nantes</i> p. 92	Using DIC for Full-Field Measurement of Long Slender Structures <i>Matlock Mennu, NASA Langley Research Center [Hampton]</i> p. 93	Evaluation of Conduction Thermography for Surface Crack Detection in Titanium Specimens: Preliminary Offline Tests and Initial Online Monitoring During Fatigue Tests <i>Rosa De Finis, Università del Salento</i> p. 94

18:10	Keynote Room Chair: Johan Hoefnagels
	Measuring and modelling the elastoplastic transition in engineering alloys at the microstructural scale <i>João Quinta da Fonseca, University of Manchester [Manchester]</i> p.95

Thursday October 31, 2024

Morning

08:30	Fracture Room A0002 Chair: Jan Neggers
08:30	Automated crack detection in laminated composite materials from optical flow measurements <i>Matthieu Nicol, ONERA, DMAS, Université Paris-Saclay, 29 avenue de la Division Leclerc, 92320 Châtillon, France</i> p. 96
08:50	Stereocorrelation to analyze crack propagation until failure during a shaking table test <i>Amelie Fau, Laboratoire de Mécanique Paris-Saclay</i> p. 97
09:10	In-situ 2D-DIC as a crack growth analysis tool for high-cycle fatigue bending tests <i>linamaria Gallegos Mayorga, École Nationale Supérieure d'Arts et Métiers</i> p. 98
09:30	Enhanced snow fracture toughness estimates through digital image correlation analysis of the elastic behaviour of weak snowpack layers <i>Melin Walet, WSL Institute for Snow and Avalanche Research SLF, Davos Dorf</i> p. 99
09:50	Study of different DIC approaches to measure crack opening/closing levels in a biaxial crack growth trial with combined HCF/LCF loads <i>Andreas Blug, Fraunhofer Institute for Physical Measurement Techniques IPM</i> p. 100
10:10	A new methodology exploiting digital image correlation to detect crack initiation <i>Sylvia Feld-Payet, DMAS, ONERA, Université Paris Saclay [Châtillon]</i> p. 101

11:00	Keynote Room A0002 Chair: Robin Bouclier
	Preconditioned conjugate gradient solver for the linearized optical flow systems <i>Pierre Gosselet, Laboratoire de Mécanique, Multiphysique, Multiéchelle - UMR 9013</i> p.102

11:50	Minisymposium: Math & Algorithms Room A0002 Chair: Robin Bouclier
11:50	Large Motion Tracking Regularization with the Finite Strain Formulation of the Discrete Equilibrium Gap Principle <i>Martin Genet, Mathematical and Mechanical Modeling with Data Interaction in Simulations for Medicine</i> p. 103
12:10	A Procedure for Global Non-Local Digital Image Correlation (NL-DIC) <i>Tushar Bhandari, Indian Institute of Technology Kharagpur</i> p. 104

13:15	iDICs meeting - Standardization Committee Room 109 Chair: Mark Iadicola
-------	--

Thursday October 31, 2024

Afternoon

14:00	Uncertainty quantification Room 109 Chair: Thorsten Siebert	Thermography Room 110 Chair: Xavier Balandraud	Minisymposium: Math & Algorithms Room 223 Chair: Julien Réthoré
14:00	Development of a virtual DIC approach to improve measurement accuracy and assess experimental setups <i>O. Tyley, University of Bristol [Bristol]</i> p. 105	An efficient approach for identifying the coefficients of thermal expansion of CFRPs <i>Janice Dulieu-Barton, Bristol Composites Institute, School of Aerospace, and Mechanical Engineering, University of Bristol</i> p. 106	High-Performance Mechanically Regularized Finite-Element Digital Volume Correlation for Complex Architected Materials <i>Lucas Person, Ecole Normale Supérieure Paris-Saclay, Institut Clément Ader, Institut de Mathématiques de Toulouse UMR5219</i> p. 107
14:20	Image-based data pipeline for fusion engineering qualification and model validation <i>Adel Tayeb, UKAEA</i> p. 108	Study of Non-Adiabatic Thermoelastic Effect in Face-sheet/Core Debonded Composite Sandwich Structures by Means of Full Field Imaging <i>Emily H. L. Leung, Bristol Composites Institute, School of Aerospace, and Mechanical Engineering, University of Bristol</i> p. 109	Beyond Nyquist Theorem: Reconstruction algorithms of down-sampled signals for vision-based vibration measurements <i>Davide Mastrodicasa, Siemens Industry Software NV, Vrije Universiteit [Brussel]</i> p. 110
14:40	Practical assessment of DIC uncertainties in view of FE model validation <i>Fabrice Pierron, MatchID NV</i> p. 111	Characterization of deformation behavior in metallic alloys using high-temperature digital image correlation analysis <i>Seung-Yong Lee, Materials Characterization Center, Korea Institute of Materials Science</i> p. 112	IBIS : Imaging bifurcations in 2D periodic metamaterials <i>Fabien Amiot, Franche-Comté Électronique Mécanique, Thermique et Optique - Sciences et Technologies (UMR 6174)</i> p. 113
15:00	FE validation from DIC data: a practical case study in bending <i>Vahid Firouzbakht, MatchID NV</i> p. 114	Thermal investigations of supercritical CO2 jet impingement and jet structure influence on its cooling ability <i>Maha El nahas, Institut Clément Ader</i> p. 115	The impact of metrics in mechanical imaging <i>Jean-François Witz, Laboratoire de Mécanique, Multiphysique, Multiéchelle - UMR 9013</i> p. 116
15:20	Vibration Measurements: Effect of Varying Exposure Time on Digital Image Correlation <i>Hubert Schreier, Correlated Solutions Inc.</i> p. 117	Multi-physic calibration for coupled IR Thermography - Stereo DIC sensor: from target to software <i>Théo SENTAGNE, DGA Techniques aérospatiales, Institut Clément Ader</i> p. 118	Isogeometric surface fitting from tomographic images <i>Dorian BICHET, Institut de Mathématiques de Toulouse UMR5219, Institut Clément Ader</i> p. 119

Chasing anticracks - how PTV and DIC revolutionized snow avalanche research

A. van Herwijnen and many others

WSL Institute for Snow and Avalanche Research SLF, Davos, Switzerland

Abstract — Snow is an extraordinary material, characterized by its high porosity, proximity to its melting point, and a microstructure that continuously evolves. These properties make snow highly compressible and one of the most fragile materials on Earth. Yet, remarkably, when fractured, it can 'heal' within minutes. Accurately describing snow's unique mechanical behavior is crucial for improving our understanding and prediction of snow avalanches, which are triggered by the mechanical failure of weak layers buried within the snowpack. While avalanches have been studied for decades, the introduction of particle tracking velocimetry (PTV) and digital image correlation (DIC) techniques in the early 2000s revolutionized our understanding of the failure and fracture processes that lead to avalanche release. In this presentation, I will provide an overview of how these methods have offered new insights into fundamental processes, such as structural collapse during fracture, and how they have contributed to the development of new models explaining avalanche release.

Keywords — DIC, PTV, Snow avalanches, crack propagation, field experiments

Outline Snow slab avalanches, the deadliest type, are governed by processes that span scales from failures between snow crystals to the release of large snow volumes across mountain flanks (Fig.1). These avalanches originate from the failure of a porous weak snow layer buried beneath a cohesive slab (Fig.1, middle). Weak layers are typically porous and composed of large angular grains (Fig. 1, right), while slabs consist of denser, fine-grained snow. Since dry-snow slab avalanches are typically triggered by external loading (e.g., snowfall or a skier), understanding snow mechanics is critical to improve

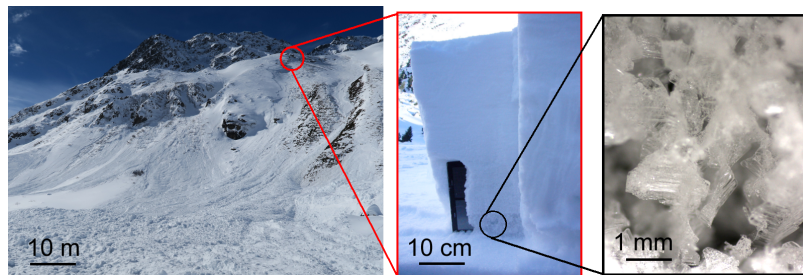


Figure 1: Dry-snow slab avalanche release is a multi-scale problem. Left: Large dry-snow slab avalanche. Middle: Close-up of a fracture line showing the dense slab on top of the porous weak layer. Right: Close-up of a weak layer showing the complex structure composed of large angular grains.

avalanche prediction.

Traditionally, avalanche release was believed to result from an imbalance between the shear strength of weak layers and the load from the overlying slab. However, stability indices (stress-to-strength ratios) often failed to predict avalanches accurately. The key to resolving this discrepancy was fracture mechanics, which explains how failures propagate even when stress levels remain below the strength of the weak. In the early 2000s, researchers and practitioners therefore set out to develop new tests to assess crack propagation, fundamentally shifting avalanche science.

Videos of these field tests recorded with portable high-speed cameras revealed that weak layer collapse plays a crucial role in crack propagation [1]. Particle tracking velocimetry (PTV) showed surprisingly low crack speeds, suggesting that collapse waves, rather than shear cracks, drive crack propagation [2]. These findings led to new theoretical and numerical frameworks, introducing the concept of "anticrack" to describe compressive failures in snow [e.g. 3, 4]. Unlike most materials, the porous nature of snow allows weak layers to fail in compression (anti-mode I) rather than tension (mode I).

New models, validated by increasingly detailed field measurements using digital image correlation [DIC; 5], have provided deeper insight into avalanche release, including how remote triggering from flat areas is possible. Recently, however, numerical simulations and detailed avalanche video analyses have suggested a shift from collapse-driven anti-crack propagation to "supershear" crack propagation on steep slopes [6], once again challenging our understanding of avalanche processes. Continued use of DIC in field observations will be crucial to validate these findings and push the boundaries of our understanding of avalanche behavior, with the potential to improve both theoretical models and practical avalanche forecasting.

About the author After growing up and studying in the flatlands of Belgium and the Netherlands, Alec embarked on a journey to learn about snow and avalanches. This quest began with a PhD thesis at the University of Calgary, within the research program of prof. Dr. Bruce Jamieson. Here, Alec was the first to bring a high-speed camera into the mountains to observe crack propagation in snow. This led to fascinating discoveries that triggered substantial changes in our understanding of avalanche release. Eventually, his journey led him to the WSL Institute for Snow and Avalanche Research in Davos, Switzerland, where he now leads the research group 'Avalanche Formation and Dynamics'. Although the tools to study snow and our understanding of avalanches have drastically improved over the years, Alec remains deeply fascinated by snow, and he enjoys digging in it almost as much as skiing on it.

References

- [1] A. van Herwijnen and B. Jamieson. High-speed photography of fractures in weak snowpack layers. *Cold Regions Science and Technology*, 43(1-2):71–82, 2005.
- [2] A. van Herwijnen, J. Schweizer, and J. Heierli. Measurement of the deformation field associated with fracture propagation in weak snowpack layers. *Journal of Geophysical Research*, 115:F03042, 2010.
- [3] J. Heierli, P. Gumbsch, and M. Zaiser. Anticrack nucleation as triggering mechanism for snow slab avalanches. *Science*, 321(5886):240–243, 2008.
- [4] J. Gaume, T. Gast, J. Teran, A. van Herwijnen, and C. Jiang. Dynamic anticrack propagation in snow. *Nature Communications*, 9(1):3047, 2018.
- [5] B. Bergfeld, A. van Herwijnen, B. Reuter, G. Bobillier, J. Dual, and J. Schweizer. Dynamic crack propagation in weak snowpack layers: insights from high-resolution, high-speed photography. *The Cryosphere*, 15(7):3539–3553, 2021.
- [6] B. Trottet, R. Simenhois, G. Bobillier, B. Bergfeld, A. van Herwijnen, C. F. F. Jiang, and J. Gaume. Transition from sub-rayleigh anticrack to supershear crack propagation in snow avalanches. *Nature Physics*, 18(9):1094–1098, 2022.

X-ray digital image correlation for deformation measurements in extreme environments

E.M.C. Jones

Sandia National Laboratories, Albuquerque, NM, USA

Abstract – Optical DIC can suffer when applied to complex test configurations from disturbances in the air between the surface of interest and the camera, like heat waves or shocks. Moreover, optical DIC does not allow for internal measurements, where the surface of interest is not directly visible. X-ray imaging for DIC addresses many of the challenges with visible light imaging as X-rays do not refract through density gradients in air and are able to penetrate visibly opaque objects. This presentation will discuss four applications of X-ray DIC at Sandia National Laboratories in extreme environments including heat waves, shock tubes, combusting specimens, and explosions.

Keywords – DIC, X-rays

Introduction Optical, non-contact diagnostics such as Digital Image Correlation (DIC) are advantageous over their physical probe counterparts for kinematic measurements, as they are non-intrusive to the system being studied and provide full-field data instead of only point data. While extremely powerful and increasingly common for experimental mechanics, optical DIC can suffer when applied to complex test configurations from disturbances in the air between the surface of interest and the camera, like heat waves or shocks. Moreover, optical DIC does not allow for internal measurements, where the surface of interest is not directly visible.

X-ray imaging for DIC addresses many of the challenges with visible light imaging as X-rays do not refract through density gradients in air and are able to penetrate visibly opaque objects. X-ray DIC has been successfully used for many applications, where a high contrast image intensity pattern was created as X-rays were attenuated through either a naturally heterogeneous test unit or through a random pattern of a dense material applied onto or inside of a test unit. In simplified experimental configurations, where only a single object of interest is patterned and moves, the X-ray images can be treated identically to optical images and correlated with standard DIC software. However, for more complex configurations, where multiple objects move independently, conservation of intensity may be violated and standard DIC software may fail to correlate the images. To address this issue, path-integrated DIC (PI-DIC) was developed, wherein the fundamental matching criterion of DIC was modified to account for multiple, independently moving components contributing to the final image intensity.

This presentation will discuss several applications of X-ray DIC at Sandia National Laboratories, including (1) a careful comparison of optical DIC and X-ray DIC in the presence of heat waves, to verify the accuracy of X-ray DIC [1]; (2) vibrations of a bolted assembly in response to fluid loading from a shock front and subsequent vortex shedding in a shock tube [2]; (3) pressurization and thermal deformation of an aluminum-skinned, fiber-epoxy composite subjected to radiant heating and ultimately combustion [3-5]; and (4) deformation of internal components of an assembly subjected to a light-initiated explosive detonation.

Methods & Results Optical and/or X-ray DIC was performed in four applications of extreme environments. In the first validation experiment, a hot plate was placed between the cameras and a static specimen to induce heat waves. Optical DIC measured false displacements of up to 30 μm and resulting strains of 1300 $\mu\text{m}/\text{m}$, while X-ray DIC had errors of only 1–2 μm and strains 2–3 times lower (Fig. 1a), demonstrating the power of X-ray DIC to provide accurate results of specimen motion and deformation in harsh environments [1]. In the second experiment, stereo X-ray DIC was performed at 10 kHz on the internal surface of a jointed structure in a shock tube at a shock Mach number of 1.42 and compared with optical DIC measurements on the outer, visible surface of the structure (Fig. 1b). Density gradients in the air caused by the shock front and vortex shedding caused bias errors in optical DIC measurements

due to beam steering, but had minimal influence on the X-ray DIC measurements [2]. In the third experiment, an aluminum-skinned, fiber-epoxy composite cylinder was subjected to radiant heating mimicking an adjacent fire, where the specimen heated to surface temperatures $>700\text{ C}$, pressurized, deformed, and ultimately combusted and was engulfed in flames. Stereo X-ray DIC successfully measured the change in radius *in situ* in this extreme environment (Fig. 1c), where physical strain gauges and optical DIC were precluded [3–5]. Finally, in the fourth experiment, four interior components of a ring assembly were all imaged at 12.5 kHz with X-rays while a light-initiated explosive was detonated on the outer surface of the ring (Fig. 1d). Not only were the regions-of-interest not optically visible, but the light from the both the initiating lamps as well as the explosive detonation completely saturated optical imaging and prevented optical DIC.

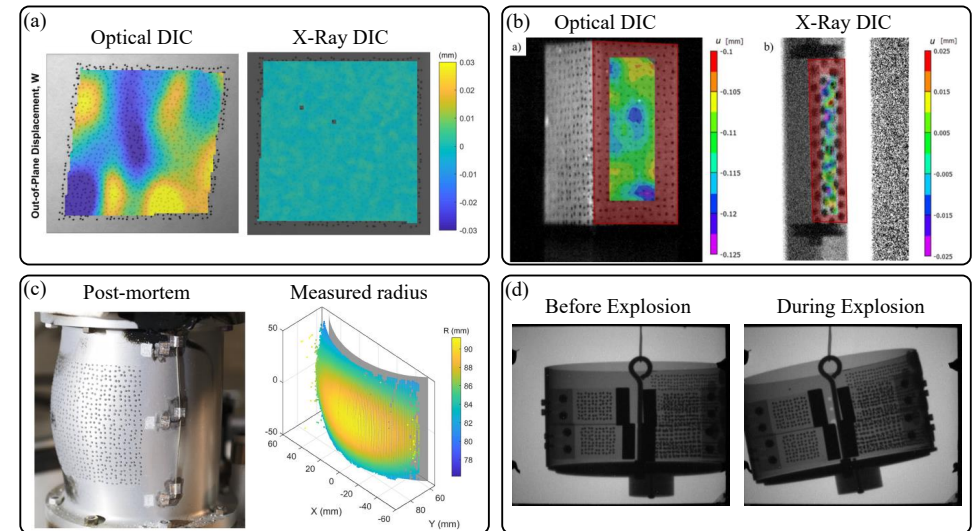


Figure 1: (a) Optical DIC suffers false displacement caused by heat waves, while X-ray DIC is robust [1]. (b) Optical DIC suffers false displacements from a shock front and vortex shedding, while X-ray DIC provides vibration measurements of the interior of a bolted structure tested in a shock tube [2]. (c) X-ray DIC measures the change in radius *in situ* of an aluminum-skinned fiber-epoxy composite subjected to radiant heating, pressurization, and ultimately combustion [4]. (d) X-ray images capture motion of interior components of an assembly subjected to a light-initiated explosion.

Discussion and Conclusion X-ray DIC is a powerful technique to garner full-field deformation measurements of a test article in extreme environments, where physical gauges and optical DIC are not feasible. This talk presents four applications of X-ray DIC performed at Sandia National Laboratories, from heat waves to combusting samples, and from shock tubes to explosive tests.

Acknowledgements Innumerable people contributed to the experiments described in this work, and the author especially thanks key team members E. Quintana, P. Reu, J. Wagner, J. James, K. Lynch, B. Halls, S. Fayad, C. Winters, B. Houchens, and E. Zepper. SNL is managed and operated by NTESS under DOE NNSA contract DE-NA0003525.

References

- [1] E.M.C. Jones, et al. *Exp. Tech.*, 44:159–174, 2020, DOI: 10.1007/s40799-019-00339-7
- [2] J.W. James, et al. *Exp. Tech.*, 46:1061–1068, 2022, DOI: 10.1007/s40799-021-00508-7
- [3] E.M.C. Jones, et al. *Exp. Mech.*, 63:681–701, 2023, DOI: 10.1007/s11340-023-00949-8
- [4] E.M.C. Jones. *Exp. Mech.*, 64:405–423, 2024, DOI: 10.1007/s11340-023-01029-7
- [5] S.S. Fayad, et al. *Exp. Tech.*, 2024, DOI: 10.1007/s40799-024-00707-y

Deformation of CANDU Pressure Tube under Biaxial Stress State at High Temperatures

C. Azih¹, H. Mazhar², R. MacCoy¹, C. Bramburger¹, R. McGrath¹

¹Canadian Nuclear Laboratories, Chalk River, Canada; ²Canadian Nuclear Safety Commission, Ottawa, Canada

Abstract

The CANDU (CANadian Deuterium Uranium) nuclear reactors are pressure tube reactors, with fuel channels that are comprised of a calandria tube and a smaller diameter, concentric pressure tube (pressure boundary), which houses the nuclear fuel and pressurized coolant. In some postulated accident scenarios, the pressure tube gets heated to high temperatures ($> 650^{\circ}\text{C}$) and deforms ($\sim 18\%$) into contact with the calandria tube. This deformation establishes a path to remove heat from the fuel. A method was developed to apply Digital Image Correlation paired with thermography images to measure deformation of prototypical biaxial stress tests and compare results to historical models developed from tests on uniaxial specimens.

Keywords – DIC, Thermography, Nuclear Reactor, High Temperature

Background and Introduction

The CANDU (CANadian Deuterium Uranium) nuclear reactors are pressure tube reactors, where the fuel channel consists of a calandria tube and a concentric pressure tube (pressure boundary), which houses the nuclear fuel and pressurized coolant. In some postulated accident scenarios, the pressure tube gets heated to high temperatures (600 to 900°C) and deforms ($\sim 18\%$) into contact with the calandria tube forming a path to remove heat from the fuel through boiling of the water (moderator) on the outside of the calandria tube. The pressure tube is heated at a high rate of 10 to 30°C/s and the temperature at which the pressure tube contacts the calandria tube is a primary parameter that determines the boiling regime that will occur. Therefore, precise prediction of the pressure tube strain is crucial. Best estimate prediction of this scenario is desired to demonstrate adequate heat removal; thus, prediction methodologies are compared against experiments that mimic the accident scenario. The International Atomic Energy Agency (IAEA) facilitated a benchmarking exercise where various institutions performed a total of 13 blind simulations of an experiment of the accident scenario (heating rate of 22°C/s) [1]. All but one simulation predicted contact temperatures in the range of 700 to 810°C , whereas the measured value was 875°C . At a heating rate of 22°C/s , overestimated strain rate predictions will lead to pressure tube calandria tube contact occurring earlier than in the experiments, and thus occurring at a temperature notably below the measured contact temperature. All simulations used the Shewfelt correlation for predicting pressure tube strain rate [2].

This work applies digital image correlation (DIC) technique on prototypical-diameter pressure tubes heated to high temperatures to better understand the degree of conservatism of the Shewfelt equations in predicting transient pressure tube strain. DIC measurements are paired with thermography images to obtain a field measurement of temperature and strain.

Experimental Methods

Through three successive trials, a suitable method for performing DIC on pressure tubes experiencing high temperatures and large deformations was developed. The high temperatures result in large deformation as the pressure tube (Zirconium alloy) exhibits superplastic behaviour as it undergoes α to β transformation in its crystalline structure. The experimental setup consisted of a vertically mounted pressure tube with a nominal outer diameter of 112.4 mm that is pressurized to 3.5 MPa with argon, and then heated with an internal graphite heater. The internal pressure subjects the tube to biaxial stress conditions. Before the tests, a white coating is applied to the outside surface of the tube using an alumina-based high temperature paint. A black speckled pattern is created against this white backdrop using a graphite-based coating compound. This pattern is developed to withstand temperatures in excess

of 800°C . Two DIC systems, both Aramis 12M model, set up orthogonal to one another, captured the transient deformation of the PT surface (1 Hz). Two Forward Looking InfraRed (FLIR) thermal cameras, models A325sc and A6261, simultaneously measured the surface temperature (10 Hz), calibrated over a range of 200 to 2000°C . A first-surface mirror was also used with one of the systems to further increase the circumferential field of view. Data from the two systems are amalgamated into a single analysis. To avoid saturation of the camera at high temperatures due to metal incandescence, blue light band-pass filters are applied to the DIC camera lenses. The surface is also illuminated with a blue light source.

Results

A power of 42 kW heated the tube from room temperature up to a maximum temperature of 821°C at a heating rate of 7.5°C/s . The measured deformation profile from the DIC system was mapped onto a structured grid using linear interpolation. The thermal images were reoriented, projected, and interpolated onto the same grid. The temperature mapped onto the deformed geometry is shown in Figure 1(a), where time origin, $t = 0$, corresponds to the time when a temperature of 200°C is measured. Plastic deformation occurred on the pressure tube with up to 26.3% change in radius measured through DIC.

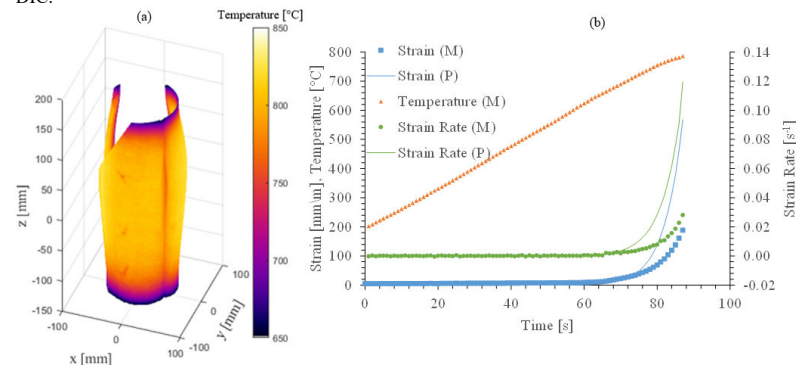


Figure 1: Temperature and deformation profiles: (a) 3D DIC and thermal plot at $t = 87$ s; (b) measured (M) and predicted (P) temperatures, strains, and strain rates at $x = 0, z = 0$.

Discussion

Deformation results from the present measurement are compared against predictions from the Shewfelt equations in Figure 1(b). Although the thickness to radius ratio of the pressure tube is 12% , thin wall theory is applied for this comparison. Transient data in Figure 1(b) is extracted at the axial centre ($z = 0$), and the $x = 0$ location defined in Figure 1(a). The results confirm that the Shewfelt equations overestimates the pressure tube strain and strain rate, with an end-of-test measured strain of 26.3% and a predicted strain of 56.7% , respectively. Under the selected conditions, Figure 1(b) shows that the overestimation of the strain rate increases with increasing temperature, therefore, compounding the overestimation of strain. The measured and predicted time for pressure tube to calandria tube contact (i.e. strain of 18%) is 85 s and 81 s, respectively. At a heating rate of 7.5°C/s this would result in underestimation of the contact temperature by a margin of 30°C .

References

- [1] IAEA, "Heavy water reactor moderator effectiveness as a backup heat sink during accidents", *IAEA Tecdoc Series*, IAEA-TECDOC-1890, 2019.
- [2] R.S.W Shewfelt, L.W. Lyall, and D.P. Godin, "A high-temperature creep model for Zr-2.5 wt% Nb pressure tubes", *Journal of Nuclear Materials*, 125, p. 228–235, 1984.

A SHPB digital twin for the optimization of specimens dedicated to heterogeneous high strain rate tests

T. Fourest, N. Leconte

DMAS, ONERA, 59000, Lille, France

Abstract — A finite element (FE) model of the ONERA Split Pressure Hopkinson Bars (SHPB) device is built. It is validated by comparing the experimental and numerical incident, reflected and transmitted force signals of a campaign featuring cylindrical specimens. The SHPB validated digital twin can thus now be used so as to explore specimen design and to find "optimal" geometries for the identification of viscoplastic behavior using optical measurements and inverse methods.

Keywords — Split Hopkinson Pressure Bar, Digital Twin, Specimen Optimization

Introduction Characterizing the behavior of materials at high strain rates is commonly accomplished using uniaxial tests. These tests, along with their setups, often stem from standards initially designed for quasi-static tests. They typically rely on a statically determinate approach, assuming specific conditions during experiments. Consequently, the analysis presupposes uniform strain and strain rate across the specimen's gauge length. Thus, for materials with rate-dependent behavior, conducting the test campaign becomes more demanding, as it requires a significant number of experiments to characterize the behavior across various strain and strain rate ranges.

Thanks to the progress in imaging technology, it is now feasible to measure kinematic fields at numerous points across a test specimen's surface at high frame rates. Based on these measurements, several inverse methods have been developed for the identification of material parameters from full-field measurements. Using these methods results in a paradigm shift, in which it is of prime importance to design specimens that will fulfil two somewhat conflicting objectives: generating heterogeneous strain/stress states and allowing robust optical measurements. The former leads to complex specimen geometries, while the latter tends to require simple ones [1].

Methods In this study, we adopt a digital twin approach, similar to the methodology outlined in [2], to investigate the influence of measurement biases on identification results relative to different configurations of specimen geometry. Our approach involves developing a finite element (FE) model of both the testing device and the specimen. To do so, a FE model of ONERA Kolski-type Split Hopkinson Pressure Bar (SHPB) device is built using *EUROPLEXUS* FE solver. It follows a 1D/3D FE approach, similarly to a model built for pre-stretched Split Hopkinson Tension Bar [3]. Note that the contact between the

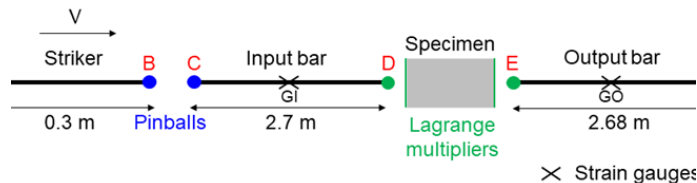


Figure 1: Sckematics of the SHPB FE model.

striker and the input bar is handled by means of pinballs, while the interfaces between the specimen and the input or output bars are handled by means of Lagrange multipliers, see Figure 1.

Results The SHPB numerical model was validated by comparing the incident, reflected, and transmitted experimental and numerical force signals at input and output bar gauge locations in a campaign considering cylindrical specimens, see Figure 2.

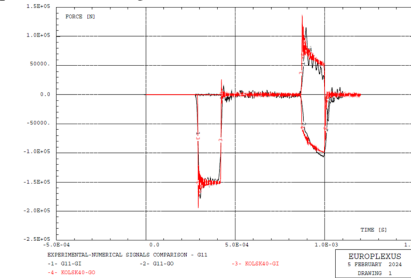


Figure 2: Experimental (black) and numerical (red) force signals recorded at input and output bar gauge locations.

Discussion and Conclusion Subsequently, since the developed SHPB model is validated, it will be used to optimize a perforated plate specimen geometry (Figure 3). This will be done by parametrizing the specimen shape, here the hole position and radius in a rectangular specimen. Then, the FE results will be used to generate synthetic images that will be processed by DIC and the Virtual Field Method in an attempt to determine a compromise between the two objectives mentioned previously.

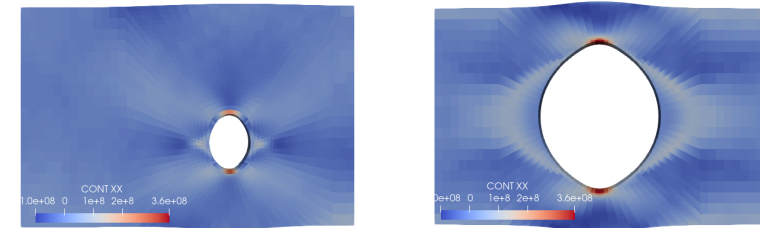


Figure 3: Axial stress at the final stage of the simulations for two specimen geometries with a hole, depending on the hole radius and position.

Acknowledgements This work has been funded within the frame of the Clean Aviation Joint Undertaking, Multi-MW Hybrid-Electric Propulsion System for Regional Aircraft, being part of the Horizon Europe research and innovation funding program of the European Commission.

References

- [1] Jean-David Thoby, Thomas Fourest, Bertrand Langrand, Delphine Notta-Cuvier, and Eric Markiewicz. Robustness of specimen design criteria for identification of anisotropic mechanical behaviour from heterogeneous mechanical fields. *Computational Materials Science*, 207:111260, 2022.
- [2] Pascal Bouda, Bertrand Langrand, Delphine Notta-Cuvier, Eric Markiewicz, and Fabrice Pierron. A computational approach to design new tests for viscoplasticity characterization at high strain-rates. *Computational Mechanics*, 64(6):1639–1654, 2019.
- [3] Grégory Haugou, Nicolas Leconte, and Hervé Morvan. Design of a pre-stretched tension hopkinson bar device: Configuration, tail corrections, and numerical validation. *International Journal of Impact Engineering*, 97:89–101, 2016.

Universal Tomographic Calibration: Achieving 1/100th Voxel Digital Volume Correlation (DVC) Displacement Precision

A. Arzoumanidis¹, H. Lu², A.B. Phillion³, B.K. Bay⁴

¹Psylotech, Inc. Evanston, IL, USA

²Department of Mechanical Engineering, The University of Texas at Dallas, Dallas, Texas, USA

³Department of Materials Science and Engineering, McMaster University, Hamilton, Ontario, Canada

⁴Department of Mechanical, Industrial & Manufacturing Engineering, Oregon State University, Corvallis, Oregon, USA

Abstract Stereo digital image correlation (stereo-DIC) uses calibration targets and the associated procedures to compensate for imperfect camera mounting geometry and optical component distortion. We propose an analogous volumetric representation of tomography system geometry, coupled with parameterized models for the apparatus imperfections, and calibration through a spherical marker tracking process. The framework provides corrections for scanning and *in situ* hardware misalignments, sample rotation axis imperfections, and detector optics distortions in both cone-beam and parallel beam systems. The goal is to enable digital volume correlation (DVC) at the same levels of sub-pixel/voxel accuracy routinely achieved with contemporary stereo-DIC technique.

Keywords – Digital Volume Correlation, DVC, metrology, computed tomography

Introduction Digital Volume Correlation continues to expand as a powerful tool for volumetric deformation measurements, but significant challenges remain, for example: (1) x-ray tomography (XCT) systems are not, in general, routinely calibrated to ensure accurate dimensional measurements, and (2) the axis around which an object rotates is not necessarily consistent in position or alignment as required in the tomographic reconstruction process. Rotation stages, particularly when subjected to *in situ* loads, exhibit non-repeatable eccentricity, wobble, and axial excursion. These problems are not quantified or corrected by established methodologies and have been documented as common and significant in tomography systems [1]. Limited *kinematic* precision constrains the full potential of XCT, even as improvements in x-ray source and detector technologies have brought high-resolution (sub-micron) projection imaging to a growing number of research laboratories. Imaging resolution now routinely exceeds the kinematic accuracy of even high-precision mechanical bearings. These problems are exacerbated by rotating load train universal testing systems, where two axes must be aligned, and each contributes to alignment errors. We have developed an approach to mitigate these errors.

Methods The technique has both hardware and software components. Let us consider a universal material test system with a rotating load train (Fig. 1). Spherical markers are held within the radiograph field of view. The holders are relatively X-ray transparent, while the markers are radiodense to a level appropriate for a particular sample composition. The software methodology unfolds in three steps: 1) tracking markers through 2D projection image sequences as a sample rotates, 2) utilizing numerical optimization to ascertain the optimal sample rotation axis position/orientation within the 3D instrumentation space, and 3) adjusting individual projection images to correct misalignment and distortion. The process defines a single axis for tomographic reconstruction and a set of optimally matched projection images as a substitute for the original images. No adjustments of the system tomographic reconstruction software are required. Image adjustments will use high-performance interpolation methods validated within the stereo-DIC realm to eliminate subtle dimensional bias effects, and FEA-style spatial mapping procedures for projection image position/rotation/distortion corrections.

Results Figure 2 illustrates the progression of the methodology. A sample of coralline hydroxyapatite was imaged (Nikon 225 kV μ CT, 10 μ m voxel size) while held within a dual-axis *in situ* test device (Psylotech, Inc.). Spherical steel markers attached to upper and lower rotation axes (Fig. 2a) were tracked through the 720 projection image sequence and centroid positions were mapped onto the projection detector plane (Fig. 2b). Circular paths of virtual marker locations at the sample position within the 3d scanner space were created by optimizing elliptical fits between the actual marker locations and projections of the virtual markers onto the detector plane. The result is the ideal reconstruction axis associated with each rotation stage, plus deviations between the projection images and the idealized paths (Fig. 2c). Correction involves creating a new projection sequence by moving/rotating/distorting each projection back to a single unified axis for reconstruction, replacing the original.



Figure 1: Axial+torsion rotating load train universal test system, incorporating spherical marker holders to measure axes rotation.

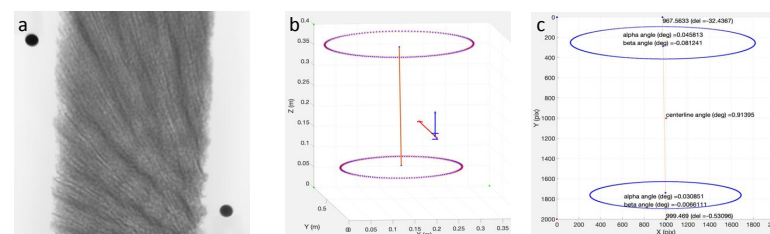


Figure 2: Projection image of the sample with fixed spherical markers and the detected and corrected trajectories. a) Markers within a projection image, b) a 3D model of the tomography system, and c) quantification of bearing rotation axis positions and orientations.

Discussion and Conclusion This work is developing under the hypothesis that image-based metrology via x-ray tomography, particularly at the extreme of sub-voxel precision demanded by DVC, cannot be achieved outside of a calibration process linked to a model of scan system geometry and an understanding of hardware characteristics and limitations. The process outlined here is universal in the sense that no scanner hardware or software modifications are required. We have demonstrated the ability to track markers during a representative scan, and have developed an optimization process to link data collected in the projection space to 3D scanner and tomographic reconstruction geometry. We are currently working on a full demonstration of the method.

Reference

Boundary conditions and constitutive parameter identification

A. Vintache^{1,2}, P. Baudoin¹, R. Gras¹, F. Mathieu¹, F. Hild²

¹ EikoSim, Montrouge, France

² Université Paris-Saclay, CentraleSupélec, ENS Paris-Saclay, CNRS, LMPS - Laboratoire de Mécanique Paris-Saclay, Gif-sur-Yvette, France.

Abstract — This study proposes a method to determine boundary conditions outside of the full-field measured area and calibrate elastoplastic parameters, allowing for a simulation of the full specimen geometry. This method has been compared to traditional routes and shows a better match between computed and measured displacement data. Measurement uncertainties are propagated at each procedure step, enhancing confidence in the optimized model.

Keywords — Finite Element Model Updating, boundary conditions, uncertainty propagation

Introduction Calibrating Finite Element (FE) models from experimental data, including DIC measurements, is a common practice to determine constitutive parameters. Ensuring the faithfulness of the boundary conditions (BCs) is essential to calibrate material parameters. Classical methods imply using part of the measured displacement data as BCs in the FE model. However, two main downsides can be mentioned:

1. measured displacement data are subjected to noise that corrupt the measured BCs (usually mitigated by filtering the measured data);
2. BCs may not be located in the full-field measurement area or hidden by fixtures (e.g., clamps). In that case, intermediate boundary conditions cannot be created far enough from the region of interest to satisfy Saint-Venant's principle.

This study proposes a method to address these challenges. By identifying parameterized BCs outside of the measurement area, measurement uncertainties have lowered impact on kinematic fields, and the simulation of the whole structure can be considered. This method is demonstrated through a tensile test on an aluminum alloy specimen with three holes (Figure 1), which is modeled by Ludwig's law (i.e., with five constitutive parameters). The results will be compared with previous experiments on the same material [1, 2].

Methods The BCs are modeled as 3D rigid body motions applied to two node sets, each located at opposite ends of the dogbone specimen. This approach limits the instantaneous BCs to twelve degrees of freedom (i.e., six translations and six rotations), thereby simplifying their calibration. Among the multiple identification schemes [3, 4], the chosen method is the so-called weighted Finite Element Model Updating (FEMU) method [5]. It aims to minimize the Mahalanobis distance between the measured and computed data, considering the uncertainty in the measured data. This method is applied to determine, at each time step, the twelve boundary condition parameters using displacement data (FEMU-U) and initialized with the results of the previous step. Then, the constitutive parameters are identified using displacement and load data (FEMU-UF). The weighted FEMU method has already been proven effective when using multiple data sources [6, 7] or even multiple experiments [2]. Regularization is often necessary to achieve good convergence results [5, 8]. One of the most used methods is the so-called Tikhonov regularization [9], allowing the variation of the parameters to be controlled and kept close to the initial set. This process is repeated until convergence of BCs and constitutive parameters has been reached. The measurement uncertainties are propagated to the identified parameters at each step of the procedure.

Results The test was monitored using multiple measurement techniques, including 2D digital image correlation (DIC) on one face, stereocorrelation on the opposite face, strain gauges, and load measurements. As a first step, the method was applied in 2D (i.e., 6 BC parameters to identify) using 2D-DIC measurements and is compared to a situation where the measured displacement data are applied directly to the FE model as BCs. Then, the FEMU-UF procedure is run for each case to determine optimized constitutive parameters. The displacement uncertainties propagated through the BCs to the force measurement shows lower levels for the proposed method. A global match of the experimental and computed displacement data with respect to uncertainty levels has been observed. The mentioned results are summarized in Table 1 in terms of signal to noise ratios (SNR). In the case of identified BCs, only one iteration of the whole procedure (i.e., FEMU-U to determine BCs and FEMU-UF to determine constitutive parameters) was considered; it was not looped.

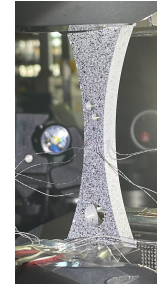


Figure 1: Tested dogbone sample with three holes

Table 1: Results for two different BC determination methods.

BC determination method	DIC measured BCs	Identified BCs
Propagated force uncertainty	36 N	18 N
Displacement residual	8.5 SNR	5.3 SNR

Discussion and Conclusion The present method shows that calibrating remote boundary conditions results in lower force uncertainties and more faithful displacements in comparison with the direct use of measured boundary conditions (e.g., via DIC). Its application in 3D situations (i.e., 12 BCs parameters, and use of stereocorrelation data) is the next step. Computational costs will be higher to determine the BC parameters. Potential applications of this method to industrial scales will be also explored.

References

- [1] J. Negggers, F. Mathieu, F. Hild, S. Roux., N. Swiergiel Improving full-field identification using progressive model enrichments *International Journal of Solids and Structures*, 118–119:213–223, 2017.
- [2] J. Negggers, F. Mathieu, F. Hild, S. Roux. Simultaneous full-field multi-experiment identification. *Mechanics of Materials*, 133:71–84, 2019.
- [3] S. Avril, M. Bonnet, A.S. Bretelle, M. Grédiac, F. Hild, P. Lenny, et al. Overview of Identification Methods of Mechanical Parameters Based on Full-field Measurements. *Experimental Mechanics*, 48(4):381–402, 2008.
- [4] S. Roux and F. Hild. Optimal procedure for the identification of constitutive parameters from experimentally measured displacement fields. *International Journal of Solids and Structures*, 184:14–23, 2020.
- [5] R. Gras, H. Leclerc, F. Hild, S. Roux, J. Schneider. Identification of a set of macroscopic elastic parameters in a 3D woven composite: Uncertainty analysis and regularization. *International Journal of Solids and Structures*, 55:2–16, 2015.
- [6] F. Mathieu, H. Leclerc, F. Hild, S. Roux. Estimation of Elastoplastic Parameters via Weighted FEMU and Integrated-DIC. *Experimental Mechanics*, 55(1):105–19, 2015.
- [7] M. Bery. High-temperature tests for ceramic matrix composites: from full-field regularised measurements to thermomechanical parameter identification. *Université Paris-Saclay*, 2020.
- [8] T. Archer, M. Bery, P. Beauchêne, F. Hild. Creep behavior identification of an environmental barrier coating using full-field measurements. *Journal of the European Ceramic Society*, 40(15):5704–18, 2020.
- [9] A.N. Tikhonov and V.J. Arsenin. *Solutions of ill-posed problems*. Winston, Washington, D.C (USA), 1977.

Deformation Behavior Analysis of Honeycomb Structure Under In-plane Compression Using Global DIC

Y. Yamaguchi, K. Iizuka, S. Yoneyama

Aoyama Gakuin University, Department of Mechanical Engineering, Japan

Abstract – The purpose of this study is to analyze the deformation behavior of a honeycomb structure that has undergone large deformation due to in-plane compression. The local strains of a fabricated honeycomb structure are measured using global DIC with a reference image updating method, in which DIC is performed by updating the reference image using a mesh overlapping the images taken during the test. The results demonstrate that the position of strain concentration shifts after significant deformation, and both the displacement of the overall deformed shape and local strains can be measured.

Keywords – DIC, Global-DIC, Honeycomb Structure

Introduction In recent years, improvements in technologies such as 3D printers have made it possible to manufacture micro parts with complex shapes such as lattice structures and honeycomb structures, which are now used in automobiles, medicine, shoe midsoles, and other applications. Such structures are subject to crushing, brittle fracture, and buckling under large deformation due to compressive loads, making them unrecyclable. In order to study structures and materials that can be reused, it is important to observe the deformation behavior under large compressive loads and local strain concentrations that cause failure during the compression process. To measure the displacement and strain of large deformations, strain gauges used for conventional strain measurement are not applicable. Therefore, digital image correlation (DIC), which can measure strain without contact, is used to measure local strain during large deformation. By combining the quantitative analysis of local strain obtained from the DIC with the stress-strain response obtained from mechanical data, the purpose is to elucidate the deformation behavior of honeycomb structures when subjected to large compressive loads. The method used in this study is slightly different from this method, and uses global DIC, which defines a finite element mesh overlapping the image and uses the correlation of images inside the mesh to obtain the displacement of a nodal point. The reason for using global DIC is that when a specimen contains many free boundaries, as in the case of the specimen used in this study, conventional DIC has a problem that the measurement accuracy decreases if the background is included in the subset. Global DIC, however, creates a mesh for the object to be measured and focuses on the interior of the mesh. In order to measure the displacement and strain of a greatly deformed shape, the image correlation method requires that the reference image be updated by dividing it into small sections where the deformation is small so that the images can be correlated. However, it is time-consuming to create a mesh for the reference image for each update. In this study, the displacement and strain are measured using a global DIC that updates the reference image by adding the calculated displacement to the nodal coordinates of the mesh created for the reference image and then creating a new mesh for the reference image. The mesh is then updated to create a new reference image mesh.

Methods A Computer aided design (CAD) model of the specimen is created by changing the 20 mm cubic unit cell shape into a triangular honeycomb structure with a beam thickness of 1 mm, which is printed by a 3D printer (Mark two, Markforged). The material used for the specimens is thermoplastic polyurethane (TPU). The experimental images used are taken from 0 mm to 6.5 mm displacement of the crosshead of the testing machine, and the reference image is updated as 0.33 mm for each interval. Therefore, the number of cycles up to 6.5 mm is 19.

Results Figure 1(a) below shows the stress-strain diagram and Fig. 1(b),(c) show the typical experimental images for 0 mm and 6.5 mm crosshead displacement. The u_{ch} in this case represents the displacement of the crosshead of the testing machine. Figures 2 and 3 show the results of the Global

DIC at each of the intervals indicated by the red dots in Fig. 1(a). Figure 2 shows the distribution of the normal strains in the y direction of each interval, and Fig. 3 shows distribution of the displacement in the y direction up to that interval.

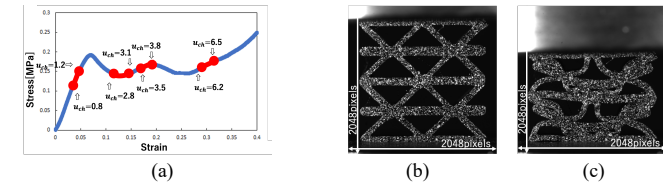


Figure 1 : Compression behavior.
(a) Stress strain diagram. (b) $u_{ch} = 0$ mm. (c) $u_{ch} = 6.5$ mm.

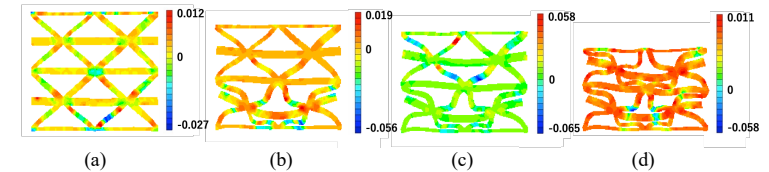


Figure 2 : ϵ_y of Global DIC.
(a) 0.8mm-1.2mm. (b) 2.8-3.1mm. (c) 3.5mm-3.8mm. (d) 6.2mm-6.5mm.

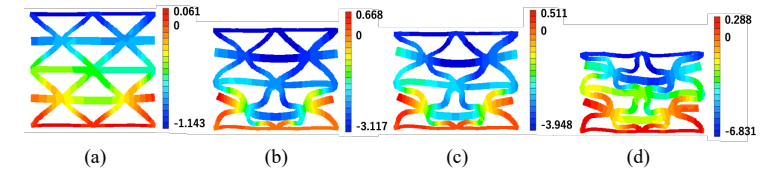


Figure 3 : u_y of Global DIC.
(a) 0.8mm-1.2mm. (b) 2.8-3.1mm. (c) 3.5mm-3.8mm. (d) 6.2mm-6.5mm.

Discussion and Conclusion Figure 1 shows the compressive behavior of the specimen, with a wavy stress-strain diagram in the plastic region. As can be seen from the shape of Fig. 2, buckling occurs in the lower beams and the stress decreases, but when the cell collapses, the stress increases due to densification. The same phenomenon is thought to occur in other cells as the buckling position changes, resulting in the compressive behavior shown in Fig. 2. From Fig. 2(a), it can be observed that strain is concentrated in the buckling region before buckling occurs. As shown in Fig. 2(b), buckling occurred in the upper beams when the cells in the lower layers collapsed. The strain concentration at the buckling point can be observed in Fig. 2(c), which is before the buckling, indicating that the location of the changed strain concentration can be captured. Figures 2 and 3(d) shows that $u_{ch} = 6.5$ mm, which indicates that displacement and strain of a large deformed shape are captured. These results indicate that the global DIC with reference image updating method can be used to measure local strain in the case of large deformation.

References

- [1] S. Yoneyama, J. Koyanagi, S. Arikawa. Discontinuous Displacement/Strain Measurement Using Mesh Based Digital Image Correlation. *Journal of the Japan Society for Composite Materials*, 40 : 180-188, 2014.
- [2] H. Jin, W. Lu, S. Scheffel, T.D. Hinnerichs, M.K. Neilsen. Full-field characterization of mechanical behavior of polyurethane foams. *International Journal of Solids and Structures*, 44 : 6930-6944, 2007.

Dual X-ray and Neutron tomography to observe hydro-mechanics in porous media

H. Gregg¹, A. Tengattini^{1,2}, O. Stamati¹, S. Roux³

1: Université Grenoble Alpes, Grenoble INP, 3SR, Grenoble, France
 2: ILL Neutrons for Society, Grenoble
 3: Université Paris Saclay, CentraleSupélec, École Normale Supérieure Paris Saclay, CNRS, LMPS, Gif-sur-Yvette, France

Abstract — This study exploits the synergies of X-ray and Neutron tomography to monitor saturation levels over time during a fluid injection test in a porous medium. It showcases how leveraging the capability of Neutron imaging to track fluid complemented by a porosity map from registered X-ray scan of higher spatial resolution can be used to enhance spatial and temporal resolution.

Keywords — X-ray tomography, Neutron tomography, Flow in porous media

Introduction X-ray tomography gives access to 3D attenuation fields at high-resolution, which is useful for differentiating between the pores and solid phases within porous materials. However, X-rays are very weakly absorbed by water, making them unsuitable for tracking fluids without introducing contrasting agents. Neutrons, on the other hand, interact strongly with hydrogen and have different sensitivities to various isotopes; H₂O has a much higher attenuation coefficient (or scattering cross-section) than D₂O, overcoming this limitation. Despite this advantage, neutron scanning is highly susceptible to noise, especially for short exposure time as required by high temporal resolution. Bi-modality has proven to be an effective method for balancing the shortcomings of each modality, resulting in a synergistic approach to studying hydro-mechanical processes [1]. NeXT 2.0 combines the world-leading flux of the ILL for neutron scanning with an X-ray setup on the same instrument [2]. In this study, dual X-ray and Neutron tomography acquired at this facility are used to determine saturation levels over time, fully showcasing the complementary of X-rays to yield high spatial resolution and neutrons to track fluid fronts.

Methods Water flow in a cylindrical porous sample of 25 mm in diameter and 50 mm in height is studied. The material is Idaho Gray sandstone with a mean grain size of approximately 300 μm and an estimated porosity of 30% [3]. An initial X-ray scan of the sample at a pixel size of 30 μm is paired with 60 neutron scans captured in 1-minute intervals with a pixel size of 200 μm. These scans were conducted on sandstone initially saturated with heavy water (D₂O) in which distilled water (H₂O) was slowly injected. The high contrast in neutron imaging between these two “similar” fluids allows to track the saturation over time and extract information about the flow field.

Although both tomographies are acquired on the same sample and set-up, it is important that both reconstructed volumes do share the same frame of reference, so that any material point can be labelled with a unique coordinate system. One difficulty is that the two modalities have different spatial resolutions. To map the two volumes with each other, the X-ray tomography is first gaussian-filtered at the neutron voxel size, and subsampled to obtain a similar resolution. Then, the SPAM [4] multimodal registration function is used to identify the transformation between the two “natural” coordinates systems (voxel numbering). In spite of the high definition of the X-ray tomography to access the detail of the pore space, since fluid flow is tracked with a low resolution, it was chosen to resort to a homogenized description, where porosity and saturation are both described as continuous fields spanning the entire volume. For this, a finite-element description based on a tetrahedral mesh is selected as a suited discretization. The

X-ray measured porosity field, $\phi(x)$, at the X-ray voxel scale, is thus approximated by its finite-element description. The set of nodal values $\hat{\phi}$ is obtained as the minimizer of the following equation, Eq. (1)

$$\hat{\phi} = \arg \min_{\hat{\phi}} \sum_x [\phi(x) - \hat{\phi} \cdot \hat{N}(x)]^2 \quad (1)$$

Finally, the saturation fields of invading H₂O as captured by the neutron scans were derived on the same FE-mesh after normalization using the attenuation assigned to H₂O and D₂O. Attenuation maps were calibrated to account for instability in beam flux and the pores were assumed to be initially fully saturated with heavy water.

Results Figure 1 presents the saturation field resulting from the analysis. It can be seen that the saturation map follows the localization of attenuation due to the invasion of H₂O.

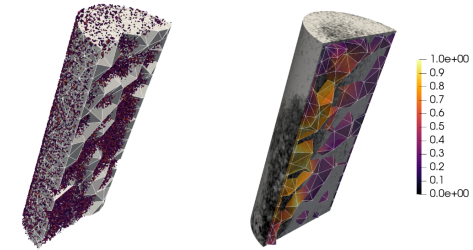


Figure 1: Left: Overlap of the FE-mesh with the porosity raster image derived from X-ray tomography. Right: Overlap of the FE-based mapping of saturation and neutron image attenuation from scan 55. Darker gray areas indicate higher attenuation due to the presence of H₂O in the sample.

Discussion and Conclusion The approach presented here uses accurate X-ray scans combined with neutron scans that have high temporal resolution but poor spatial resolution. A homogenised and continuous evolution of saturation over time within the sample, mapped onto a FE-mesh, is obtained. The finer spatial definition from the X-ray image, unavailable in the neutron images, enhances the porosity description and thereby improves the estimation of saturation maps. This synergy of the dual imaging at the NeXT facility allows for high temporal resolution and an improved continuous description of saturation.

Let us underline that this approach can be reversed, reconstructing a voxelwise volume from any arbitrary saturation field, allowing for a detailed validation of the description (or relevance of a continuous picture). Finally, from the projections of such saturation fields, and a suited basis for non-local temporal description, one may envision to resolve the 3D saturation field in time directly from radiographs [5], thereby enhancing dramatically temporal resolution.

References

- [1] Hall, S.A., Characterization of fluid flow in a shear band in porous rock using neutron radiography. *Geophysical Research Letters* 40, 2613–2618, 2013. <https://doi.org/10.1002/grl.150528>
- [2] Tengattini, A., Lenoir, N., Andò, E., Giroud, B., Atkins, D., Beaucour, J., Viggiani, G., NeXT-Grenoble, the Neutron and X-ray tomograph in Grenoble. *Nuclear Instruments and Methods in Physics Research Section A* 968, 163939, 2020. <https://doi.org/10.1016/j.nima.2020.163939>
- [3] Vieira Lima, F., Hall, S.A., Engqvist, J., Tudisco, E., Woracek, R., Tengattini, A., Vestin, P., The influence of heterogeneity and confining pressure on the hydromechanics of sandstone using neutron and x-ray imaging. In *IS-Grenoble 2024*.
- [4] Stamati, O. et al., ‘SPAM’: Software for Practical Analysis of Materials. *Journal of Open Source Software*, 5(51), 2286, 2020. <https://doi.org/10.21105/joss.02286>
- [5] Jailin, C., Etegarai, M., Tudisco, E., Hall, S. A., Roux, S., Fast tracking of fluid invasion using time-resolved neutron tomography. *Transport in Porous Media*, 124(1), 117-135, 2018. <https://doi.org/10.1007/s11242-018-1055-9>

Characterization of anisotropic hyperelastic behavior with a data-driven approach

A. Morch¹, M. Coret¹, A. Leygue¹, J. Réthoré¹,
P. Lecomte-Grosbras², J.-F. Witz²

¹ Nantes Université, Ecole Centrale Nantes, CNRS, GeM, UMR 6183, F-44000 Nantes, France.
² Univ. Lille, CNRS, Centrale Lille, UMR 2016 - LaMcube - Laboratoire de mécanique multiphysique multiéchelle, Lille F-59000, France

Abstract — Textile meshes are used to restore the physiological behavior of failing soft tissues. These meshes, once implanted in the body and colonized by scar tissue, form biological composites that typically exhibit an anisotropic hyperelastic behaviour. Experimental data, coupled with a data-driven identification approach, allow to identify the anisotropic signature and explore the choice of adequate features for constitutive modelling.

Keywords — Large strain, Anisotropy, DDI

Introduction Soft tissue pathologies often require surgical intervention and the implantation of a textile mesh. From a mechanical point of view, meshes help to limit extreme mobility or stiffen failing biological tissues. Their in vivo integration could be improved if the mechanical behavior of the mesh-tissue composite formed after implantation were similar to that of native physiological tissues, namely anisotropic hyperelastic behavior at finite strain. We propose a comparative experimental study of a textile-reinforced silicon that mimics the biological composite formed after implantation, coupling Digital Image Correlation (DIC) and Data Driven Identification (DDI) to investigate and model its anisotropic behavior.

Methods Two types of specimens were tested: isotropic pure silicon specimens and textile-reinforced silicon composites mimicking biological composites. The samples, see Fig.1, are loaded in a complex in-plane path using a hexapod (BREVA, Symetrie), coupling monotonic vertical translation with cyclic horizontal translation and in-plane rotation. Forces are measured using a 6-axis sensor (K6D40, ME Systems) and images are captured using a 47 MPx camera (Vieworks VA-47MC). A speckle pattern is applied to the sample to perform digital image correlation. Displacement fields are initiated by a coarse scale calculation using DISFlow [1] and optimised to finer scales using UFreckles software [2].

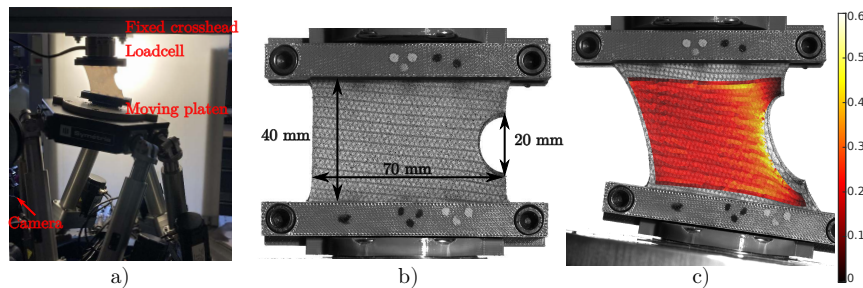


Figure 1: Sample testing - a) Hexapod and loading conditions, b) Composite sample, c) Green Lagrange strain field - E11

DDI aims to estimate the balanced stress field within the specimen from the measured displacement field and the applied forces, without prior knowledge of the constitutive law. The phase space describing the state of the material, called "mechanical state", consists of the finite strain Hencky tensor, $\mathbf{H} = \ln \mathbf{V}$, and the Cauchy stress tensor, $\boldsymbol{\sigma}$ [3]. Considering that similar deformation states generate similar stresses, the DDI consists of a clustering method P_{ei} to associate the e mechanical states with i "material states". The material and mechanical states are computed by minimising the variance between the mechanical and material states while ensuring stress equilibrium: $\min \sum_{e,i} \|(\mathbf{H}_e, \boldsymbol{\sigma}_e) - P_{ei}(\mathcal{H}_i, S_i)\|_2^2$ while ensuring the stress equilibrium, $\text{div}(\boldsymbol{\sigma}_e) = \underline{f}_e$.

Results The measured strain and corresponding stress tensors are symmetric and diagonalisable. The evaluation of the angle between principal stresses and strains, shown in Figure 2 a), clearly shows the signature of the anisotropy of the textile composite. The angular dispersion is wider and not centred around 0° as it is for the isotropic sample.

Following the work of [4], the strain energy density was also calculated from the DDI stresses as : $W = \int \boldsymbol{\sigma}_{DDI} : \mathbf{D} dt$ with $\mathbf{D} = \frac{1}{2}(\dot{\mathbf{F}}\mathbf{F}^{-1} + \mathbf{F}\dot{\mathbf{F}}^{-1})$.

The maps in Figure 2-b-c) show the evolution (in probability) of the error ratio between the energy densities evaluated in the experimental database and the average W for each pair of Hencky invariants (K_2, K_3). For smaller strains, *i.e.* small values of K_2 , this error remains large in both the isotropic and anisotropic cases. This may be due to the significant noise at these measurement levels. When K_2 (larger strain) increases, the deviation from the mean of the isotropic specimen decreases significantly. On the other hand, this deviation remains high for the anisotropic sample. The (K_2, K_3) pair represents isotropic invariants that can be used for isotropic modelling but, as expected, are not sufficient for anisotropic modelling. This type of mapping could therefore be useful to identify model parameters or anisotropic invariants to replace (K_2, K_3) and minimise the error.

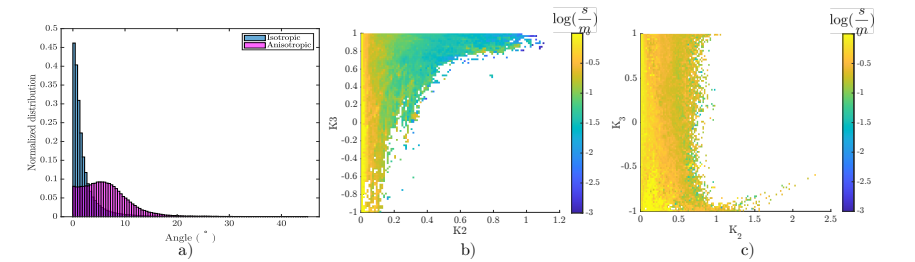


Figure 2: a) Distribution of the angle between principal stresses and strains, b-c) Joint histogram of the error s to the mean value m of W with regards to the Hencky invariants for an isotropic and anisotropic material respectively.

Discussion and Conclusion Thanks to DIC coupled with the DDI approach, the stresses and energy density of the material have been calculated without a priori selection of a model. It is capable of capturing the anisotropic signature in complex material under complex loading. It has previously been used on isotropic material to shorten the model identification process on complex geometries and loading conditions [4]. It offers new perspectives for the development of large strain anisotropic modelling by assessing the relevance of model parameters.

References

- [1] T. Kroeger, R. Timofte, D. Dai, L. Van Gool, *Fast optical flow using dense inverse search*, Computer Vision ECCV 2016
- [2] J. Réthoré, "UFreckles" 2018. doi: 10.5281/zenodo.1433776.
- [3] M. Dalémat, M. Coret, A. Leygue, E. Verron., *Measuring stress field without constitutive equation*, Mech Mater, 2019.

Full-Field Mechanical Deformation Behaviour of Different Metallic Laser Welded Joints under Tensile Loadings

P. E. Carrion¹, A. R. Jones^{1*}, E. Barrick², K.N. Karlson³, A. Polonsky⁴.

¹ Experimental Solid Mechanics

² Metallurgy & Materials Joining

³ Multi-Physics Modeling & Simulation

⁴ Materials Mechanics & Tribology

* Corresponding author's email : ajones1@sandia.gov

Sandia National Laboratories, 1515 Eubank SE, Albuquerque, NM, USA.

Abstract – Metal laser welding is a joining method widely implemented among aerospace, automotive, electronics, and other industries; however, the laser welding process often is susceptible to undesired cracking, part distortion, and specifically porosity formation. Hence, quality evaluation of welded components to predict and assess mechanical performance during and after fabrication is key. This study aims to characterize the effect of welded joints nonconformances on porosity generation and resultant mechanical performance of two individual material systems, including Aluminium and 304L stainless steel. Each material system was characterized by the following process: (i) Specimens were fabricated with varying laser weld depths and plate misalignments (i.e., varying gaps and offsets). (ii) Non-destructive evaluation of specimen porosity was conducted via X-ray CT scans and followed by destructive tensile tests. (iii) Digital Image Correlation (DIC) was used to examine the deformation behaviour and failure mechanisms of the welds during destructive testing. (iv) CT scans were used to incorporate porosity effects into the modelling and simulation of laser welds, which enabled mechanical performance predictions of each material system under monotonic tensile loading. Lastly, a similar characterization process is extended to evaluate novel joining methods used in the fabrication of dissimilar metal welds combining 304L stainless steel and Ti-6Al-4V into one material system.

Keywords – DIC, Welding, Dissimilar Metals, Material characterization

Introduction. Metal laser welding has increasingly been adopted in aerospace, automotive, small size electronics, and other industries since it offers substantial improvements over typical welding techniques. Laser welding advantages include reduced production time, reduced part distortion, as well as increased design flexibility, manufacturing speed, and increased weld parameters control (e.g., weld shape and penetration depth) [1, 2]. Typically, all components of the welded joint are all from the same material system; however, laser welding has enabled exploration in the realm of joining of dissimilar metals such as Aluminium and Copper [3]. Dissimilar metals laser welding may potentially increase design flexibility by enabling the combination of multiple material systems to obtain tailored mechanical properties such as maintaining ductility while increasing strength, reducing weight while maintaining strength, or increased corrosion resistance, etc.

Laser welded components can range from static non-load bearing to critical structural applications, which demand process quality control of the joints during and post fabrication. Weld quality evaluation methods include non-destructive and destructive techniques. For example, X-ray computed tomography, acoustic emissions, and mechanical testing [2] have all been utilized. Weld quality is influenced by several parameters such as laser beam properties and the gap/alignment between joint parts. Weld nonconformances created by varying the above mentioned parameters lead to induced porosity, lack of fusion regions, or premature cracking [2]. Therefore, investigation of weld parameter nonconformances to establish a design envelope that results in laser welded parts with an acceptable mechanical performance is highly desired. In this study, several laser weld nonconformances, including varying penetration depths and plate misalignments, are explored to characterize their effect on porosity generation and mechanical performance. Two material systems including an Aluminium alloy and 304L stainless steel (SS) are investigated. Lastly, novel dissimilar weld joining methods combining 304L (SS) and Ti-6Al-4V alloy into one material system are investigated, and the resultant mechanical performance is discussed.

Methods. The first part of the experiments includes the fabrication of same-metal welded specimens with several gaps (space between plates) and offsets (out of plane plate misalignments) using Aluminium and 304L stainless steel. The second part involves the fabrication of dissimilar metals welded specimens composed of 304L SS and Ti-6Al-4V joined together by an interlayer of Vanadium. Both sets of specimens were polished, etched, and evaluated via X-ray CT to have full local geometry characterization and internal porosity. Afterwards, monotonic tensile tests were conducted in displacement control at a rate of 0.1 mil/s. During tensile testing, Digital Image Correlation (DIC) was used to capture the deformation behaviour and failure mechanisms of the welds. The resultant mechanical data will be used to predict weld performance as shown in **Fig. (1)**.

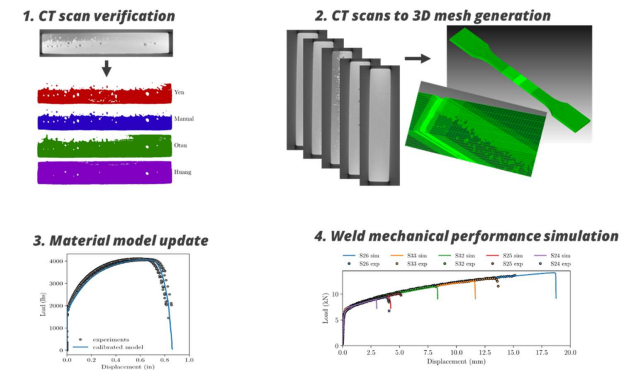


Figure 1: Schematic of the experimental characterization and simulation process. CT data (1) is used to generate a precise mesh of the weld geometry (2), and material model parameters are generated for the materials of interest (3). The ability of simulation to predict weld performance using CT based descriptors has shown promise in prior work (4).

Results. Preliminary load-displacement results for weld specimens fabricated with 304L SS are presented in **Fig. (2)**. It is observed that an increase in offset leads to a drastic reduction in overall ductility (maximum displacement at failure), while the impact of gap on mechanical performance is less severe. Moreover, the yield and deformation hardening behaviour remains similar for all conditions. The generated CT data for weld performance simulation and porosity evaluation was implemented using the methods described in [4, 5]. The CT data and simulation analysis revealed that a key laser weld feature for determining maximum load and displacement to failure is the net weld surface area, which is determined by including the weld depth and porosity. On the other hand, it was found that neither pore size nor weld offset were features that could be used to predict weld performance. The inclusion of CT data in simulation will be assessed for its usefulness in improving model predictivity. Similarly, a second material system (Aluminium) will be compared and contrasted with the present 304L results. Lastly, the current work will be applied to novel dissimilar weld joints. Preliminary dissimilar metal results indicate that the weld performance may be adjusted based on interlayer alloy selection, in this case, Vanadium.

Discussion and Conclusion. To quantify margins in the mechanical performance of laser welds, mechanical characterization was successfully correlated to CT-based simulation of laser welded joints with a suite of nonconformances including different gaps and offsets. This work represents a large-scale effort to build the technical basis for understanding the effect of geometric misalignments and porosity on weld performance, as well as the potential to predict the deformation behaviour using local geometry descriptors in simulation. Future work scope will involve the use of DIC to evaluate dissimilar metals welds complexity and interactions under loading and tie the behavior with CT based geometry data to enable the simulation-based prediction framework.

Optical Scanning Tomography to measure harmonic displacement fields and to identify visco-elastic parameters distributions

P. Doumalin¹, J.-C. Dupré¹, S. Kurtz^{2,3}, E. Van Houten³, B. Wattrisse²

¹ Institut P⁺, CNRS, Université de Poitiers
² LMGC, CNRS, Université de Montpellier
³ Mechanical Engineering Dept., Sherbrooke University, Canada

Abstract.

In this paper we propose to adapt the Optical Scanning Tomography proposed in [1] to measure 3D, time-harmonic displacement fields within a transparent material mimicking the visco-elastic phantoms used to characterize the performance of Magnetic Resonance Elastography methods. A thorough analysis of the measurement chain is performed in order to characterize the metrological performance of the method. Displacement fields obtained on different samples are analysed and the possibility to identify fields of material properties is demonstrated.

Keywords – Optical Scanning Tomography, Digital Volume Correlation, harmonic solicitations, soft material, heterogeneity detection

Introduction

The concept of elastography was introduced more than 30 years ago [2]. During that time span, numerous theoretical and technical developments were proposed to improve the sensitivity and the accuracy of the reconstruction of the fields of mechanical properties (elasticity, visco-elasticity, ...). In general, the identification methods are tested using computer-generated data or experimental data obtained using a single imaging modality (namely, the one used in practical applications). This can lead to ignore the influence of possible errors inherent to the imaging modality. In this paper, we propose to develop a specific Optical Scanning Tomography methodology to measure harmonic displacement fields in transparent materials. These fields could then be compared in future studies to the ones obtained by different clinically applicable methods such as ultrasound, or Magnetic Resonance Imaging (MRI).

Methods

The Figure 1 illustrates the setup for the developed Optical Scanning Tomography setup.

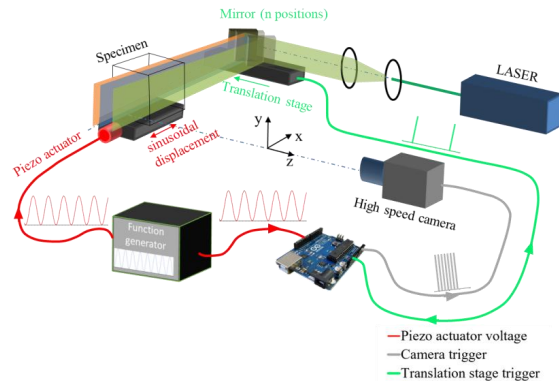


Figure 1: Optical scanning tomography setup and control device

A high speed camera records images of a slice of the sample illuminated by a planar laser beam. The laser beam is reflected by a mirror mounted on a translational stage. The sample is mounted on a stage linked to a linear piezoelectric actuator applying a sinusoidal displacement at a controlled frequency. A specific control device allows the synchronization between sinusoidal motion of the stage, the mirror's motion (allowing the slicing of the observed cube) and the image acquisition. Different cubic samples of RTV silicon gels were moulded (homogeneous and heterogenous). A white polyamide powder is added to the material during the mixing (average granulometry of 150 micrometres) in order to generate a speckle.

Results

A thorough metrology analysis was performed to characterize different biases of the method (intensity attenuation, parallax error, systematic and random DVC errors, ...). The harmonic displacement fields obtained for the maximum applied displacement are represented on Figure 2. They show the ability of the method to measure the perturbations caused by the sample heterogeneity. These displacement fields are then projected on harmonic shape functions in order to get results comparable to those given by other techniques such as MRI.

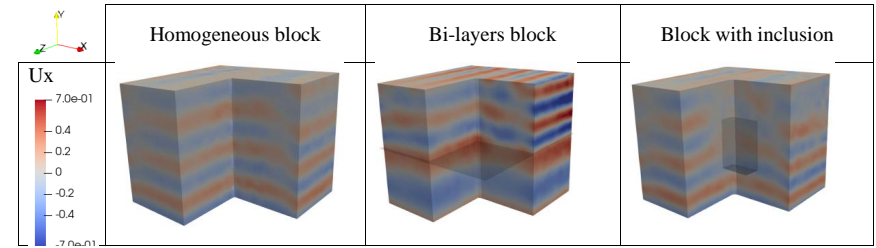


Figure 2 : Ux displacement fields relative to a harmonic solicitation in the direction x at 80 Hz for the maximal imposed displacement and three types of cubes

Discussion and Conclusion

The proposed technique is capable of measuring harmonic displacement fields in transparent phantoms. Numerical simulations corresponding to the different experimental configurations give consistent results with the experiments. The next steps of this work will be to use the measured displacement field to identify the mechanical property fields, and to confront these measurements to the ones obtained on the same samples and for the same solicitations with different techniques (MRI, ...).

References

[1] P. Morandi, F. Brémand, P. Doumalin, A. Germaneau, and J. C. Dupré, New Optical Scanning Tomography using a rotating slicing for time-resolved measurements of 3D full field displacements in structures, *Opt. Lasers Eng.*, 58, 2014.
 [2] J. Ophir, I. Céspedes, H. Ponnekanti, Y. Yazdi, and X. li, Elastography: A Quantitative Method for Imaging the Elasticity of Biological Tissues, *Ultrason Imaging*, 13(2), pp. 111–134, 1991.

Image-based B-Spline beam models of architected materials using Virtual Image Correlation with variable cross-section.

J.-C. Passieux¹, R. Bouclier^{1,2}, O. Weeger³

¹ ICA, INSA/ISAE Supaéro/Mines Albi/UT3, Toulouse, France. passieux, bouclier@insa-toulouse.fr

² IMT, INSA/UT1/UT2/UT3, Toulouse, France.

³ CPS, TU Darmstadt, Germany. weeger@cps.tu-darmstadt.de

Abstract — The characterization of architectural materials sometimes requires the construction of so-called *sample-specific* models. A method for building an explicit B-Spline lattice image-based model suitable for numerical simulation is presented. More specifically, we propose an extension of the Virtual Image Correlation method to the case of multiple interconnected beams with variable cross-sections. The method's performance is demonstrated through a series of synthetic and real image examples of lattice materials and more general cellular materials.

Keywords — isogeometric analysis, image based models, beams

Introduction Cellular materials like foams and lattice structures have complex architectures with material concentrated in small struts or webs. Recent advancements in manufacturing, particularly in metal additive manufacturing, have pushed these materials forward. Key challenges include modeling, characterization, simulation, and understanding geometric defects.

Foams have random architectures, making their geometry locally variable and unknown. Additive manufacturing processes introduce significant geometric biases in lattice structures. Therefore, accurately characterizing sample geometry is crucial for understanding mechanical properties [1].

This talk presents a model fitting technique focusing on lightweight beam models tailored to material morphology. It extends the Virtual Image Correlation algorithm to spline beam lattices and aims, in addition, to characterize strut thickness. An automatic initialization strategy is proposed for situations where initial topology is unknown, such as in foams.

Methods The sample is described as a network of interconnected B-Spline quadratic beams. Each control point is associated with two degrees of freedom that control the position of the centerline, while additional degrees of freedom describe section thickness evolution.

Like most recent versions of VIC [4] it is proposed to formulate the optimisation problem in the isoparametric space. The centerline position λ_c and the thickness λ_t of the interconnected beams are sought to minimize the difference between the real image and a synthetic virtual image:

$$\lambda_c, \lambda_t = \arg \min_{\lambda_c^*, \lambda_t^*} \sum_i \left(g(\xi_i, \eta_i; \lambda_c^*, \lambda_t^*) - f(\mathbf{x}(\xi_i, \eta_i; \lambda_c^*)) \right)^2, \quad (1)$$

where λ_c and λ_t are the control parameters of the centerline position and thickness evolution, respectively. f is the real image and g is a so-called *virtual* image with parametric thickness and \mathbf{x} is an hybrid mapping consisting of a univariate spline mapping \mathbf{x}_c plus a identity mapping along its normal \mathbf{n}_c :

$$\mathbf{x}(\xi, \eta; \lambda_c) = \mathbf{x}_c(\xi; \lambda_c) + \eta \mathbf{n}_c(\xi; \lambda_c), \quad (2)$$

for any point $(\xi, \eta) \in [0, 1] \times [-h, h]$ in the parametric space.

Results The method successfully constructs explicit B-Spline beam models from real images of complex foam microstructures, even without prior CAD knowledge. Image processing techniques and labeling yield an initial mesh, providing an excellent starting point for the proposed algorithm. The optimization process drastically reduces residual maps, effectively representing complex geometries. The resulting lightweight B-Spline beam model accurately captures the architecture with remarkable detail. Simulation results demonstrate the correspondence between the proposed B-Spline beam model and traditional finite element models in predicting deformation patterns under compression, particularly in nonlinear regimes.

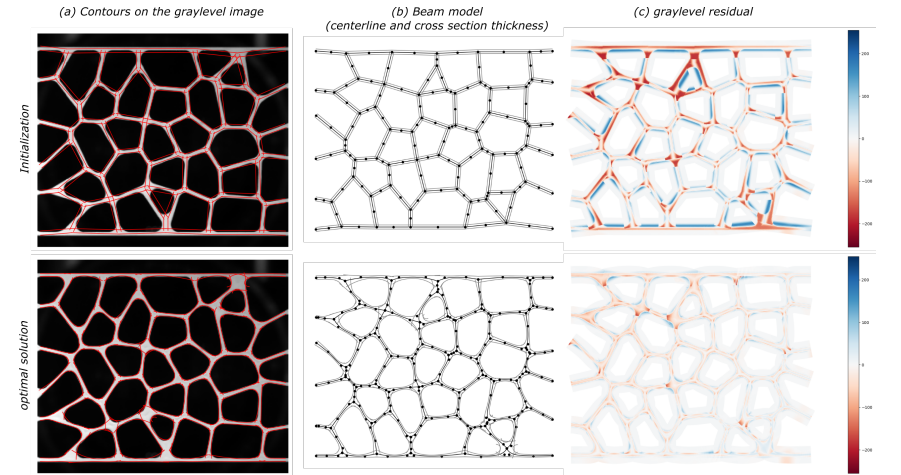


Figure 1: Initial (top) and optimized (bottom) CAD description of a real lattice: (a) estimation of the shape and thickness, (b) centerline, control points and thickness and (c) residuals.

Discussion and Conclusion The study presents a highly precise, numerically efficient method for constructing mechanical twins of complex cellular materials from grayscale images. The proposed approach, leveraging physics-based modeling and data-driven strategies, enables the creation of extremely reduced, predictive models, showcasing the continued potential for advanced modeling techniques in material science.

Acknowledgements This research was supported by the French Agence nationale de la recherche under grant ANR-22-CE46-0007 (AVATAR).

References

- [1] A. Rouwane, P. Doumalin, R. Bouclier, J.C. Passieux, J.N. Périé, Architecture-Driven Digital Volume Correlation: application to the analysis of in-situ crushing of a polyurethane foam, *Experimental Mechanics*, 63(5) (2023) 897–913.
- [2] M. L. François, B. Semin, H. Auradou, Identification of the shape of curvilinear beams and fibers, in: *Applied Mechanics and materials*, Vol. 24, Trans Tech Publ (2010) 359–364.
- [3] J.C. Passieux, R. Bouclier, O. Weeger, Oliver, Image-based isogeometric twins of lattices with virtual image correlation for varying cross-section beams, *Int. J. Numer. Meth. Engrg.* 124(10)(2023) 2237–2260
- [4] M. Baconnais, J. Réthoré, M. François, Improvement of the digital image correlation close to the borders of an object, *Strain* 56 (3) (2020) e12340.
- [5] R. Bouclier, J.C. Passieux, IGA: non-invasive coupling with FEM and regularization of digital image correlation problems, *Wiley*, (2023)

DIC for Detection of Embedded Structures

I. Nowakowska, Y. Chen, D. Hand

School of Engineering and Physical Sciences, Heriot-Watt University, Edinburgh, United Kingdom

Abstract

This study aims to establish the feasibility of detecting embedded structures and anomalies in human tissue during robotic surgery using DIC. Although there have been studies on using DIC as a tool for cancer detection [1,2], the tumour nodule was often on or very close to the tissue surface, which would significantly limit the application in surgery. Our study was conducted on silicon phantoms with a stiffer nodule embedded up to 20mm underneath the surface. Tension was applied first in an Instron tensometer, and then with surgical grippers in a laparoscopic trainer to investigate the effect of surgical conditions on the quality of the detection. A surgical endoscope was used to record the videos which were analysed using DuoDIC [3] and Ncorr [4]. The depth of the embedded nodule was found to affect the accuracy of the detection, as did the method of tension application to the samples.

Keywords – DIC, Heterogeneous materials, tissue mechanics

Introduction

There has been some research to determine if DIC can be used to find heterogeneous regions in biological tissues for purposes such as detecting cancer regions. Most of these studies align the camera in such a way that the inclusion is visible on the surface of the specimen [1,2], which can assist with the detection of skin cancer margins. However in many cases, tumours are embedded in the tissue and not visible from the surface. This study investigates if DIC can be used to find embedded heterogeneities in silicon phantoms and if these can be found in non-standard testing conditions such as applying the tension through laparoscopic surgical instruments.

Methods

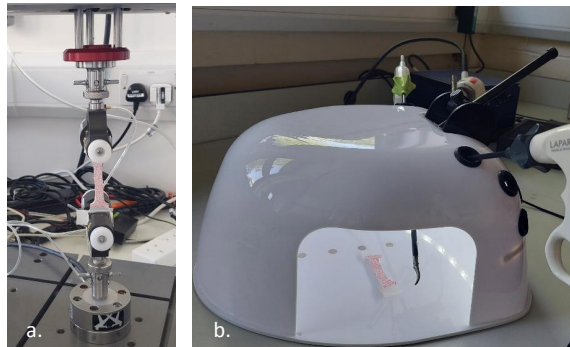


Figure 1: Experimental set-up with speckled silicone dogbone a. in Instron Tensometer b. in laparoscopic trainer

The experiment was conducted in two different settings, first in a standard tensile test on an Instron tensometer and then in a laparoscopic trainer with tension introduced by surgical grippers, operated by experienced surgeons, when the procedures were recorded by an endoscopic camera to simulate surgical conditions. The test specimens were prepared in a standard dog-bone shape and consisted of silicone and deadener mix with a matrix of main material intended to mimic pig liver, and an embedded nodule of a greater stiffness to mimic tumour. Three samples were tested with Instron, a uniform material sample, a sample with the nodule protruding on the surface of the specimen, and a

sample with the nodule embedded 1mm beneath the surface of the specimen. Further samples were tested in the laparoscopic trainer, with nodules embedded up to 20mm under the surface of the specimen respectively.

Results and Discussion

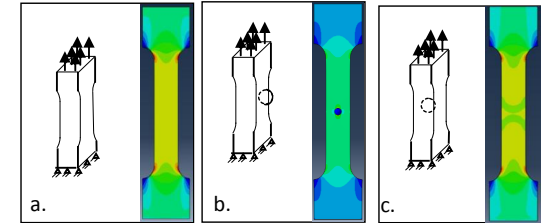


Figure 2: Strain field produced by FEA in dogbone under tension a. Without embedded nodule b. With nodule protruding at the surface c. With nodule embedded 1mm beneath the surface

The images were processed using the DuoDIC [3] plug-in for stereo DIC in Ncorr [4]. The detection method of the location of the nodule followed the methods proposed in [2], where the strain gradient was used to locate the boundary of the nodule. The accuracy of tumour nodule detection was found to increase with the difference in stiffness between the matrix and the nodule, and decrease with its increased depth in the phantom. A larger nodule also facilitated the detection of nodules at a greater depth. The uneven grip from the surgical clamps affect the tension applied to the tissue and thus the detection of the nodule.

Conclusion

This study investigates the feasibility of detecting a heterogeneity embedded in silicon using DIC. Silicone samples with varying depths of embedded nodule up to 20mm underneath the surface were put under tension and their strain fields were computer using stereo DIC to detect the nodule. It was found that the depth of the nodule and its difference in material properties to the matrix it was embedded in affected the accuracy of detection. This work could potentially lead to DIC being used for detection of tissue irregularities during surgery to improve clinical outcomes. Future work for this application includes optimisation of the force/displacement application to the tissue for an even application across full organs.

References

- [1] D. Claus, M. Mlikota, J. Geibel, T. Reichenbach, G. Pedrini, J. Mischinger, S. Schmauder, W. Osten, Large-field-of-view optical elastography using digital image correlation for biological soft tissue investigation. *Journal of Medical Imaging*, 4: 014505-014505, 2017
- [2] J.D. Krehbiel, J. Lambros, J.A. Viator, N.R. Sottos, Digital Image Correlation for Improved Detection of Basal Cell Carcinoma. *Experimental Mechanics*, 50:813-824, 2010
- [3] D. Solav, A. Silverstein, DuoDIC: 3D Digital Image Correlation in MATLAB. *Journal of Open Source Software*, 7:4279, 2022
- [4] J. Blaber, B. Adair, A. Antoniou, Ncorr: Open-Source 2D Digital Image Correlation Matlab Software. *Experimental Mechanics*, 55:1105-1122, 2015

Towards color X-ray tomography: Detection of small quartz grains via contrast-enhanced 3D images of carbonate rocks using a CdTe Photon Counting Detector

F. Decroos¹, P. Aïmedieu¹, S. Brisard², M. Bornert¹

¹Laboratoire Navier, Ecole des ponts, CNRS UMR 8205, Univ. G. Eiffel, Champs-sur-Marne, France

²Laboratoire de Mécanique et d'Acoustique, Univ. Aix-Marseille, Centrale Marseille, CNRS UMR 7031, Marseille, France

Abstract – A new generation Photon Counting Detector is used to distinguish quartz grains from nanoporous calcite grains in a carbonate rock sample imaged by absorption contrast X-ray tomography. Unlike standard so-called K-edge imaging techniques, the proposed method makes use of the smooth evolution with photon energy of the relative absorption between the chemical constituents, over the energy range adapted to the imaging of representative centimetric samples.

Keywords – X-Ray tomography, Photon Counting Detector, carbonate rock, chemical contrast.

Introduction Absorption X-ray Computed Tomography(CT) is a non-destructive imaging technique particularly relevant to study the behavior of heterogeneous geomaterials under mechanical load [1]. This requires to consider sufficiently large samples to be representative of their macroscopic behavior. If in addition they are imaged at a sufficiently fine spatial resolution to resolve their microstructure, the contribution of each constituent to the overall deformation can be investigated for an improved micromechanical insight on their behaviour. However, some materials exhibit very dim contrast between their constituents, either because of similar X-ray absorption properties of different chemical phases or because of the presence of nano-porosity in some components, not resolved with the used instrument resolution and thus rendered as a less absorbing phase. This is the case of the porous Saint Maximin carbonate rocks investigated in this study, in which dense carbonate (CaCO_3) larger grains (10-100 μm), nano-porous ones and smaller (~10 μm) quartz particles (SiO_2) are present besides macropores [2]. In standard absorption contrast tomography, it is difficult to distinguish quartz from nanoporous calcite grains. The use of Photon Counting Detectors (PCD) has a strong potential for contrast enhancement due its ability to count photons above a chosen energy threshold and thus take advantage of the specific dependance of linear absorption which energy between different phases to distinguish them. The CT technique called K-edge imaging makes in particular use of the strong discontinuity of this dependance near the characteristic rays of the elements. It has been developed and widely used for medical imaging [3]. However, this technique cannot be applied to geomaterials due to K-edge energy levels much lower than usual CT working conditions for centimetric samples (a few keV in comparison to about 100keV).

Method The proposed alternative method relies on using PCD thresholds to perform three different CT scans where constituents show sufficiently different relative absorption behavior, as shown in Figure 1. We selected data corresponding to the ranges i) 35-50 kV, ii) 55-70kV and iii) above 70 kV. Generator tension was set up to 100 kV and intensity to 110 μA . The used imager is a XC-Thor detector from the Direct Conversion company which has been integrated into the Ultratom CT device available at laboratoire Navier (Marne-la-Vallée, France). It features a 1024x256 square pixels sensor with a pixel size of 100 μm , associated with a 2mm thick CdTe sensor material. Two energy thresholds can be selected and two images are recorded at the same time, each counting the photons above selected thresholds. A new calibration methodology not detailed here had to be developed to produce radiographs without artifacts. The recording procedure corrects also for the presence of a gap of 100 μm between the 8 tiles of 128x256 pixels that constitute the sensor. The 14mm in diameter Saint Maximin sample was scanned two times with 1216 projections, using different low and high threshold. 20 images were averaged for each projection angle, resulting in a total scan time of 13 hours. The three 3D images associated with the three energy bands were reconstructed using the Xact software provided by the manufacturer of the CT device (RX-Solutions, Annecy). Voxel size was 14 μm .

Results A resulting slice relative to the 35-50 kV range can be seen in Figure2a, and is very similar with CT scan performed with Energy Integrating Detector (EID). Contrast-enhancement is then enabled by combining corresponding slices of the three CT scans in one color image using RGB channels. Resulting slice can be seen in Figure 2b and dominantly exhibits grey shades similarly to Figure 2a. This indicates that the relative absorption between brighter and darker areas does not depend on photon energy and is thus made of the same elements. However one can also clearly distinguish many small particles exhibiting the same blue shade, which correspond to another chemical component, with less relative absorption at low energy and more at high energy, resulting in a low R channel value and a high B one. Consistently with Figure1, these small grains are made of non-porous quartz, which can also be observed by more conventional (surface) Energy Dispersive Spectroscopy in a Scanning Electron Microscope.

Conclusion Contrast enhancement by Photon Counting Detectors has been shown to be applicable to phase detection in strongly absorbing large geomaterials samples. This open wide perspectives for the detailed full 3D microstructural analysis of complex materials and their evolution under various thermo-hydro-chemo-mechanical loads.

References

[1] T. Baxevanis, E. Papamichos, O. Flornes, and I. Larsen, “Compaction bands and induced permeability reduction in Tuffeau de Maastricht calcarenite,” *ACTA Geotech.*, vol. 1, no. 2, pp. 123–135, Sep. 2006, doi: 10.1007/s11440-006-0011-y.

[2] C. Doré-Ossipyan, J. Sulem, M. Bornert, and A. Dimanov, “Analyse multi-échelle de la déformation, de la localisation et de l’endommagement des carbonates poreux sous conditions de chargement triaxiales,” presented at the 11èmes journées nationales de géotechnique et de géologie de l’ingénieur, Jun. 2022. Accessed: May 16, 2024. [Online]. Available: <https://hal.science/hal-03719793>

[3] P. He, B. Wei, W. Cong, and G. Wang, “Optimization of K-edge imaging with spectral CT,” *Med. Phys.*, vol. 39, no. 11, pp. 6572–6579, Nov. 2012, doi: 10.1118/1.4754587.

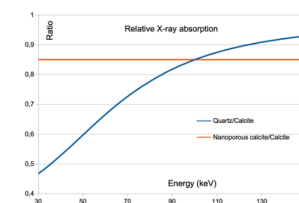


Figure 1: Relative linear X-Ray attenuation coefficient of Quartz (SiO_2) and Calcite (CaCO_3) as a function of photon energy (data source: NIST)

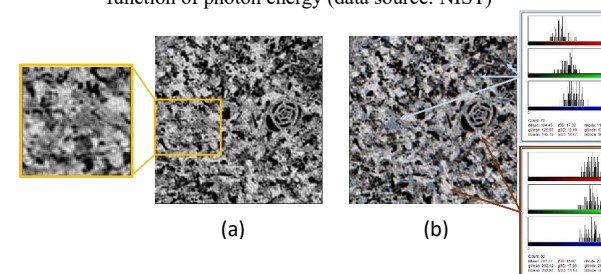


Figure 2: Horizontal slice through reconstructed CT volumes (field of view = 3x3mm). Standard CT image (a), three energy channels image (b)

Material testing 2.0 for viscoelasticity : characteristic time sensitivity vs experiment duration

M. Leclercq, R. Legroux, E. Vennat, J. Neggers

Université Paris Saclay, ENS Paris-Saclay, CentraleSupélec, CNRS, LMPS, 91190, Gif-sur-Yvette, France

Abstract — 3D-printed polymers are viscoelastic materials that exhibit time-dependent mechanical behavior requiring identification of many parameters over several time scales. A recent approach referred to as "Material testing 2.0" (MT2.0) is based on optimizing the testing conditions for identifying constitutive parameters with inverse methods. This study examines the sensitivities to constitutive viscoelastic parameters sought to determine Maxwell parameters for a range of time scales with a single test by Integrated Digital Image Correlation (I-DIC).

Keywords — Integrated Digital Image Correlation (IDIC), Viscoelasticity, Prony series, Sensitivity

Introduction Recent additive manufacturing processes such as PolyJet (Stratasys) enable printing gradient-properties structures by combining soft and rigid photopolymer materials, offering significant benefits, especially in the medical field. However, these materials exhibit complex process-structure-properties relationships, underscoring the need to deepen our understanding of their mechanical behavior [1]. In particular, these viscoelastic polymers exhibit time-dependent mechanical behavior requiring characterization on several time scales. A recent approach referred to by some authors as "Material testing 2.0" (MT2.0) combines full-field measurements and inverse methods to determine the constitutive parameters with optimized testing conditions [2]. Only some authors have studied the sensitivities of test variables such as displacement field to constitutive parameters sought as metrics for improving test design [3]. This approach has yet to be widely studied to characterize viscoelastic behavior. The proposed presentation investigates sensitivities to optimize the identification of viscoelastic constitutive parameters on several time scales using Integrated Digital Image Correlation (I-DIC) [4].

Methods Uniaxial and equi-biaxial relaxation-interrupted tensile tests were performed under temperature and humidity controlled conditions on VeroClear samples printed with a PolyJet J750 (Stratasys).

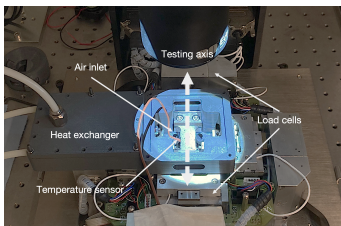


Figure 1: Experimental set-up

This study focuses on the stress relaxation observed for a uniaxial loading at a constant deformation level of 3% maintained during 300 sec, capturing 1 image per 2 seconds. Digital Image Correlation (DIC) was

computed with Correli 3.2 [5]. The linear viscoelastic behavior was parametrized with a Prony series. The set of unknown parameters with N viscoelastic modes is therefore :

$$\{p\} = \{E, \nu, g_i, k_i, \tau_i\}_{i=1\dots N}$$

with E, ν the elastic parameters and $\{g_i, k_i, \tau_i\}_{i=1\dots N}$ the normalized prony parameters of the $N = 5$ viscoelastic branches that have relaxation time τ_i ranging from 1 to 10^4 sec (logarithmically spaced). The sensitivity of a parameter p_i is measured as the influence of its perturbation on the data. One way to study sensitivity is to diagonalized the Hessian matrix $[H]$ used to minimize the cost function of the I-DIC problem, which is build on displacement field and force sensitivities weightned by the noise of each data sources.

Results The eigenvectors and eigenvalues of $[H]$ are presented in fig. 2. All modes have eigenvalues above the acquisition noise level, meaning that all viscoelastic branches are captured, even above the duration of the relaxation step. In practice, the duration of relaxation tests is adapted to the desired characteristic times, in order to cover all decades corresponding to real loading conditions. We show here that a single test of relatively short duration (a few minutes) can identify viscoelastic parameters over large time scales. However, the viscoelastic parameters in modes associated with the lowest eigenvalues have a meager contribution to the sensitivity field, making them challenging to identify.

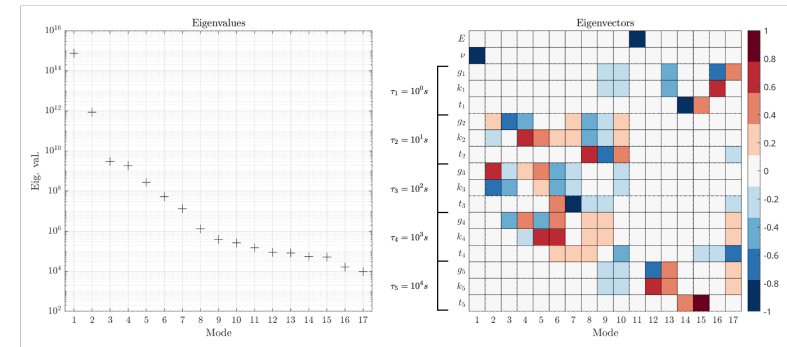


Figure 2: Eigenvalues and eigenvectors of the Hessian matrix (Signal-to-Noise ratio)

Discussion and Conclusion Modeling the time-dependent behavior of viscoelastic materials requires multiple and long-time testing. This study demonstrates that a single relaxation test allows the identification of viscoelastic behavior on a large time scale. The data obtained from uni- and biaxial tensile tests will then be used to enrich the identified behavior law with hyperelastic and anisotropic contributions. Thus, modeling the mechanical behavior of printed polymers involves complex characterization and many parameters, making MT2.0 methods particularly interesting for these identification cases [2].

References

- [1] Yun Lu Tee, Phuong Tran, Martin Leary, Philip Pille, and Milan Brandt. 3D printing of polymer composites with material jetting: Mechanical and fractographic analysis. *JOM* 36:101558.
- [2] Fabrice Pierron. Material testing 2.0: A brief review. *Strain* 59(3):e12434.
- [3] Morgane Chapelier. Non-invasive spline-based shape optimization strategies development for experimental mechanics. *PhD thesis report*. 2021.
- [4] Leclerc H., Périé J.N., Roux S. and Hild F. Integrated digital image correlation for the identification of mechanical properties. *Computer Science*, pages 161–171. 2009.
- [5] Leclerc, H., Neggers, J., Mathieu, F., Hild, F., Roux, S. Correli 3.0. *Agence de Protection des Programme* IDDN.FR.001.520008.000.S.P.2015.000.31500. 2016.

Application of digital image correlation in the characterization of metal powder spreadability for additive manufacturing

Lukas Daut¹, Brian K. Bay¹

¹Oregon State University, Corvallis, USA

Abstract Spreading metal powder layers uniformly and consistently is critical to the success of powder bed additive manufacturing processes such as selective laser melting. However, powder “spreadability” is poorly defined, and proxy measurements of related characteristics are currently used in attempts to improve build quality. This work sets out to define and quantify spreadability directly by measuring powder surface profiles using stereo digital image correlation (stereo-DIC). We have successfully integrated stereo-DIC with a commercial powder spread test system, evaluated surface profile measurement precision, and developed automated methods to detect and quantify spread anomalies.

Keywords – Stereo-DIC, Additive Manufacturing, Spreadability

Introduction Metal powder bed additive manufacturing has disrupted the manufacturing space dominated by conventional machining during the past years. In high fidelity applications like aerospace and automotive, however this technique is still limited by its vulnerability to building defects like inclusions and pores. Many of these faults can be traced back to the powder spreading during processing. Since the spreading is done in linear motions in most of the existing machines, trenches or elevated regions can form that follow the spreading direction. Stereo-DIC has proven successful in monitoring powder beds during the printing process [1]. We chose to refocus this approach to evaluate powder spread characteristics and improve powder production and handling methods, complimenting and expanding current approaches that use secondary characteristics (hall flow, particle shape, size distribution) to predict spread quality [2]. In addition, powder “spreadability” is poorly defined which is a problem for quantifying it, something this works aims to tackle. To introduce a new measurement technique that can bridge the gap between raw powder measures and tracking the manufacturing process, this paper discusses the deployment of digital image correlation in combination with a spreading simulation process. The aims of this study therefore were to make novel measurements of surface deviations and prove that stereo-DIC has the capability to characterize the powder surface.

Methods Stereo-DIC imaging capabilities (Fig. 1a, Table 1) were integrated within a commercial powder spread evaluation system (SpreadStation, Mercury Scientific Inc, CT, USA). An industry standard powder (SS316L) with spherical particles between 45-125 μm was used. The powder surface itself provided texture, without marking, for measurement of surface profiles (Vic3D, Correlated Solutions, SC, USA) over a $\sim 40\text{mm} \times 40\text{mm}$ region of interest (Fig. 1b). The profiles provide a simple and direct initial evaluation of spreadability in the form of surface height variation (Fig. 1c).

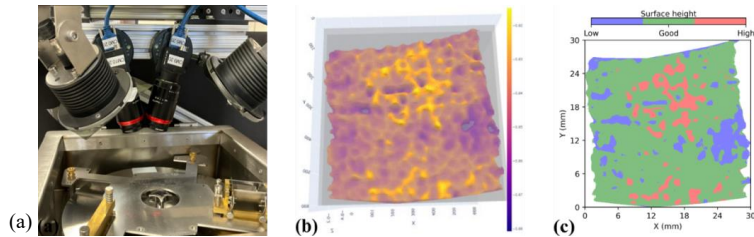


Figure 1: (a) Digital image setup with cameras, lights and lenses above the SpreadStation. (b) Surface profile generated by VIC 3D. (c) Evaluation of spreading based on desired height.

Camera	FLIR BFS-U3-200S6M-C	Stereo-Angle	27°
Image Size	5472 × 3648 px ²	Field-of-View	67.5x45 mm ²
Lens	Kowa LM16FC24M	Stand-Off Distance	85 mm
Aperture	f/16	Image Scale	12.5 $\mu\text{m}/\text{px}$

Table 1: Stereo-DIC hardware and imaging configuration.

Results A high-resolution point cloud of the powder surface is the result of the image correlation. The measurement region size of 35 mm by 45 mm establishes a good balance between resolution and area of interest. Precision of the surface height measurement was evaluated from repeat measurements of a static powder surface. For a set of 12 test images, the standard deviation of apparent displacement at each measurement point ranged over approximately $\pm 0.20 \mu\text{m}$ (Fig. 2a), with a maximum value of $0.46 \mu\text{m}$. We also developed a procedure for locating and quantifying streak artifacts within the region of interest, based on gradient orientation γ (Eq. 1). From the local gradients in x and y per pixel of the surface S, regions with similar orientations can be grouped together. This renders features virtually invisible in single-camera views of the powder surface highly visible (Fig. 2b).

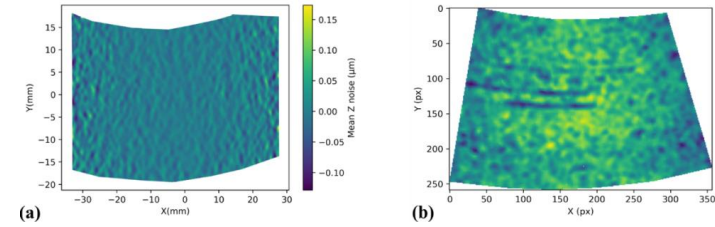


Figure 2: (a) Mean noise from 12 still images per pixel location. (b) Powder surface with linear, trench-like spreading error that can be detected with gradient orientation.

$$\gamma(\mathbf{px}) = \arctan\left(\frac{dS/dx(\mathbf{px})}{dS/dy(\mathbf{px})}\right) \quad (1)$$

Discussion and Conclusion The results show that it is possible to measure the surface of metal powder even though it is at the very limit of typically recommended image correlation speckle patterns. Measured noise and positional accuracy demonstrate that meaningful data can be obtained from this setup, paving the way for establishing its results as a spreadability parameter. Obtained point clouds can be used to evaluate what percentage of the surface is lower or higher than desired as well as the overall spread height. Feature detection for the gradient orientation-based approach and classification of low/high regions are automated and fast. Therefore, a digital image correlation approach to spreadability quantification is suitable and relevant for production facilities. Preliminary results also indicate that faster spreading speeds create more spreading defects, and that thinner layers show worse spreading quality in the first layers. Future work will focus on comparing the new method covered in this paper to the existing powder metrics and checking how the results agree and where the DIC improved method may help predicting behavior that otherwise was not predicted.

References

- [1] Filipa G. Cunha, Telmo G. Santos, José Xavier. In Situ Monitoring of Additive Manufacturing Using Digital Image Correlation: A Review. *Materials*, 14:1511, 2021.
- [2] Laura Cordova, Ton Bor, Marc de Smit, Mónica Campos, Tiedo Tinga. Measuring the spreadability of pre-treated and moisturized powders for laser powder bed fusion. *Additive Manufacturing*, 32:101082, 2020.

Measuring residual stresses in 3D woven composite fan blades via DVC

Y. Yasothan, L. Turpin, J. Neggers, A. Mendoza, J. Schneider, S. Roux

Université Paris-Saclay, CentraleSupélec, ENS Paris-Saclay, CNRS, LMPS, 91190, Gif-sur-Yvette, France.
 Safran Tech, 78 117 Châteaufort, France.
 Safran Aircraft Engines, 77 550 Moissy-Cramayel, France.

Abstract — Managing residual stresses in structural composite parts of the aerospace industry is highly challenging due to their complex shape that must be accurately captured. This work proposes a method based on global Digital Volume Correlation (DVC) on tomographic images to measure the residual stresses released after performing water-jet cuts in the fan blades of the LEAP engine. The results show that, despite tomographic images being intrinsically prone to noise and artifacts, the proposed method accurately captures the small strains induced by the relaxation.

Keywords — DVC, Brightness and Contrast Correction, X-ray Computed Tomography

Introduction Fan blades for LEAP engines are 3D woven composite manufactured by resin transfer molding. During the cooling phase of the manufacturing process, residual stresses appear, which can be detrimental to the strength and the geometrical specification of the structure [1].

Classically, blade residual stresses are measured using the contour method [2], which involves performing planar cuts in the structure. The relaxation of the residual stresses induced by these cuts slightly deforms the blade. These strains are measured manually at different positions on the blade. This method inevitably leads to losing the 3D information available during the test. This work aims to improve the contour method to estimate the 3D residual stress field using DVC.

For this, the blade internal structure is imaged before and after the cuts by X-ray Computed Tomography (XCT). Global DVC is applied to these XCT images, using the natural weave of the composite as a texture. The main difficulty in implementing this method is using noisy XCT images, subject to numerous artifacts, to measure low-amplitude strains. The solution proposed in this work to overcome this difficulty is the implementation of a mechanically regularized DVC with regularized Brightness and Contrast Correction (BCC). On the one hand, mechanical regularization overcomes noise and low-contrast texture to ensure DVC convergence by penalizing displacement field wavelengths below a certain regularization length to satisfy mechanical equilibrium. Regularized BCC, on the other hand, corrects artifact problems without eliminating signal texture.

Methods The contour method is implemented by inserting six water-jet cuts into the blade, giving it a comb-like shape (Figure 1). Global DVC is performed on the teeth 3, 5 and 7 of the blade between two XCT images, before g and after f cuts. After aligning the finite element mesh required for the DVC on

f , the Rigid Body Motion (RBM) between f and g is obtained by performing a DVC with kinematics restricted to the corresponding six degrees of freedom. This step is followed by a regularized BCC and a mechanically regularized DVC, for which the regularization lengths are obtained using L-curves.

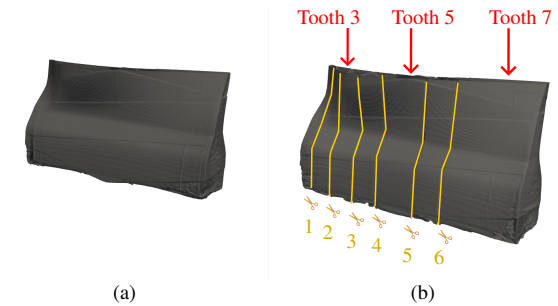


Figure 1: XCT images of a blade. (a) image before cuts g and (b) image after cuts f .

Results Figure 2 shows the equivalent strain field obtained at DVC convergence. The field is rich, with a shape that cannot be summed up simply by bending the teeth. This richness would have been impossible to capture using manual measurement methods.

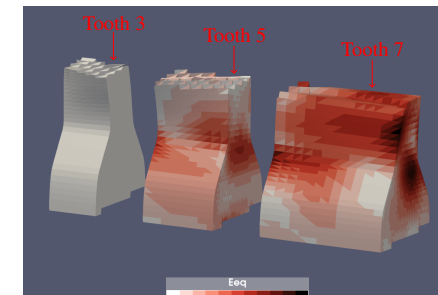


Figure 2: Equivalent strain field of the teeth 3, 5 and 7.

Discussion and Conclusion These results show that the proposed approach is able to reveal valuable information during the post-processing of the contour method. The residual stress fields in the blade can then be estimated as an inverse problem from the measured fields.

References

- [1] A. Courtois, L. Marcin, M. Benavente, E. Ruiz and M. Lévesque. Numerical multiscale homogenization approach for linearly viscoelastic 3D interlock woven composites. *International Journal of Solids and Structures*, 163:61-74, 2019.
- [2] M. B. Prime. Cross-sectional mapping of residual Stresses by measuring the surface contour after a cut. *Journal of Engineering Materials and Technology*, 123:162-168, 2001.

Optimising test sequences for robust material identification using a data assimilation approach

M. Guerder¹, R. Bouclier^{1, 2}, J.C. Passieux¹, J.N. Périé¹, L. Barrière³

¹ Institut Clément Ader, Université de Toulouse, CNRS UMR 5312, INSA / ISAE-SUPAERO / IMT-Mines Albi / UPS, Toulouse, France

² Institut de Mathématiques de Toulouse, Université de Toulouse, CNRS UMR 5219, INSA / UPS, Toulouse, France

³ IRT Saint-Exupéry, Toulouse, France

Abstract — This study investigates the optimisation of test sequences for robust material identification. Traditional approaches for constitutive behaviour characterisation usually consist in a sequence of independent identification problems, each one considering one single experiment and a small subset of parameters. Conversely, data assimilation approaches consider all measurements stemming from all experiments at once. This work demonstrates the potential of data assimilation to improve multiple parameters identification by optimising the experimental set-up of the tests sequence.

Keywords — Identification, Inverse methods, Optimisation, Full-field measurement, Uncertainties.

Introduction Image-based full-field measurements have had a significant impact on material characterisation, by providing a wider range of data compared to traditional mechanical tests (e.g., strain measurements using strain gauges). For constitutive parameters identification, full-field measurements opened new paradigms, one of those being the possibility of identifying various parameters at once [1, 2]. However, it has also introduced challenges such as determining parameter sensitivity within the measured field, and quantifying uncertainties affecting these parameters, in relation with data noise [3]. Consequently, there is a growing interest in exploring different test configurations to take advantage of full-field measurements, while addressing their specific requirements. In this context, optimal tests design aims at improving parameter identification by reducing uncertainties through the development of innovative test approaches. One possible approach is to modify the loading path, for example by imposing load cycles, or to modify the geometry of the sample, typically by adding holes or notches. Nevertheless, when it comes to optimal tests design, the principal challenge is not only in solving the optimisation problem itself, but also (and above all) in the definition of a cost function that objectively improves identification. For a deeper understanding of the issue of optimal tests design, we propose to consider a simplified scenario by means of a toy problem.

Methods In this scenario, we follow the ASTM standard test procedure for determining in-plane tensile properties of composite laminates [4], which includes four moduli. Three tensile tests are performed, each test coupon being designed with a different lay-up. The layups are of the form $[+\theta, -\theta]_{2S}$ for all coupons, with stacking angles of 0° , 90° and 45° respectively. The tensile tests are assumed to produce a uniform stain state throughout the coupon, so local strain measurements are made using strain gauges. Another strong assumption for the processing of the tests results is that each test is independent of the others. Under these hypotheses, the classical laminate theory provides straightforward expressions for the identification of the constitutive parameters, using the local strain measurements. This approach is advantageous as it allows easy processing of the data thanks to simple relationships, and does not assume any covariance between the parameters. Nevertheless, it requires a large number of experiments and specimens, with relatively limited instrumentation, meaning that each test provides little information concerning the studied material. In order to benefit from the whole data produced throughout the testing procedure, we propose a different approach: we consider all measurements as potentially contributing to the identification of all four parameters. In other words, we do not consider the three tests are independent

one of the others. We believe that this approach is consistent with the objective of identifying the in-plane tensile properties of a single material (or ply). This is done by using a data assimilation framework, in the sense that we aggregate data from all measurements (i.e., the measurements stemming from all three tests). More precisely, the methodology involves modelling the tests using classical laminate theory, and solving an identification problem based on these simulated data.

Returning to the objective of optimal test design, it can be highlighted that including all measurements in the identification problem relaxes the constraints on laminate angles. This allows for the exploration of alternative test designs to improve parameter identification. In this work, we propose to retain the same number of tests in the sequence, yet using different stacking angles. With regard to the optimisation itself, it is necessary to determine a quantity that shall be minimised. In accordance with standard practice, the covariance matrix of the identified parameters is studied as a measure of uncertainty [5, 6]. Consequently, the focus is on adjusting the coupons stacking angles to minimise the covariance matrix over the entire test series. Nevertheless, it should be acknowledged that minimising a matrix is not a straightforward process. A common approach is to examine the eigenvalues of the matrix in question and to derive a scalar quantity from those values. A number of criteria have been proposed. For instance, reducing the largest eigenvalue ensures that the uncertainty associated with the initially worst-identified parameter will not increase. However, it does not guarantee the identification of the remaining parameters will not deteriorate compared to the initial design. Another criterion is to use the determinant of the matrix, which may not enhance the sensitivity to all parameters.

Results In our study, we chose to focus on minimising the trace of the covariance matrix, which is a novel and interesting criterion for uncertainty reduction. Using the trace of the covariance matrix proves to be advantageous for uncertainty minimisation as it includes all eigenvalues equally. While it could be argued that the determinant also includes all eigenvalues, the key difference is that the trace sums the eigenvalues whereas the determinant multiplies them. Opting for summation rather than multiplication helps to avoid artificially lowering the criterion while actually degrading the solution. The results indicate that using the trace as a criterion to reduce the covariance matrix, and subsequently the uncertainties, is a favourable approach. Based on the chosen optimisation framework, the methodology successfully identifies sequences of angles that could improve the identification of ply in-plane tensile properties.

Discussion and Conclusion The application of this study to a simplified scenario, following the ASTM standard test procedure, highlights the interest of using a data assimilation framework for parameter identification. Optimal design of experiments can therefore benefit from such an approach, by attempting to reduce the uncertainties of the identified parameters. This work also demonstrates the utility of multiple objectives (including the trace and determinant) in a multi-objective optimisation setting. This approach may prove beneficial in exploring the design space and identifying different locally optimal designs. Subsequent work will be conducted in the near future to demonstrate the interest of this framework for more complex examples.

References

- [1] J. Negggers, F. Mathieu, F. Hild, and S. Roux. Simultaneous full-field multi-experiment identification. *Mechanics of materials*, 133, 71-84, 2019.
- [2] F. Pierron and M. Grédiac. Towards Material Testing 2.0. A review of test design for identification of constitutive parameters from full-field measurements. *Strain*, 57(1), 2021.
- [3] J. Réthoré. A fully integrated noise robust strategy for the identification of constitutive laws from digital images. *International Journal for Numerical Methods in Engineering*, 84(6), 631-660, 2010.
- [4] ASTM D3039. *Standard Test Method for Tensile Properties of Polymer Matrix Composite Materials*. 2002.
- [5] M.B.R. Bertin, F. Hild, and S. Roux. Optimization of a Cruciform Specimen Geometry for the Identification of Constitutive Parameters Based Upon Full-Field Measurements. *Strain*, 52(4), 307-323, 2016.
- [6] M. Chapelier, R. Bouclier, and J.-C. Passieux. Spline-based specimen shape optimization for robust material model calibration. *Advanced Modeling and Simulation in Engineering Sciences*, 9(1), 2022.

Development of a digital image correlation system for in-situ epoxy cure shrinkage, thermal expansion, and wafer warpage measurements

Alexander K Landauer

Material Measurement Laboratory, National Institute of Standards and Technology, Gaithersburg, MD, USA

Abstract — This work focuses on developing a digital image correlation (DIC)-based system for measuring displacement and strain during epoxy curing and thermal cycling of microelectronics wafers. This is a key area for assuring packaging success and reliability in the build-up of chips assembled with advanced packaging techniques. These chips involve 3D architecture with heterogeneous integration across large areas for a high-performance, reliable chip. Modeling and predicting strain and stress distributions is a significant challenge facing the industry. The packaging materials, typically highly filled epoxies, undergo chemical shrinkage during cure and the components and packaging often have mismatched thermal expansion. Thus, this work describes development of a method for wide field-of-view displacement and strain measurements, under relevant environmental conditions, of cure shrinkage, thermal expansion, and wafer-level warpage with DIC. These measurements will inform testing standards and mechanics modeling to improve and streamline the chip design process.

Keywords — DIC, electronics packaging, polymer characterization

Introduction The next generation of microelectronics involves a significantly expanded role for 3D architectures, heterogeneous integration, and chiplets. Assembly designs incorporating these features typically require advanced packaging with intensive engineering design to optimize thermal performance and physical integrity. To achieve the performance necessary for modern design requirements, materials such as underfills, molding compounds, and organic substrates have become increasingly sophisticated with fillers and additives for viscosity modification, coefficient of thermal expansion (CTE) reduction and other functional properties modification. To effectively design these integrated microelectronics systems, predictive modeling requires measurement of the cure shrinkage, CTE, and warpage to inform accurate, validated material models that capture chemo-thermomechanical properties of packaging materials.

Experimental characterization of cure shrinkage and CTE of packaging materials and wafer-level warpage for large-area assemblies with controlled environmental conditions is needed for material model development and validation of predictive models. The critical measurands include in-plane and out-of-plane displacement and strain, making it a measurement task well suited to digital image correlation (DIC). Often measurements use interferometric or Moiré methods, although DIC has been deployed in this field, for example the introduction of JEDEC standard JESD22-B112A which discusses the use of DIC. To address limitations and expand the depth of metrologies available, this work describes development efforts for a DIC system and example data for these measurements. This is part of a broader effort at the National Institute of Standards and Technology (NIST) that aims to develop measurements and measurement tools for accurate cure kinetics, stress, mechanical properties, and warpage measurements for next-generation microelectronics packaging under device relevant conditions.

Methods A research grade test material (RGTM) is under development by collaborators for highly filled epoxy underfill resins. It includes typical epoxy chemistries and inorganic fillers that NIST has worked with industry partners to identify. This material will form the basis of the characterization as a repeatable and representative test material.

To quantify the cure shrinkage, CTE, and warpage, a stereo DIC system with environmental control is developed. A cartoon of the system is shown in Fig. 1. This consists of a custom environmental chamber with a large window (approximately 200 mm square) with antireflective coating installed in the top. Since device operation is at elevated temperatures above the laboratory dewpoint, fogging is rarely a concern. To improve accuracy a calibration is determined for thermally varying imaging artifacts introduced by the window glass. Fans are used to mix air to avoid thermal gradient artifacts. A pair of cooled scientific cameras is used in a stereo fixture, either in a narrow or wide field-of-view placement and lens configuration, for DIC imaging. The stereo calibration is conducted at moderately elevated window temperature. The cameras are synchronized and triggered with a data acquisition system that is integrated with the test controller for the environmental chamber. This allows configurable temperature control up to about 300 °C.

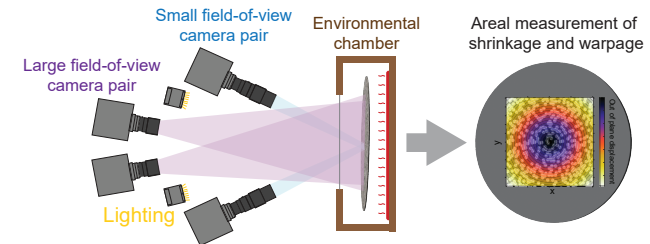


Figure 1: (Right) A sketch of the core components of the DIC measurement system including the environmental chamber, lighting, stereo camera pair (in narrow and wide field-of-view modes), and specimen. (Left) A cartoon of resultant data, showing the typical warpage mode of a wafer.

Results The open-source methods developed to perform these measurements and associated measurement uncertainty quantification are the key results of this work. These will be translated to our industry stakeholders to inform measurements on their proprietary epoxy formulations.

For cure shrinkage, the experimental program consists of developing widefield digital image correlation (DIC) to spatially map displacements and strains. Using this, the spatially varying post-gelation cure-driven chemical shrinkage and thermal expansion can be quantified. Specimens consist of the gelled RGTM material, speckled for DIC, in a custom dish that is placed such that the speckled plane at roughly the center of the focal volume.

For warpage, a 300 mm wafer-scale setup is used. The same environmental chamber and stereo DIC system is used as in the cure shrinkage case, with different lenses as appropriate for the field-of-view necessary for the test specimen. A wafer-based test artifact is instead used, with a custom *in-situ* fixture that places the surface of the wafer in the center of the focal volume.

Discussion and Conclusion The system will have quantified uncertainty and be used to establish and validate calibration protocols and artifacts that are specialized to the needs of industry for large field-of-view cure shrinkage, CTE, warpage measurements. This informs material model development and predictive models for 3D and heterogeneously integrated chips. The work expands on the baseline information given in JEDEC standard JESD22-B112A and will be used to inform the implementation of displacement and strain quantification standards. These tools will be open source but supported with commercial DIC software. We will cross-validate the metrology with in-house confocal microscopy and collaborators' interferometric and fiber-Bragg techniques.

Using DVC to measure manufacturing differences in 3D woven composite parts

A. Mendoza^{a, b}, J. Schneider^a

^a Safran Group, France

^b Université Paris-Saclay, CentraleSupélec, ENS Paris-Saclay, CNRS, LMPS, France

Abstract – Digital Volume Correlation is used in a different setting than the usual one. Here, DVC is used to compare two specimens of 3D woven composite parts. The found displacement field informs on the differences that may have been present during the manufacturing of the specimens. The found displacement field contains useful information for material analysis and design of new parts. Insights into how to interpret the results are also provided. Furthermore, the results obtained herein employ state-of-the-art DVC techniques.

Keywords – Digital Volume Correlation, Tomography, Composites, Regularization

Introduction The use of Image Correlation techniques is almost exclusive to the realm of experimental mechanics. Pairs of images from a single specimen are used to study how it deforms when subjected to external loads. As proposed in [1], here we explore a radically different use of Image Correlation where pairs of specimens are analyzed. As such, the measured displacement field does not represent a “real” transformation, but rather the “hypothetical” transformation that would convert one specimen into the other. More precisely, this transformation depicts the differences in manufacturing that led to the final state observed in the specimens. As such, Image Correlation can prove useful for inspecting and even monitoring an industrial manufacturing process.

The specimens of interest for this study come from the dovetails of two aircraft fan blades from the LEAP engine family. Hence, they are 3D woven composite parts with a textile reinforcement composed of carbon fiber-based yarns woven in a 3D interlock pattern and an epoxy resin as matrix. Both blades are nominally identical; however, each blade was obtained using different manufacturing protocols currently being studied.

Methods Each sample is scanned using high-resolution X-ray tomography. The obtained volume images are numerically down-sampled and result into volumes of dimension $500 \times 600 \times 800$ voxels (240×10^6 voxels). It is important to note that the imaging parameters (in tomography) were optimized so to guarantee a good image contrast within the natural texture of the woven composite. As such, the material microstructure in itself can be used as the “speckle pattern” for Digital Volume Correlation.

FE-based DVC (global approach) with mechanical regularization [2] and regularized brightness and contrast correction [1] is used here. The solution is implemented using Correli 3.2, an in-house library for Image Correlation developed at LMPS. Moreover, Gmsh software is used to generate an unstructured conformal mesh of tetrahedral elements with characteristic length of 50 voxels on average. This results in a mesh composed of 815 nodes and 2971 elements (2445 degrees of freedom).

Correlation is carried out in three steps. Each one runs for a fixed number of 20 iterations and the displacement with lowest residual (amongst iterations) at each step is used as initialization for the next one. First, a DVC procedure with rigid-body motion kinematics (rotation and translation) provides a good initial relative positioning of the specimens. Then, the second and third steps are complete DVC calculations with regularization lengths roughly three and two times the element size respectively. This results in smooth (and mechanically admissible) displacement fields that progressively get more detailed. The entire calculation takes a little less than 3 minutes on a 10-th generation Intel processor over 40 parallel cores and requires at most 13.4 Gb of memory.

Results The measured displacement field u is shown in Fig. (1). It is important to note that the continuous nature of this field is not to be taken to the letter, but rather as a mean of expressing how the textile architecture must deform (displacement of yarns) to conform from one sample to the other. As such, the computed strain tensor ϵ and its invariants must be analyzed through this viewpoint. Then, given that the warp and weft textile orientations are roughly aligned with the z and x axes respectively, the normal strain ϵ_{yy} concerns with separation of warp and weft planes, while ϵ_{xx} and ϵ_{zz} represent separations of warp and weft columns respectively. Moreover, Fig. (1) shows the trace of the strain tensor and the equivalent strain [1]. The former accounts for normal deformations (volume change), while the latter represents shear deformation magnitude at constant volume. It should be noted that all strain quantities are normalized with respect to an arbitrary ϵ_0 value.

Discussion and Conclusion The obtained results show very localized phenomena that can be used to investigate the variations in manufacturing (and therefore on the mechanical response) between the studied samples. For example, the compression zone indicated by the negative region at the bottom of $\text{tr}(\epsilon)$ indicates that the yarns in the second sample are farther apart than those in the first one. This could be read as the second sample having locally a lower Fiber Volume Fraction than the first one. Further analyses of this type can be carried out by analyzing the various computed strain quantities.

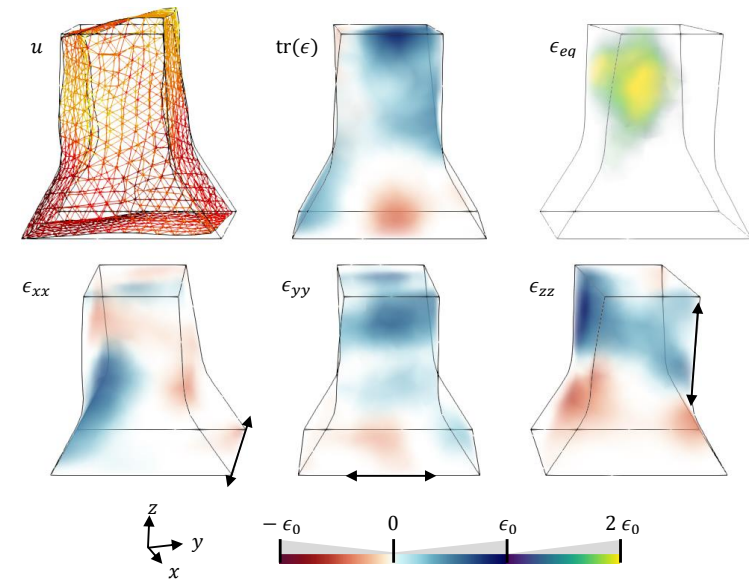


Figure 1: Measured displacement field and various computed strain quantities

References

- [1] A. Mendoza, J. Schneider, E. Parra and S. Roux, *Measuring yarn deformations induced by the manufacturing process of woven composites*, Composites Part A: Applied Science and Manufacturing, 120, 127–139, 2019
- [2] A. Mendoza, J. Neggers, F. Hild and S. Roux, *Complete mechanical regularization applied to digital image and volume correlation*, Computer Methods in Applied Mechanics and Engineering, 355, 27–43, 2019

Constitutive model validity evaluation for MT 2.0 applications

A. Peshave, P. Lava, F. Pierron

MatchID NV, Leiekaai 25A, 9000 Ghent, Belgium

Abstract – Material Testing 2.0 is a new trend in material testing combining heterogeneous tests, full-field deformation (like Digital Image Correlation) and inverse identification (like the Virtual Fields Method). Unfortunately, this new paradigm generally requires *a priori* selection of a material model to be identified. This paper describes and illustrates the use of data-rich metrics based on stress equilibrium to *a posteriori* rank models in terms of performance.

Keywords – DIC, Virtual Fields Method, Material Testing 2.0, Model identification, Model ranking

Introduction There is growing interest in inverse constitutive model identification techniques that use full-field optically measured deformation data. This new paradigm has recently been named Material Testing 2.0 (MT 2.0) [1]. Of particular interest in view of MT 2.0 is the Virtual Fields Method (VFM) [2]: a computationally efficient identification technique that leverages the full-field optically-measured deformation fields. The heterogeneity of the deformation fields used for VFM identification significantly affects the identifiability of the material parameters. Therefore, while on one hand, the study of the identifiability of the material constants pertaining to a certain test configuration is an important research topic [1, 3], this work on the other hand deals with metrics for evaluation of the relevance of the identified constitutive model once the identification is complete. Two such metrics were used in this work; namely, the equilibrium gap indicator (EGI) and the force reconstruction error (FRE) [4]. These metrics use different virtual fields to evaluate the validity of the identified constitutive model than the ones used for the identification itself. EGI relies on evaluating the static admissibility of the stress fields reconstructed from the constitutive model by calculating the local stress equilibrium in a small window of DIC data points. This window can be sampled across the region of interest for generating a map of EGI. FRE relies on reconstructing the force at a cross section of the test sample and comparing it to the known applied force.

Methods Two cases are investigated in this paper. The first one is a tensile test on a high-density polyethylene (HDPE) specimen with two asymmetrical notches, loaded in tension. Several hyperelastic models have been considered to represent the behaviour of the material, combined with an early linear-elastic part [4]. They were identified using the Virtual Fields Method and the identified parameters were then used to calculate EGI and FRE. The second one is a tensile deep notched specimen as used in [5]. Data was simulated using Abaqus with an anisotropic Hill48 yield function and linear hardening. EGI and FRE were calculated using the exact model and parameters, but also using the exact yield stress but a Von Mises yield surface.

Results The results from the HDPE test in Figure (1) shows that, surprisingly, models with the larger number of parameters do not necessarily provide better results. The worst of the three is Mooney-Rivlin model (2 parameters), and there is not much difference between Neo-Hookean (1 parameter) and Yeoh (3 parameters). The results on the elasto-plastic case (Figure (2)) clearly reveal the wrong material model both on the EGI and FRE indicators.

Discussion and Conclusion This paper will show more experimental results for the case of plasticity. The conclusions are sometimes surprising and call for systematic *a posteriori* validation of models. Full-field deformations provide a unique opportunity to define data-rich metrics for thorough investigation of *a posteriori* model performance.

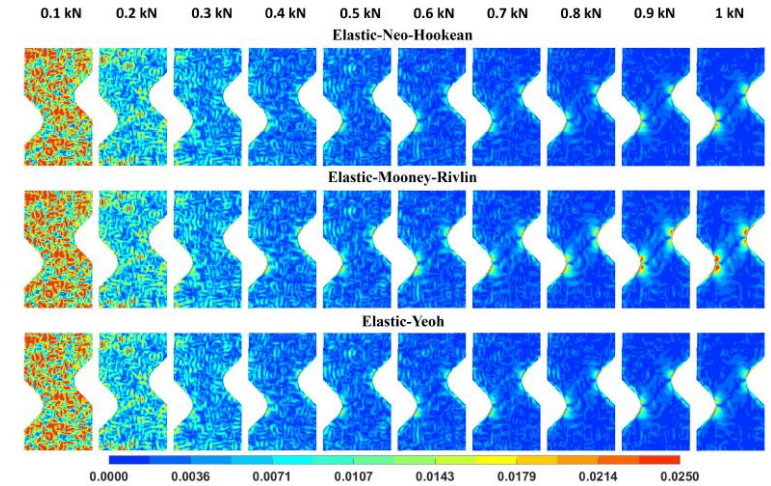


Figure 1: EGI indicator for the elastic-hyperelastic models

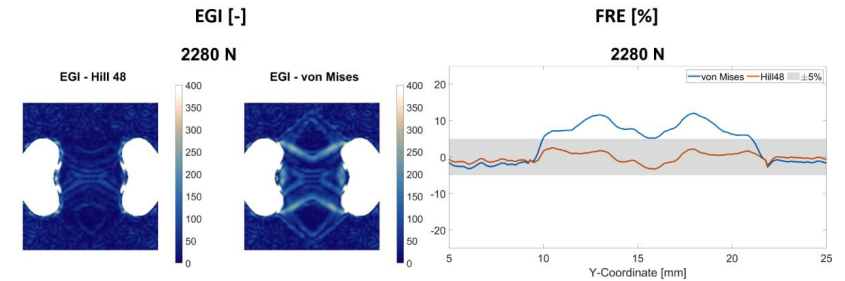


Figure 2: EGI and FRE for the anisotropic plasticity case

References

- [1] Pierron, F. and M. Grédiac, Towards Material Testing 2.0. A review of test design for identification of constitutive parameters from full-field measurements. *Strain*, **57**(1): pages. e12370, 2021.
- [2] Pierron, F. and M. Grédiac, *The virtual fields method*. New-York Springer, 2012.
- [3] Pierron, F., Material Testing 2.0: A brief review. *Strain*, **59**(3): pages. e12434, 2023.
- [4] Peshave, A., et al., Metrics to evaluate constitutive model fitness based on DIC experiments. *Strain*, **n/a**(n/a): pages. e12473, 2024.
- [5] Marek, A., et al., Experimental Validation of the Sensitivity-Based Virtual Fields for Identification of Anisotropic Plasticity Models. *Experimental Mechanics*, **60**(5): pages. 639-664, 2020.

The Stereo-DIC Challenge 2.0: DIC Strain Comparisons Using Common Images

P. Reu¹, W. Ahmad², E.M.C. Jones¹, A. Jones¹, M. Iadicola³, S. Bossuyt²

1. Sandia National Laboratories, Albuquerque, NM, USA. 2. University Aalto, Finland. 3. Nat. Inst. of Standards & Tech., USA

Abstract – Digital Image Correlation (DIC) is a powerful tool in experimental mechanics because it can take images of a sample and turn them into full-field strain. This process, however, requires many decisions by the experimentalists both in the experimental setup, analysis software decisions, and even down to the coding of the strain calculation. The Stereo-DIC Challenge 2.0, “The Tensile Experience”, was setup to provide a standard data set of tensile-test images for analysis using a wide range of codes, including university/research and commercial software. We tested both a standard tensile dog bone with nominally uniform strain prior to localization, and a bespoke geometry that produces a heterogeneous strain field. In this talk, we present the preliminary analysis showing a first comparison from multiple codes of full-field data in both the linear elastic regime, as well as at the limit of the strain measurement where the virtual strain gauge may not be converged.

Keywords – DIC, Strain Measurement, Measurement Uncertainty

Introduction The DIC Challenge, under the auspices of iDICs and the Society for Experimental Mechanics (SEM), seeks to provide images to the metrology community for verifying and validating their DIC code. The Challenge was founded in 2012 and continues to this day, with research and publications in 2D-DIC [1, 2], volumetric DIC [3], Scanning Electron DIC, and Stereo-DIC (in process with journal). The “Stereo-DIC Challenge 2.0: The Tensile Experience”, continues the important work from the first stereo challenge in providing high-quality experimental images to test the strain calculation in the DIC algorithms. Strain calculation is particularly interesting as it involves both the DIC matching algorithm, plus one of at least 4 post-processing algorithms to calculate strain [4]. The Stereo-Challenge 2.0 working group has successfully conducted the experiments and completed a preliminary analysis of the results presented here. Current participation includes most commercial codes, some university/research codes, and importantly a global code. See Table 1 for a list of participants.

Participant	Type of Code
DICe	Subset Based
LaVision	Subset Based
Dantec Dynamics	Subset Based
Correlated Solutions	Subset Based
Eikosim	Global Code
MatchID	Subset Based
ALDIC	Subset Based
Your Name Here	

Table 1. Current Participants in the Stereo-DIC Challenge 2.0

Methods The Stereo-DIC Challenge team at Sandia conducted two tensile experiments in June of 2023 following all guidelines in the DIC Good Practices Guide [4]. Interested parties were invited to participate in the experiment either in person or virtually to be able to observe the experimental efforts. Participants sent us calibration targets appropriate to the experimental FOV, for a total of five different target types. During the test, the calibration images were distributed live to the attendees to ensure that adequate coverage of the measurement volume and successful calibration of their system. We gathered between 113 and 201 images of each target type guaranteeing adequate images for a successful calibration. Furthermore, we captured a rigid speckle plate to aid in calibration if desired. After calibration, we conducted two experiments, one using a standard tensile dog-bone and one using a bespoke specimen. Loading was quasi-static. Contact plreu@sandia.gov for access to the images. After the preliminary analysis, we will release them on Google Drive with the other image sets.

Results Comparison between multiple codes is difficult. We are taking an incremental approach, first defining methods of coordinate transforms to place all the data in the same coordinate system. We are currently analyzing the linear elastic and plastic deformation region with 4 different virtual strain gauge (VSG) sizes to determine the strain noise floor and compare the Lagrangian strain for the preliminary results. Figure 1 shows the comparison between four codes showing reasonable agreement. Work is also progressing on comparing the strain results near failure where strains are very high, challenging the spatial resolution of the codes.

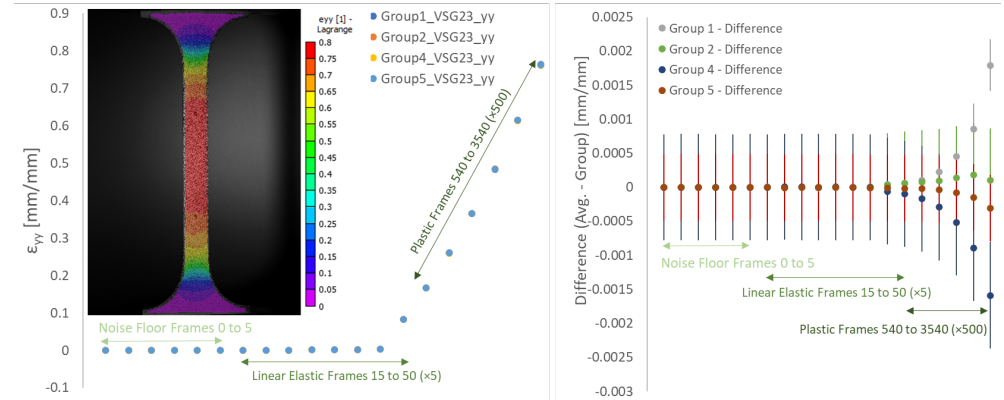


Figure 1: Comparison of 4 codes for loads up to noticeable necking. (Left) ϵ_{yy} for a VSG size of 23 pixels (inset is the full-field strain from one participant). Noise floor, linear elastic and plastic region labeled. (Right) Difference between codes for the same regions (subtracted from average strain). Error bars are the average of the standard deviation for the noise floor images.

Discussion and Conclusion The Stereo-DIC Challenge committee hopes to work with the participants and encourage other codes to participate and write a journal article over the next 6-12 months. As in previous challenges, we will maintain anonymity, allowing contributors the ability to optimize their results and fix any code deficiencies found during the analysis before submitting final results.

Acknowledgements

Sandia National Laboratories is a multimission laboratory managed and operated by National Technology and Engineering Solutions of Sandia, LLC., a wholly owned subsidiary of Honeywell International, Inc., for the U.S. Department of Energy's National Nuclear Security Administration under contract DE-NA-0003525. SAND2024-04410A

We would like to thank the Center for Integrated Nanotechnology (CINT) for use of their facilities and Dave Johnson for his expert experimental support.

References

1. Reu, P.L., et al., *DIC Challenge: Developing Images and Guidelines for Evaluating Accuracy and Resolution of 2D Analyses*. Experimental Mechanics, 2017.
2. Reu, P.L., et al., *DIC Challenge 2.0: Developing Images and Guidelines for Evaluating Accuracy and Resolution of 2D Analyses*. Experimental Mechanics, 2022.
3. Croom, B.P., et al., *Interlaboratory Study of Digital Volume Correlation Error Due to X-Ray Computed Tomography Equipment and Scan Parameters: an Update from the DVC Challenge*. Experimental Mechanics, 2021. **61**(2): p. 395-410.
4. *A Good Practices Guide for Digital Image Correlation*, E.M.C. Jones, Iadicola, M.A., Editor. 2018, International Digital Image Correlation Society.

Debonding quantification via Digital Volume Correlation. Application to a mortar reinforcement pull-out

S. Langlois, A. Fau, B. Smaniotto, F. Benboudjema, M. Maaroufi, F. Hafid, F. Hild

Université Paris-Saclay, CentraleSupélec, ENS Paris-Saclay, CNRS, Laboratoire de Mécanique Paris-Saclay, Gif-sur-Yvette, France

Abstract – In composite materials, the debonding phenomenon is challenging to quantify directly via standard tests. This study applies Finite Element-based Digital Volume Correlation (FE-DVC) to investigate debonding between a mortar matrix and a reinforcement during an in-situ pull-out test within an X-ray tomograph. A 3D mesh replicates the foundation and reinforcement geometry. By splitting the nodes at the interface, the reinforcement kinematics is better captured, and debonding is assessed with displacement jumps.

Keywords – DVC, Mechanical regularization, Pull-out, Decohesion, Mortar

Introduction Debonding is a frequent phenomenon in composite materials, like reinforced concrete, which occurs within the material bulk and cannot be quantified directly via macroscopic measurements [1]. One way to overcome this issue is to use Computed Tomography (CT) coupled with Digital Volume Correlation (DVC) to measure displacement fields in samples with scans acquired during in-situ tests. Measuring phenomena such as debonding remains a challenge with DVC, given the finesse of the kinematic field. Global DVC [2] coupled with finite element methodology allows one to measure displacement fields on fine meshes with sub-voxel resolution.

In the present study, FE-DVC with mechanical regularization was used to quantify debonding at the interface between a Glass-Fiber-Reinforced-Polymer (GFRP) and mortar during an in-situ pull-out test. A mesh was created to describe the geometry of both materials from computed tomography reconstructions. Employing twin nodes to characterize the interface significantly reduces the correlation residual in the reinforcement and allows to measure displacement jumps.

Methods The specimen consists of a GFRP reinforcement anchored in a small-scale mortar foundation. Pull-out is performed by prescribing a vertical (z -axis) displacement with a stroke speed of 3 $\mu\text{m/s}$. The foundation is loaded in steps to perform scans along the loading history. Global DVC is used to measure displacement fields of the sample during the in-situ test and consists in minimizing the global image residual Φ_c over the entire Region Of Interest (ROI) between a reference volume $f(\mathbf{x})$ and a deformed volume $g(\mathbf{x})$

$$\Phi_c^2 = \sum_{ROI} [f(\mathbf{x}) - g(\mathbf{x} + \mathbf{u}(\mathbf{x}))]^2 \quad (1)$$

The displacement field $\mathbf{u}(\mathbf{x})$ is expressed in terms of finite element discretization using 4-noded tetrahedra (T4). Let \mathbf{v} denote the vector gathering all degrees of freedom (DOFs). For the reported analyses, DVC was regularized by adding an elastic-based cost function Φ_m derived from the equilibrium gap

$$\Phi_m^2 = \frac{1}{2} \mathbf{v}^T [\mathbf{K}]^T [\mathbf{K}] \mathbf{v} \quad (2)$$

Both cost functions are normalized through a unitary displacement field. DVC consists in minimizing the sum of these two cost functions, with a weight w_m dependent on a regularization length l_{reg}

$$\mathbf{u}(\mathbf{x}) = \text{Argmin}(\tilde{\Phi}_c^2(\mathbf{v}) + w_m(L_{reg})\tilde{\Phi}_m^2(\mathbf{v})) \quad (3)$$

The considered mesh is shown in Fig. 1(a) which involves split nodes to allow displacement jumps between mortar and GFRP at their interface [3].

Results The DVC computation was performed between an unloaded state and a deformed one, where the specimen had experienced failure at the chimney but bore the pull-out force in the slabs. The uncertainty of u_z in the GFRP reinforcement increases from 0.02 to 0.05 voxel compared to an interface with single nodes, with no significant influence observed in mortar. The root mean square level residual in the GFRP decreases from 10.0 to 9.6, indicating improved capture of the kinematics in the fiber when allowing displacement jump at the interface with the mortar. Debonding is quantified by the displacement jump at the interface:

$$du = \mathbf{u}_{interface}^{GFRP} - \mathbf{u}_{interface}^{mortar} \quad (4)$$

Fig. 1(b) displays the displacement jump du_z along the loading axis, as a function of the vertical z -coordinate of the mortar foundation. Mortar underwent downward sliding at the foundation upper section, while no significant debonding is observed in the chimney area. Chimney cracking occurred at $z = 450$ voxels, coinciding with the highest debonding amplitude. Interestingly, this amplitude is negative, indicating a slight elevation of the mortar in the upper part of the crack, coupled with sliding in the lower part.

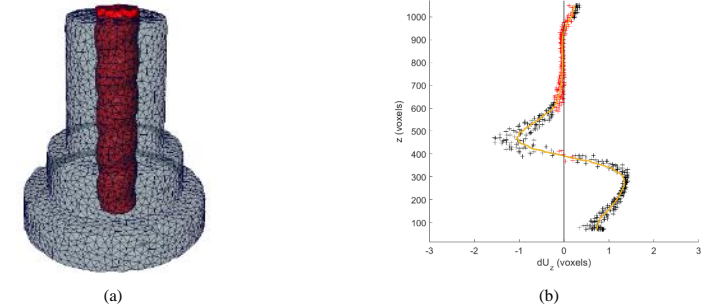


Fig. 1 Mesh of the specimen (a). Vertical displacement jump as a function of height of the studied foundation (b)

Discussion and Conclusion Node splitting at the interface of the studied composite enabled DVC to reduce the registration residual in the fiber. The displacement fields are calculated with better reliability, but at the cost of higher uncertainties. Debonding was quantified by the displacement jumps at the interface between GFRP and mortar. The mortar foundation cracked at the chimney, which induced large strains in the corresponding element. Additional split nodes may be introduced in the DVC analyses, or reduced regularization in these areas.

References

- [1] E.D. Reis, R.C. de Azevedo, A.L. Christoforo, F.S.J Poggiali, A.C.S. Bezerra. Bonding of steel bars in concrete: A systematic review of the literature. *Structures* 49:508–519, 2023
- [2] S. Roux, F. Hild, P. Viot, D. Bernard. Three-dimensional image correlation from X-ray computed tomography of solid foam. *Composites Part A: Applied Science and Manufacturing* 39:1253–1265, 2008
- [3] G. Jänicke, A. Vintache, B. Smaniotto, A. Fau, I. Farina, F. Fraternali, F. Hild. Debonding analysis via digital volume correlation during in-situ pull-out tests on fractal fibers. *Composites Part C: Open Access* 9:100302, 2022.

Identification of heterogeneous elastic parameters with the Equilibrium Gap Method

R. Haustrate, A. Fau, F. Hild

Université Paris-Saclay, CentraleSupélec, ENS Paris-Saclay, CNRS, LMPS - Laboratoire de Mécanique Paris-Saclay, Gif-sur-Yvette, France

Abstract — Full-field measurements, such as Digital Image Correlation, have led to the development of multiple methods for mechanical property identification. The Equilibrium Gap Method offers a good computational efficiency. Identifying properties of heterogeneous materials leads to multiple challenges, such as computational cost and under-determination. This work extends the Equilibrium Gap method to identify heterogeneous elastic properties. A reduced basis for the heterogeneous property field is introduced based on the hypothesis that the field is random and smooth at a chosen scale.

Keywords — identification, inverse problem, heterogeneity

Introduction Full-field measurement methods, such as Digital Image Correlation, allow for identifying mechanical parameters. The Equilibrium Gap Method (EGM) [1, 2, 3] minimizes the equilibrium discrepancy calculated with measured displacement fields. The associated optimization problem is easy to minimize, particularly in linear elasticity.

For heterogeneous materials, if the heterogeneity is reducible to a small number of subdomains with different properties, the parameter identification procedure is similar to a homogeneous state but with a larger number of unknowns. When the spatial distribution is unknown, its representation may require a large number of unknowns. This increase leads to expensive computational costs, to an amplification of the uncertainties and possibly even to under-determined problems.

This work uses the Equilibrium Gap Method, including equilibrium and resultant forces, reformulated to use a covariance-weighted least squares cost function. The stiffness field is parameterized using a reduced basis constructed from a spatial correlation hypothesis to identify heterogeneous elastic properties. The basis allows the number of degrees of freedom of the identification to be controlled and the effect of the discretization mesh on the results to be mitigated.

Equilibrium Gap Method with reduced basis The EGM was initially used for damage field identification [1] and later on for damage law identification with a reconditioned formulation [2]. Its main advantage is its cost function, which is quadratic when the stiffness tensor field is linear with respect to the unknown parameters.

The identification problem is handled numerically within the finite element (FE) framework. The EGM does not simulate a displacement field such as the Finite Element Method Updating (FEMU) [4] and instead searches for the parameter vector \mathbf{p} such that the measured displacement \mathbf{u}_m satisfies the equilibrium equations $\mathbb{K}\mathbf{u} = \mathbf{f}$. In addition, the gap with the measured resultant forces can be added. As the measurements are corrupted by uncertainties, the problem is solved by minimizing the residuals of the equations instead. The weighing of the different residuals is performed using the inverse covariance matrix $\mathbb{C}_{egm}^{-1}(\mathbf{p}_0)$, calculated at the initial point of the material parameters \mathbf{p}_0

$$\mathbf{p} = \operatorname{argmin} \left\| \begin{bmatrix} \mathbb{E}_{eq} \\ \mathbb{E}_T \end{bmatrix} (\mathbb{K}(\mathbf{p})\mathbf{u}_m - \mathbf{f}) - \begin{bmatrix} \mathbf{0} \\ \mathbf{T}_m \end{bmatrix} \right\|_{\mathbb{C}_{egm}^{-1}(\mathbf{p}_0)}^2 \quad (1)$$

with \mathbb{E}_{eq} the matrix extracting the known equilibrium equations (excluding Dirichlet boundaries), \mathbb{E}_T the matrix calculating the resultant forces, and \mathbf{T}_m the measured resultant forces.

The simplest parameter field discretization with an FE mesh is using one degree of freedom per element. This field discretization induces a large number of unknowns (possibly leading to underdetermined problems with triangular meshes). A reduced basis is used to represent the heterogeneity of a property with a limited number of degrees of freedom. Without prior knowledge on the material microstructure, it is assumed that the property field is smooth up to a certain scale. This hypothesis is expressed mathematically with an auto-correlation model of the property field. The reduced basis is constructed from a Karhunen-Loève expansion [5].

Results The proposed approach is tested for a biaxial experiment on an E-glass fiber mat in a vinylester matrix [1, 2]. A equibiaxial loading up to 11 kN (before failure) was applied. Displacement fields were measured on an FE mesh made of 3,700 triangular elements, with a mean element length of 13.8 px. The Young's modulus field is identified using a reduced basis of 120 modes. Figure 1 shows the identified stiffness field at $F = 11$ kN. Failure occurred just after 11 kN and initiated on the top/left part of the specimen.

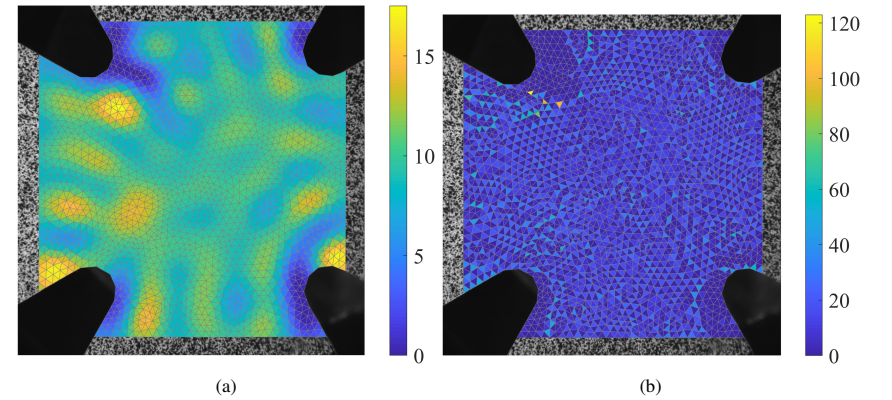


Figure 1: Young's modulus field in GPa before failure ($F = 11$ kN) identified by the EGM with (a) and without (b) the reduced basis

Discussion and Conclusion The Equilibrium Gap Method is a computationally efficient method to identify heterogeneous elastic properties. Identifying heterogeneous properties from mechanical experiments presents multiple challenges due to the high number of parameters. Selecting a reduced basis allows the user to control the number of unknowns for describing heterogeneous property fields.

References

- [1] Claire, D., Hild, F., and Roux, S. A finite element formulation to identify damage fields: the equilibrium gap method. *International Journal for Numerical Methods in Engineering*, 61(2):189–208, 2004.
- [2] Roux, S. and Hild, F. Digital image mechanical identification (DIMI). *Experimental Mechanics*, 48(4):495–508, 2008.
- [3] Amiot, F., Périé, J.-N., and Roux, S. *Equilibrium Gap Method*, chapter 12, pages 331–362. John Wiley & Sons, Ltd, 2013.
- [4] Pagnacco, E., Caro-Bretelle, A.-S., and Ienny, P. *Parameter Identification from Mechanical Field Measurements using Finite Element Model Updating Strategies*, chapter 9, pages 247–274. John Wiley & Sons, Ltd, 2013.
- [5] Sudret, B. and Der Kiureghian, A. Stochastic finite element methods and reliability a state-of-the-art report. Technical report, Department of Civil & Environmental Engineering, University of California, Berkeley, 2000.

R3XA: Toward a metadata standard for experimental (photo)mechanics datasets

B. Blaysat¹, R. Bonnaire², P. Bouda³, J.E. Dufour², S. Feld-Payet⁴, R. Fouque⁵, T. Fourest⁶, T. Jailin¹, R. Langlois⁷, J. Lachambre^{12,8}, C. Le Bourlot⁸, J.C. Passieux², J.N. Périé², J. Réthoré⁷, T. Rose⁹, E. Roubin¹⁰, T. Sentagne^{2,5}, J.F. Witz¹¹

1. Université Clermont Auvergne, Clermont Auvergne INP, CNRS, Institut Pascal, Clermont-Ferrand, France
2. ICA, Université de Toulouse, CNRS-INSA Toulouse-UPS-ISAE Supaero-IMT Mines Albi, Toulouse, France.
3. CEA Saclay, France
4. DMAS, ONERA, Université Paris Saclay, 92320 Châtillon, France
5. DGA Techniques aérospatiales (DGA TA), Direction générale de l'Armement (DGA), Balma, France
6. DMAS, ONERA, 59000, Lille, France
7. Nantes Université, Ecole Centrale Nantes, CNRS Gem UMR 6183, Nantes, France
8. MATEIS, INSA Lyon, CNRS, Université Claude Bernard Lyon 1, UMR 5510, 69621 Villeurbanne, France
9. Safran Tech, France
10. 3SR, CNRS, Université Grenoble Alpes, Grenoble, France
11. LamCube, Université de Lille, Lille, France
12. LAMCOS, CNRS, INSA Lyon, UMR 5259, 69621 Villeurbanne, France

Abstract — Open-data are digital data whose access and use are free to users, and which may be provided under public funding. They are distributed in a structured manner following a metadata standard. The number of opendatasets increases in experimental mechanics, but, to our knowledge, there is no metadata standard specific to the field of experimental mechanics yet. In this talk, an initiative in this direction is presented.

Keywords — open-data, metadata, standard

Introduction More and more experimental mechanics datasets are made available on public repositories, as it becomes a standard practice required when they are the result of public research funding. Experimental mechanics dataset can include heterogeneous multimodal data such as: CAD (or mesh) of the sample, sensors signals (extensometry, load cells...) and images of different nature. Without metadata, there is no way to understand or use the data at hand. This is why, most of the time, authors do their best to accompany data with parameters, hardware/software information and explanations. But this information is usually incomplete and very differently organized from one author to another. In experimental mechanics, metadata can cover: material of the sample, lighting, acquisition parameters, testing rig capacity/model/dimensions, position of the light/machine/camera with respect to the sample, position of strain gauges, to name just a few.

There are many available metadata standards, one of which is Dublin Core [1]. A metadata standard is a requirement intended to establish a common understanding of the meaning or semantics of data, in order to ensure correct and appropriate use and interpretation of the data by its owners and users.

Building a perfectly agnostic metadata format is feasible, but generally leads to a format that is too conceptual and cumbersome to use. The difficulty lies in creating a standard that is sufficiently general, yet simple to understand and use. That's why metadata standards for specific domains are often derived from the definition of communities of interest.

Methods To achieve this, a number of data characteristics or attributes, also known as metadata, have been defined specifically for experimental (photo)mechanics datasets. The idea is to provide experimenters and data analysts in the field of mechanics with a common base of descriptive elements sufficiently structured to enable minimal interoperability between independent software/libraries.

A language must be chosen to write and structure this metadata. Among the many existing tag-based text languages, JSON language [2] was chosen because it can be read and written by the main scripting languages used in experimental mechanics (python, matlab, C).

Results R3XA "*Remember, Reuse and Replicate eXperiments and Analyses*" is another metadata file format whose goal is to provide a data representation scheme compatible with the variety of data types encountered in experimental and computational photomechanics, and to provide a convenient framework for software coupling and data fusion. The keywords for image data and DIC parameters also comply with the terminology of the iDICs Good Practices Guide [3].

Given the complexity of mechanical experiments and the large number of data (e.g. hundreds/thousands of images for a single test), writing by hand r3xa files rapidly becomes a nightmare. To avoid such complex tasks, the group is also working on the development of an open-source python library to help users read, write and visualize the meta-data of an experiment in a more convenient way, see Fig. 1 for a screenshot.

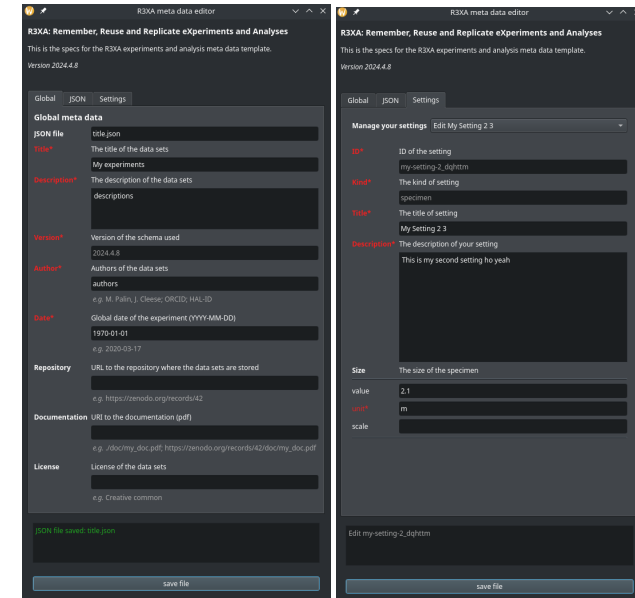


Figure 1: Screenshots of the python library under development to help writing, visualising and editing metadata r3xa files.

Discussion and Conclusion This initiative, supported by the PhotoMechanics Association, is a first step toward metadata standardisation in experimental photomechanics. A structure, a list of keywords and a language have been defined and a python library is under open collaborative development to help users write, read and visualize meta-data.

References

- [1] Dublin Core Metadata Initiative (DCMI) <https://dublincore.org>
- [2] JavaScript Object Notation (JSON) <https://json5.org/>
- [3] Jones, E.M.C. and Iadicola, M.A. (Eds.) (2018) A Good Practices Guide for Digital Image Correlation. International Digital Image Correlation Society, DOI: 10.32720/idics/gpg.ed1

Projection enhanced DVC to analyze relaxation and crack propagation until failure on architected aluminum alloy

V. Kosin^{1,2}, A. Gravi¹, A. Pujol¹, A. Fau¹, C. Jailin¹,
B. Smaniotto¹, T. Wick^{2,1}, G. Tarantino¹, F. Hild¹

¹Université Paris-Saclay, CentraleSupélec, ENS Paris-Saclay, CNRS LMPS-Laboratoire de Mécanique Paris-Saclay, Gif-sur-Yvette, France
²Leibniz Universität Hannover, Institut für Angewandte Mathematik (IFAM), Hannover, Germany

Abstract — The present study aims at demonstrating the possibility of extending standard protocols of *in-situ* (tomography) experiments for the analysis of time-dependent phenomena and kinematic measurements until failure. A modal procedure is proposed such that spatial fields are constructed using Digital Volume Correlation (DVC) and the corresponding temporal amplitudes are measured with Projection-based Digital Volume Correlation (P-DVC). The framework is applied to a porous metamaterial fabricated using additive manufacturing to investigate the interactions between manufacturing defects and the geometric mesoporosity.

Keywords — digital volume correlation, *in-situ* tests, spacetime analyses, tomography

Introduction *In-situ* experiments are generally based on scans reconstructed from a large number of projections acquired under constant deformation of samples. With a laboratory CT scanner, each acquisition may take a few minutes up to a few hours. Therefore, measurements of phenomena that are faster than one scan period or occur just after a scan are not possible with standard scan-based DVC. One route to circumvent this restriction consists in performing projection-based measurements [1]. To benefit from standard DVC and P-DVC, both techniques are combined in the present study using a space-time approach [2].

Methods The overall procedure is carried out in three different steps. First, an experimental protocol for the *in-situ* tensile test was defined, consisting of a sequence of loading and dwell phases. During the loading phases of a mesoporous metamaterial made of AlSi10Mg (Figure 1(a)), on-the-fly radiographs were collected, while dwell phases corresponded to tomographic scans of the loaded specimen. Around the expected point of fracture, a higher number of scans was acquired (Figure 1(b,c)).

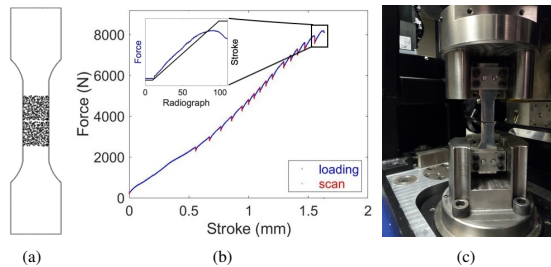


Figure 1: (a) CAD model of the mesoporous metamaterial. (b) Force-stroke curve of the *in-situ* tensile test. (c) Broken sample.

To measure the displacement fields, a global DVC approach was utilized [3] and the final fracture process was analyzed with P-DVC. This method allows the radiographs acquired on-the-fly to be registered and, therefore, the measurements to be temporally enriched. Specifically, P-DVC was used to study the damage process between the last tomographic scan and the final material fracture as proposed in Ref. [2]. This method is based on the minimization of the squared differences between a radiograph and a projection of the deformed volume. The latter is computed from the reference volume, which is deformed by DVC displacement fields weighted by unknown amplitudes to be determined.

Results Failure occurred instantaneously at approx. 8.2 kN with very little macroscopic softening (Figure 1(b)). The DVC results provided information on the 3D displacement and the residual fields. In particular, the gray level residuals were used to identify the crack initiation sites (Figure 2(a)). The latter ones correspond to two manufacturing defects, characterized by a local lack of material induced by the printing strategy. The DVC results were complemented by P-DVC analyses, which provided high temporal resolution insights into damage growth within the specimen up to its final failure. The P-DVC residuals remain very low, indicating that the kinematics is well described. Instantaneous fracture is revealed by a large increase in the P-DVC residuals in the failure zone between the first radiograph acquisition after the last scan and the last one (Figure 2(b,c)). It is concluded that, first, the existing manufacturing defect grew under increasing deformation. Then, this crack propagated toward the closest manufacturing defects and eventually traversed the geometric pores. This crack path was confirmed by observing the first post-mortem radiograph.

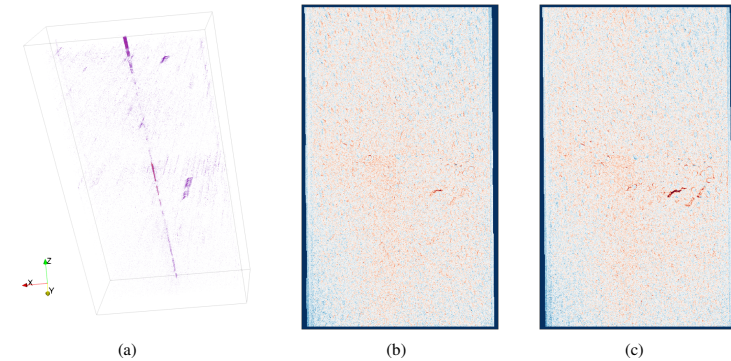


Figure 2: (a) 3D thresholded DVC residuals for the last tomographic scan (15). P-DVC residuals for the first radiograph after scan 15 (b) and the last radiograph before failure, highlighting the crack growth (c).

Discussion and Conclusion The use of P-DVC enriched the DVC results since it allowed the radiographs acquired on-the-fly to be registered until final failure. The results of this study showed that manufacturing defects triggered the failure response of the specimen in tension and that the interaction with the mesoporous structure occurred only at the very end of the fracture process. The results of this study indicated that manufacturing defects need to be taken into account in order to predict damage and failure of such mesoporous metamaterials.

References

- [1] C. Jailin et al. Sub-minute In Situ Fracture Test in a Laboratory CT Scanner. *Integrating Materials and Manufacturing Innovation*, 8: 413-422, 2019
- [2] V. Kosin et al. A projection-based approach to extend digital volume correlation for 4D spacetime measurements. *Comptes Rendus de Mécanique*, 351: 265-280, 2023
- [3] S. Roux et al. Three dimensional image correlation from X-Ray computed tomography of solid foam. *Composites Part A: Applied Science and Manufacturing*, 39(8): 1253-1265, 2008

Spatial mapping of plastic properties in welds with the VFM

R. Hamill¹, A. Marek¹, A. Harte², F. Pierron^{1,3}

¹University of Southampton, University Road, Southampton SO17 1BJ, UK

²UK Atomic Energy Authority, Culham Science Centre, Oxfordshire, UK

³MatchID NV, Leicaakai 25A, 9000 Ghent, Belgium

Abstract – Welding is a common method for joining metal components. Because of the complex thermomechanical history, elasto-plastic properties vary within the weld. Digital Image Correlation (DIC), combined with the Virtual Fields Method (VFM), offers a unique opportunity to map elasto-plastic properties in welds. This paper proposes an application example relevant to nuclear fusion.

Keywords – DIC, Virtual Fields Method, Weld, Heterogeneous material

Introduction The characterization of the mechanical behaviour of welds is complex because of the spatially variable properties with the weld and the heat affected zone. In the past, Digital Image Correlation has been used to address this complexity but exclusively on butt welds in tension perpendicular to the weld line, either using the assumption that the stress is uniform [1] or with the Virtual Fields Method [2, 3]. In the former, one has to assume that the properties are uniform per transverse section, while the VFM allows for spatial parameterisation [2, 3]. However, a specific difficulty arises when the weld is overmatched or when dissimilar materials are welded and the weld yield stress is higher than that of the base material. This is the case here where a steel/steel laser weld is considered. If a butt weld is tested in tension, the base material will yield and no information will be available in the weld region. To overcome this problem, the paper shows how the geometry of the test can be tuned to ensure that the weld zone develops enough plastic strain for identification. Of course, in this case, the constant stress approach cannot be used anymore. Here, the VFM will be employed, and the properties parameterized as constant throughout each transverse section.

Methods The experimental setup is depicted in Figure (1). Two back-to-back cameras have been used as in [4] to account for possible out-of-plane movement and out-of-plane bending. For such high magnification (close to 1), stereo DIC proved impossible because of the size of the lenses. Speckling was performed with an air brush and the MatchID DIC package was used to process the data. The specimen is a laser weld between a GR91 steel grade and 316L stainless steel. GR91 has a high yield stress of more than 600 MPa, while 316L offers a much lower yield stress, at around 350 MPa. To promote localization in the weld zone, several designs were explored numerically. Finally, the geometry shown in Figure (2) was adopted. The pink zone represents the laser weld line. The specimen was loaded in tension and images were continuously recorded until cracking occurred.

Results Figure (3) shows the equivalent plastic strain at the end of the test. The two yellow hotspots represent cracks and these strain values should be ignored. One can see however that plastic strains are present in the weld, though not in the entire welded zone. The identification was performed up to the onset of the cracks using slice-wise virtual fields. A linear isotropic elasto-plastic model was selected. A map of yield stress was obtained as shown in Figure (4). At the bottom of the map, the yield stress of 316L is retrieved, while at the top, the yield stress of GR91 is broadly recovered (on average over all the slices), but the results are much noisier as there is much less plastic deformation there (the transparent zones indicate elastic deformation only). In the weld, the yield stress is between that of 316L and GR91, at around 500 MPa. The hardening modulus map (not shown here) shows little contrast and stays close to 3 GPa, which was the initial value used for the optimization process. This insensitivity of the hardening modulus is likely due to the plastic strains remaining small because of the onset of cracking in the weld.



Figure 1: Experimental setup

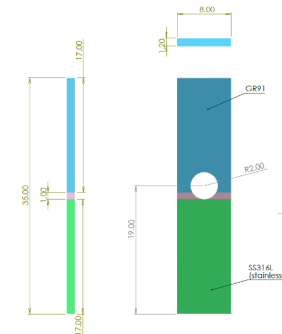


Figure 2: Specimen geometry with dimensions in mm.

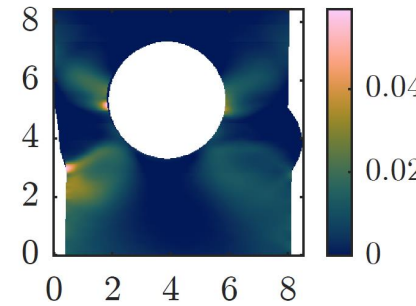


Figure 3: Equivalent plastic strain at the last step

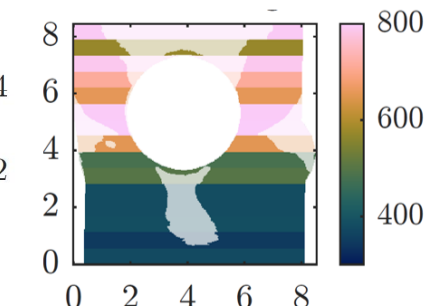


Figure 4: Identified yield stress (MPa)

Discussion and Conclusion These initial results show that the geometry selected was successful to generate plastic strains in the weld, allowing for identification of the yield stress. Future work involves comparison with a hardness map and the use of an automated parameterization tool.

References

- [1] Wu, X., et al., Determination of local true stress-strain response of X80 and Q235 girth-welded joints based on digital image correlation and numerical simulation. *International Journal of Pressure Vessels and Piping*, **188**: pages. 104232, 2020.
- [2] Sutton, M.A., et al., Identification of heterogeneous constitutive parameters in a welded specimen: uniform stress and virtual fields methods for material property estimation. *Experimental Mechanics*, **48**(4): pages. 451-464, 2008.
- [3] Saranath, K.M., A. Sharma, and M. Ramji, Zone wise local characterization of welds using digital image correlation technique. *Optics and Lasers in Engineering*, **63**(0): pages. 30-42, 2014.
- [4] Moulart, R., S. Avril, and F. Pierron, Identification of the through-thickness rigidities of a thick laminated composite tube. *Composites Part A: Applied Science and Manufacturing*, **37**(2): pages. 326-336, 2006.

iDVC - Open-Source Interactive Software for Digital Volume Correlation

D. Sugic¹, L. Murgatroyd¹, I. T. Mitchell², J. M. Létang³, J.-Y. Buffière⁴, J. Lachambre⁴, G. Fardell¹, F. P. Vidal¹, B. K. Bay⁵, E. Pasca¹

¹Scientific Computing Department, STFC, UKRI, Rutherford Appleton Laboratory, Didcot, UK
²School of Computer Science & Engineering, Bangor University, Bangor, UK
³INSA-Lyon, Université Claude Bernard Lyon 1, UJM-Saint Étienne, CNRS, Inserm, CREATIS UMR 5220, U1294, 69373 Lyon, France
⁴INSA Lyon, Université Claude Bernard Lyon 1, CNRS, MATEIS UMR5510, 69621 Villeurbanne, France
⁵School of Mechanical, Industrial and Manufacturing Engineering Oregon State University, Corvallis, OR 97331-6001, USA

Abstract — iDVC is a software interface for configuring and running digital volume correlation (DVC). The software capabilities are presented with examples: 1) x-ray computed tomography (CT) of synthetic magma subjected to *in situ* heat/compression, and 2) CT of a mechanical component compared with a virtual CT scan derived from CAD geometry.

Keywords — DVC, Computed tomography, Mechanical manufacture, Sample compression

Introduction iDVC is open-source software [1] for interactively configuring and running DVC, the core DVC analysis code was written by B. K. Bay [2]. This can be used on reconstructed CT data, as well as other volumetric imaging modalities, such as confocal microscopy, optical slicing, and magnetic resonance imaging. X-ray imaging, routinely used to investigate materials and structures, is used here in the form of actual and virtual x-ray CT reconstructed volumes to illustrate the capabilities of iDVC.

The software was designed to facilitate, through visualisation, difficult aspects of the DVC process: point cloud creation, initial point registration, subvolume configuration. A set of tools are provided to tune analysis settings for specific problems. The software generates, or imports, a region of interest in the form of a point cloud. Automated and manual processes are provided to adjust for rigid body translation between image volumes. Fundamental DVC parameters (subvolume characteristics, optimisation degrees of freedom, objective function type, etc.) can be set and investigated with batch analysis tools.

Methods The capabilities of iDVC are demonstrated with two examples: 1) mechanics of materials analysis of a synthetic magma sample (Fig. 1) and 2) design vs manufacture comparison of a mechanical component (Fig. 2). In the first case, x-ray CT imaging was performed on a sample of synthetic magma subjected to *in situ* heat/compression [3]. Data was acquired at the Diamond Light Source with a bespoke thermo-mechanical rig (P2R) on the I12 beamline. The second example quantifies and visualises how a part of an *in situ* tensile testing machine differs from the CAD model guiding manufacture (Fig. 2 a, b). An 1120 projection CT scan was acquired with the DTHE scanner at INSA-Lyon, reconstructed to a voxel space of $400 \times 400 \times 1250$ at a 0.114 mm^3 voxel size. A virtual CT scan was generated from the CAD model using realistic X-ray simulations created with gVirtualXray (gVXR) [4] and the Core Imaging Library [5] for volume reconstruction. The two CT volumes are then compared using iDVC.

Results The iDVC software generates coordinated 2D and 3D visualisations of downsampled volumetric data to facilitate rapid user interaction (Fig. 1). The analysis point cloud is explicitly rendered, with individual subvolume positions, size, shape, and overlap shown (Fig. 1 b). Displacement vectors for the synthetic magma sample, rendered within the image volume, demonstrate the expected compression and

Poisson expansion, with deformation concentrated in the lower half.

For the mechanical component, correlation between the sample scan and virtual CAD reconstruction was successful for a cloud of surface points, with displacement vectors indicating location and magnitude of discrepancies (Fig. 2 c). The larger discrepancies are concentrated in the three holes on the face of the object, as well as the two screw holes.

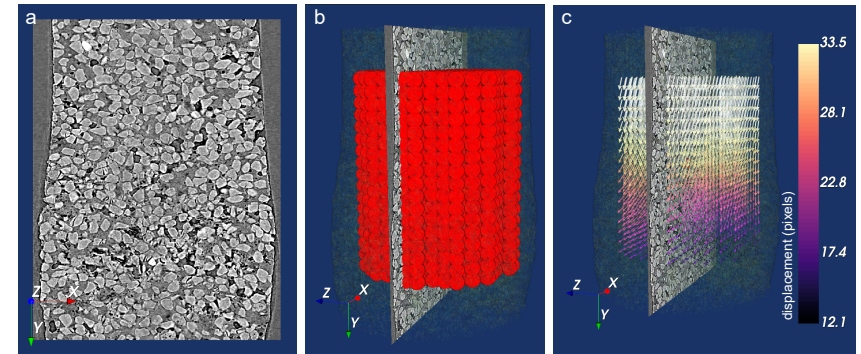


Figure 1: CT reconstruction of magma data. a) slice view, b) region of interest with point cloud and spherical subregions, c) displacement vector display.

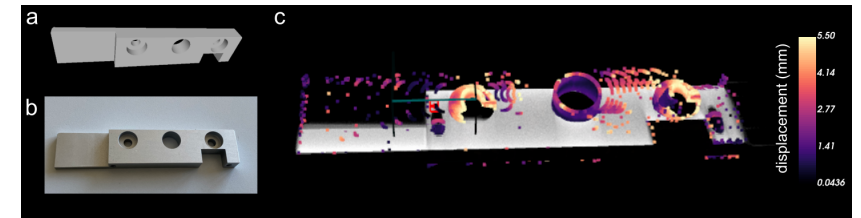


Figure 2: Mechanical component of an in-situ tensile testing machine. a) Original CAD model, b) component manufactured from the CAD model, c) displacement field between the 3D volumes of the experimental CT scan and of the virtual CT scan of the CAD model.

Discussion and Conclusion The iDVC software and DVC configuration visualisations are presented with examples of the synthetic magma subject to *in situ* heat/compression and mechanical-component manufacturing geometry validation. It was shown that iDVC offers tools to directly visualise compression analysis and quantify the discrepancies between manufactured components and CAD models.

References

- [1] <https://tomographicimaging.github.io/iDVC/>
- [2] B. K. Bay Methods and applications of digital volume correlation. *J. Strain Anal. Eng. Des.* 43(8):745-760, 2008.
- [3] L. Peter *et al.* Dataset. *Zenodo* DOI: 10.5281/zenodo.4835667, 2022
- [4] J. L. Poinon *et al.* Simulation of X-ray projections on GPU: Benchmarking gVirtualXray with clinically realistic phantoms. *Comput. Methods Programs Biomed.* 234:107500, 2023.
- [5] J. S. Jørgensen *et al.* Core Imaging Library Part I: a versatile python framework for tomographic imaging. *Phil. Trans. R. Soc* 379:20200192, 2021.

3D virtual image correlation (3D-VIC) for lattice structures metrology using x-ray radiographs

L. Calmettes, J. Réthoré, M.L.M. François

Nantes Université, Ecole Centrale Nantes, CNRS, GeM, UMR 6183, Nantes, France

Abstract — Due to the recent progresses in additive manufacturing, architected materials became more and more promising for designing materials with optimized properties. Lattice materials are among the possible architectures that can be considered for this purpose. However, the control of such materials cannot be achieved using standard metrology. Among the main challenges is the control of beam shapes inside a 3D lattice structure. We thus developed a 3D Virtual Image Correlation (3D-VIC) method that allows using a CAD model and only a few X-ray radiographs to measure the 3D shape of the lattice structure with sub-voxel accuracy.

Keywords — VIC, lattice materials, X-ray tomography

Introduction The evolution of additive manufacturing technologies (3D printing) has made it possible new complex structures such as architected materials. Architected materials possess an internal structure at some meso scale [1, 3] which is intermediate between the macroscopic scale of the whole structure, and the micro scale of the constitutive material. Lattice materials composed of beams (3D trusses) belong to this class of materials. In order to measure the shape of an architected material after 3D printing, it is necessary to carry out checks from the mesoscopic to the macroscopic scale. Conventional post-fabrication inspection methods (gages, ultrasound, etc. . .) are suitable for classical bulk materials but are no longer applicable to architected materials [1]. For this reason, both 2D and 3D image-based inspection methods, such as the one presented hereafter, are under development [4, 2].

Methods The method consists in the registration of virtual and real projections obtained by X-ray tomography through the minimization of the following cost function:

$$\Psi(\lambda_0, \dots, \lambda_n) = \frac{1}{n_\theta L_1 L_2} \sum_{\theta} \int_0^{L_1} \int_0^{L_2} (F_\theta - G_\theta)^2 dX dY \quad (1)$$

where (L_1, L_2) are the size of the detector, $\lambda_0, \dots, \lambda_n$ parameters to be optimized, F_θ real projections acquired by the tomograph for a collection of rotating stage angle θ and G_θ are simulated using a virtual tomograph model. In the case where the bulk material is considered to be homogeneous in terms of absorption coefficient μ , then G_θ simply reads

$$G_\theta(M) = \mu L(M), \quad (2)$$

$L(M)$ being the distance over which the ray reaching point M on the detector travels through the material. This distance is computed using a triangulation of the CAD model of the printed lattice structure and a rasterization procedure that is implemented in combination with a Z-buffer to evaluate this distance for each pixel of the detector.

In a first step, the virtual tomograph model is calibrated by adjusting its parameters (source to detector distance, source to rotating axis distance, angular position of the rotating stage with respect to the

tomograph frame, . . .) considered to be $\lambda_0, \dots, \lambda_n$. After this calibration, a shape correction is searched for using Radial Basis Function (RBF) to deform the initial CAD model until the stationarity of Ψ is reached, i.e. until the correlation between F_θ and G_θ is maximized. In practice, $\lambda_0, \dots, \lambda_n$ are now the displacement of the RBF control points.

Results A performance analysis is carried out using synthetic tomographic data. It is shown that the proposed method allows for sub-voxel accuracy even if only a few projections are used (3 to 5) and even if the level of noise in these projections reaches 50% (as expected from [5]).

An experiment has been performed on a tetrahedral lattice structure printed in ABS. A set of 5 projections (among the 1800 projections that were acquired) of 187×235 pixels are used. A set of 35 control points are regularly placed along the tetrahedral structure for a first global shape correction and a set of 165 control points are then added around the top vertex of the structure in order to obtain a more refined measurement of the printed structure shape compared to the reference CAD model. The result is shown in Figure 1.

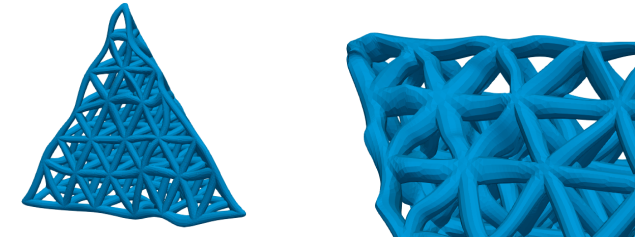


Figure 1: Measured shape showing displacements relative to theoretical shape. Left: global view with displacements magnified $\times 10$. Right: zoom on the upper vertex with displacements magnified $\times 3$

Discussion and Conclusion Based on the original idea of virtual image correlation [6], an extension to 3D in volume shape measurement is proposed. Virtual images are virtual projections computed using a virtual tomograph mimicking the imaging process. It is shown that the method is robust with respect to noise and that sub-voxel accuracy can be obtained even with only a few radiographs. Applied to images of a printed tetrahedral lattice structure, the method allows for capturing defects of different nature like beam thickness variation, beam deflection, misalignment at junctions. . .

References

- [1] Y. Brechet and J.D. Embury. Architected materials: Expanding materials space. *Scripta Materialia*, 68(1):1–3, 2013. Architected Materials.
- [2] M.A. de Pastre, Y. Quinsat, and C. Lartigue. Shape defect analysis from volumetric data - Application to lattice struts in additive manufacturing. *Precision Engineering*, 76:12–28, July 2022.
- [3] Y. Estrin, Y. Beygelzimer, and R. Kulagin. Design of architected materials based on mechanically-driven structural and compositional patterning. *Advanced Engineering Materials*, 21, 07 2019.
- [4] C. Fragnaud, C. Remacha, J. Betancur, and S. Roux. CAD-based X-ray CT calibration and error compensation. *Measurement Science and Technology*, 2022.
- [5] M.L.M. François. Uncertainty of the virtual image correlation method. *International Journal for Numerical Methods in Engineering*, 123(18):4367–4390, September 2022.
- [6] B. Semin, H. Auradou, and M.L.M. François. Accurate measurement of curvilinear shapes by Virtual Image Correlation. *European Physical Journal: Applied Physics*, 56(1):10701, October 2011. Publisher: EDP Sciences.

A crystal plasticity-based intragranular stress fields identification framework: application to commercially pure aluminium

R. Langlois, J. Réthoré, R. Seghir

Nantes Université, Ecole Centrale Nantes, CNRS GeM UMR 6183, Nantes, France
raphael.langlois@ec-nantes.fr

Abstract — Crystal Plasticity models are difficult to define then to calibrate as they rely on numerous internal variables, at the microscopic scale, whereas only surface kinematic data and the macroscopic load response can be measured. In this work, we propose a numerical framework to estimate intragranular stress fields from surface full-field kinematic measurements without postulating the actual form of the constitutive equation. It combines two inverse identification methods, (1) a sparse projection of the strain measurements on a relevant family of function to evaluate plastic slip magnitudes and (2) a Data-Driven Identification (DDI) strategy tuned to the physics at hand. Some examples on synthetic data are given to showcase the relevance of the methods. Finally, the framework is applied on samples of pure aluminium to characterize the evolution of intragranular stress fields.

Keywords — Full-field measurements, Inverse methods, Sparse Identification, Data-Driven Methods,

Introduction The deformation of polycrystals involves interactions between different scales of material organisation from the macroscopic scale to the atomic scale. At each scales, different tools exist to describe the core mechanisms of deformation and degradation of an initially “pristine” material. More specifically, Crystal Plasticity (CP) has been developed as a bridge between the scale of the polycrystalline aggregate and the mesoscopic “material” scale and provides a robust modeling tool [1]. In its simplest form, CP relies on the knowledge of grain orientations to define slip planes and a plastic slip evolution law to update critical resolved shear stresses (CRSS). Mesoscopic plastic strain and stress tensor can be recovered through the summation over the different systems. A large set of CP model exist allowing to recover macroscopic aggregate response. However we can not ascertain the relevance of their prediction at the intragranular scale as there is no way to locally probe, without strong assumptions, the evolution of the stress state. In particular, the proper way to introduce grain size effects, to handle grains interactions and grain boundary behavior in models remains an open question. In this talk, we propose a new numerical framework for estimating the fields of intragranular stress tensors. It relies on full-field kinematic data (e.g. obtained from digital image correlation (DIC)) and electron backscatter diffraction (EBSD) [4], as well as load measurement and original identification methods for: (1) plastic slip magnitudes (γ_i) and (2) resolved shear stress (RSS) (τ_i) identification.

Plastic slip magnitude extraction Slip magnitude quantification methods do exist in the literature [4, 5] but they are not able to extract the magnitude of all potentially activated slip systems. Indeed, in the general case the projection of 6 strain components onto a larger family of slip systems (e.g. 12 for FCC or 24 for BCC) is not unique. We propose a sparse promoting projection of the plastic strain following the seminal contributions of Brunton and his collaborators [3, 6] on sparse identification. In the spirit of [6], we define a regularized least-squares projection of a measured strain onto the family of Schmid-Boas tensors \mathcal{T}_i for each slip system i , which reads using vectorized notation as :

$$\min_{\tilde{\gamma}, \gamma_{sp}} \frac{1}{2} \|\mathbf{T}\tilde{\gamma} - \tilde{\epsilon}^p\|^2 + \lambda \mathcal{R}(\gamma_{sp}) + \frac{\kappa}{2} \|\tilde{\gamma} - \gamma_{sp}\|^2 \quad (1)$$

where \mathbf{T} is the vectorized Schmid-Boas tensors, $\tilde{\gamma}$ is the regularized least-squares solution, γ_{sp} is a sparse representation close to $\tilde{\gamma}$ in the sense of the norm $L2$, $\tilde{\epsilon}^p$ is an estimation of the plastic strain tensor

(see next part), \mathcal{R} is a sparsity promoting metric and finally λ and κ are regularization weights which promote (or cancel) respectively the degree of sparsity in γ_{sp} and the closeness between the two outputs. This problem can be efficiently solved using a prox-gradient descent algorithms proposed in [6].

Stress fields identification Second, we propose a modification of the DDI method developed by Leygue and co-authors [7] to be consistent with Crystal Plasticity. Therefore, a new constitutive space is introduced using $\{(\tau_i, \gamma_i)\}_{i \in [1, N_s]}$ leading to a problem of the form:

$$\min_{\tau, \gamma, \tau^*, \gamma^*} \frac{1}{2} \sum_{i=1}^{N_s} \int_t \int_{\Omega} (\gamma_i(t) - \gamma_i^*) \mathbb{G}(\gamma_i(t) - \gamma_i^*) + (\tau_i(t) - \tau_i^*) \mathbb{G}^{-1}(\tau_i(t) - \tau_i^*) dV dt \quad (2)$$

under the constraint of mechanical quasi-static equilibrium:

$$\forall t : \begin{cases} \text{div}(\sum_{i=1}^{N_s} \tau_i(t) \mathcal{T}_i) = 0 & \text{in } \Omega \setminus \partial\Omega_F \\ \int_{\partial\Omega_F} \sum_{i=1}^{N_s} \tau_i(t) \mathcal{T}_i \cdot n = F(t) & \text{on } \partial\Omega_F \end{cases}$$

where N_s is the number of slip systems of the crystal(s), Ω the domain defined by the sample comprised of multiple crystals and $\partial\Omega_F$ the boundary where the load is measured, \mathbb{G} a scaling operator akin to a shear modulus, (τ_i^*, γ_i^*) a collection of discrete point sampling the material response in the constitutive space (τ_i, γ_i) . This problem is solved using a staggered scheme alternating between updating the plastic slip magnitudes eq. (1) and computing the RSS eq. (2) until convergence on slips and RSS.

Results First, some examples on synthetic data are given to highlight the ability of the method to retrieve relevant quantities (slips and RSS). Second, the framework is applied on pure aluminium samples with quasi-2D coarse grain microstructure under tensile load. The software *NEPER* [8] is used to generate microstructure conforming triangular FE meshes used for DIC analysis. The evolution of (1) “microscopic” (slip and RSS) and (2) mesoscopic (stress and plastic strains) quantities of interest will be presented and an in-depth analysis of intragranular stresses is proposed.

References

- [1] Miehe, C. & Schotte, J. (2004), *Crystal Plasticity and Evolution of Polycrystalline Microstructure*, Encyclopedia of Computational Mechanics
- [2] Guery, A., et al. (2016), *Identification of crystal plasticity parameters using DIC measurements and weighted FEMU*, Mechanics of Materials,
- [3] Brunton, S. et al. (2016), *Discovering governing equations from data by sparse identification of nonlinear dynamical systems*, Proceedings of the National Academy of Sciences
- [4] Berger, A. et al. (2022), *Experimental investigation of early strain heterogeneities and localizations in polycrystalline α -Fe during monotonic loading*, International Journal of Plasticity
- [5] Vermeij, T. et al. (2023), *Automated identification of slip system activity fields from digital image correlation data*, Acta Materialia
- [6] Zheng, P. et al. (2019), *A Unified Framework for Sparse Relaxed Regularized Regression: SR3*, IEEE Access
- [7] Leygue, A. et al. (2019), *Non-parametric material state field extraction from full field measurements*, Computational Mechanics
- [8] Quey, R. &avernersade, R. (2018), *Optimal polyhedral description of 3D polycrystals: Method and application to statistical and synchrotron X-ray diffraction data*, Computer Methods in Applied Mechanics and Engineering

uCheckMate : An open-source python library for research and development of Finite element stereo digital image correlation

H. MATAR, B. BLAYSAT, T. JAILIN, O. AIT-AIDER,
M. GREDIAC, H. CHANAL

Université Clermont Auvergne, Clermont Auvergne INP, CNRS, Institut Pascal, Clermont-Ferrand, France

Abstract — Stereo Digital Image Correlation (SDIC) is a powerful technique used in experimental mechanics for precise 3D displacement measurements on sample surfaces. Global methods of SDIC show the advantage of facilitating comparisons between measurements and simulations. Indeed, when coupled with Finite Elements (FE), the experimental measurements are represented in the same discretization framework as the simulation. This abstract introduces a novel Python library designed to perform (SDIC) with (FE) analysis, with the advantage of working directly in the reference system of interest.

Keywords — Finite Element, Global SDIC, Image Processing, Stereo Vision, OpenCV

Introduction Stereo Digital Image Correlation (SDIC) needs at least two cameras to calculate the displacement field of a surface in three dimensions. This technique can be divided into two main branches: Local methods and Global methods. **Local methods** focus on multiple independent image subsets to retrieve the whole surface displacement field. On the other hand, **Global methods** consider a region of interest within the image to compute the kinematic fields across its surface in a unique minimization, providing a more holistic perspective of the material behavior. Despite the seminal works on **Global SDIC** proposed twenty years ago, almost no free software is available today. This mainly explains why its spread is still reduced in the Experimental Mechanics community. The first motivation of the present work is to fill that gap by proposing an open-source solution for research and development.

The most common **Global** approach for SDIC is based on **Finite Elements**, leading to the Finite Element Stereo Digital Image Correlation (**FE-SDIC**) method. In **FE-SDIC**, a mesh, composed of elements connected to their neighbors, is used to define the kinematics. It is worth mentioning that **FE-SDIC** can be performed either in the image coordinate system or in the physical coordinate system. In the latter case, the displacement is directly expressed in the coordinate system of interest. This considerably simplifies and strengthens the link with the observed material, the latter being the quantity of interest in Experimental Mechanics. Following this idea, the **uCheckMate** framework is here proposed to retrieve the 3D-surface displacement of an object by **FE-SDIC** directly in the physical coordinate system. It is worth noting that since the test-simulation model is simple, regularization within the object itself can easily be performed, simplifying materials characterization.

Methods A **Unified framework** is proposed to carry out three different tasks: (i) multi-camera system calibration, (ii) fine-tuned shape measurements, and (iii) kinematic measurements. In the formalism of **FE-SDIC** the problem reads with N cameras:

$$\underline{\theta}^*, \underline{F}^* = \frac{1}{2} \operatorname{argmin}_{(\underline{\theta}, \underline{F}) \in \mathbb{R}^{6N} \times \mathbb{L}^2} \sum_{i_{cam}=0}^{N-1} \sum_{j_{cam}=i_{cam}+1}^N \left(I_{i_{cam}}^0 \circ P(\underline{X} + \underline{F}(\underline{X}), \underline{\theta}_{i_{cam}}) - I_{j_{cam}}^0 \circ P(\underline{X} + \underline{F}(\underline{X}), \underline{\theta}_{j_{cam}}) \right)^2 \quad (1)$$

- N: Number of cameras
- $I_{i_{cam}}$: Image taken by camera numbered i_{cam}
- \underline{X} : 3D integration points
- P : Projection function of the i_{cam} camera
- \underline{F} : Field of interest, defined by the FE-model
- $\underline{\theta}$: Extrinsic parameters of a given camera

(i) **Multi-camera system calibration**: Corresponds to the position and orientation of the camera in the world coordinate system.

(ii) **Fine-tuned shape measurements**: Measures the actual form and adjust the CAD-generated mesh accordingly based on this measurement.

These first two tasks aim to verify the **conservation of gray levels** between the reference images of the specimen captured by each camera.

When all the cameras are calibrated, and the shape is corrected, it becomes possible to (iii) **measure the displacement** through stereo image correlation :

$$\underline{F}^* = \operatorname{argmin}_{\underline{F} \in \mathbb{L}^2} \frac{1}{2} \sum_{i_{cam}=0}^{N-1} \left(I_{i_{cam}}^0 \circ P_{i_{cam}}(\underline{X} + \underline{F}(\underline{X})) - I_{i_{cam}}^t \circ P_{i_{cam}}(\underline{X} + \underline{F}(\underline{X})) \right)^2 \quad (2)$$

A Gauss-Newton algorithm is used : $\underline{F}^{(n+1)} = \underline{F}^{(n)} + d\underline{U}^{(n)}$ with $d\underline{F}^{(n)} = \sum_{i=1}^{N_c} \varphi_i(\underline{X}) \underline{s}_i^{(n)} = \underline{\Phi}(\underline{X}) \underline{s}^{(n)}$, where t_0 the reference state and t the deformed state of the image.

Results Figure 1 shows the 3D finite element mesh, the reference image of the DIC Challenge data set [1], and the superposition of the two. The **Pose** of each camera and the **sample shape** can then be optimized, followed by the **kinematic measurements**.

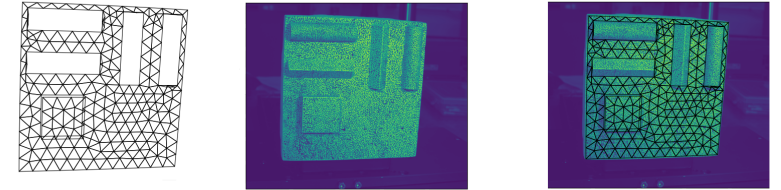


Figure 1: Mesh Projected into the reference image.

Discussion and Conclusion Once implemented the algorithms lead to fast convergence. The displacement expressed in the finite element space is calculated in the 3 directions between a reference state and deformed state based on a 3D geometry. This latter is expressed in the same discretization space as that used in the simulations. A study on the robustness of the three algorithms will be presented. The use of more than two cameras will be presented. Contrast and brightness correction based on the mesh elements and regularization will also be discussed.

References

- [1] Balcaen, R., Wittevrongel, L., Reu, P.L. et al. StereoDIC Calibration and Speckle Image Generator Based on FE Formulations.
- [2] COLANTONIO, Guillaume, MARENIC, Eduard, et PASSIEUX, Jean-Charles. Stéréo-DIC globale appliquée à l'identification des paramètres d'une loi de comportement. In : 24e Congrès Français de Mécanique (CFM). 2019.

Automated, quantitative identification of slip system, twinning & boundary sliding activity maps from EBSD-SEM-DIC data

J.P.M. Hoefnagels^{1,*}, G. Slokker¹, D. König¹, C.J.A. Mornout¹, T. Vermeij^{1,2}

¹ Eindhoven University of Technology, Eindhoven, The Netherlands.

² Empa - Swiss Federal Laboratories for Material Science and Technology, Thun, Switzerland

Abstract — Quantitative identification of the plasticity mechanisms active at the microstructure, such as crystallographic slip, twinning, and grain boundary sliding, is crucial to unravel the often-complex small-scale deformation pathways controlling the performance in engineering applications. We present and demonstrate multiple methods for objective, automatic identification of activity maps of these plasticity mechanisms, by pixel-wise matching the measured in-plane displacement gradient tensor to the kinematics of the optimal combination of the mechanisms' activities.

Keywords — plasticity, SEM-DIC, slip system identification, grain boundary sliding, EBSD

Introduction Quantitative identification of the active crystallographic slip families and slip systems is crucial for understanding plastic deformation of materials, quantitative comparison to simulations, and development of new alloys. Current slip system identification methods (i) use of the Schmid Factor to select the slip system with the highest critical resolved shear stress, (ii) match observed slip traces to theoretical slip traces (from Electron Backscatter Diffraction (EBSD)), or (iii) match the 'Relative Displacement Ratio' (RDR) along a pre-determined slip trace, [1] using strain fields measured by Scanning Electron Microscopy based Digital Image Correlation (SEM-DIC). [2] However, (i) the Schmid Factor suffers from unknown local boundary conditions, [1] (ii) the slip trace analysis disregards the slip direction, and (iii) the RDR method needs clear and straight slip traces in the strain field, whereas plasticity often involves more complex mechanisms such as cross-slip, curved slip, and/or diffuse slip. Therefore, a new method is required that performs a one-step, pixel-wise identification on the SEM-DIC displacement/strain field, i.e., without requiring an initial identification of slip trace lines in the strain map.

Besides crystallographic slip, often also other deformation mechanisms are active at the micron scale, such as twinning and grain boundary sliding. Therefore, quantitative identification of all plasticity mechanisms active at the microstructure is crucial to understand the mutual interactions between these plasticity mechanisms and to elucidate the essential deformation pathways controlling the performance in engineering applications.

Methods All identification are based on high-quality microstructure-correlated SEM-DIC strain maps. To this end, a nanoscale digital image correlation (DIC) patterning method [3] is applied to create the optimum pattern for in-situ SEM-DIC testing, yielding strain fields with a spatial resolution (of the strain) in the order of 40 nm. Then, a novel nanomechanical testing and alignment framework [4] is used to align the heavily warped EBSD grain orientation maps onto the strain field within 100nm accuracy. First, a novel slip system identification framework, termed SSLIP (for Slip Systems based Local Identification of Plasticity), [5] is presented, in which the measured displacement gradient fields are locally matched to the combined kinematics of multiple theoretical slip systems, based on the measured crystal orientations. To identify the amount of slip that conforms to the measured kinematics, an optimization problem is solved for every datapoint individually, yielding a slip activity field for every slip system. Next, the SSLIP method is extended to a dedicated cross-slip identification method. In cross-slip the

slip direction remains constant, while the dislocations transfer onto the 'neighboring' slip plane. This knowledge is used by limiting the kinematics in the SSLIP framework to one slip direction (or two slip directions in case of two active cross-slip families), while making the slip plane angle a degree of freedom, thus yielding (a) cross-slip plane angle map(s) next to (a) cross-slip intensity map(s).

Moreover, the SSLIP method was extended to identify and quantify possible twinning systems, by adding the twinning plane / shear direction of each twinning system as kinematics to the SSLIP framework.

In addition, the SSLIP method was modified to identify the magnitude and nature of grain boundary sliding, including the apparent 2D sliding angle w.r.t. the grain boundary. [6] In this method, the displacement data along a line perpendicular to the grain boundary is extracted, which requires additional analysis steps of the EBSD and DIC data to achieve robust identification of the grain boundary sliding. The robust version of this method was renamed as Local Identification of Boundary Sliding (LIBS).

Finally, it was found that for HCP crystal structures the complete identification of all slip systems from all possible slip families is more challenging, due to the strong kinematic similarity between slip systems, posing limitations on automation and flexibility. We therefore present a significant extension to the original SSLIP framework, named +SSLIP, [7] to achieve robust, automated slip system identification of highly similar slip systems. The main extensions of the +SSLIP method include (i) a pre-selection of slip systems using a Radon transform, (ii) robustness to measured rigid body rotation by simultaneous identification of the local elastic rotation field, and (iii) identification of the two best matching slip systems for each data point, yielding the full (HCP) slip system activity maps with all slip systems for each grain.

Results First, the original SSLIP identification framework is demonstrated on different experimental FCC and BCC case studies showing full-field identification of discrete slip, diffuse slip, and cross-slip, even for 48 slip systems for BCC. Moreover, the value of the cross-slip identification method is shown. The other methods are demonstrated in a challenging case of HCP plasticity: zinc corrosion coatings for steel. Over 300 zinc grains of a skin-passed zinc coating have been automatically analyzed. It is shown that the +SSLIP and twinning method robustly identify the HCP slip system and twinning activity fields, while the LIBS method robustly identifies the grain boundary sliding activity maps, quantifying, e.g., the apparent sliding angle. Examples of statistical analysis of these plasticity activity fields are presented.

Conclusions Quantitative identification of the plasticity mechanisms at the microstructure, such as crystallographic slip, twinning, and grain boundary sliding, is crucial to unravel the complex small-scale deformation pathways controlling the performance in engineering applications. Here multiple methods for objective, automatic identification of these plasticity mechanisms are presented and their effectiveness in yielding quantitative activity fields of the different plasticity mechanisms is demonstrated.

References

- [1] Z. Chen & S.H. Daly. Active slip system identification in polycrystalline metals by digital image correlation (DIC). *Experimental Mechanics*, 57:115, 2017.
- [2] T. Vermeij & J.P.M. Hoefnagels. Plasticity, localization, and damage in ferritic-pearlitic steel studied by nanoscale digital image correlation. *Scripta Materialia*, 208:114327, 2021.
- [3] J.P.M. Hoefnagels, M.P.F.H.L. van Maris & T. Vermeij. One-step deposition of nano-to-micron-scalable, high-quality digital image correlation patterns for high-strain in-situ multi-microscopy testing. *Strain*, 55(6):e12330 2019.
- [4] T. Vermeij, J.A.C. Verstijnen, T. Ramirez y Cantador, B. Blaysat, J. Neggens & J.P.M. Hoefnagels. A nanomechanical testing framework yielding front & rear-sided, high-resolution, microstructure-correlated SEM-DIC strain fields. *Experimental Mechanics*, 62:1625, 2022.
- [5] T. Vermeij, R.H.J. Peerlings, M.G.D. Geers & J.P.M. Hoefnagels. Automated Identification of Slip System Activity Fields from Digital Image Correlation Data *Acta Materialia*, 243:118502, 2023
- [6] C.J.A. Mornout, G. Slokker, D. König, T. Vermeij & J.P.M. Hoefnagels. Automated Identification of Grain Boundary Sliding from Digital Image Correlation Data (working title). *In preparation*, 2024
- [7] T. Vermeij, G. Slokker, D. König, C.J.A. Mornout & J.P.M. Hoefnagels. +SSLIP: Automated Radon-assisted and Rotation-corrected identification of complex HCP slip system activity fields from DIC data. *Submitted for publication*, 2024

High resolution 3D stereo DIC for small FOV using the Scheimpflug principle

H.Pulju, P.Mäckel

isi-sys GmbH, Germany

Optical diffraction is a practical limitation for high-resolution sensors with small pixel sizes, especially in digital image correlation. The depth of field decreases exponentially with working distance in small fields of view, complicating resolution due to the need for smaller apertures and resulting diffraction. While 2D systems can simplify measurements by eliminating depth of field issues, they are prone to errors from optical distortion and out-of-plane movements, making 3D stereo DIC systems preferable for accurate deformation and strain measurements. Conventional stereo systems have limited field of view due to depth of field constraints, but this can be improved by tilting the focal planes using the Scheimpflug principle. This adjustment allows both cameras in a stereo setup to maintain focus over a larger field of view, enhancing measurement accuracy.

Keywords – 3D-DIC, Micro-DIC, small FOV, Scheimpflug, Diffraction-limit

For common photography diffraction hardly plays a role, except already in macro photography. Since high-resolution sensors with corresponding smaller pixel require very small permissible circles of confusion, the optical diffraction moves into the range of practical limitation for the resolution at small field of view for systems operating with a high pixel density.

Operating with an object distance less than a quarter of the hyperfocal distance (as for small field of view) the depth of field scales not linear but unfortunately exponential with the working distance. In general, it can be said that, as smaller the aperture diameter, as larger is the optical diffraction, which limits the optical resolution and thus the required spatial resolution of the system. All this can be described and seen by the principle equations describing optical diffraction and depth of field combined with the geometric basics of optical imaging and the practical embodiment and dimension of lens and aperture.

On this background a measurement with small field of view at high resolution is much easier to achieve with a simple 2D system, because no depth of field is required, as in an ideal case the object surface is flat and observed from the normal direction. The errors of 2D DIC resulting from the optical distortion can be reduced using telecentric lenses. However, in these applications the error in the measurements can be also high due to unknown out of plane movements and curvatures, which already occur simply due to the deformation of the object itself caused by the transverse contraction. The plastic deformation also especially occurs in the region of strain peaks. So, the 2D application is not a reliable solution even though the shape is not taken into account and a 3D stereo DIC system should be preferred for deformation and strain measurements.

In conventional stereo systems, the usable FOV width is strongly limited due to the small depth of field of each camera and the viewing angle such as explained in the previous section and shown by the stereo image pair of Fig. 1 (left) compared to the case of a stereo image pair of Fig. 1 (right) of the same surface but show fully in focus over the complete field of view. The color scales in Fig. 1 shows the preview for the uncertainty estimation function in VIC-Snap, indicating the loss of focus (left example). It is clearly visible that the focus reduces towards the left and right side of the image.

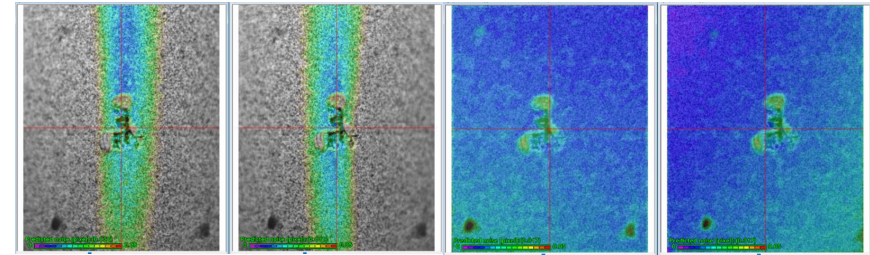


Figure 1: Example of two stereo image pairs showing left and right view of a small FOV (approx. 8 mm x 7 mm) with a conventional setup (left image pair) and using the Blue-Falcon camera module (right image pair).

Depending on the required stereo angle α , this results from the restricted small overlapping region of the DOF and the object surface as shown in the sketch of Fig. 2 (left). The correlation is only possible in the overlapping area of the focal planes of the two cameras of the stereo setup. The focal planes are indicated by the red and blue dashed lines. The red and blue areas represent the DOF range where the image is sufficiently sharp for a single camera for the 2D application case. The colored regions mark the overlapping area, where the image quality is adequate for both cameras to compute a 3D-DIC correlation with sufficient accuracy. This results in a rather narrow usable FOV width range L_{ref} , which is considerably less than the field of view width of each individual sensor.

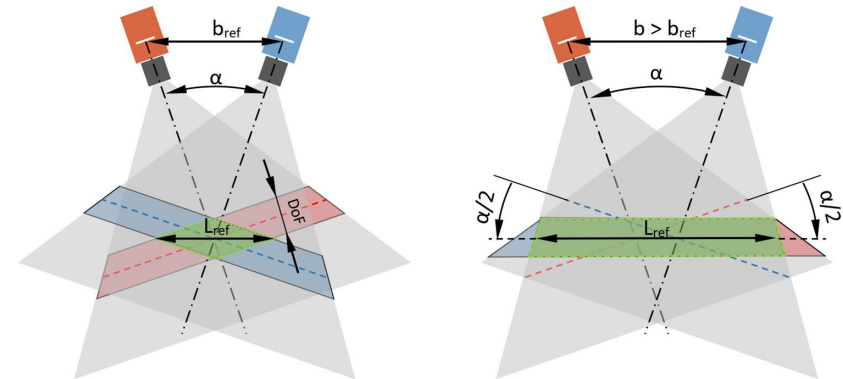


Figure 2: Left: Conventional stereo DIC setup with reduced overlapping region due to crossed focal planes of each camera. Right: Aligned focal planes using Blue-Falcon cameras for the stereo setup.

In contrast, the example of Fig. 1 (right) shows the complete field of view of both images is in focus. This requires rotating the focal planes of both cameras by half of the stereo angle $\alpha/2$, such as shown in the sketch of Fig. 2 (right). The principle used for the rotation of the focal planes is named after the inventor Theodor Scheimpflug. The graphical construction of the angle required for the tilted the image plane (sensor) corresponding to the Scheimpflug requirements is shown in Fig. 3.

Study of strain localization and crystal reorientation at the early stage of plastic deformation using LSCM, HR-EBSD and DCT-6D

 D. Texier¹, S. Vallot¹, J. Genée¹, J.-C. Passieux¹, H. Proudhon², W. Ludwig³, J.-C. Stinville⁴
¹Institut Clement Ader (ICA) - UMR CNRS 5312, Université de Toulouse, CNRS, INSA, UPS, Mines Albi, ISAE-SUPAERO, Campus Jarlard, 81013 Albi Cedex 09, France

²Centre des Matériaux - Mines Paris PSL - UMR CNRS 7633; Evry, France

³MATEIS - UMR CNRS 5510, Villeurbanne, France

⁴Materials Science and Engineering, UIUC; Urbana-Champaign (IL), USA

Abstract – High resolution digital image correlation using laser scanning confocal microscopy was applied to a polycrystalline Ni-based superalloy to capture both in-plane and out-of-plane kinematics fields at the sub-grain scale. In addition to discrete and intense strain localization events, a particular attention was paid on crystal reorientations that inform on deformation incompatibilities from grains to grains. High resolution EBSD and diffraction contrast tomography (6D-DCT) measurements confirmed grain reorientations at the surface and in the volume, respectively.

Keywords – High resolution Digital image correlation, crystal plasticity, topographic measurement, laser scanning confocal microscopy, strain localization, grain reorientation

Introduction High-resolution digital image correlation (HR-DIC) techniques are well established for measuring sub-granular strain localization in polycrystalline materials [1]–[4]. HR-DIC has generally been performed under scanning electron microscopy (SEM) to gain in spatial resolution and micrograph repeatability. However, HR-DIC under SEM only provides information on the in-plane kinematic field at the surface of deformed samples. This technique is particularly appropriate when the out-of-plane motion associated with the three-dimensional (3D) localization of deformations can be assessed from another source, i.e. slip events in combination with EBSD analyses [5]. The localization of non-crystallographic deformations, such as grain boundary sliding, requires the development of 3D measurement techniques [6]. Confocal laser scanning microscopy (LSCM) using a near-UV monochromatic source provides less resolved in-plane micrographs but highly accurate topographic information (< 10 nm in height) [7], [8]. A 3D formulation of the HR-DIC problem has therefore been implemented to assess the location of full-field 3D deformation in a Ni-based superalloy at room temperature. Access to the topography of the deformed sample also enabled the study of crystal reorientation due to deformation. These crystal lattice reorientations were also compared with high-resolution EBSD data to probe the gradual and discrete nature of these crystal reorientations.

Methods The present study was conducted on a flat dogbone specimen extracted from a wrought Alloy 718 plate. The nominal composition of the alloy is bal. Ni, 18.57 % Cr, 18 % Fe, 5.02 % Nb, 2.86 % Mo, 0.11 % Co, 0.58 % Al, 0.97 % Ti, <0.01 % Ta (weight percent). The flat dogbone specimen was mechanically ground using SiC papers, then polished with diamond paste and surface-finished with colloidal silica. This surface finish allows for initial EBSD characterization of the microstructure (grain morphology and orientation) prior to deformation. EBSD maps were obtained using a JEOL JSM 7100F SEM and an Oxford EBSD SYMMETRY S2 system. After EBSD characterization, a short-term oxidation at 650 °C for 15 minutes in air aimed to form a randomly distributed gray level speckle pattern resulting from the specific surface reactivity of the γ - γ' - γ'' microstructure of Alloy 718. This speckle pattern enables sub-grain measurement of the kinematics field compatible with dissociation of distinct microplasticity events far from 600 nm, as demonstrated in Ref [6]. Images for HR-DIC experiments were acquired before and after deformation using an Olympus laser scanning confocal microscope (LSCM) LEXT OLS5100 with a x100 lens magnification (WD = 350 μ m and NA=0.95). A mosaic of 11x11 images was automatically acquired for each deformation step with a numerical resolution of

1024x1024 pixels (pixel size of 125 nm) and an image overlap of 10 %. Both the laser intensity and height maps were obtained. HR-DIC calculations were performed on individual images using the Heaviside-DIC method [5]. Quasi-HR EBSD was also performed after deformation to capture grain reorientations. Diffraction Contrast Tomography (DCT) was performed at the ESRF using a monochromatic near-field 3D X-ray diffraction technique to reconstruct the polycrystalline microstructure morphology in 3D with the crystallographic orientation in each grain.

Results Tensile tests were interrupted at 0.8 % plastic strain to investigate strain localization at the microstructural scale. A portion of the in-plane and out-of-plane displacement jump maps were illustrated in Fig. 1, showing discrete displacement jumps. Profiles along individual bands show maximum jumps in the core of the grain while minimal jump is in the vicinity of the grain boundaries. Interestingly, grain reorientation maps is maximal in the vicinity of the grain boundaries and minimal in the core of the grain (Fig. 1(c)). Such local antagonist responses clearly demonstrate how localized plastic incompatibility in adjacent grains is accommodated by grain reorientations. Such grain reorientations were also evidenced using topographic and 6D-DCT characterizations.

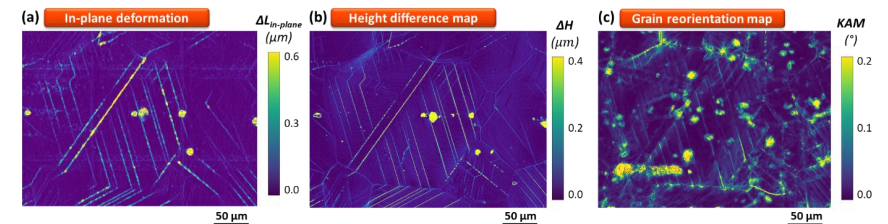


Figure 1: (a) In-plane displacement jump map, (b) out-of-plane displacement jump map, (c) grain reorientation map.

Discussion and Conclusion The present work highlighted the importance of both displacement fields and rotation fields at the sub-grain level to better quantify and analyze crystal plasticity in polycrystalline materials. HR-DIC with LSCM measurement was able to provide both displacement and rotation fields at the sub-grain level, which are not accessible with HR-DIC with SEM alone.

References

- [1] M. A. Sutton, N. Li, D. C. Joy, A. P. Reynolds, and X. Li, “Scanning electron microscopy for quantitative small and large deformation measurements Part I: SEM imaging at magnifications from 200 to 10,000,” *Exp. Mech.*, vol. 47, no. 6, pp. 775–787, 2007.
- [2] J. C. Stinville, M. P. Echlin, D. Texier, F. Bridier, P. Bocher, and T. M. Pollock, “Sub-grain scale digital image correlation by electron microscopy for polycrystalline materials during elastic and plastic deformation,” *Exp. Mech.*, vol. 56, pp. 197–216, 2016.
- [3] A. Guery, F. Hild, F. Latourte, and S. Roux, “Slip activities in polycrystals determined by coupling DIC measurements with crystal plasticity calculations,” *Int. J. Plast.*, vol. 81, no. February, pp. 249–266, 2016.
- [4] F. Di Gioacchino and J. Quinta da Fonseca, “Plastic strain mapping with sub-micron resolution using digital image correlation,” *Exp. Mech.*, vol. 53, no. 5, pp. 743–754, 2013.
- [5] F. Bourdin *et al.*, “Measurements of plastic localization by heaviside-digital image correlation,” *Acta Mater.*, vol. 157, pp. 307–325, 2018.
- [6] D. Texier *et al.*, “Strain localization in the Alloy 718 Ni-based superalloy: From room temperature to 650 °C,” *Acta Mater.*, vol. 268, no. October 2023, p. 119759, 2024.
- [7] J. H. Liu, N. Vanderesse, J. C. Stinville, T. M. Pollock, P. Bocher, and D. Texier, “In-plane and out-of-plane deformation at the sub-grain scale in polycrystalline materials assessed by confocal microscopy,” *Acta Mater.*, vol. 169, pp. 260–274, 2019.
- [8] W. Yin, F. Briffod, H. Hu, T. Shiraiwa, and M. Enoki, “Three-dimensional configuration of crystal plasticity in stainless steel assessed by high resolution digital image correlation and confocal microscopy,” *Int. J. Plast.*, vol. 170, no. June, p. 103762, 2023.

Elevated temperature High Resolution Digital Image Correlation in a Scanning Electron Microscope

A. Harte¹, D. Lunt¹, B. Poole¹, A. Smith², E. Pickering³, C. Hamelin¹

¹UK Atomic Energy Authority, Culham Campus, Abingdon, OX14 3DB, United Kingdom

²TESCAN-UK Ltd, Wellbrook Court, Girton, Cambridge, CB3 0NA, UK.

³Department of Materials, University of Manchester, Oxford Road, Manchester, M13 9PL, UK

Abstract

High resolution digital image correlation (HRDIC) in a scanning electron microscope (SEM) is becoming a routine tool, valued as a way to explore the micro-mechanisms of plasticity and the validation of microstructurally informed deformation models. To date, there has been limited development of HRDIC to enable its use at elevated temperature. Here, we present recent results that demonstrate fully automated, in-situ thermal and mechanical loading of metallic materials with simultaneous capture of micrographs for HRDIC. We show the effect of microscope parameters, sample preparation and speckle pattern on the noise floor as a function of temperature for different mechanical loading modes, enabling us to identify deformation mechanisms and correlate them to macroscopic flow.

Keywords – High Resolution DIC, Scanning electron microscopy, Elevated temperature, Uncertainty

Introduction

Structural materials for nuclear fusion devices must undergo integrity assessment for combined thermal-mechanical-irradiation loads, but representative testing facilities do not exist. One approach to materials qualification is to pair multi-physics loadings where possible, employ data-rich diagnostics to validate high fidelity models, use those models to make predications in untestable environments, and then update those predications based on in-service monitoring. Room temperature HRDIC has previously been used to validate such crystal plasticity models [1], but HRDIC at elevated temperature is immature. Here, we present progress in enabling elevated temperature HRDIC and in quantifying the associated measurement uncertainty. This lays the groundwork for best practice documentation.

Methods

The metallic materials used in this work were oxygen-free high conductivity copper and Grade 91 ferritic-martensitic steel, both of which are materials used in the designs of in-vessel components for fusion devices. All thermal and mechanical loading was performed with a NewTec Scientific MT1000 mechanical tester, fully integrated with a TESCAN CLARA field emission SEM. Software integration between the in-situ stage and microscope enables fully automated testing and image capture as a function of applied deformation. Tensile specimens were electric discharge machined and mechanically polished to a deformation-free surface. Nanoscale speckle patterns were applied by either the styrene-assisted gold remodelling technique [2] or the silver chemical remodelling technique [3]. After patterning, plasma cleaning was performed in some cases to assess the effect of sample cleanliness on the measured kinematics. Imaging was performed using three detectors: 4 quad diode backscatter detector, a water-cooled scintillator backscatter detector and an Everhart-Thornley secondary electron detector. The speckle pattern stability was measured by calculating the spatial noise floor as a function of time-at-temperature up to a maximum temperature of 400 °C. Quasi-static tension and static tensile creep loads were applied to specimens at elevated temperature. Deformation mechanisms were quantified in the maps of effective strain (Equation 1) using in-house pythonic routines and linked to the underlying microstructure via electron backscatter diffraction orientation measurements.

The effective in-plane strain is

$$\epsilon_{eff} = \sqrt{\frac{1}{2} \left(\frac{\partial u_1}{\partial x_1} - \frac{\partial u_2}{\partial x_2} \right)^2 + \frac{1}{2} \left(\frac{\partial u_1}{\partial x_2} + \frac{\partial u_2}{\partial x_1} \right)^2} \quad (1)$$

Where u_1 and u_2 are displacements on the x_1, x_2 plane with normal x_3 .

Results

Secondary electron (SE) detection shows promise for elevated temperature HRDIC, as the SE detector is less susceptible to IR radiation than the backscatter detectors. However, SE detection is particularly sensitive to surface cleanliness. Post-speckling plasma cleaning reduces noise in SE-collected HRDIC strain maps, Figure 1. Temperatures above 400 °C result in IR radiation swamping detectors and/or oxide formation and surface cracking.

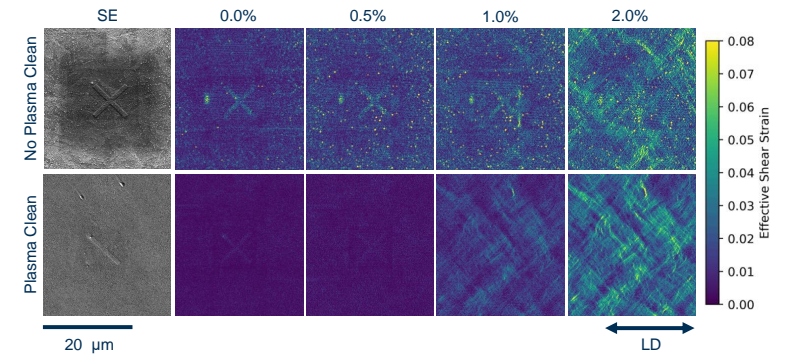


Figure 1: In-plane effective shear strain at 250 °C in Grade 91 steel. Maps show local strain as a function of total strain under quasi-static tensile load in the loading direction (LD), with (bottom) and without (top) plasma cleaning after speckle pattern application. The cross shaped features in the image centres are electron-beam deposited fiducial markers.

In copper, the automated mapping permits many strain steps, which allows us to correlate the onset of different deformation mechanisms with macroscopic parameters. Early plasticity shows no hardening, correlated with a grain boundary diffusion/sliding mechanism. The onset of macroscopic hardening is correlated to the interaction of dislocation-mediated slip with grain boundaries, causing backstresses on dislocation sources. In Grade 91 steel, we observe changes to the slip character as a function of temperature, suggesting a change in the deformation mechanism that should be captured in models.

Conclusion

We have demonstrated elevated temperature deformation of copper- and iron-based alloys with simultaneous HRDIC in a field emission SEM under both quasi-static and static loading up to a maximum temperature of 400 °C. Plasma cleaning and secondary electron detection can produce low noise strain maps that are suitable for the quantification of deformation mechanisms and for simulation validation. However, temperatures higher than those presented here cause large amounts of IR radiation that swamp the detectors and/or oxide formation and surface cracking. Therefore, HRDIC at temperatures exceeding 400 °C remains a challenge for commercially available systems.

References

- [1] C. Hardie, et al., Simulation of crystal plasticity in irradiated metals, *Acta Materialia*, 241, 118361, 2022.
- [2] D. Lunt, et al., Enabling high resolution strain mapping in zirconium alloys, *Materials Characterization*, 139, 355-363, 2018.
- [3] B. Poole, et al., Nanoscale speckle patterning for high resolution strain mapping of environmentally sensitive materials, *Strain*, in press, 2024.

Micro-computed topography from SEM backscattered electron multidetector images

J. Negggers¹, M. Bonnet¹, E. Héripré², S. Hallais³, S. Roux¹

1: Université Paris-Saclay, CentraleSupélec, ENS Paris-Saclay, CNRS, LMPS - Laboratoire de Mécanique Paris-Saclay, F-91190, Gif-sur-Yvette, France
 2: Arts et Métiers Institute of Technology, CNRS, CNAM, HESAM University PIMM - Procédés et Ingénierie en Mécanique et Matériaux, F-75013 Paris, France
 3: CNRS, Ecole Polytechnique, LMS - Laboratoire de Mécanique des Solides, Palaiseau, F91128 Palaiseau, France

Abstract — Using the BSE contrast due to the surface orientation in an SEM, multiple images captured by different BSE detectors can be combined to reconstruct the surface topography (up to a scale factor). A very general approach is introduced to perform such an analysis with an arbitrary number of detectors (greater or equal to three) and any characteristics (geometry, position, orientation, gain, etc.). The method is applied to a calibrated (mono-material) specimen and is shown to reconstruct a few micrometer tall topography with an uncertainty of about 15-35 nm.

Keywords — SEM, Topography, Backscattered electrons (BSE)

Introduction BSE images are known to be dependent not only on the chemical composition but also on the orientation of the surface. Therefore, when a multidetector is used, multiple images (one per detector) can be acquired without having to tilt the sample, and examining the different intensities at any position may inform the orientation of the surface. Popular topography reconstruction methods often use a specific configuration of detectors (for instance, a four-quadrant annular detector centered on the beam). The present work aims to design a more versatile approach that deals with an arbitrary number of detectors (larger or equal to 3) and any shape, position, orientation, offset, or gain. More details on the approach can be found in Ref. [1].

Methods The topography is denoted as $h(\mathbf{x})$, where $\mathbf{x} = (x, y)$ are the coordinates of the mean sample surface and z the direction of the normal to the mean surface.

The first step of the topographic reconstruction is to infer the response of each detector as a function of the local surface topography, which can be formalized as a sensitivity ψ to h and its gradients at all orders. The sensitivity to the local orientation of the surface indicates that each detector response strongly depends on ∇h . A refined modeling could include other dependencies on h or the surface curvature as minor corrections. Therefore, the image of the surface, as captured by detector i , written $f^{(i)}(\mathbf{x})$, should be accounted for by the detector response, $\psi^{(i)}$,

$$f^{(i)}(\mathbf{x}) = \psi^{(i)}(\nabla h(\mathbf{x})) \quad (1)$$

Each response $\psi^{(i)}(\mathbf{g})$ is expected to display a smooth variation with the surface orientation, \mathbf{g} , because of the solid angle over which the flux of electron is integrated. Thus, it may be approached by a low-order Taylor expansion in \mathbf{g}

$$\psi^{(i)}(\mathbf{g}) = p_0^{(i)} + \mathbf{p}_1^{(i)} \cdot \mathbf{g} + \mathbf{p}_2^{(i)} \cdot (\mathbf{g} \otimes \mathbf{g}) + h.o.t. \quad (2)$$

In particular, each offset p_0 and gain (scale factor in \mathbf{p}_j for $j \geq 1$) are considered free. The contrast (included in the gain) should depend on the chemical composition of the surface. However, in the present

case, only a mono-material is considered, and thus, the different coefficients $\mathbf{p}_j^{(i)}$ are treated as constant parameters that characterize each detector. A second-order expansion (at least) is needed to account for the position and orientation of the detector, but higher order may be required for topographies with steep slopes.

After calibration of the detectors, the collection of “gray levels” at each point of the surface, $f^{(i)}(\mathbf{x})$, should allow ∇h to be estimated as an inverse problem, to minimize the discrepancy (L2-norm of the difference) between the recorded values and the expected response, $\psi^{(i)}(\mathbf{g}(\mathbf{x}))$, where $\mathbf{g}(\mathbf{x})$ should be equal to the local slope $\nabla h(\mathbf{x})$. Let us emphasize that there is no way to set an absolute contrast scale, and therefore, in the end, the topography will be determined up to an unknown scale factor.

Finally, the last step consists of assembling a topography $h(\mathbf{x})$ from all local estimates of its gradient \mathbf{g} (In theory, the curl of \mathbf{g} should vanish, which is never true in practice). This last step is classically solving for $\nabla^2 h(\mathbf{x}) = \nabla \cdot \mathbf{g}(\mathbf{x})$.

These different steps are organized to provide a self-calibration. Namely, a very poor description of the detector responses is used as a starting point (essentially giving the orientation of the detectors). The surface topography is estimated, and the detector responses are refined. The process is repeated until the detector responses $\mathbf{p}_j^{(i)}$ and the surface $h(\mathbf{x})$ reach a stationary solution.

Results This approach was tested on different calibration objects, including a homemade sample shown in Figure 1, produced by FIB-milling of a Pt-deposited layer. The base of the cone has a diameter of 5 μm and a total height of 1.55 μm . Its shape was measured independently by AFM to provide a ground truth comparison.

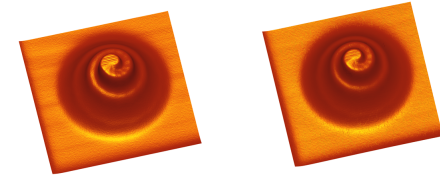


Figure 1: Reconstructed topography using the proposed approach (right) as compared to the ground truth measured by AFM (left)

The geometry could be reconstructed using three or four BSE detectors, leading to comparable results. After adjusting the arbitrary scale factor to match, at best, the AFM measurements, the rms value of the error on the entire $h(\mathbf{x})$ was measured to be less than 20 nm for the sample shown in Fig. 1, and for two other calibrated samples, it amounts to 15 nm and 32 nm.

Discussion and Conclusion The proposed approach is very general and flexible. Any BSE detector geometry (as long as it is not axisymmetric) can be dealt with. Moreover, the level of sophistication of the detector response modeling can be tuned at will and validated from the measured discrepancy. The present work can be seen as a proof-of-concept validation.

Many developments are yet to be considered. In particular, allowing for different materials (and hence contrasts) in the response is required for broader applications. Early attempts are encouraging, but algorithm stability has to be enhanced for a more robust approach. Steep slopes that may reach shadowing limits may also affect the quality of the results. Appealing developments concern in situ mechanical tests where, in addition to in-plane deformation from DIC, the surface topography evolution could be tracked (after the BSE detectors calibration, their response can be set constant) since the present methodology does not require a rotation of the sample, hardly compatible with an SEM testing device.

References

- [1] J. Negggers, E. Héripré, M. Bonnet, S. Hallais and S. Roux. A generic topography reconstruction method based on multidetector backscattered electron images. *Strain*, 58:e12416, 2022.

Identification of heterogeneous elastic limits in polycrystalline 316L austenitic stainless steel during tensile loading

Q. Hu, JF. Witz, A. Beaurain, A. El Bartali, D. Najjar

Univ. Lille, CNRS, Centrale Lille, UMR 9013 - LaMcube - Laboratoire de Mécanique, Multiphysique, Multiéchelle, F-59000 Lille, France

Abstract — Composed of an aggregate of grains with different sizes and local orientations, the deformation of polycrystalline metals exhibits heterogeneity at the microstructure scale under loading. The investigation of this heterogeneous localization has been greatly facilitated by the development of full-field measurement techniques such as Digital Image Correlation (DIC) and Quantitative InfraRed Thermography (QIRT). However, the measurement of stress fields still remains an open problem. In this study, a more straightforward method is proposed to estimate the local stress distribution in a polycrystalline material with the measured heterogeneous deformation fields.

Keywords — Polycrystalline metals, heterogeneities, stress identification

Introduction It is well known that the macroscopic mechanical response that controls the mechanical properties of a material originates from the microstructure. During the mechanical loading, the deformation field of polycrystalline metals is usually highly heterogeneous due to their varying grain size, morphology, and crystallographic orientation. The influence of microstructural features on heterogeneous deformation or localized plasticity has been investigated in many experimental and numerical studies [1, 2]. Usually, plasticity occurs gradually when a material is subjected to a stress beyond its yield stress. To determine this macroscopic yield stress, several phenomenological models have been proposed, including one based on the thermal effects [3] induced during a mechanical loading.

With the application of full-field measurement techniques, such as digital image correlation, the deformation mechanisms from the bulk specimen to the local zone and even to the activation of slip systems have been studied in depth. It provides rich experimental data (local displacement and strain fields) for gaining insight into and characterizing the mechanical behavior of materials at the microstructure scale. Combined with finite element simulations, heterogeneous elasto-plastic properties of the material, including yield stress and hardening modulus, can be identified by solving inverse problems [4, 5].

In contrast to previous studies, which require a large number of experimental and simulation datasets, this paper proposes alternative methods for the identification of local elastic limit through the elastic/plastic strain partitioning measured over the full-field measurements. Basically, the material undergoes recoverable elastic deformation before the loading reaches the elastic limit, with the evolution of strain over time being linear. Once local plasticity occurs, the previously linear response of the material changes, manifesting an elasto-plastic transition followed by progressive hardening regimes. This simple method is in fact a phenomenological approach, which does not require a complex constitutive model. Furthermore, it is based on direct and precise measurements of the strain fields and avoids strong assumptions and quantification of certain microstructure parameters.

Material and methods The studied material is an AISI polycrystalline 316L austenitic stainless steel. The as-received specimen underwent an annealing heat treatment at 1200 °C for 3h in a vacuum, followed by furnace cooling, to coarsen the grain size. The observed surface was polished up to 1 μm with a diamond suspension, followed by electrochemical etching. A contrasted speckle pattern for the DIC calculation is prepared by covering calcium carbonate particles on the surface of a uniform black matte paint primer. Fig. 1(b) shows the designed test consisting of two loading phases with different acquisition frequencies of images. In this investigation, we focus on the analysis of the results of phase I which allows a detailed investigation of deformation mechanisms, such as the activation of early plasticity.

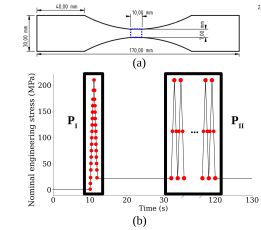


Figure 1: (a) The geometrical dimension of the studied specimen; (b) loading curve and image acquisition moments

Full-field kinematic measurements were conducted on the homemade YaDICs platform [1], which is based on the finite element global method. The coarse-to-fine approach is applied to speed up the algorithm, with a median filter of radius of 3 at each level. In the current work, XIMEA CB500 camera paired with a LAOWA 25mm f/2.8 2.5-5X Ultra-Macro lens was applied to acquire images with a magnification of X2.5, which gives a pixel size of 1.84 μm . It results in a spatial resolution of about 30 μm \times 30 μm for the kinematic fields with an element size of 16 pixels \times 16 pixels.

Results With the fact that when the stress is below the elastic limit, the mean strain exhibits a linear response to time. The fitted curve, obtained through linear regression of the measured strain data before plasticity onset, shows a desirable positive correlation with the actual measured data, indicated by the R-squared value (R^2) remaining almost constant and close to 1. However, once the stress exceeds the elastic limit, the fitted curve and the measured data gradually lose their correlation, leading to a gradual decrease in R^2 . Therefore, the moment of plasticity onset (t_{el}) is considered as the point where R^2 shows a local maximum value before its subsequent decrease. The elastic limit corresponds to the stress calculated by Hooke's law at t_{el} , $\sigma_{el}^g = E\varepsilon^g(t_{el})$. The grain-scale identified elastic limits are shown in Fig. (2), with mean and standard deviation values of 132 ± 45 MPa (including twins) and 95 ± 30 MPa (excluding twins), respectively.

Discussion and Conclusion The mean elastic limit with considering twins is closer to the macroscopic elastic limit (124 MPa) determined from the macroscopic curves. In addition, the histograms of the identified elastic limits show that the distribution with considering twins is closer to a Gaussian distribution. From these statistical analyses, it appears that the elastic limit distributions considering twins are more consistent with the real behavior of the material. This simple identification method is based on the obtained strain fields, which avoids strong assumptions and quantification of certain microstructure parameters. The average value of the elastic limits for the case with consideration of twins is closer to the value obtained through the macroscopic stress-strain curve. This suggests the necessity to consider twins in the identification of the elastic limits. Regarding the perspective, the identified elastic limits based on the local strain evolution need more validation methods, such as the inverse identification methods. Such methods necessitates full-field DIC measurements with a combination of finite element simulations which will be the scope of future work.

Statistical study of intermittent calorific phenomena associated to the Portevin-Le Chatelier effect in an aluminum alloy

A. Jury, X. Balandraud

Université Clermont Auvergne, Clermont Auvergne INP, CNRS, Institut Pascal, Clermont-Ferrand, France

Abstract

In the present study, uniaxial tensile tests were conducted on a 5052 aluminum alloy at four different strain rates: 0.4, 1, 2, and 4 %/s. During the loading process, the temperature of the sample was measured by infrared thermography at a frequency of 181 Hz using a high-definition quantum camera with a resolution of 1024×1280 pixels, giving a spatial resolution of 102 μm. Next, heat source reconstruction (HSR) was applied to the thermal data to obtain calorific information associated with deformation events, in particular plastic instabilities known as the Portevin-Le Chatelier effect (PLC). Statistical analysis revealed a negative correlation between the intensity of thermal events and their frequency. Furthermore, the probability density function of small thermal events follows a power law.

Keywords: Infrared thermography, Deformation calorimetry, Intermittency, Self-organized criticality, PLC effect

Introduction

A crystalline material, in response to external stress, exhibits a jerky behavior due to nucleation and motion of dislocation networks. In aluminum alloys, this plasticity phenomenon takes the form of different types of shear bands and jumps in the macroscopic stress-strain response, known as the Portevin-Le Chatelier effect (PLC) ¹. At the crystallographic scale, the PLC effect results from avalanches of dislocation motion with no intrinsic time or length scale. This phenomenon is referred to as self-organized criticality (SOC). SOC has been observed in various physical systems, including earthquakes, rearrangement of magnetic domains, the Barkhausen effect, avalanches in granular materials, acoustic emission from volcanic rocks, and fracture processes ². These avalanches, often referred to as intermittency, can be evidenced by acoustic emission (AE) and full-field mechanical methods such as localized spectrum analysis (LSA), for example in shape memory alloys during martensitic transformation ^{3,4}. The purpose of the present study is to investigate calorific intermittency in aluminum alloy at a mesoscopic scale using another full-field measurement techniques: infrared (IR) thermography.

Materials and Methods

Material and specimens: Aluminum alloy 5052, measuring specimens 40 mm in width, 120 mm in length and 1 mm in thickness were used. Front sides were coated with black aerosol paint with a known thermal emissivity of 0.96. For displacement measurement by digital image correlation (DIC), a black and white speckle pattern was applied to the back sides.

Setup: Mechanical loading was applied using a 15 kN MTS uniaxial testing machine. Specimen gage length between the machine jaws was approximately 85 mm. Four tests were conducted at different strain rates: 0.4, 1, 2, and 4 %/s. During the loadings, specimen temperatures were collected by infrared thermography at a frequency of 181 Hz using a high-definition quantum camera (1024×1280 pixels, resulting in a spatial resolution of 102 μm). Transformation from Eulerian to Lagrangian configuration of the thermal fields was performed using the procedure described in ⁵.

Deformation calorimetry: Heat source reconstruction (HSR) was applied to the Lagrangian thermal fields (T). To recall, HSR is a direct method based on suitable versions of the heat equation (2D-1D-0D) and thermal signal processing ⁶ aimed to identify the heat power density produced or absorbed by the material due to mechanical stresses only. Here, HSR was based on a 2D version of the heat equation: see eq. 1 where the left-hand side part, s_{int} , represents the heat source produced by the material here expressed in $K.s^{-1}$.

$$s_{int} = \frac{dT}{dt} - \frac{\lambda}{\rho \times C} \times \left(\frac{d^2T}{dx^2} + \frac{d^2T}{dy^2} \right) + \frac{2 \times h}{\rho \times C \times th} (T - T_{\infty}) + \frac{2 \times \sigma \times \epsilon}{\rho \times C \times th} (T^4 - T_{\infty}^4) \quad (1)$$

The time derivative term dT/dt was reconstructed by performing discrete convolution of a first-order differentiated Gaussian function to the noisy thermal field ⁷. The Laplacian terms, namely d^2T/dx^2 and d^2T/dy^2 , were pre-filtered using spatial smoothing spline ⁸ and differentiated using a centered finite difference scheme. In eq. (1), ρ is the density of the material, C the specific heat capacity, th the specimen thickness, λ the thermal conductivity, T_{∞} the temperature of the ambient air, σ the Stefan-Boltzmann constant ($5.67 \times 10^{-8} \text{ W.m}^{-2}.\text{K}^{-4}$) and ϵ the specimen surface emissivity (considered equal to 0.96, corresponding to the value for the paint used to coat the material surface in the experiments). **Statistical analysis:** First and foremost, it was necessary for us to select the dataset from those measured to extract the essence of the intermittent phenomena related to the PLC effect. After analyzing the data, it was determined that source values exceeding 5 $K.s^{-1}$ were suitable for statistical analysis, resulting in a dataset of approximately two-hundred

millions of pixels involved for each test. Probability density functions with two thousand and one segments were then calculated for each test.

Results

Figures 1-a and -b depict the 1D spatiotemporal (averaged in the transversal direction) thermal response and heat source maps, respectively, for the test conducted at 2 %/s¹ resulting in a total duration of 3.16 s before rupture. The red curve on the right Y-axis represents the load. These figures reveal that the temperature initially decreases for the first 0.45 s due to thermoelastic effects. Subsequently, upon reaching the onset yield at approximately 7500 N, hardening occurs, leading to a rise in temperature as a result of heat release due to plasticity effects. At the mesoscopic scale, no localized events were detected either on the loading curve (jumps) or on the temperature and heat source maps. Predominant events observed consist of three pairs of jerky shear bands moving from the machine jaws to the center of the specimen. Ultimately, a significant amount of heat is released at the bottom part of the specimen, corresponding to its rupture. Figure 1-c shows a \log_{10} - \log_{10} plot of the occurrences of heat source event versus heat source magnitudes. The black crosses indicate the subset of the dataset exhibiting a linear trend, i.e. a power-law relationship in natural plot. The yellow line is the linear fit of the power law, with a coefficient of 1.722. There are approximately five hundred thousand occurrences of events with the lowest mean values (i.e., below 5 $K.s^{-1}$), with a single occurrence at 174.35 $K.s^{-1}$.

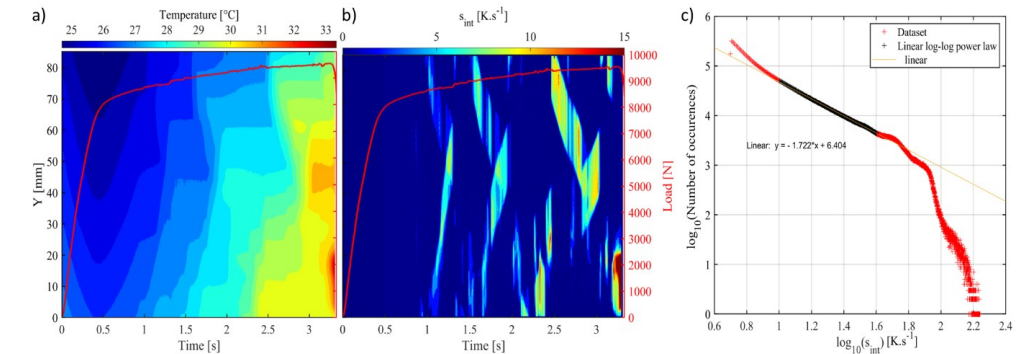


Figure 1: a) 1D spatiotemporal thermal field; b) 1D spatiotemporal heat source field; c) \log_{10} - \log_{10} plot of the occurrences of heat source event versus heat source magnitudes. The black crosses exhibit a power-law and yellow line the linear fit of the power-law with as coefficient 1.722.

Discussion and Conclusion

This study investigated the thermal and mechanical behavior of an aluminum alloy subjected to different strain rates, focusing on the calorific events associated with the Portevin-Le Chatelier (PLC) effect. Utilizing simultaneous full-field thermal and mechanical measurements, several critical observations were made. Statistical analysis revealed that higher intensity calorific events associated with plasticity are rarer. Moreover, the probability density function of small calorific events follows a power law with an exponent of 1.722. This value is consistent with those reported in the literature based on acoustic emission and stress rate measurements. These findings offer valuable insights into the complex interplay between stress, dislocation motion, and heat generation in aluminum alloys under mechanical loading. The study demonstrates the effectiveness of heat source reconstruction and spatiotemporal thermal measurements in capturing and analyzing the PLC effect and related phenomena.

References

1. Albert, P. & François, L. C. Sur un phénomène observé lors de l'essai de traction d'alliages en cours de transformation. *C. R. Hebd. Seances Acad. Sci.* **176**, 507–510 (1923).
2. Sethna, J. P., Dahmen, K. A. & Myers, C. R. Crackling noise. *Nature* **410**, 242–250 (2001).
3. Vives, E. *et al.* PHYSICAL REVIEW LETTERS Distributions of Avalanches in Martensitic Transformations. **72**, 1694–1697 (1994).
4. Blaysat, B. *et al.* Concurrent tracking of strain and noise bursts at ferroelastic phase fronts. *Commun. Mater.* **1**, 1–7 (2020).
5. Alarcon, E. & Heller, L. Deformation infrared calorimetry for materials characterization applied to study cyclic superelasticity in NiTi wires. *Mater. Des.* **199**, 1–23 (2021).
6. Chrysochoos, A. & Louche, H. An infrared image processing to analyse the calorific effects accompanying strain localisation. *Int. J. Eng. Sci.* **38**, 1759–1788 (2000).
7. Delpueyo, D., Balandraud, X. & Grédiac, M. Heat source reconstruction from noisy temperature fields using an optimised derivative Gaussian filter. *Infrared Phys. Technol.* **60**, 312–322 (2013).
8. R., J. & de Boor, C. *A Practical Guide to Splines. Applied Mathematical Sciences* vol. 27 (2001).

Identifying forces in 2D granular materials using the Virtual Fields Method from strains measured by Localized Spectrum Analysis

K. Jongchansitto^{1,2}, X. Balandraud², B. Blaysat², M. Grédiac², T. Jailin², J.-B. Le Cam³, P. Jongchansitto¹, I. Preechawuttipong¹

¹Dep. Mech. Eng., Faculty of Engineering, Chiang Mai University, 239 Huay Kaew Rd., Muang, Chiang Mai 50200, Thailand

²Université Clermont Auvergne, Clermont Auvergne INP, CNRS, Institut Pascal, Clermont-Ferrand, France

³Institut de Physique, Université de Rennes 1, Rennes, France

Abstract – This paper proposes an experimental approach to measure contact forces in a two-dimensional granular system using the Virtual Fields Method (VFM), which relies on the knowledge of the strain distribution in the particles. An experimental application was performed on a three-particle system subjected to confined compression by processing strain maps obtained using Localized Spectrum Analysis (LSA) for each particle. In addition to the VFM equations, equilibrium and Newton’s third law of motion were taken into account to propose a relevant strategy for processing the experimental strain measured by LSA.

Keywords – Localized Spectrum Analysis, LSA, Granular material, Force measurement, VFM

Introduction Force measurement is a classic and sometimes challenging problem in engineering, for instance, between particles in a granular material. A granular medium is a collection of solid particles whose macroscopic behavior is governed by interparticle contact forces. In the past, many studies have been performed using numerical simulations, for instance, the Discrete Element Method (DEM). It has been widely used to investigate the influence of many parameters, such as contact stiffness, particle shapes, friction, dispersity, etc. On the contrary, only some full-field experimental techniques have been proposed to measure interparticle contact forces in granular systems. A few decades ago, photoelasticity was applied to identify interparticle force networks in two-dimensional (2D) granular systems, i.e. *Schneebeli materials*, by Majmudar and Behringer [1]. The present study aims to develop a new methodology for identifying the interparticle forces in a 2D multi-contact system composed of cylinders by using the Virtual Fields Method (VFM) relying on strain data measured by the Localized Spectrum Analysis (LSA).

Methods The experiment was performed on a system made of three particles under confined compression. PA66 cylinders with diameters of 40 mm, 50 mm and 60 mm and length of 30 mm were used to make the particles. LSA allows to retrieve strain fields obtained from images of a periodic pattern placed at the material surface before and after loading. The benefit of using this technique is to obtain measurement fields with a good compromise between strain resolution and spatial resolution [2]. A checkerboard pattern with a unit square width of 75 μm (3 pixels) was deposited on the surface of the cylinders using a laser printer [3]. The cylinders were then placed in a frame 150 mm wide and subjected to confined compression using a uniaxial testing machine. Before starting the measurements, three preliminary compression cycles were applied to ensure that the system was mechanically stabilized. Then the compressive loading was maintained at -30 N to keep the contacts between the cylinders, before applying a loading up to -10 kN with a constant loading rate of -328.7 N/min (about 30 min). A CCD camera was used to capture images of the checkerboard pattern during loading and unloading, at an acquisition frequency of 0.1 Hz, see Fig. (1-a). The benefit of such a slow loading rate is to avoid the appearance of viscous strains. Afterwards, the images were processed by LSA to retrieve the displacement and strain fields within the three particles. The contact forces were then obtained using the VFM equations fed with measured strain fields. The classic VFM procedure was enriched with Lagrange multipliers to ensure global equilibrium and Newton’s third law of motion.

The VFM is a technique based on the Principle of Virtual Work which was first developed to identify the parameters governing the constitutive equations of materials. It can be regarded as the weak form of the local equations of equilibrium as follow [4]. Inversely, this technique can be used to identify the external forces acting on the material.

Results Figure (1-b) shows the contact forces identified for the maximum force level (-10 kN). All the results are presented in [5]. Various strategies were tested to propose kinematically admissible virtual displacement fields. The robustness of the identification technique was also studied with respect to various sources of error, such as noise in the strain field, missing data along the boundaries, and possible spurious shifts between real and virtual fields.

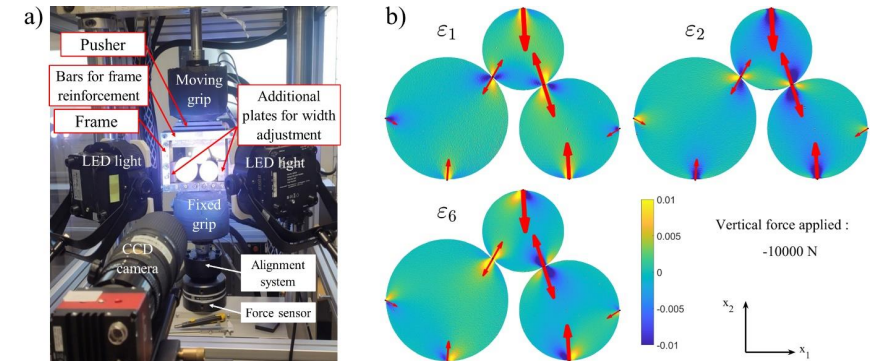


Figure 1: a) Experimental setup; b) measured strain fields and contact forces identified.

Discussion and Conclusion The objective of this study was to propose a new experimental approach to measure interparticle contact forces in 2D granular systems, relying on the measurement of the strain distribution in the 2D particles obtained by LSA. Identification was performed using the VMF equations with Lagrange multipliers to strictly respect force and moment equilibrium for each particle and Newton’s third law of motion at each interparticle contact. The application to much higher numbers of particles is in progress.

References

- [1] T.S. Majmudar and R.P. Behringer, Contact force measurements and stress-induced anisotropy in granular materials. *Nature*, 435, pages 1079-1082, 2005.
- [2] M. Grédiac, B. Blaysat, and F. Sur, On the Optimal Pattern for Displacement Field Measurement: Random Speckle and DIC, or Checkerboard and LSA? *Experimental Mechanics*, 60(4), pages 509-534, 2020.
- [3] Q. Bouyra, B. Blaysat, H. Chanal, and M. Grédiac, Using laser marking to engrave optimal patterns for in-plane displacement and strain measurement. *Strain*, 58(2), e12404, 2022.
- [4] F. Pierron and M. Grédiac, *The Virtual Fields Method: Extracting Constitutive Mechanical Parameters from Full-field Deformation Measurements*. Springer, New York, NY (USA), 2012.
- [5] K. Jongchansitto, X. Balandraud, B. Blaysat, M. Grédiac, T. Jailin, J.-B. Le Cam, P. Jongchansitto, and I. Preechawuttipong, Measuring forces in a 2D multi-contact system using the Virtual Fields Method: principle, simulations and experimental application to a three-particle system. *European Journal of Mechanics - A/Solids*, 106, 105315, 2024.

An imaging technique for the strain-engineering of deformable electrodes

A. Thiam¹, C. Rousselot², Y. Gaillard¹, M. Raschetti¹, M. Vieira¹, F. Kanoufi³, F. Amiot¹

¹ FEMTO-ST Institute, CNRS-UMR 6174 / UBFC, 24 chemin de l'Épitaphe, F-25030 Besançon, France

² FEMTO-ST Institute, CNRS-UMR 6174 / UBFC, 4 place Tharradin, F-25200 Montbéliard, France

³ ITODYS, CNRS-UMR 7086 / Univ. Paris Cité, 15 rue Jean-Anoine de Baif, 75013 Paris, France.

Abstract — It is crucial for the hydrogen economy to improve the efficiency and reduce the costs of the electrolytic hydrogen production. In order to avoid the use of critical materials as electrodes, we investigate to which extent deformable electrodes made of much more abundant materials could be tailored in terms of electrocatalytic activity. We propose an original imaging method which allows to reveal the footprint of the early stages of the hydrogen reaction. It allows to demonstrate the role of the mechanical state on the electrocatalytic activity.

Keywords — strain-engineering, imaging, electrocatalytic activity

Introduction Hydrogen is today mainly obtained by hydrocarbon steam reforming, which produces large CO_2 quantities. Because of the rising concern about greenhouse gas emissions, the widespread use of hydrogen as an energy carrier requires the development of a carbon-free production chain. In case it makes use of renewable electricity sources, hydrogen production by electrolysis may be the key to trigger the expansion of this promising sector. However, only a few percent of the total hydrogen production comes today from water electrolysis, mainly because of its cost, which is about four times higher than the cost of hydrogen obtained by steam reforming. Electrolysis requires an electrocatalyst, typically platinum, which is rare and expensive. Electrolytic production of hydrogen is thus handicapped by its dependence on platinum. It is therefore crucial, in order to minimize the cost and energy losses, to avoid materials like platinum as much as possible. It has already been demonstrated that elastic strains can modulate the electrocatalytic activity of metals [1, 2, 3, 4], so that more abundant materials could be strained in order to compare with platinum in terms of electrocatalytic activity. The question of the optimal position in the 6-dimensional strain space is however open, and we propose an experimental approach based on an in-operando imaging technique to address this issue.

Methods It is chosen to focus on the hydrogen evolution reaction (HER) in acidic media. The $Zr_{65}Ni_{35}$ binary metallic glass is a known HER catalyst [5] which may be processed by standard microfabrication techniques [6]. Starting from a silicon (100) wafer, a $Zr_{65}Ni_{35}$ layer is sputtered onto the surface from a composite target and further structured by lift-off. Suspended structures are subsequently obtained by etching the underlying silicon, so that uniform matrices of $80 \times 15 \times 0.5 \mu m^3$ cantilevers are obtained. Gold and $Zr_{65}Ni_{35}$ films have also been deposited for reference purpose and extensively characterized. These micro-cantilevers have been used as the working electrode, together with a platinum counter-electrode and an acidic (pH 3.1 or pH 4.3) KCl solution possibly containing a metal hydroxide. The electrochemical behavior has been studied by performing chrono-potentiometric measurements for varied charge steps (varied cathodic current values) during 50s. The current is then set to 0 (self-discharge or recovery step). During these experiments, images of the surface and of the cantilever have been recorded under constant illumination, for different illumination wavelengths (490 and 700 nm). This allows to monitor the reflectivity of the surface at the early stage of hydrogen production. A glass capillary could

also be used to impose an initial deformation to the cantilever, so that these chrono-potentiometric and reflectivity measurements have been performed for cantilevers with varied external mechanical loadings.

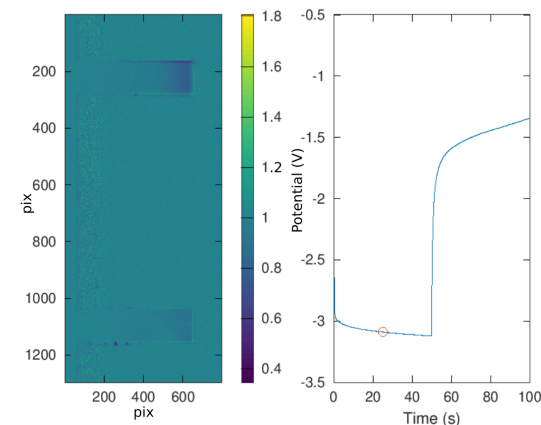


Figure 1: Left : Relative reflectivity change at 700nm for two adjacent cantilevers (unitless), the bottom one being bent down by $5.8 \mu m$. Right : Chrono-potentiometric measurements at $-78 \mu A.cm^{-2}$ from 0-50s then followed by a recovery at zero current (or open circuit) from 50-100s : the image corresponds to the 25s timestamp.

Results Figure (1) displays a typical relative reflectivity change (left) observed under 700 nm illumination on two adjacent cantilevers during the chrono-potentiometry displayed on right ($-78 \mu A.cm^{-2}$). During chrono-potentiometry, the cantilever on top is left free while the cantilever at the bottom of the image is bent away from the observed surface. On one hand, the contrast clearly reveals that the hydrogen production is not uniform on the cantilever surface. On a second hand, the hydrogen production is significantly altered on the surface under tension of the bent cantilever, in comparison with the free one. Opposite effects have been observed when the mechanical loading is inverted.

Discussion and Conclusion A real-time in-situ imaging technique is proposed to reveal the non uniform hydrogen production on deformable electrodes. This technique also clearly reveals the effect of the strain on the HER. Further works will focus on making these measurements quantitative, in order to study in details the role of the mechanical state of the electrode on the electrocatalytic activity.

References

- [1] M. Mavrikakis, B. Hammer, and J. K. Nørskov. Effect of Strain on the Reactivity of Metal Surfaces. *Phys. Rev. Lett.*, 81, 2819, 1998.
- [2] L. A. Kibler, A. M. El-Aziz., R. Hoyer and D. M. Kolb. Tuning Reaction Rates by Lateral Strain in a Palladium Monolayer. *Angew. Chem. Int. Ed.*, 44, 2080, 2005.
- [3] J. Weissmüller, R.N. Viswanath, L.A. Kibler, D.M. Kolb. Impact of surface mechanics on the reactivity of electrodes. *Phys. Chem. Chem. Phys.*, 13, 2114-2117, 2011.
- [4] C. Martínez-Alonso, J. M. Guevara-Vela and J. LLorca. Understanding the effect of mechanical strains on the catalytic activity of transition metals. *Phys. Chem. Chem. Phys.*, 24, 4832-4842, 2022.
- [5] L. Mihailov, T. Spassov and M. Bojinov. Effect of microstructure on the electrocatalytic activity for hydrogen evolution of amorphous and nanocrystalline Zr-Ni alloys. *Int. J. Hydrogen Energy* 37, 14, 10499-10506, 2012.
- [6] A. Volland. Etude des effets d'échelle sur le comportement mécanique de film mince en verre métallique. PhD thesis, Université de Grenoble, 2012 (in french).

High Throughput Tensile Testing for Characterization of Static Strain Aging

Ville Björklund, Sven Bossuyt

Aalto University School of Engineering, Department of Mechanical Engineering, PO Box 14200, FI-00076 Aalto, Finland

Abstract

A novel high throughput method for characterizing static strain aging (SSA) behavior in materials is presented. A tapered specimen with increasing cross-section is used for pre-straining to induce a pre-strain gradient along the gauge length. A second machining step with electric discharge machining (EDM) is used to remove the taper after pre-straining, making the specimen more typical “dog bone” shaped. An aging treatment is then applied to induce static strain aging in the specimen. Finally, an ordinary tensile test until rupture is conducted, using stereo digital image correlation (DIC) to obtain full-field strain measurements from the whole gauge section. The full-field strain data enables extraction of local stress-strain curves along the gauge length of the specimen, thus sampling material pre-strained to different levels in the original tapered specimen. However, the stress strain curves obtained from one continuous specimen with pre-strain gradient cannot accurately reproduce the yield point in detail as a drop in the engineering stress is not possible when multiple pre-strain levels are loaded in series. Therefore, the stress-strain data obtained needs a stress correction which is possible based on the local strain rate data obtainable from the DIC measurement. A variable smoothing process for the noisy strain rate data is proposed to accurately estimate the strain rate peak and a strain rate-based stress correction is applied to obtain accurate local stress-strain data from the tapered specimen.

Keywords – DIC, Tapered specimen, High throughput, Static strain aging

Introduction

The development of full-field measurement techniques such as DIC has opened the possibility to gather experimental data more efficiently than previously. Typically, static strain aging is characterized on conventional tensile test specimens, pre-straining, doing an aging treatment, and then final tensile test. This type of testing is very laborious and requires a large set of specimens to gather data at different pre-strain levels and aging conditions. Utilizing a tapered specimen to create a specimen with a pre-strain gradient makes it possible to gather extensive data for combinations of pre-strain, aging temperature, and aging time. What would otherwise require tens or hundreds of conventional two step tensile tests, is possible to obtain from only a few of these experiments. Thus, the method presented makes it practical to do test campaigns that would otherwise require hundreds or thousands of tests and specimens. The use of tapered specimens in mechanical testing is not entirely new. However, the two-step process inducing pre-strain gradient for uniformly shaped tensile specimen to characterize SSA of material has not been done.

Methods

A tapered specimen with increasing cross section is used to induce pre-strain gradient to tensile specimen. EDM is used to cut the pre-strained specimen straight to get uniform tensile specimen with existing pre-strain gradient. Aging treatment is applied to induce SSA on the material. DIC is then used to extract local stress-strain curves for different pre-strain levels. Finally Strain rate-based stress correction is applied to bring the sharp yield point back to results extracted from the tapered specimen.

The strain rate-based stress correction brings unique challenges regarding the smoothing of the, usually rather noisy, local strain rate data as we are now interested in having as accurate a reading as possible regarding the maximum strain rate amplitude and moment of time it occurs. The smoothing is

challenging as too conservative smoothing doesn't smooth the data enough and aggressive smoothing results in underestimating the strain rate peak. We propose a variable smoothing approach which aims to smooth the data heavily before and after the yield point and more conservatively at yield point to better estimate the true strain rate behavior.

Results

Figure 1 shows the measured pre-strain variation along the length of a tapered specimen, and a preliminary analysis of the stress-strain curves obtained from this specimen after aging at 100 °C for one day and removing the taper. The figure illustrates the range of data that is obtained from a single test, but the density of data in that range is much greater than shown in the figure. If the final testing were done on the specimen after removing the taper with EDM. This is to ensure that all pre-strain levels in the specimen will experience substantial yielding in the final tensile test were as otherwise the specimen would just break in the narrowest section before any meaningful strain in the larger cross-sections.

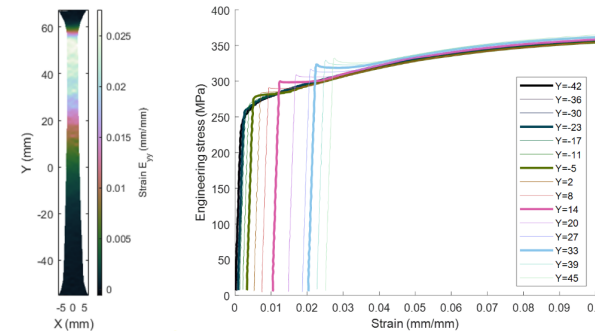
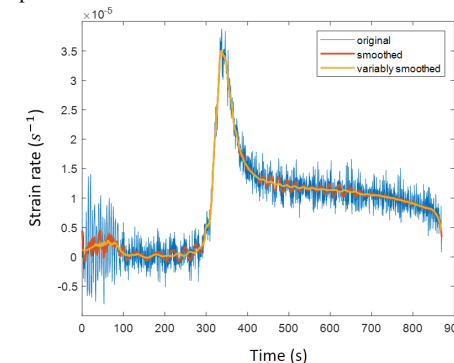


Figure 1. (left) Tapered specimen with pre-strain gradient. (right) Preliminary analysis of local stress-strain curves obtained with the specimen on the left after aging 1 day at 100 °C and removing the taper, including a stress correction to account for variations in the local strain rate.

Figure 2 illustrates the sudden increase in local strain rate upon yield point and shows the original data and preliminary results of differently smoothed versions of the original data. Doing a strain rate-based stress correction to the measured stress value, to approximate an effective stress strain curve for constant strain rate, results in the stress-strain curves shown in Figure 1 that do exhibit a sharp yield point.



Simultaneous thermal and kinematic full-field measurements on optimal patterns based on thermography and spectral analysis

T. Jailin, A. Jury, B. Blaysat, A. Vinel, X. Balandraud, M. Grédiac

Université Clermont Auvergne, Clermont Auvergne INP, CNRS, Institut Pascal, Clermont-Ferrand, France

Abstract — A method is proposed to measure simultaneously temperature and strain fields at the same location and time on optimal patterns, using a single high-resolution infrared (IR) camera. The kinematic field is measured by Localised Spectrum Analysis (LSA), and the thermal field is obtained from IR imaging. The method is applied to study the phase transformation of a shape memory alloy during heating and cooling cycles. In the end, the method enables extracting richer datasets per camera, which is of great interest for identification purposes. It also enables calculating energy balances, which is valuable information for studying the thermomechanical couplings within materials.

Keywords — DIC, PhotoMechanics, Thermography

Introduction Being able to measure both temperature and strain fields at the same location and time is particularly appealing in experimental mechanics. It enables studying thermomechanical couplings and makes it possible to compute key information, like energy balances. Yet, measuring simultaneously and with high-resolution these two kinds of fields is not straightforward because significantly different conditions are required for each method. Concerning the kinematic methods, a maximal gradient of grey level is usually sought in the images in order to obtain the best metrological performances [1]. This is opposed to infrared (IR) thermal measurements, where a well-known and uniform emissivity on the sample surface is usually sought. Another contradiction between kinematic and thermal methods is that the former is usually based on the optical flow conservation assumption in the images, which may not be respected if the temperature varies during the test.

Several methods have already been proposed to measure the two fields on the sample surface during a test, but no one enables having these two fields with high spatial resolutions [2]. In some studies, both IR and standard cameras were used. Data interpolations were performed for the modality fusion to obtain the two sought fields at the same location and time, which is a source of errors. Other research teams directly performed DIC on IR images to avoid interpolation [3], but with poor spatial resolution and non-optimised patterns. In [4], a novel method was proposed to combine thermographic phosphor (TP) paint and Digital Image Correlation (DIC) for simultaneous temperature and strain measurements with a standard camera. The drawback is that the pattern obtained with such paint was coarse leading to significantly lower metrological performance of the kinematic field.

It was shown in [1] that the optimal pattern for kinematic full-field measurements is the chequerboard in order to maximise the grey level gradients in the images. However, such a pattern is difficult to analyse with DIC because of its periodicity. In this work, we propose to combine IR imaging with Localised Spectrum Analysis (LSA) to enable working on chequerboard patterns [5]. Coupling LSA with IR imaging, would enable obtaining temperature and strain fields simultaneously with high metrological performance on controlled patterns for the very first time.

Methods & Results In this work, we propose to combine LSA and IR thermography to measure temperature and strain fields simultaneously on optimal patterns (i.e. chequerboards). The method developed will be presented and applied to study the phase transformation of a shape memory alloy (SMA). A high-resolution IR camera was used, leading to a pixel size of around $18 \mu\text{m}$. It is worth noting that since LSA works in the Fourier domain, brightness and contrast changes have negligible impacts on the phase modulations, which are then used to retrieve the displacement.

Figure 1 shows preliminary results where a martensite needle is created within the SMA sample upon cooling. The transformation induces both a strain and a heat release. This latter is immediately followed by a conduction phenomenon, where the local temperature catches up with the overall temperature of the sample.

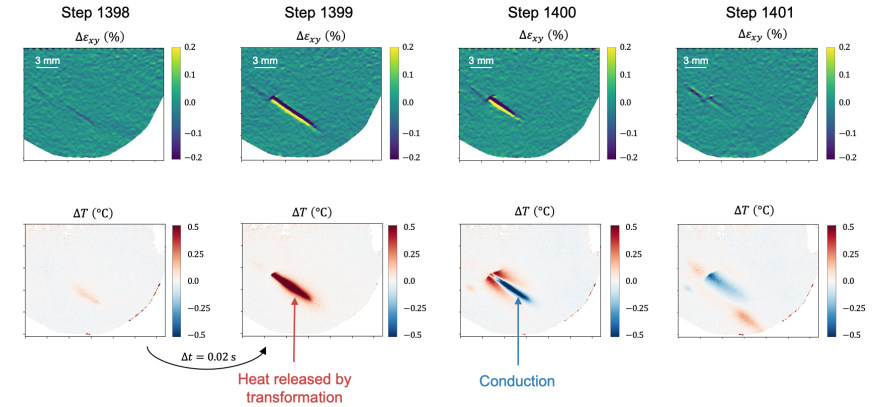


Figure 1: Nucleation of a martensite needle on the SMA sample upon cooling.

Conclusion A novel method is presented to extract displacement and temperature fields from optimal patterns by combining LSA with IR imaging. This enables obtaining the best metrological performance on the displacement field, since an optimal pattern is used. This also avoids doing any interpolation between the two kinds of fields. Finally, it is worth noting that obtaining temperature and strain fields would make it possible to reduce the number of experiments needed for materials characterisation and go towards sober experimental campaigns, which falls within the "Materials testing 2.0" concept.

In the long term, such results would enable computing energy balances during the test, which is highly valuable for studying thermomechanical couplings. This would, for example, help understand how much energy is required for a phase transformation to occur and what changes can be expected in the material's properties.

References

- [1] G. Bomarito, et al. Increasing accuracy and precision of digital image correlation through pattern optimization. *OLEN*, 2017.
- [2] A. Chrysochoos, et al. Local energy analysis of high-cycle fatigue using digital image correlation and infrared thermography. *J. of Strain Anal. for Eng. Des.*, 2008.
- [3] A. Maynadier, et al. One-shot measurement of thermal and kinematic fields: infrared image correlation (IRIC). *Exp. Mech*, 2012.
- [4] E. M. Jones, et al. Combined thermographic phosphor and digital image correlation (TP+ DIC) for simultaneous temperature and strain measurements. *Strain*, 2022.
- [5] M. Grédiac, et al. Extracting displacement and strain fields from checkerboard images with the localized spectrum analysis. *Exp. Mech*, 2019.

Characterization of the effect of roughness on dynamic ruptures along frictional interfaces

S. Robinary, V. Rubino, I. Stefanou

Nantes Université, École Centrale Nantes, CNRS, GeM, UMR 6183, F-44000 Nantes, France

Abstract — Dynamic ruptures are relevant to various engineering and geophysics applications, and in particular to the study of earthquakes. Roughness plays an important role in controlling interface rheology, which affects dynamic rupture nucleation, propagation and arrest. Here we use laboratory experiments to characterize the effect of roughness on dynamic rupture propagation. To study rupture behavior, we measure the full-field displacements, particle velocities and stresses using the digital image correlation method.

Keywords — Dynamic rupture, roughness, friction

Introduction The study of dynamic shear cracks along frictional interfaces is relevant to a wide range of engineering and geophysics applications, including the study of earthquakes. An earthquake occurs via a dynamic rupture instability, which propagates along pre-existing faults in the Earth's crust. A fault is a fracture or discontinuity in a rock mass. Fault slip and ruptures are governed by the local stress field and frictional behavior of the fault. As natural faults show deviations from planarity at all scales and have been showed to be almost of a fractal nature [1, 2], roughness becomes a very important parameter to take into account when studying earthquakes. Indeed, roughness plays an important role in rupture nucleation, propagation and arrest. In this study, we aim to quantify how frictional properties and dynamic rupture characteristics vary with the interface roughness.

Methods Dynamic ruptures are produced along the interface of two synthetic rock or PMMA quadrilateral plates of controlled roughness. The synthetic rock specimens are 3D printed using silica sand particles as the powder component (140 μm of diameter) and furfurylic alcohol as binder [3]. Specimens are loaded in bi-axial setup in order to prescribe an initial level of shear and normal stress. A speckle-pattern is applied to a portion of the specimen. Images of the propagating dynamic ruptures are captured with a high-speed camera. Surface roughness along the specimen's interface is produced using various methods including beadblasting, 3D printing, and laser engraving, which results in either random or specified patterns. Tests are conducted by either forcing constant sliding of the interface at constant velocity or by spontaneous rupture propagation. The deformed images of the propagating ruptures are analyzed with the digital image correlation method, following the approach of [4, 5], and provide the full-field displacements, particle velocities and stresses associated with the propagating ruptures.

Results Preliminary tests were conducted using a double-direct-shear (DDS) setup [6] with synthetic rock specimens [3], see Fig. (1). In these tests, a constant velocity is imposed on the vertical piston. The use of synthetic rocks, however, makes the interpretation of the results obtained using DIC rather difficult, as the material porosity leads to speckle pattern absorption. Further abrasion of the specimen close to the interface modifies the geometry. We are currently testing a slightly different composition of the sand/resin mixture of the 3D printed material, which may allow us to address these issues in future experiments. In the meantime, another material (PMMA) was chosen due to its brittle mode of rupture and low shear modulus. Tests with PMMA specimen are conducted in a direct shear setup and dynamic ruptures propagate spontaneously.

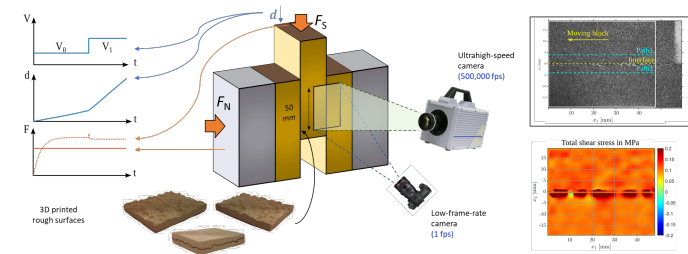


Figure 1: Schematics of the double direct shear setup with 3D printed sand specimens and associated diagnostic systems

Discussion and Conclusion Local microscopic asperities and surface topography can influence macroscopic stability of friction as well as the fault microseismicity. Rougher faults tend to be more stable and less seismogenic than the smoother faults [7]. However, the frictional stability of the fault can evolve with shearing toward unstable [8]. One key question to address is how stress heterogeneities caused by roughness can affect the near-fault dynamic friction evolution. Moreover, despite being more stable, rough faults can host supershear ruptures for relatively low levels of pre-stress [9]. A focus point of our study will be on the relation between stress heterogeneities induced by roughness and the possibility of supershear rupture to nucleate at low normal stresses. Numerical simulations have shown that supershear rupture nucleation are inhibited on smooth interfaces. However, once initiated, supershear rupture propagation is favored by smooth interfaces [9]. Previous experimental studies have developed a relationship between stress drop and geometric features of asperities [10], which leads to the question of a relation between asperities and dynamic friction evolution. Our experiments will shed light on the above mentioned issues and will lead to an improved understanding of the role of roughness on rupture behavior.

References

- [1] W. Power and T. Tullis Euclidian and Fractal Models for the Description of Rock Surface Roughness. *Journal of Geophysical Research: Solid Earth*, 96:415–424, 1991.
- [2] T. Candela, F. Renard, Y. Klinger, K. Mair, J. Schmittbuhl and E. Brodsky Roughness of fault surfaces over nine decades of length scales. *Journal of Geophysical Research: Solid Earth*, 117:B08409, 2012.
- [3] P. Braun, G. Tzortzopoulos and I. Stefanou Design of Sand-based, 3-D-printed analog faults with controlled frictional properties. *Journal of Geophysical Research: Solid Earth*, 126:e2020JB020520, 2021.
- [4] V. Rubino, A. Rosakis and N. Lapusta Full-field Ultrahigh-speed quantification of dynamic shear ruptures using digital image correlation. *Experimental Mechanics*, 59:551–582, 2019.
- [5] Y. Tal, V. Rubino, A. Rosakis and N. Lapusta Enhanced Digital Image Correlation Analysis of Ruptures with enforced traction continuity conditions across interfaces. *Applied Sciences*, 9:1625, 2019.
- [6] D. Guitiérrez-Oribio, G. Tzortzopoulos, I. Stefanou and F. Plestan Earthquake Control: An emerging application for robust control. *IEEE Transactions on Control Systems Technology*, 31:1747–1761, 2023.
- [7] B. Fryer, C. Giorgetti, F. Passelãgue, S. Momeni, B. Lecampion and M. Violay. The Influence of Roughness on Experimental Fault Mechanical Behavior and Associated Microseismicity. *Journal of Geophysical Research: Solid Earth*, 127:e2022JB025113, 2022.
- [8] Y. Fang, D. Elsworth, T. Ishibashi and F. Zang. Permeability evolution and frictional stability of fabricated fractures with specified roughness. *Journal of Geophysical Research: Solid Earth*, 123:9355–9375, 2022.
- [9] L. Bruhat, Z. Fang, and E. M. Dunham. Rupture complexity and the supershear transition on rough faults. *Journal of Geophysical Research: Solid Earth*, 121:210–224, 2016.
- [10] Y. Ju, C. Wan, G. Fu, Z. Ren, L. Mao and F. Chiang. Effects of near-fault stress evolution and surface asperities on rough fault slip: An evaluation based on photoelastic shear tests and additively printed models. *Engineering Geology*, 305:106715, 2022.

Developing a new optical strain gage for full-field measurements

A. Vinel¹, M. Grédiac¹, X. Balandraud¹, B. Blaysat¹, T. Jailin¹, F. Sur²

1: Université Clermont Auvergne, Clermont Auvergne INP, CNRS, Institut Pascal, Clermont-Ferrand, France
 2: LORIA, UMR 7503, Université de Lorraine, CNRS, INRIA, Nancy, France

Abstract — Full-field measurement methods are well established in the experimental mechanics community. Most of the time, these measuring methods require patterns to be deposited on the specimen before test. Regarding the metrological performance, it has been demonstrated that the optimal pattern is a checkerboard. However, using such a pattern is complex since its deposition remains somewhat tricky. Recent studies show that it is possible to use a laser engraver to print black dots on a specimen covered with a thin layer of white paint. The present contribution proposes to push this solution forward by printing a fine checkerboard pattern on a thin polymeric film and then gluing it on the specimen surface. This allows the separation of the manufacturing process of what can be considered as an optical strain gage on the one hand, and its use on the other hand, thus facilitating the spread of this strain measuring tool in the experimental mechanics community. The manufacturing and bonding processes of this new strain gage are described. It is then applied to an example to demonstrate its ability to capture strain fields featuring fine sharp details.

Keywords — strain gage, checkerboard, laser marking, localized spectrum analysis

Introduction Full-field measurement techniques are now commonly used in experimental mechanics. For in-plane strain and displacements measurements, the use of periodic patterns such as checkerboards leads to the best metrological performance [1]. The so-called Localized Spectrum Analysis (LSA) [2] is used to extract the displacement and strain fields from the checkerboard pattern images discussed in this study. A major hurdle is to deposit the tiny dots forming the checkerboard on the surface of the specimen to be tested. A strategy, recently presented in [3], consists in directly engraving the pattern on flat surfaces with a laser engraver, the surface being spray-painted in white beforehand. Checkerboards with squares as small as 50 μm were engraved in [3]. Further developments then enabled us to reduce this size to 30 μm [4]. This work proposes to improve this solution by printing such a pattern on a thin polymeric film, and then gluing it on the specimen surface, as routinely done with standard electrical strain gages.

Methods A 25 μm thick polyimide film manufactured by DuPont was chosen as it is the same as the film used to produce most of the electrical strain gages that are commercially available. The film supplied by ADDEV Materials, Saint-Chamond, France, is white in its bulk. Thus the black dots of the checkerboard were directly engraved on the film, following the procedure described in [3]. Then, the engraved film was bonded to the specimen using a procedure similar to that used for bonding electrical strain gages. In particular, a cyanoacrylate glue suitable for such strain gages was employed. This new optical strain gage was applied on a disk specimen of diameter 3.3 cm, made of a single-crystal of $\text{CuAl}_{13.9}\text{Ni}_{4.6}$ (wt.%) shape memory alloy (SMA) subjected to temperature-induced phase transformation. When cooled to nearly 0 $^{\circ}\text{C}$, martensite microstructures are formed within the sample [4]. These microstructures create heterogeneous strain fields with sharp details and highly localized gradients. For comparison purposes, only half of the specimen was instrumented using the proposed method (CKB #2),

while the other half was instrumented by first spray-painting in white and then engraving the pattern (CKB #1), which is the procedure used till now to deposit such patterns. The border between the two types of patterns was placed perpendicularly to a set of parallel martensite bands in order to examine if the strain measured within them remained constant when changing the type of marking. Fig. 1a shows a picture of the SMA sample marked with both methods.

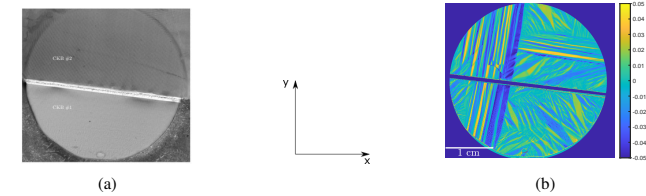


Figure 1: (a) Picture of the SMA sample marked with CKB #1 and #2. (b) Typical ϵ_{xy} strain map.

Results Two sets of images were taken in the reference configuration. The settings (light, aperture) were optimized for CKB #1 in the first set, and for CKB #2 in the second set. Similar procedure was followed when the specimen was in the deformed configuration. The strain fields obtained on both halves were then merged to form unique strain fields over the whole specimen surface. Fig. 1b shows a typical ϵ_{xy} strain map, and Fig. 2a a close-up view of the ϵ_{xy} map obtained with both markings, where y is the vertical direction. Overall, no real difference can be noticed between the global appearance of the maps obtained with both markings. Several cross-sections were then analysed in order to check along a given martensite band if the amplitude of the strain components changes or not when crossing the border (see Fig. 2b, 2c, 2d). No attenuation of the signal is observed when going from the red to the blue curves for the three components.

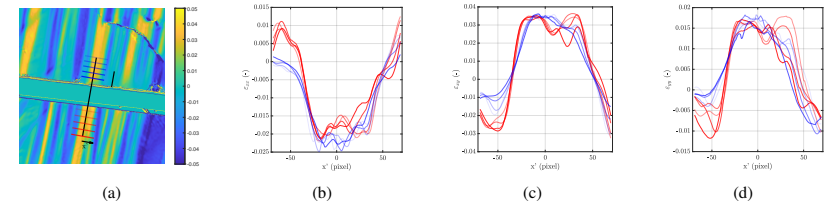


Figure 2: (a) Close-up view of the ϵ_{xy} strain map with the location of the line along which the cross sections are plotted. (b)–(d) Strain profiles. Red: CKB #1. Blue: CKB #2.

Discussion and Conclusion A procedure for engraving checkerboard patterns on polyimide films and bonding them on flat specimens is proposed in this work. A challenging testing configuration giving rise to heterogeneous strain fields with sharp localizations was used. It is shown that no significant difference in the strain maps is observed when comparing results obtained with the present gage and the classic printing procedure used so far. This illustrates the fact that this optical strain gage can be an ideal tool for analyzing heterogeneous strain fields in experimental mechanics. Printing this type of gage would help spread and popularize optimal patterns for full-field strain measurements in experimental mechanics, and contribute making such measurements more reliable and reproducible. More details concerning this optical strain gage can be found in [5].

References

- [1] G.F. Bomarito *et al.* Development of optimal multiscale patterns for digital image correlation via local grayscale variation. *Experimental Mechanics*, 58:1169–1180, 2018.
- [2] M. Grédiac *et al.* A critical comparison of some metrological parameters characterizing local digital image correlation and grid method. *Experimental Mechanics*, 57:871–903, 2017.
- [3] Q. Bouyrn *et al.* Using laser marking to engrave optimal patterns for in-plane displacement and strain measurement. *Strain*, 58, e12404, 2022.
- [4] A. Vinel *et al.* Full-field strain investigation of twinned martensite in a thermally activated Cu-Al-Ni single crystal using Localized Spectrum Analysis. *Acta Materialia*, 264, 119550, 2024.
- [5] A. Vinel *et al.* Towards strain gage 2.0. Substituting the electric resistance routinely deposited on polyimide film by the optimal pattern for full-field surface strain measurement. *Submitted*.

Using full-fields measurements to determine the influence of crack velocity and non-singular terms on K_{IC} of an epoxy resin

B. Lammens, G. Portemont, J. Berthe, R. Seghir, J. Réthoré

DMAS, ONERA, F-59014 Lille-France
Nantes Université, Ecole Centrale Nantes, CNRS, GeM, UMR 6183, 1 rue de la Noë, France

Abstract

Laminated composite materials used in the aeronautical field can be damaged by impacts, leading to crack propagation. In the literature, the critical energy release rate in mode I (G_{IC}) is usually estimated from global load measurements. In this paper, mode I fracture experiments were carried out and analysed using linear elastic fracture mechanics by full-field measurements and Digital Image Correlation (DIC). The influence of the crack velocity and non singular-terms on K_{IC} is highlighted and a model of $K_{IC}(T, B, \dot{a})$ is proposed.

Keywords — Non-singular terms, Williams' series, Digital Image Correlation, Critical stress intensity factor, High crack velocities

Introduction Organic matrix laminated composites are used in the aeronautical field for certain elements such as the fuselage. These elements are subjected to impact such as bird strikes or hailstone impacts that can lead to delamination. This is a process of macroscopic decohesion of the interlaminar environment which can be characterised by G_{IC} [1]. It is determined in mode I using a standardised experimental set-up under quasi-static loading with a Double Cantilever Beam (DCB) sample [2]. A macroscopic approach with a global analysis method is applied to analyse this experiment. However, under dynamic loading rates, there is no standardized experimental set-up. Nevertheless some authors have developed extensions of the global method used for quasi-static loading. However, the literature shows a wide disparity in measurements [4] due to incomplete decoupling of the effects of resin confinement by fibers, non-linearities behaviour and/or velocity effects. Another approach at the scale of the resin has been used by other authors using local measurements with strain gauges near the crack tip to determine K_{IC} [5]. Some others have shown the influence of the geometry specimen on the non-singular terms of the Williams' series and their influence on K_{IC} [3]. The aim of this work is to develop an experimental protocol with wide range of crack velocities to characterise K_{IC} , T , B on Hexply®M21 epoxy resin using full-field measurements based on DIC associated with the Williams' series.

Methods Mode I fracture experiments were carried out on Hexply®M21 epoxy resin with two types of geometry specimen, a Tapered Double Cantilever Beam (TDCB) and a triangular specimen. The considered experimental protocol is presented in the Figure (1). Some modifications of this protocol were applied to increase the crack velocity to have a range of \dot{a} between 10^{-6} m.s⁻¹ to near 600 m.s⁻¹.

Results The displacements fields of the DIC were projected onto the Williams' series in a least squares sense to extract K_{IC} , T , B and the crack tip position as proposed in [3]. An increase of K_{IC} has been highlighted with respect to the crack velocity. This trend has already been observed in the literature by Joudon [5] on the same material. A model was defined to determine K_{IC} by taking into account the dependence of the crack velocity and of the non-singular terms. As proposed in [6], a Kanninen model was considered to show the dependence of crack velocity to K_{IC} . A bi-linear relationship between the

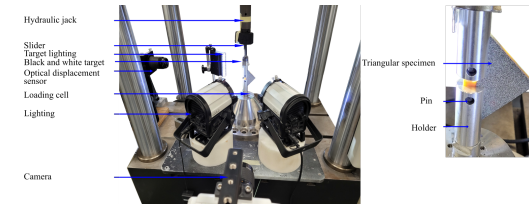


Figure 1: Experimental set-up

non-singular terms and K_{IC} was used as proposed in [3] under quasi-static loading. Figure 2 shows the evolution of K_{IC} with respect of B and \dot{a} , K_{IC} evolves between $0.8 \text{ MPa}\cdot\text{m}^{\frac{1}{2}}$ and almost $3 \text{ MPa}\cdot\text{m}^{\frac{1}{2}}$.

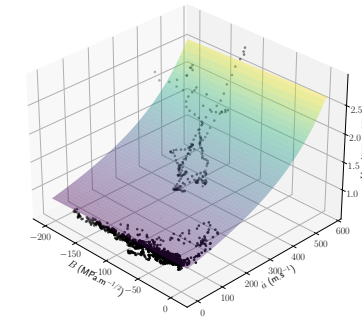


Figure 2: Evolution of K_{IC} with respect to B and \dot{a}

Discussion and Conclusion The proposed method developed in [3] allowed to determine a model of $K_{IC}(T, B, \dot{a})$ on Hexply®M21 epoxy resin. Even if the considered model could be questionable, it allowed to give a first trend of the evolution of K_{IC} with respect to T , B and \dot{a} . It would be interesting to carry out mode I fracture experiments on other specimens such as a Single Edge Notched Tension (SENT) in order to extend the range of B values and improve the accuracy of the model.

References

- [1] A.A. Griffith VI. The phenomena of rupture and flow in solids. *Philosophical transactions of the royal society of london. Series A, containing papers of a mathematical or physical character*, 221:163–198, 1921.
- [2] B.R.K. Blackman and A.J. Kinloch and Y. Wang and J.G. Williams. The failure of fibre composites and adhesively bonded fibre composites under high rates of test: Part II Mode I loading dynamic effects. *Journal of Materials Science*, 31:4451–4466, 1996.
- [3] B. Lammens and G. Portemont and J. Berthe and R. Seghir and J. Réthoré. Determining singular and non-singular Williams expansion terms from full-field measurements: Consideration of structural effects on fracture. behaviour. *Theoretical and Applied Fracture Mechanics*, 130:104304, 2024.
- [4] S. Mall and G.E. Law and M. Katouzian. Loading rate effect on interlaminar fracture toughness of a thermo-plastic composite. *Journal of composite materials*, 21:569–579, 1987.
- [5] V. Joudon and G. Portemont and F. Lauro and B. Bennani. Experimental procedure to characterize the mode I dynamic fracture toughness of advanced epoxy resins. *Engineering Fracture Mechanics*, 126:166–177, 2014.
- [6] E.Eid and R.Seghir and J. Réthoré. Crack branching at low tip speeds: spilling the T. *Journal of Theoretical, Computational and Applied Mechanics*, 2023.

Quantifying thermo-elastic cooling and heating during tensile strength testing of solid engineering alloys with a highly sensitive cooled infrared camera

S. Boubanga-Tombet¹, J. Carrock¹, A. Dumont¹, J. Gagnon¹, S. Burns², C. Pratt², & A. Sefkow²

¹Telops, 100-2600 Saint-Jean-Baptiste Ave, Québec, QC, G2E 6J5, Canada

²Department of Mechanical Engineering, University of Rochester, 236 Hopeman Hall, Rochester, New York 14627, USA

Abstract

When pulled uniaxially to failure, metallic specimens undergo two periods of reversible elastic stress. The first occurs during the initial elastic portion of the stress-strain curve prior to the on-set of plastic deformation. The effect, first theorized and derived by Lord Kelvin in 1857 is adiabatic thermo-elastic cooling or heating depending on the sign of the stress. To identify and document this effect, tensile strength tests were performed on both 4340 steel and aluminum 2024 alloy samples by an MTS Model 43 system, and a thermal profile of the events was collected by a highly sensitive Telops broadband infrared camera. After analysis, thermo-elastic stress cooling was detected and quantified at a rate of -1.70K/GPa for aluminum and -0.61 K/GPa for steel. Additionally, thermo-elastic stress heating was detected and quantified at a rate of -1.56K/GPa for aluminum and -1.16 K/GPa for steel.

Keywords – Thermal, Infrared, Imaging, Thermo-Elastic, Tensile

Introduction

One common diagnostic tool used to establish mechanical properties in materials is the tensile strength test. A tensile test standardly applies uniaxial stress to a test object and retrieves as record the magnitude of that stress as well as the strain or force applied to achieve it. By plotting stress against strain, one can establish a stress-strain curve. Stress-strain curves and their features have been the subject of numerous pieces of research and are well characterized for common solids. In the initial stage of this relationship, as strain is engaged, stress varies linearly as a function of strain, this is called the elastic region and represents strain which remains reversible. Past this region, plastic stress deformations occur, which are non-linear with respect to strain and are irreversible. As fracture occurs the strain is rapidly released, once again denoting an elastic process.

Of particular interest to our research, temperature changes due to elastic stresses were studied in uniaxial stressed solids. Just as a gas cloud subject to rapid compression or expansion would be expected to heat or cool, the same is expected of a solid, stressed rapidly and elastically. Where plastic deformation regions exhibit irreversible thermal stresses and significantly heat the material, thermo-elastic process are isentropic, fully reversible, and will have a net effect of either heating or cooling corresponding to the sign of the change in stress. In the initial elastic portion of the stress-strain curve, the sample will undergo isentropic stress cooling due to positive strain. This cooling will dominate the overall net temperature change of the sample until plastic deformation begins bringing with it sheer stresses which greatly increase the average temperature of the sample. At the moment of fracture, strain is rapidly relieved, at which time negative strain differential causes a rapid elastic gain in temperature.

Methods

With an ultimate goal of measuring thermo-elastic stress heating and cooling, a Telops M3k system was deployed to image both aluminium and steel samples uniaxially pulled to fracture by an MTS Criterion Model 43 testing system. The Telops camera provided quantitative full field temperature measurements with average NETD of just 25mK. The low NETD specification of the M3k was crucial for this application as theoretical predictions originally derived by Lord Kelvin in 1857, suggest very small temperature changes on the order of just a few degrees K from thermo-elastic stress heating and cooling. The MTS is a precision instrument which preforms the tensile test and returns engineering stress and strain data. The MTS as configured collected stress and strain measurements at a rate of 100hz. Though capable of much faster speeds, the M3k was set to match this acquisition rate asynchronously with a framerate of 100hz to ensure simplicity of post processing.

Results

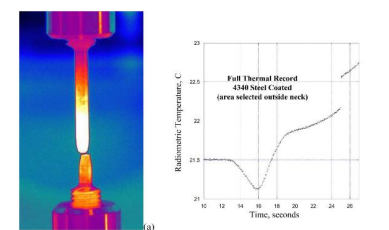


Figure 1: (1a) Thermal image of a steel sample just after fracture. (1b) The full thermal record versus time for a region of interest selected outside of the necking region.

Material	Experimentally Measured Thermo-Elastic Cooling:	Experimentally Measured Thermo-Elastic Heating	Lord Kelvin's Prediction for Thermo- Elastic Heating
Aluminum	-1.70 K/GPa	-1.56 K/GPa	-2.8 K/GPa
Steel	-0.61 K/GPa	-1.16 K/GPa	-0.97 K/GPa

Figure 2: Experimentally quantified rates of thermo-elastic cooling for 4340 steel and 2024 aluminum with a comparison to lord kelvins predicted value for thermo-elastic heating.

Discussion and Conclusion

Quasi-isentropic thermoelastic stress cooling and heating have been imaged and quantified in solid tensile bars. The quantified rates of thermoelastic heating align well with predictions from Lord Kelvin's derivations. Additional derivations and comparisons are provided in the published work. After analysis, thermo-elastic stress cooling was detected and quantified at a rate of -1.70K/GPa for aluminum and -0.61 K/GPa for steel. Additionally, thermo-elastic stress heating was detected and quantified at a rate of -1.56K/GPa for aluminum and -1.16 K/GPa for steel.

References

- [1] Burns, S. J., Pratt, C. E., Carrock, J., Gagnon, J. P., & Sefkow, A. B. (2023). Experimental investigation of Lord Kelvins isentropic cooling and heating expression in tensile bars for two engineering alloys. arXiv preprint arXiv:2311.06371.

LLNL-ABS-863546



LAWRENCE
LIVERMORE
NATIONAL
LABORATORY

iDICs 2024 Abstract John Graham

J. T. Graham

April 24, 2024

PhotoMechanics - International DIC Society 2024
Clermont-Ferrand, France
October 29, 2024 through October 31, 2024

Digital Image Correlation Study of Surface Defects on Plastic Bonded Explosives

John T. Graham

Lawrence Livermore National Laboratory, Livermore, California, USA

Abstract

Many Plastic Bonded Explosives (PBXs) are created by coating an explosive crystalline material with a polymeric binder, and compressing the resultant powder to create a solid piece. Due to the aggregate nature of these materials, their mechanical performance can be quite difficult to understand, often exhibiting non-linear visco- and thermoelastic response. In this work, our goal is to understand the mechanical response of defected material, by adding 3-D features to a cylindrical tensile test sample and using Digital Image Correlation (DIC) to analyse the resultant strain fields around the feature.

Keywords – Digital Image Correlation (DIC), Plastic-bonded Explosive (PBX), Mechanical Properties

Elimination of Interpolation Error in Digital Volume Correlation

S. Wantz^{1,2}, R. Brault¹, Y. Pannier², V. Valle²

¹ CETIM, Senlis, 60304, France

² Institut PPrime, UPR 3364 CNRS – Université de Poitiers – ISAE-ENSMA, Poitiers, 86000, France

Abstract

A strategy called Shift-DVC is presented to reduce systematic error in Digital Volume Correlation (DVC) caused by intensity interpolation. In classical DVC techniques, the subset points are situated at integer locations. In contrast, the proposed Shift-DVC strategy introduces specific offsets to the conventional locations. This method, easy to implement in a classical DVC code, decreases the intensity interpolation error by a factor up to five and significantly improves the required computational time for convergence.

Keywords – Digital Volume Correlation (DVC), Systematic error, Interpolation bias error

Introduction

One major factor affecting the metrological performance of Digital Volume Correlation (DVC) is the systematic error caused by intensity interpolation, namely the S-shaped bias error [1]. Although random error can be eliminated by improving image quality, systematic error cannot be avoided.

This study extends and improves on the approach initially presented in 2D by *Su et al* [2]. This improved method, called Shift-DVC, introduces a specific offset to the conventional location of the subset points (i.e., the center of the voxel). This causes the subset points to fall at non-integer positions where the S-shaped bias error is reduced. This method was compared with the conventional DVC approach using numerically translated experimental data, followed by an in-situ tensile test.

Methods

A sample of polypropylene polymer with added copper particles (approximately 50 μm) was used as an internal volumetric speckle pattern for DVC. To evaluate the systematic interpolation error, the method commonly used in the literature was applied. Two identical volumes (800 x 800 x 1350 voxels) were acquired with a micro-tomograph with a resolution of 10 μm per voxel. The first scanned volume served as a reference for the correlation while the second volume was numerically translated from 0.05 voxels to 1 voxel by increments of 0.05 voxels. Additionally, a tensile test was conducted to demonstrate the efficacy of the Shift-DVC for real in-situ tests. A load of 600N was applied to the sample, corresponding to a few voxels of displacements along the height of the sample. Strain maps were computed by deriving the displacement fields using a central difference algorithm.

Calculations were performed using the GPU-accelerated X-DVCorrel software [3] with a subset size of 33 x 33 x 33 voxels, with both conventional DVC and Shift-DVC computation schemes with trilinear and tricubic interpolation methods.

Results

Fig. 1 shows the comparison between conventional DVC and Shift-DVC strategies for both trilinear (a) and tricubic interpolation (b). The Shift-DVC virtually eliminates the intensity interpolation error, reducing it to below the level of random error.

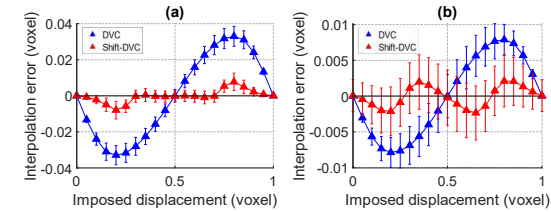


Fig. 2. S-shaped bias error for trilinear (a) and tricubic (b) interpolation using conventional DVC and Shift-DVC strategies

Fig. 2 shows the G_{yy} component (along the axis of traction) of the strain tensor G for both methods with trilinear interpolation.

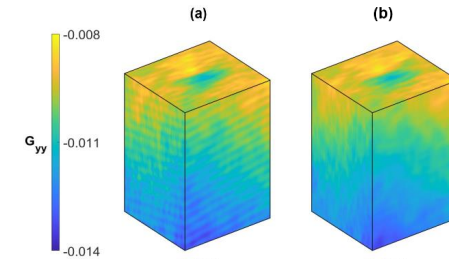


Fig. 1. G_{yy} component of the strain tensor G for standard DVC (a) and for Shift-DVC (b)

Ripples visible on the strain components correspond to the interpolation bias error. For trilinear interpolation, the Shift-DVC method allows for a reduction in the interpolation error by a 5-fold factor on average, and a 40% reduction in the required computation time.

Discussion and Conclusion

A comparative study was conducted between DVC and Shift-DVC using experimental volume data from a tensile test. It was demonstrated that the use of Shift-DVC results in a reduction in interpolation error by a factor of up to five. In the case of tomographic acquisition, the use of Shift-DVC virtually eliminates interpolation error, placing it below the random error, even when a simple trilinear interpolation is employed. It should be emphasized that the Shift-DVC also significantly reduces computation time by reducing the number of iterations required before convergence. Furthermore, it is simple to change existing DVC codes that use a conventional approach to codes that use an offset strategy. The performance of the Shift-DVC method will be further investigated for mechanical application that require very high accuracy.

References

- [1] Schreier HW. Systematic errors in digital image correlation caused by intensity interpolation. *Opt Eng* 2000;39:2915. <https://doi.org/10.1117/1.1314593>.
- [2] Su Y, Zhang Q, Fang Z, Wang Y, Liu Y, Wu S. Elimination of systematic error in digital image correlation caused by intensity interpolation by introducing position randomness to subset points. *Optics and Lasers in Engineering* 2019;114:60–75. <https://doi.org/10.1016/j.optlaseng.2018.10.012>.
- [3] Valle V, Bokam P, Germaneau A, Hedan S. New Development of Digital Volume Correlation for the Study of Fractured Materials. *Exp Mech* 2019;59:1–15. <https://doi.org/10.1007/s11340-018-0415-2>.

Measuring the displacement of masonry stones by motion capture

J. Archez, G. Cumunel, D. Garnier

Université Clermont Auvergne, Clermont Auvergne INP, CNRS, Institut Pascal, Clermont-Ferrand, France

Abstract

A motion capture system has been adapted on masonry structures to measure the displacement field of stones. Full-scale retaining wall and bridge were tested in an outdoor environment, and the measurements were validated using a laser tracker and a DIC analysis. It was possible to access the displacement of every stone during loading helping to describe the behaviour of masonry structure and to improve analytical and numerical analyses.

Keywords – motion capture, masonry, full-scale experiment

Introduction

Stone masonry is a building technique massively used in the nineteenth century that represents more than 60 % of all civil construction in France and consists on fitting interlocking stones together. Some research has already been performed to describe the dry-stone masonry for instance using yield design and homogenization theories [1]. To verify these theories, masonry structures such as retaining walls, dams, or bridges are typically tested at full scale and stone displacement under loading is usually measured using DIC, laser, or cable methods [3]. Motion capture involves sensing infrared light reflected from markers with several cameras previously calibrated in order to measure the position of these markers in three-dimensional space. This technique is widely used in film, video game development, and health and biomechanics studies. We propose here to adapt it to assess stones displacements in masonry structures.

Methods

Two full-scale masonry structures have been analysed by motion capture within the framework of the LaubaPro regional project and Dolmen national project: respectively a curved dry-stone retaining wall and a bridge built around 1880.

(i) The retaining wall was loaded with gravel; the latter was then loaded by a cylinder until failure of the wall (**Figure 1-a**). The displacement of 46 stones was tracked using three $\varnothing 19$ mm markers on each stone (3 markers = 1 rigid body), measured by 10 cameras (Prime x17 and x22) placed between 3 and 4 meters away from the wall (**Figure 1-a'**). To minimize brightness variation and sun interference, a tarpaulin was installed, and the cameras' aperture was set to $f/8$ with a 1 ms time exposure. To validate the motion capture measurements, six markers were replaced by corner cube markers at each loading stage in order to make measurements with a AT403 Leica tracker laser.

(ii) The bridge has been loaded by adding 150 cement blocks on the first arch with a total of 360 tons (**Figure 1-b**). Motion capture measurements were conducted with 10 cameras placed between 15 to 22 meters away from the bridge and with 150 $\varnothing 50$ mm markers. The calibration was performed at night to avoid parasitic reflections cause by the surroundings (**Figure 1-b'**). DIC analysis have also been performed with a high-resolution camera (151 Mpx) and a spatial resolution of 1.2 mm/ pixel.



Figure 1: Photos of (a) the retaining wall and motion capture system and (a') the $\varnothing 19$ mm markers, (b) the loading of the bridge and (b') the reflective markers by night

Results

The displacement norm of one marker at the middle top of the wall measured with the motion capture and tracker laser techniques are displayed in **Figure 2-a**. The two techniques showed similar results during loading, confirming the motion capture's efficacy in quantifying stones displacements. The displacement of each stone of the bridge is depicted in **Figure 2-b**. The keystone of the bridge arch presents the highest displacement with a norm equals to 11 mm.

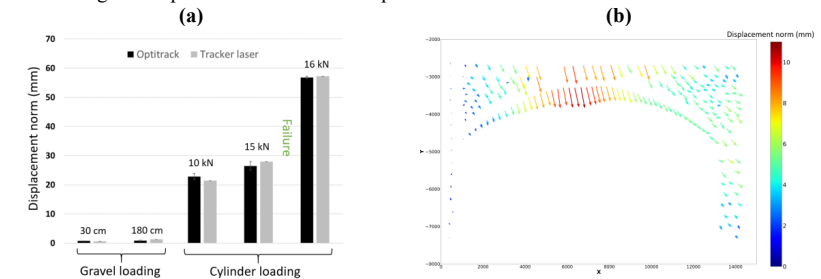


Figure 2: Displacement norm of (a) one marker at the middle top of the wall (b) and of every stone of the bridge after loading

Discussion and Conclusion

Displacement of stones has been successfully measured on full-scale masonry structure thanks to a motion capture system. The measurements have been validated by a tracker laser and a DIC analysis. These measurements will enhance the understanding of masonry structure behaviour and improve numerical analysis and modelling. An active wand will be tested in the future to facilitate motion capture calibration in an outdoor environment.

References

- [1] A.S. Colas, J.C. Morel, D. Garnier. Yield design of dry-stone masonry retaining structures-comparisons with analytical, numerical and experimental data. *International journal for numerical and analytical methods in geomechanics*, 32:1817–1832, 2008.
- [2] H.H. Le, J.C. Morel, A.S. Colas, B. Terrade, D. Garnier, Assessing the three-dimensional behaviour of dry stone retaining walls by full-scale experiments, *International journal of Architectural Heritage*, 9:1373–1383, 2018.



INTERNATIONAL
DIGITAL IMAGE CORRELATION
SOCIETY

PhotoMechanics - iDICs Conference

29-31 Oct 2024, Clermont-Ferrand, France

Michelin's Talk for PM-iDICs 2024 abstracts

Florian Umrani, Sophie Charpin

2D/3D imaging team, Ladoux R&D Center, Manufacture Française des Pneumatiques Michelin, Clermont-Ferrand, France

Michelin, a leader in innovation within and beyond tire, heavily invests in research and development, with a dedicated microscopy team, alongside our materials & mechanical engineers. Digital image correlation offers a crucial approach to understand the behaviour of materials and structures. The latter topic is jointly led internally and externally, through collaborations with universities. Michelin's engagement on PhD theses is key to strengthen knowledge and expertise on long term vision.

Keywords – DIC, DVC, FIB-SEM, Micro-CT

Michelin is widely recognized as a company focused on research and innovation. Since its inception, Michelin has heavily invested in research and development of new technologies related to tires and mobility. They have been at the forefront of numerous advances in the tire industry, particularly in terms of durability, performance, and safety. Michelin's research and development center features a Microscopy division. A modern and well-equipped machine platform provides researchers and engineers with the ability to visualize and analyze structures at the microscopic scale, and to conduct DVC/DIC experiments. Digital image/volume correlation approaches offer a powerful method to study the behavior and properties of our materials' structures. They enable a deep understanding of material and structural mechanics, which is crucial for our concerns. These topics can be developed internally or through partnerships with academia, including doctoral programs with our company.

We will illustrate DIC use on 2 topics:

Topic - Residual Stress Measurements on curved surfaces using Focussed Ion Beam [1]

We aim to measure and model the residual stresses of a drawn metal wire. For this purpose, we employ digital image correlation and a FIB-SEM setup, where the FIB component is used for stress relief while the SEM part is used for imaging.

Results

The numerical theory of residual stress release is developed with the parameters of our experiment. Then we create a suitable mesh, and we carry out a finite element simulation corresponding to the experiment.

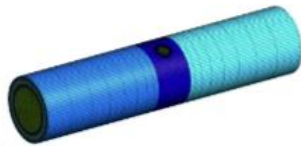
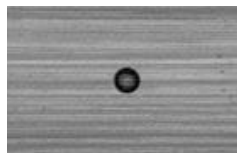


Figure 1: Mesh of a metal wire FEM simulation

The parameters of the experiment are identified, and the experimental protocol is constructed. Then the experiment is carried out using FIB-SEM by capturing images regularly as the sample is pierced by the ion beam.

Figure 2: SEM image of the drilled hole



Finally, digital image correlation is used to determine all the vector components of the residual stress release.

Topic - Rubber crack growth

Fields surrounding crack tips into rubber play a key role in explaining resistance to crack growth. We wish to determine the quality of numerically determined displacement fields by comparing with measurements experiment.

Results

First, numerical simulation is done according to the experiment parameters.



Figure 3: Numerically determined displacement field around the crack

The experiment utilizes Micro-CT in conjunction with an in-situ mechanical cell. Initially, a controlled-size cut is made on the sample, followed by the application of 14 successive load levels to the material. At each level, a 3D tomographic volume is acquired.



Figure 4: Tomograph Xradia Versa 520 & in-situ load cell Deben CT 5000 tec

As our material is full of ZnO particles that are denser than the rubber matrix, we use them applying segmentation to measure the displacement field on each load step. To measure particles displacements, we use a Feature-Vector-based Relaxation Method [2] on our segmented particles. When applied on acquired data, focusing on the 1000 or 2000 largest points, one manages to pair 77 % of those points and 3.9 % of these pair look erroneous. The approach finds realistic displacements fields and can even identify a rigid body displacement.

Discussion and Conclusion

Digital Image Correlation (DIC) represents an innovative avenue for Michelin. It enables the observation of how structures deform or behave during various experiments, crucial for designing, optimizing structures, and understanding materials, essential for our fields. Each DIC project, whether internal or in external collaboration, brings forth its share of answers and new questions. This can be an opportunity to establish partnerships with universities, providing an enhanced platform for both parties, bolstering their visibility and expertise in both academic and industrial realms. Hosting theses allows Michelin to facilitate knowledge exchange between academia and industry, collaborate with universities, recruit talents, innovate, and strengthen their reputation in the research and development domain. Moreover, access to advanced machinery (such as Micro CT's, FIB-SEM, AFM, etc.) offers additional opportunities to conduct cutting-edge research and develop new technologies.

References

- [1] Xiaolei CHEN, Jan Neggers, Veronique Aubin, Eva Hérippe, Aurelie Jamoneau Residual Stress Measurements on curved surfaces using Focussed Ion Beam [Thesis not yet published] Université Paris-Saclay, Central Supélec
[2] X. Feng, M. S. Hall, M. Wu, C.-Y. Hui, An adaptive algorithm for tracking 3D bead displacements: application in biological experiments, *Measurement Science and Technology*, vol. 25, paper n°055701, 7 pages, 2014.

Analyses of grain-scale strain heterogeneities to provide input for polycrystalline models

J.P. Goulmy, D. Depriester, F. Guittonneau, S. Jégou, L. Barrallier

Arts et Métiers Institute of Technology, MSMP, HESAM Université, F-13617 Aix-en-Provence, France

Abstract

The objective of this talk is to present the methodology implemented to analyse grain-scale strain heterogeneities by Digital Image Correlation (DIC) in order to provide input for polycrystalline models. In-situ tensile tests were performed on pure copper at room temperature and DIC measurements were made from SEM micrographs. These measurements are then compared with EBSD data and modelling. A discussion on the limitations of current measurements and modelling is proposed.

Keywords – DIC, In-situ test, EBSD, polycrystalline models

Introduction

Understanding and modelling the mechanisms at the microstructure scale is of great importance to be able to model the behaviour of materials at different scales. For this purpose, digital image correlation (DIC) is an effective method of measurement to evaluate plastic strains generated by various loading conditions [1-2]. However, it requires the development of a precise methodology to observe mechanisms at sub-micrometer scales. The choice of speckle, measurement conditions and image correlation are all parameters to be considered for the success of the tests. It also appears relevant to develop a coupling method with other experimental measurements and modelling method to adapt the aforementioned choices.

Methods

The investigated material is pure copper. After polishing, chemical etching is performed to reveal a fine microstructure serving as speckle for digital image correlation. Based on statistical parameters, SEM measurement conditions are defined so that the images are stable with low standard deviations on the strain computed from DIC [3]. Two magnifications are investigated (x300 and x5000) during the tests on the same specimen. The acquisition of images at x300 provides a "macroscopic" view of the microstructure with a resolution of 300 nm/px. Thus, it is possible to determine the macroscopic strain applied to the specimen during the test. The acquisition of the x5000 images allows a resolution of 19 nm/px, making it possible to evidence the intragranular slip bands during the mechanical loading. Stitching of several images at this magnification is necessary to obtain a representative number of grains in the field of observation. 8x6 images are produced (i.e. a total of 48 images per loading step) at a magnification of x5000 with a 10% overlap between the images. The final images give a measurement field of 177x100 μm^2 . The acquisition time for a set of images is approximately 75 minutes.

The test is carried out using a Kammrath & Weiss 5 kN in-situ tensile testing machine, on specimens with a gauge section of 1.75x6mm² and a gauge length of 16 mm. Four stages are carried out. At each step the displacements is fixed, and the evolution of the force is recorded. An increase of the strain induces an increase of relaxation during the measurement steps. In order to avoid relaxation, a waiting time is applied before SEM acquisition. Thus, the maximum stress variation observed during imaging is less than 1.3 MPa. DIC is then performed using the Ncorr software [4].

Results

The von Mises equivalent strain, assuming a purely Isochoric Generalized Plane (IGP) strain ϵ_{IGP} was used to compare the experimental results with modelling. Based on the work carried out in [5-6], several outstanding results will be discussed, such as: the influence of image correlation parameters on the strain fields (Figure 1) and the comparison between experiments and CPFEM model (Figure 2).

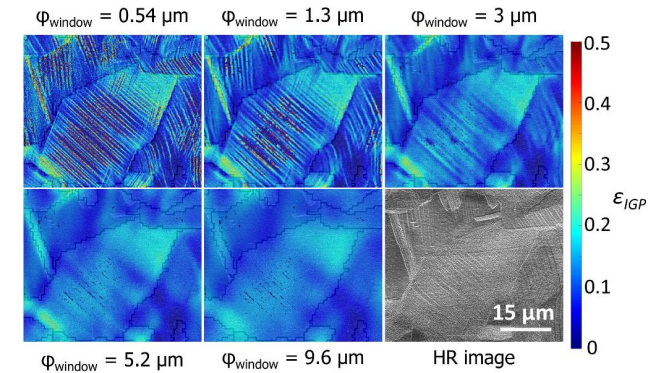


Figure 1: Effective shear strain in function of image correlation parameters [5].

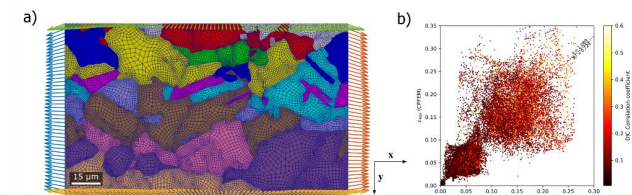


Figure 2 : a) CPFEM meshing of tensile test and DIC boundary conditions , b) Equivalent strain simulated by CPFEM as a function of the experimental values given by DIC [6].

References

- [1] Stinville, J. C., P. G. Callahan, M. A. Charpagne, M. P. Echlin, V. Valle, et T. M. Pollock. Direct Measurements of Slip Irreversibility in a Nickel-Based Superalloy Using High Resolution Digital Image Correlation. *Acta Materialia* 186, pages 172- 89, 2020.
- [2] Di Gioacchino, Fabio, et João Quinta da Fonseca. An Experimental Study of the Polycrystalline Plasticity of Austenitic Stainless Steel. *International Journal of Plasticity*, pages 92- 109, 2015.
- [3] J.-P. Goulmy, F. Guittonneau, S. Jégou, and L. Barrallier, "Classification of the acquisition conditions driving the accuracy of strain measurements during in situ DIC with scanning electron microscope," *Strain*, 2023, doi: 10.1111/str.12456.
- [4] J Blaber, B Adair, and A Antoniou, "Ncorr: Open-Source 2D Digital Image Correlation Matlab Software." *Experimental Mechanics* (2015).
- [5] J. P. Goulmy, D. Depriester, F. Guittonneau, L. Barrallier, and S. Jégou, "Mechanical behavior of polycrystals: Coupled in situ DIC-EBSD analysis of pure copper under tensile test," *Materials Characterization*, vol. 194, p. 112322, Dec. 2022, doi: 10.1016/j.matchar.2022.112322.
- [6] D. Depriester, J. P. Goulmy, and L. Barrallier, "Crystal Plasticity simulations of in situ tensile tests: A two-step inverse method for identification of CP parameters, and assessment of CPFEM capabilities," *International Journal of Plasticity*, vol. 168, p. 103695, Sep. 2023, doi: 10.1016/j.ijplas.2023.103695.

DIC data filtering proposal for complex environments

G. Alonso Aruffo¹, Y. Lalau², L. Penazzi¹, R. Bonnaire¹

1- IMT Mines Albi, Centre ICA-A (Institut Clement Ader Albi), Albi, France

2- IMT Mines Albi, Centre RAPSODEE, Albi, France

Abstract - A filtering method has been developed to provide reliable experimental results obtained using 3D DIC stereo correlation measurement method in cases noise cannot be controlled. This method based on numerical post processing, has shown to be efficient for experiments lead in complex environments, when noise sources cannot be controlled nor quantified (wind, vibrations, variable lighting, humidity...). Furthermore, this work describes a reliable filter parameter optimisation procedure.

Keywords – DIC, Spatial filtering, Complex environments

Introduction DIC field measurements are frequently used in experimental mechanics. Different test conditions and environments, such as high temperatures, vibrations and lighting variations, are involved in these measurements. To correct the noise induced by these testing conditions, experimental development can be conducted. For instance, a fan can be added to an oven to reduce temperature and air heterogeneity [1]. Post-processing can be used in 2D or 3D imaging contexts, particularly for heat flux noise, to obtain a distortion-free reference image [1,2]. Our work aims to develop a post-processing filtering technique that can handle any type of noise source, whether quantifiable or not, such as outdoor test conditions that lead to complex environments. The work proposed here is based on an optimization procedure for the parameters of a low-pass spatial Gaussian filter.

Methods 1 – DIC field measurements

Allied Vision cameras with 5 MPX resolution and Kowa CCTV lenses (LENS 1”50mm/F1.4) were used to conduct 3D-DIC tests. Image acquisition was carried out at a frequency of two images per minute using Vic-Snap software by Correlated ©Solutions. Subsequent stereo-correlation post-processing was performed using VIC-3D and Matlab. The DIC measurements were performed under outdoor conditions on a cylindrical metallic structure made of stainless steel, with heating phases reaching temperatures of 400°C within a Thermal Energy Storage (TES) system. The analysed area covered approximately 10x10 cm. Correlation tests were carried out using an MHI type light source (Dedolight 400D lamp) with two cameras positioned in parallel on a horizontal bench.

2 – Filtering Optimisation method

The parameters of the Gaussian filter, namely the filter size (r) and standard deviation (σ), can produce different results depending on their values. To achieve optimal filtering, it is essential to select the most suitable parameters. This process involves testing a series of pairs of (σ , r) values on a given image (at a particular temperature) to identify the most effective combination. Once the filtered images have been generated, they are subtracted from the non-filtered original image, resulting in the residual image. This image provides valuable insight into the two parameters of interest. The objective here is to evaluate the standard deviation of each residual image and maximise it. This will ensure optimal filtering, allowing for the ideal balance of insufficient and over-filtering.

Results 1 – Filter parameters

Figure 1 shows the optimisation results for images captured at 200°C. One shows the variation of the standard deviation of the residual image versus σ , and the other shows the variation of the standard deviation versus r . Each curve corresponds to a different value of r or σ , respectively. These plots help identify the optimal values for σ and r , which maximise the standard deviation. The procedure was repeated for different temperatures as the σ parameter values are not unique. The parameters (r ; σ) = (91; 76) were obtained for the 200°C example.

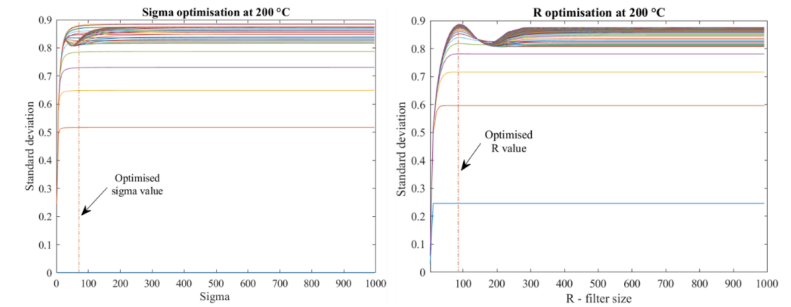


Figure 2 : Filter parameter optimization at 200°C. Standard deviation values for (σ , r) values in order to find optimized σ value (left) and Standard deviation values for (σ , r) values in order to find optimized r value (right)

2 – Displacement results

Mean displacement values and standard deviations for each displacement field U and V are illustrated in Figure 2. The evolution of standard deviations indicates a consistent decrease in the standard deviation for each image after filtering. The presented filtering results clearly demonstrate that applying this filter, along with its corresponding parameters, at different temperatures allows for the preservation of the same mean displacement value. This ensures that information loss due to filtering is avoided while concurrently reducing random noise associated with the complex interplay of temperature variations and potential environmental noise sources.

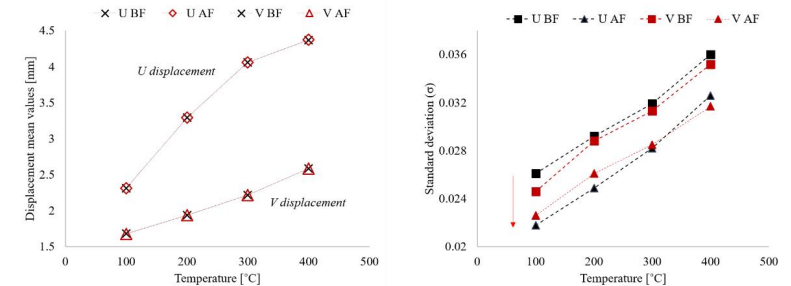


Figure 1 : Mean displacement values before (BF) and after (AF) filtering variation with temperature (left), and evolution of corresponding standard deviation of displacement fields (right)

Discussion and Conclusion The numeric correction method (Low pass Gaussian filter) is used primarily for high temperature measurements and has here shown to be effective for variable and uncontrolled noise sources due to complex outdoor conditions. The results also demonstrated the reliability and robustness of the filter parameter optimisation algorithm. This procedure could be applied to other test configurations with varying temperatures where filtration is essential for proper data analysis.

References

- [1] E. M. C. Jones and P. L. Reu. Distortion of digital image correlation (DIC) displacements and strains from heat waves. *Experimental Mechanics*, 58(7), 1133-1156, 2018.
- [2] L. P. Luong, Development of the two-dimension Digital Image Correlation method at high temperatures applicable for titanium alloys forming process (Doctoral dissertation, Ecole des Mines d'Albi-Carmaux). 2021.

Residual stress measurement in tire cables by FIB hole drilling

R. Engel¹, J. Neggers¹, V. Aubin¹, A. Jamoneau²

¹Université Paris-Saclay, CentraleSupélec, ENS Paris-Saclay, CNRS, LMPS - Laboratoire de Mécanique Paris-Saclay, 91190, Gif-sur-Yvette, France

²Michelin, Clermont-Ferrand, France

Abstract – Residual stress measurement is a real challenge as they are a key factor in fatigue life of industrial pieces such as tire cables. The method presented here is FIB-hole drilling. An incremental hole is performed with a FIB beam and the displacement field for each step is observed thanks to DIC. With these fields, an inverse method allows to deduce the residual stresses around the hole.

Keywords – FIB; hole drilling; Inverse method

Introduction The analysis of Residual Stress (RS) in wire-shaped metal reinforcements enables the selection of optimized process parameters to increase tire fatigue life. One possible RS characterization method is FIB-hole drilling. This involves drilling a hole by layers with an ion beam. These holes are tens microns wide and one micron deep. At each step, the RS relaxation is incrementally observed via displacement fields on the surface around the hole. FIB drilling is suitable for parts with radii of less than a hundred microns. Displacement field analysis is performed by Digital Image Correlation (DIC) and coupled with an inverse method in order to find the RS.

Methods However, there are many sources of uncertainties of various types which prevent accurate observation of displacement fields. These are present at every stage of the process and are listed in Table 1.

Table 1: details on error sources of FIB-DIC in tire cables.

Error source	Description	Solution
FIB contouring	The zone drilling by the FIB beam is not a perfect round shape	Find a better way to shape round shape
SEM drifting	The scanning of the stage is not perfect, step between rows and columns of measurement is not precise	Plot the drift field
Database	The database uses materials parameters and hypothesis to model the process	The influence of some hypothesis might be studied
Stage position	Between FIB and SEM mode, the stage is not in the same position then the repositioning is not precise	Avoid changing position between modes
Curved shape	The tire wire surface is curved so this z-differences must be considered	Calculate the relative height

As mentioned in the table, those artifacts can be avoided. Two of them are considered in the protocol developed here. The first, related to the device itself, is electron beam drift. The difference between the actual and theoretical position of the beam is then calculated to obtain a constant error field. The second is the curvature of the wire and the distance of its surface from the source pivot point. The focal plane is quite important in SEM. The actual distance between the sample surface and the source pivot point is calculated for a cylinder of known radius.

Results/Conclusion At the end, we are able to measure the actual displacement field around the FIB-hole with a picometer precision. The figure 1a shows cross-sections of the holes taken with SEM. Two components of the displacement field are measured as it is shown in the Figure 1b. Thanks to the

inverse method used, we are then able to find all the 6 components of the RS along the FIB-hole. The Figure 1c shows one of them for different samples.

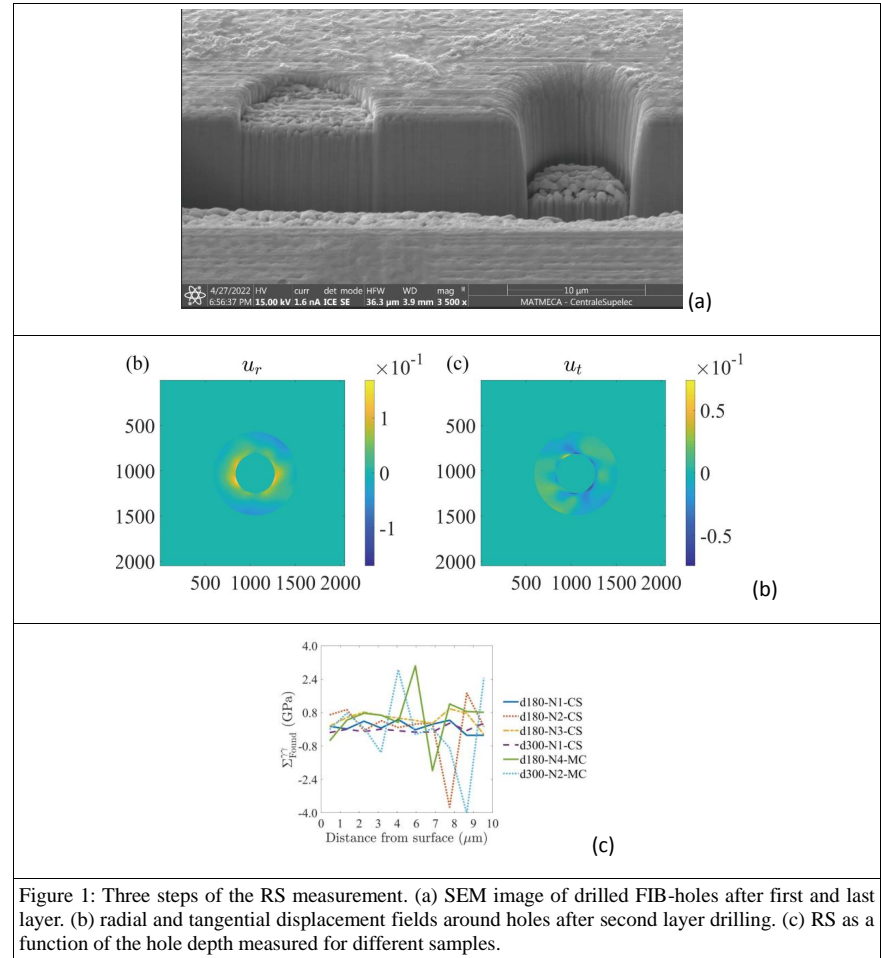


Figure 1: Three steps of the RS measurement. (a) SEM image of drilled FIB-holes after first and last layer. (b) radial and tangential displacement fields around holes after second layer drilling. (c) RS as a function of the hole depth measured for different samples.

Abhishek G. S. Raviprakash

Pyrodynamics, Bengaluru, India

Abstract –

In recent decades, India has made extensive strides in Aerospace Research and Engineering. Predominant being Space Technology, Spacecraft, Satellite, Moon Mission, Mars Mission, Aircraft Testing and Research, Development of bulletproof jackets, Helicopter, etc. In the process, new composite materials and additive manufactured materials have been developed. Pyrodynamics introduced Digital Image Correlation to several Aerospace Research Organizations, to be employed for the validation/verification of Design / FEM, material characterisation, ODS, and structural health monitoring. The authors have extensive experience and expertise in DIC, for Aerospace Research Applications and this paper highlights several case studies and end-user applications of DIC in aerospace engineering including mechanical testing of aircraft components, characterization of composite materials, and more. These examples demonstrate the versatility and effectiveness of DIC in addressing the unique challenges faced in the aerospace industry.

Keywords – DIC, Strain Measurement, Aerospace Engineering

Introduction

Through, DIC researchers were able to visualize and quantify structural phenomena around aircraft surfaces, such as wings and fuselages. By analysing surface deformation under aerodynamic loads, engineers could improve the understanding of airflow behaviour, optimize aerodynamic designs, and enhance overall aircraft performance.

Methods

VIC-3D, 3D Digital Image Correlation System was used for these tests. Prior to the introduction of DIC, the experiments/tests were conducted using conventional sensors viz:- strain gage, accelerometers, LVDT, etc. As a cross-verification for the DIC data, in all tests, conventional sensors were also used and there has been an excellent match between DIC and strain gages.

Results

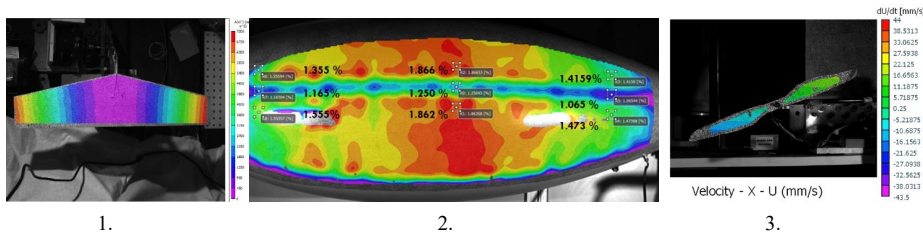


Figure 1: ODS of an aircraft wing model under vibration.

Figure 2: Scaled Aerostat under pressure load.

Figure 3: Propeller model under rotation.

Figure	Figure 1	Figure 2	Figure 3
Camera Used	Camera Link 2 MP Camera	Camera Link 2 MP Camera	Photron AX 100
Frame Rate	240 fps	10 fps	4000 fps
Subset for DIC	29 Pixels	35 Pixels	35 Pixels
Step Size for DIC	7 Pixels	7 Pixels	7 Pixels
Strain Filter Size	15 Pixels	15 Pixels	21 Pixels

References

- [1] M.A. Sutton, J.-J. Ortu, H. Schreier, *Image correlation for shape, motion and deformation measurements: Basic Concepts, Theory and Applications*, Springer, New York, NY (USA), 2009.
- [2] Ashwin Rai, S Nadeem Masood, S R Viswamurthy, Saurabh Chandrakar, Arun Kumar Singh, Kodukula Swapna & Kotresh M Gaddikeri, *Buckling & Post-buckling Behavior of Thin Composite Panels*, *iDICs Dublin, Sep 15-18*
- [3] V. Ravulapalli, G. Raju and V. Narayanamurthy, *Experimental studies on snaking in 3D-printed cylindrical shells under axial compression using photogrammetry*, The Royal Society Publishing, IIT Hyderabad, India, 2023
- [4] Pavan Hiremath, Sathyamangalam Ramanarayanan Viswamurthy, Manjunath Shettar, Nithesh Naik and Suhas Kowshik, *Damage Tolerance of a Stiffened Composite Panel with an Access Cutout under Fatigue Loading and Validation Using FEM Analysis and Digital Image Correlation*, MDPI Fibers, CSIR-National Aerospace Laboratories, Bengaluru, India.
- [5] Digendranath Swaina, Jeby Philip, S Karthigai Selvana, S Annamalai Pillai, *Digital Image Correlation (DIC) – An Invaluable Tool for Non-contact and Full-field Assessment of Critical Regions on Launch Vehicle Structures*, National Seminar on ‘Aerospace Structures Technologies-Progress & Outlook’ ASET-2014, June 13-14, 2014, Thiruvananthapuram, Vikram Sarabhai Space Center (VSSC), India.
- [6] Yogesh Jamthe, S. Raviprakash, Suhasini Gururaja, *Strain Measurement Using Digital Image Correlation (Dic) During Orthogonal Cutting Of Idealized Cfrp Plates*, INCCOM-12, Vikram Sarabhai Space Center (VSSC), Thiruvananthapuram, India.
- [7] Digendranath Swain, Soumit Kumar Biswal, Binu P. Thomas, S. Santhosh Babu, Jeby Philip, *Performance Characterization of a Flexible Nozzle System (FNS) of a Large Solid Rocket Booster using 3-D DIC*, Springer Link, Experimental Techniques, Vikram Sarabhai Space Center (VSSC), Thiruvananthapuram, India, 2018

Microstructural study of additively manufactured ALF357 alloy: Effect of tensile loading and build orientations

Avinash Mohan M¹, N.Iniyan Thiruselvam², Jayaganthan Rengaswamy^{1*}

¹Department of Engineering Design, Additive Manufacturing Group, & Center of Excellence for Materials and Manufacturing for Futuristic Mobility, Indian Institute of Technology Madras, Chennai, 600036, Tamil Nadu, India

²Department of Mechanical Engineering, Birla Institute of Technology and Science Pilani, Goa, 403726, India

Abstract – Aluminium alloys have high specific stiffness, specific strength, corrosion resistance, and machinability, making them highly desirable for lightweight applications in the automotive and aerospace industries. Additive manufacturing (AM) has recently expanded the potential for using aluminium alloys in safety-critical applications. However, AM introduces uncertainties that may impact mechanical properties, especially fracture behaviour. In this study, ALF357 was fabricated using Laser Beam Powder Bed Fusion (LPBF) in vertical and horizontal printing directions to assess their quasi-static and fracture responses. Digital Image Correlation (DIC) is employed to directly assess fracture parameters by measuring in-plane surface displacements near cracks. The fracture behaviour will be further characterised using microstructural studies like optical and scanning electron microscopy. It is expected that the ALF357 will outperform commonly used aluminium alloys like AISi10Mg.

Keywords – DIC; ALF357; Microstructure; LPBF

Introduction

Additive manufacturing (AM) alloys have been employed in numerous safety-critical areas, including aerospace, biomedical, and automotive industries. ALF357, a member of the cast A356 alloy family, has been introduced by EOS, a manufacturer of L-PBF (Laser Powder Bed Fusion) machines. This alloy is specifically tailored for additive manufacturing (AM) processes. ALF357 is an ideal material for applications requiring a combination of low weight and mechanical/thermal load endurance. It is a beryllium-free derivative of the A357 (AlSi7Mg0.6) alloy. Its characteristics like light weight, corrosion resistance, and high dynamic load-bearing capacity make it suitable for applications like the aerospace industry, defence and automotive industries, and structural components requiring high strength. As the use of printable aluminium alloys grows in fracture-critical applications, it becomes essential to study how additive manufacturing (AM)-related artifacts impact the overall mechanical behaviour of aluminium parts, especially their fracture properties.

In this study, ALF357 was fabricated using Laser Beam Powder Bed Fusion (LPBF) in vertical and horizontal printing directions to assess their quasi-static and fracture responses. Digital Image Correlation (DIC) is employed to directly assess fracture parameters by measuring in-plane surface displacements near cracks. DIC setup helps to study the full-field strain of the specimen. The fracture behaviour will be further characterised using microstructural studies like optical and scanning electron microscopy.

Methods

The samples were manufactured using an EOS M 290 printer in vertical and horizontal printing directions. After printing, both build plates and the specimens were directly relieved by preheated argon gas at 270 °C for 90 min. After the stress relief step, specimens were removed from the build plate by wire electrical discharge machining, and the T6 heat treatment was done. All tests were done in this T6 condition.

Quasi-static tensile tests are done using an Instron UTM under ASTM E8/E8M standard, and the initial results are shown below in Fig 1. The fracture property will be studied using a 3-point bending test under the ASTM E399-23 standard. Detailed studies like fractography and other microstructural studies are deferred to be conducted in the coming months and will be ready soon.

Results

Figure 1 shows the stress versus strain curve for ALF357 under quasi-static tensile load. It was observed that the vertical printed samples exhibited lower UTS (330 MPa) than the horizontal printed samples (347 MPa). Figure 2 shows the DIC setup and the strain field obtained during the initial studies.

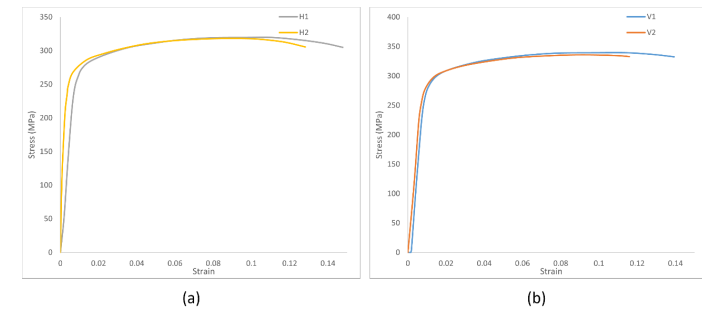


Figure 1: Stress versus Strain curve for (a) Horizontal and (b) Vertical printed samples

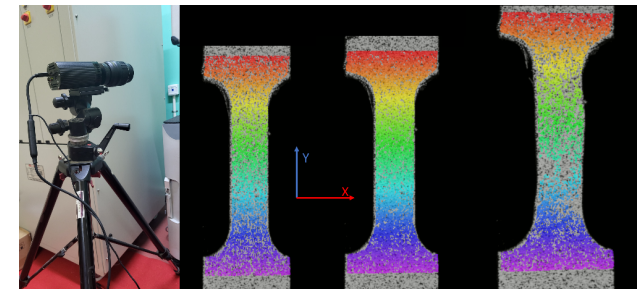


Figure 2. DIC setup and Full-field strain map

References

- [1] John P. Isaac, Seungjong Lee, Spencer Thompson, Ankit Saharan, Nima Shamsaei, Hareesh V. Tippur. Role of build orientation on quasi-static and dynamic fracture responses of additively manufactured ALF357 and AISi10Mg alloys, Additive Manufacturing, Volume 59, Part A, 2022, 103080, ISSN 2214-8604, <https://doi.org/10.1016/j.addma.2022.103080>.
- [2] Isaac, J. P., Lee, S., Shamsaei, N., & Tippur, H. V. (2022, June). Fracture Response of Additively Manufactured Aluminum Alloys: Effects of Loading Rate and Build Orientation. In Society for Experimental Mechanics Annual Conference and Exposition (pp. 13-17). Cham: Springer International Publishing.
- [3] Alexopoulos, N. D., & Tiryakioglu, M. (2009). Relationship between fracture toughness and tensile properties of A357 cast aluminum alloy. Metallurgical and Materials Transactions A, 40, 702-716.
- [4] Quanjin M, Rejab MR, Halim Q, Merzuki MN, Darus MA. Experimental investigation of the tensile test using digital image correlation (DIC) method. Materials Today: Proceedings. 2020 Jan 1;27:757-63.
- [5] He Z, Zhang K, Lin Y, Yuan S. An accurate determination method for constitutive model of anisotropic tubular materials with DIC-based controlled biaxial tensile test. International Journal of Mechanical Sciences. 2020 Sep 1;181:105715.
- [6] Gairola, Saurabh, and Rengaswamy Jayaganthan. "Xfem simulation of tensile and fracture behavior of ultrafine-grained al 6061 alloy." Metals 11.11 (2021): 1761.

Evaluation of Influences on Results of Digital Image Correlation by Window of Constant Temperature Bath

A. Seki, K. Iizuka, S. Yoneyama, Y. Takayama, K. Arakawa, M. Takanashi

Aoyamagakuin University, IHI Corporation

Abstract – This study investigates the effect of a window in a thermostatic chamber on the results of digital image correlation (DIC) measurements. The images of the sample with and without the window are recorded and the difference between images caused by the refraction of the light at the window is evaluated using digital image correlation. The effect of window for oblique observation is also evaluated. The measurement results show that the angle of incidence from the camera to the window does not have a significant effect on the measurement results.

Keywords – Digital image correlation, Constant temperature bath, Optical window, Refraction

Introduction Digital image correlation (DIC) is often used in high temperature [1]-[3], low temperature environments and impact tests [4]. In high and low temperature environments, the camera is placed in a thermal insulator or outside the window of a thermostatic furnace or oven to keep the camera at an appropriate temperature. In impact tests, the specimen may be placed in a protective device to prevent the specimen from scattering. In both cases, a window is placed between the specimen and the camera to allow the camera to take pictures. However, the presence of the window affects the DIC measurement results. Su et al [5] derived the following equation to determine the displacement Δx due to light refraction at the window when a window is placed between the camera and the specimen.

$$\Delta x = 2t \left(\frac{x}{L} - \frac{x}{\sqrt{L^2 + x^2 n_r^2 - x^2}} \right) \left(\frac{L}{L - 2t} \right) \quad (1)$$

Where t is the window thickness, x is the distance from the image center, L is the distance from the lens tip to the specimen and n_r is the relative refractive index of the window. This study clarifies how the DIC measurement results change by changing the presence or absence of windows, the number of windows, and their angles, and establish a processing method to suppress the effects of windows.

Methods In order to consider the influence of the displacement Δx caused by light refraction at an angled window relative to the camera, considered deriving an equation for determining $\Delta \theta$. Here, θ is the angle between the window and the lens and $\Delta \theta$ is the angle from the reference angle. Since the formula for the displacement Δx due to light refraction at the window requires the angle θ of the window, the formula for the angle θ is derived.

$$2t\Delta x_0 \sin^3 \theta + (t^2 n^2 - t^2 - \Delta x_0^2) \sin^2 \theta - 2tn^2 \Delta x_0 \sin \theta + n^2 \Delta x_0^2 = 0 \quad (2)$$

To perform the verification experiment for eq. 1, the window is placed on the rotation stage and the window is rotated 15 times by 1° in the direction perpendicular to the window.

Results Figure 1 shows the relationship between the angle at which the rotation stage is moved and $\Delta \theta^\circ$ calculated by eq. 2 using the value of Δx_0 obtained from the measurement. From Fig. 1, the angle calculated from eq. 2 using the measured values and the angle obtained by moving the rotation stage are almost the same, so this equation is validated. Figure 2 shows that up to about 7° , the displacement $\Delta x_{max} - \Delta x_{min}$ hardly changes even if the angle increases, indicating that the DIC measurement results are hardly affected. On the other hand, if the window angle is 8° or greater, it is necessary to consider the window angle when evaluating the DIC measurement results.

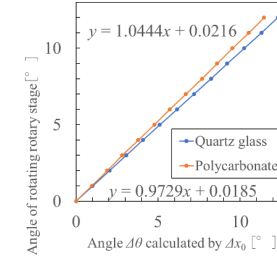


Fig. 1. Relationship between $\Delta \theta$ and angle of rotation rotary stage.

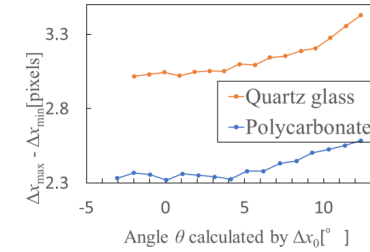


Fig. 2. Relationship between $\Delta \theta$ and $\Delta x_{max} - \Delta x_{min}$.

Discussion and Conclusion The angle between the window and the camera could be determined using the displacement Δx_0 due to light refraction at the window at the image center coordinates obtained experimentally. Using this angle, it is found that the angle of the window up to an angle of nearly 7° has little effect on the displacement due to light refraction at the window. However, when the angle of the window is 8° or higher, it is necessary to consider the angle of the window when evaluating the DIC measurement results. In the next step, derivation an equation to estimate the relationship between the angle and the effect of the window angle on the DIC measurement results is planned, and propose a correction model that includes the window angle.

References

- [1] Lyons, J. S., Liu, J., Sutton, M. A., High-temperature Deformation Measurements Using Digital-image Correlation, *Experimental Mechanics*, Vol. 36, No. 1 (1996), pp. 64-70.
- [2] Grant, B. M. B., Stone, H. J., Withers, P. J., Preuss, M., High-temperature Strain Field Measurement Using Digital Image Correlation, *The Journal of Strain Analysis for Engineering Design*, Vol. 44, No. 4 (2009), pp. 263-271.
- [3] Pan, B., Wu, D., Wang, Z., Xia, Y., High-temperature Digital Image Correlation Method for Full-field Deformation Measurement at 1200 °C, *Measurement Science and Technology*, Vol. 22, No. 1 (2010), 015701.
- [4] Z. Wei, K. Yang, X. Chi, X. Hei, X. Zhao, J. Zhang, Dynamic tensile properties, deformation, and failure testing of impact-loaded coal samples with various water content, scientific reports, Volume. 11, No.7096 (2021)
- [5] Su, Y., Yao, X., Wang, S., Ma, Y., Refraction Error Correction for Deformation Measurement by Digital Image Correlation at Elevated Temperature, *Optical Engineering*, Vol. 56, No. 3 (2017), 034106.

Real-time measurement of surface strain for understanding creep behavior in bending polymer films

Jiayi Yu^{1,2}, Masayuki Kishino^{1,2}, Kyohei Hisano^{1,2}, Atsushi Shishido^{1,2}

¹Department of Chemical Science and Engineering, School of Materials and Chemical Technology, Tokyo Institute of Technology

²Laboratory for Chemistry and Life Science, Institute of Innovative Research, Tokyo Institute of Technology

Abstract

This study introduces our developed photomechanical technique for real-time quantitative analysis of creep behavior in bending polymer films. Creep refers to the deformation that occurs over time under continuous stress. By monitoring surface strain changes during bending deformation, we revealed that creep behavior is influenced by the degree of bending, film thickness, and the viscoelastic properties of the material. These findings highlight the method's potential to predict and understand bending behavior, offering valuable insights for the design of durable substrate materials for flexible devices.

Keywords – Strain, Bending, Surface, Polymer films

Introduction

Flexible devices have emerged as next-generation solutions for addressing public health concerns and energy depletion issues. For flexible device substrates, polymer films have been used as viable alternatives to traditional rigid materials such as metals and glass. However, due to the viscoelastic properties of polymers, these films exhibit solid-like elastic deformation and liquid-like viscous flow, which leads to temporal strain increase under continuous stress—a phenomenon known as creep. Understanding creep behavior is crucial for designing highly durable devices. However, the creep behavior of polymer films subjected to bending deformation remains unexplored because most existing methods for analyzing strain in bending polymer films are macroscopic or qualitative. To understand the creep behavior thoroughly, microscopic and quantitative strain analysis is crucial.

In this study, we introduced the ‘surface labeled grating method’ to quantitatively analyze the creep behavior of various bending polymer films (Fig. 1). In this method, a label with a periodic structure is formed on the surface of a polymer film, and a laser beam is normally incident on the label. Using the change of diffracted light, we can analyze the surface strain of the polymer film in a simple, real-time, and quantitative way [1–3]. With this method, we measured and analyzed the surface strain of various bending polymer films and their creep behavior.

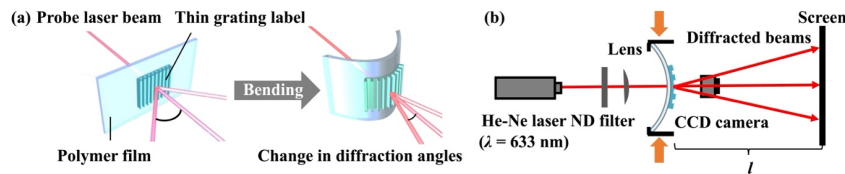


Figure 1: (a) Surface-labelled grating method. (b) Optical setup for the measurement.

Methods

Polymer films of polyethylene terephthalate (PET), polyethylene naphthalate (PEN), polyvinyl chloride (PVC), and polycarbonate (PC) were used. Thin-film grating labels with a periodic structure (lattice period: 4 μm) made from polydimethylsiloxane (PDMS) were applied to these films for light diffraction measurement. Bending deformation was induced by pressing the films from both ends longitudinally. The degree of bending was controlled by the applied strain, defined as the ratio of the change in pressed length (ΔL) to the original film length (L). After applying various strains, the films were held for 30 min to monitor temporal changes in surface strain.

Results

Fig. 2a presents cross-sectional images of a flat and bent PVC film with a thickness of 200 μm [3]. The magnified view in Fig. 2a shows that holding the applied strain at 80% for 30 min clearly sharpened the bending shape, indicating that the creep deformation occurred when they bent largely. Fig. 2b. shows that the surface strain (ϵ_s) of PVC films increased with applied strains, indicating in-plane tension on the outer bending surface.

Subsequent measurement of ϵ_s under 30 min holding of the applied strain revealed that bending creep deformation increased with applied strain and film thickness (Fig. 2c,d). This observed behavior was also noted in other bending polymer films. Additionally, different polymer materials exhibit varying degrees of bending strain and temporal strain changes, highlighting the role of polymer structures in influencing surface strain and fracture modes of bending polymer films.

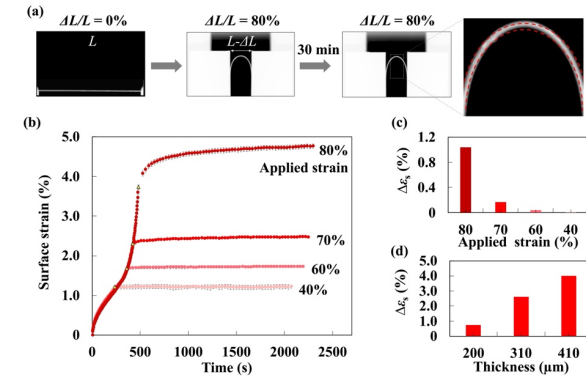


Figure 2: (a) Cross-sectional images of a flat and bent PVC film with a 200 μm thickness. The inset shows a magnified image of the film bent for 30 min. The dashed red line represents the bent shape at the beginning of the holding process. (b) Surface strain of PVC films with a 200 μm thickness bent by 80, 70, 60, and 40% applied strains. (c) Increase in surface strain ($\Delta\epsilon_s$) of the PVC films with a 200 μm thickness bent by each applied strain for 30 min. (d) Increase in surface strain of the PVC films with 200, 310, and 410 thicknesses bent by 70% applied strain for 30 min.

Discussion and Conclusion

Using our developed strain measurement system, we have successfully measured the temporal changes in strain on the surfaces of various bending polymer films at the nanometer scale with high accuracy. Our analysis successfully revealed the quantitative dependence of bending creep on the polymer structures. The observed behavior aligns with the nonlinear viscoelasticity exhibited by polymer materials, providing insights into the material-dependent creep phenomenon. Furthermore, we identified a distinct threshold for bending creep in each polymer, showing variations among different polymers. These findings suggest that viscoelastic properties obtained from tensile tests can predict the bending creep of polymer films, offering insights into the efficient design of flexible electronic device substrates.

References

- [1] N. Akamatsu, W. Tashiro, K. Saito, J. Mamiya, M. Kinoshita, T. Ikeda, J. Takeya, S. Fujikawa, A. Priimagi, A. Shishido. Facile strain analysis of largely bending films by a surface-labelled grating method. *Sci. Rep.* 4:5377, 2014.
- [2] R. Taguchi, N. Akamatsu, K. Kuwahara, K. Tokumitsu, Y. Kobayashi, M. Kishino, K. Yaegashi, J. Takeya, A. Shishido. Nanoscale analysis of surface bending strain in film substrates for preventing fracture in flexible electronic devices. *Adv. Mater. Interfaces.* 8:2001662, 2021.
- [3] J. Yu, M. Kishino, K. Hisano, A. Shishido, Bending creep behaviour of various polymer films analysed by surface strain measurement, *Soft Matter*, 20:3248–3255, 2024.

Strain signature of solid-solid phase transitions within a diamond anvil cell

R. Fréville, N. Bruzy, A. Dewaele

CEA, DAM, DIF, F-91297 Arpajon, France
Université Paris-Saclay, CEA, Laboratoire Matière en Conditions Extrêmes, F-91680 Bruyères-le-Châtel, France

Abstract —

Optical images of iron samples loaded in a Diamond Anvil Cell (DAC) were acquired in the [5-17] GPa pressure range. A femtosecond laser patterning technique was developed for these samples in order to perform Digital Image Correlation (DIC) computations on the images and obtain in-plane strain components. Deviations from linearity for the average of these components highlight phase coexistence domains. While the linear part can be exploited to compute Equation of State (EoS) parameters, the non linear part can be studied to identify strain localization areas during the α - ϵ transformation.

Keywords — DIC, Diamond Anvil Cell, Iron

Introduction Since its first development by Weir et al. [1], the DAC has become one of the most common tools to study the behaviour of matter under high pressure. It consists in enclosing a sample in a cavity, delimited by two diamonds and a metallic gasket. The cavity is filled by a Pressure Transmitting Medium (PTM), usually a gas or a fluid, to ensure hydrostatic pressurizing conditions. By moving one of the diamonds towards the other, the pressure within the cavity increases, allowing to reach up to hundreds of gigaPascals.

Since diamonds are transparent to many electromagnetic radiations, a wide range of *in situ* diagnostics are available. For crystalline materials, X-Ray Diffraction is frequently used to access the crystalline structure and the cell parameters of the material. We are interested here in complementing these data by characterizing strain, especially during solid-solid transformations. Fedotenko et al. [2] monitored length changes at the surface of a DAC sample to measure the EoS of glassy materials. To further characterize the strain field at the surface of the sample, Pandey and Levitas [3] deposited ruby particles between the sample and one of the diamonds of the DAC and performed DIC on ruby fluorescence images. In this poster, we describe a DIC set-up tailored for the study of phase transformations within a DAC, the so-called DICDAC set-up [4]. A femtosecond patterning is performed so that optical images can be used directly to compute in-plane strain components.

Methods Two samples were tested. They were cut from iron foils provided by GoodFellow (99.99% purity) with diameters of 130 and 150 μm . Their thickness is 13 μm . An Electron BackScattered Diffraction (EBSD) orientation cartography of this surface was performed using an Oxford Symmetry S2 detector installed within the chamber of a TESCAN MIRA3 Scanning Electron Microscope. A femtosecond laser (Amplitude System Satsuma) was used to draw a dot speckle pattern on one surface of the samples. They were then loaded in a DAC. Neon is used as a PTM.

DAC was coupled with a membrane pressure controller to impose pressure steps during the experiment, up to above the α - ϵ transition pressure in iron and back to ambient conditions. Pressure was

measured by spectroscopy on a material (ruby or samarium) loaded in the DACs together with the samples. At each pressure step, after stabilization, a pressure measurement and an image acquisition are performed. At some point, out-of-plane variations lead to a loss of focus. Images were taken before and after adjusting the focus so that correlation computations were run on series of images with similar settings.

DIC calculations are run using UFreckles software [5]. A mesh size of 12 pixels (around 3 μm) was used, with a Tikhonov regularization whose cut-off wavelength was equal to the mesh size. Before DIC calculations, a bilateral filter with a neighborhood distance of 3 pixels was applied on all images in an attempt to reduce noise.

Results First, in-plane strain quantities were averaged over the computation domain, highlighting two deformation regimes : a regime in which the material response is linear and a regime in which it is irregular with sudden strain jumps. The latter is attributed to the phase coexistence domain, the linear part corresponding to the hydrostatic response of the material.

To further study this hydrostatic response, we made the hypothesis of a diagonal shape of the strain tensor in these zones to compute the volume variation of the sample against pressure. Although the presented configuration does not allow for a reference volume measurement, all other measured EoS data are in good agreement with data from the literature [6, 7].

The norm of the in-plane stress tensor was then studied at the transition, revealing strong localizations during both the direct and reverse transitions. The latter seems to be smoother with several areas exhibiting strain relaxations.

Discussion and Conclusion A *post mortem* EBSD mapping of the surface of one sample could be performed, revealing the presence of reversion variants inside the microstructure. The position of the largest reversion variants coincide with strain localizations identified before, suggesting that reversion variants may be related to early transformation events.

The DICDAC set-up is then a valuable tool for the extraction of material data during high pressure experiments, namely EoS parameters, phase coexistence boundaries and insights on transformation chronologies.

References

- [1] C.E. Weir, E.R. Lippincott, A. Van Valkenburg, and E.N. Bunting. Infrared Studies in the 1- to 15-Micron Region to 30,000 Atmospheres. *J Res Natl Bur Stand A Phys Chem.*, 63(1):55–62, 08 1959.
- [2] T. Fedotenko, D. S. Souza, S. Khandarkhaeva, L. Dubrovinsky, and N. Dubrovinskaja. Isothermal equation of state of crystalline and glassy materials from optical measurements in diamond anvil cells. *Review of Scientific Instruments*, 92(6), 06 2021. 063907.
- [3] K. K. Pandey and Valery I. Levitas. Displacement field measurements in traditional and rotational diamond anvil cells. *Journal of Applied Physics*, 129(11), 03 2021. 115901.
- [4] Robin Fréville, Nicolas Bruzy, and Agnès Dewaele. Optical full-field strain measurement within a diamond anvil cell. *Review of Scientific Instruments*, 94(12):123905, 12 2023.
- [5] Julien Rethoré. UFreckles, October 2018.
- [6] Agnès Dewaele, Paul Loubeyre, Florent Occelli, Mohamed Mezouar, Peter I. Dorogokupets, and Marc Torrent. Quasihydrostatic equation of state of iron above 2 Mbar. *Phys. Rev. Lett.*, 97:215504, Nov 2006.
- [7] P. I. Dorogokupets, A. M. Dymshits, K. D. Litasov, and T. S. Sokolova. Thermodynamics and Equations of State of Iron to 350 GPa and 6000 K. *Scientific Reports*, 7, 2017.

Understanding Anisotropy of Carbon-reinforced PEEK Using Stereo DIC

Vipin Gupta^a, N. Iniyann Thiruselvam^a, Dhananjay M. Kulkarni^a, Vikas V. Chaudhari^a, Kiran D. Mali^a, Benoît Blaysat^b, Thomas Jailin^b, S. Suraj^c

^a Department of Mechanical Engineering, BITS Pilani, K. K. Birla Goa campus, Goa 403726, India ; iniyann@goa.bits-pilani.ac.in

^b Université Clermont Auvergne, CNRS, Clermont Auvergne INP, Institut Pascal, F-63000, Clermont-Ferrand, France

^c Vikram Sarabhai Space Centre, Thiruvananthapuram, Kerala, India

Abstract

Polyether ether ketone reinforced with short carbon fibers (C-PEEK) is used in various engineering applications due to its high strength-to-weight ratio, thermal stability, chemical inertness, and ease of manufacturing through fused filament fabrication (FFF). However, C-PEEK manufactured through FFF is plagued by anisotropy, the solution to which has not been reported yet. This work uses Stereo Digital Image Correlation (Stereo DIC) and Classical Laminate Theory (CLT) to study this problem. The degree of anisotropy (DoA) of the material is identified from two different raster angle configurations, namely, Single and Quasi-isotropic. It is shown that the quasi-isotropic raster configuration highlights lower DoA than Single raster configuration. The DIC strain maps provide critical insights into the variation in the material properties, which can be used to reduce the anisotropy of the 3D printed C-PEEK.

Keywords – Stereo DIC, Anisotropy, Carbon short fibers, PEEK, Raster Angle

Introduction Polyether ether ketone reinforced with short carbon fibers (C-PEEK) is renowned for its exceptional mechanical properties and chemical resistance. Despite these advantages, the application of C-PEEK in fused filament fabrication (FFF) is often limited by the material anisotropy arising from the manufacturing process. A better understanding of material anisotropy is then necessary before C-PEEK made by FFF can be used in advanced engineering applications [1, 2]. Stereo Digital Image Correlation (Stereo DIC) and Classical Laminate Theory (CLT) are employed to address this problem.

The main objectives of this work are to characterize the degree of anisotropy (DoA) of the material and to elucidate the influence of raster angle on the mechanical properties of C-PEEK made by FFF. Tensile testing was then performed on different material configurations to obtain the elastic anisotropy parameters. The strain maps returned by Stereo DIC offer significant insights into the variation in the material properties, which provide a way to reduce the anisotropy of the 3D printed PEEK composite.

Methods

Specimen Fabrication: ASTM D638 dog-bone specimens made of C-PEEK were 3D printed using KetaSpire® PEEK AM filament (CF10 LS1) through a fused filament fabrication machine (make: CHAR Z Avay Biosciences) with parameters optimized for performance. Figure 1 depicts specimen dimensions and raster angle. Two different raster angle configurations, namely, Single (0°) and Quasi-isotropic (0°/45°/-45°/90°) were printed.

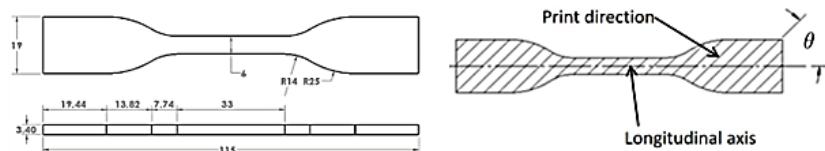


Figure 1: Dimensions (all in mm) of the ASTM D638 standard test specimens and Raster angle (θ) between the print direction and the longitudinal axis (tensile axis) of the test specimen.

Test Setup: A uniaxial tensile machine equipped with two cameras was used (see Fig. 2).

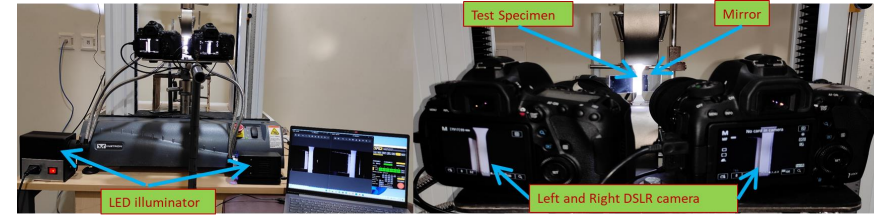


Figure 2: Stereo DIC setup.

DIC measurements: This work used an in-house Stereo DIC system and software developed at BITS Pilani Goa campus, details of which can be found in [4-7].

Degree of Anisotropy: The elastic anisotropy properties were identified based on CLT for each configuration using the strain maps obtained from DIC. The DoA was then obtained such as:

$$\text{DoA} = \left(\frac{E_1}{E_2} \right) - 1$$

where E_1 and E_2 are the Young's moduli in the axial and transverse directions, respectively.

Results and discussion: The Quasi-isotropic configuration, when compared to the Single raster angle configuration, exhibits higher tensile strength, lower anisotropy, and higher modulus of elasticity. The Quasi-isotropic layups, historically employed in composite materials, result in fibers oriented in multiple directions, thereby enhancing isotropy. Applying this concept to 3D-printed C-PEEK shows that the Quasi-isotropic raster configuration effectively minimizes directional dependence of mechanical properties, resulting in superior mechanical performance and reduced anisotropy.

Stereo DIC offers a wealth of data, which significantly enhances the ability to accurately characterize the mechanical behaviour of materials compared to the traditional strain gauge measurements. This detailed strain data allows for a better understanding of the material anisotropy.

Conclusion An in-house Stereo DIC software was used to characterize the material anisotropy in a 3D printed composite wherein polyether ether ketone is reinforced with carbon short fibers (C-PEEK). The degree of anisotropy (DoA) arising from two different raster angle configurations, namely, Single and Quasi-isotropic, was computed based on DIC data. The Quasi-isotropic raster configuration shows lower anisotropy and exhibits better tensile properties.

References

- [1] B. D. Agarwal, L. J. Broutman, K. Chandrashekhara, Analysis and Performance of Fiber Composites, 3rd Ed. John Wiley & Sons, New Jersey (USA), 2016.
- [2] M Somireddy, C.V. Singh, A. Czekanski, Analysis of the Material Behavior of 3D Printed Laminates Via FFF. *Experimental Mechanics*, 59, 871–881, 2019.
- [3] M. A. Sutton, J. J. Orteu, H. Schreier, 2009. Image correlation for shape, motion and deformation measurements: basic concepts, theory and applications. Springer Science & Business Media.
- [4] Vipin Gupta, N. Iniyann Thiruselvam, D. M. Kulkarni, V. V. Chaudhari, S. Suraj. Anisotropy and deformation heterogeneity in additive manufactured carbon-reinforced PEEK. *Journal of Mechanical Science and Technology*, 37(6), 2871–2880, 2023.
- [5] N. Iniyann Thiruselvam, S. J. Subramanian, Feature-assisted stereo correlation. *Strain*, 55, 1–14, 2019.
- [6] N. Iniyann Thiruselvam, S. J. Subramanian. On improving the accuracy of self-calibrated stereo digital image correlation system. *Measurement Science and Technology* 32, 1–17, 2020.
S. Sharma, N. Iniyann Thiruselvam, S. J. Subramanian, G. S. Kumar. Computation of strains from stereo digital image correlation using principal component analysis. *Measurement Science and Technology*, 32(10), 10520, 2021.

From random speckles to checkerboard patterns

Michel Grédiac and the Photomechanics teams, Clermont-Ferrand and Nancy, France

Université Clermont Auvergne, Clermont Auvergne INP, CNRS, Institut Pascal, Clermont-Ferrand, France

Abstract — This contribution discusses the benefits of using checkerboard patterns to measure in-plane displacement and strain fields. It also explains how the minimization of the optical residual classically performed in the spatial domain can be advantageously switched to the frequency domain in this case.

Keywords — Checkerboard, DIC, Localized Spectrum Analysis, Material Testing 2.0, Patterning, Speckle

Outline The metrological performance of DIC depends heavily on the quality of the speckle pattern deposited on the specimen. Choosing a pattern suitable for DIC measurements should ideally lead to the lowest possible errors, and this results from a trade-off between several constraints discussed in many papers available in the literature. One of the main criteria is minimizing sensor noise propagation noise in the final displacement map, which is obtained by maximizing the gradient of the pattern image. This maximal image gradient is obtained with a checkerboard [1]. However, such a pattern is periodic, so it is not used in DIC.

This presentation shows that using a spectral technique makes processing such checkerboard patterns possible. Under some mild assumptions, this is equivalent to saying that the minimization of the optical residual performed by DIC in the spatial domain is switched to the frequency domain.

In addition to processing patterns that are optimal in terms of sensor noise propagation, three interesting features must be emphasized:

1. Calculations are performed in the frequency domain, considerably reducing the computing time compared to classic DIC. In particular, retrieving the displacement field is “nearly” direct in the sense that a closed-form expression linking displacement and phase change between images of the reference and deformed patterns is available. Only a fixed-point algorithm is employed at the end of the procedure, and this algorithm all the more rapidly converges as the strain amplitude is small.
2. The phase maps retrieved with this approach are, at first approximation, their actual counterparts convolved by a known a priori filter. This led to the development of a dedicated deconvolution algorithm [2, 3]. Employing this procedure enhances localized details in the final strain maps.
3. The pattern-induced bias [4, 5], which mainly affects the displacement fields returned by the measuring system when high spatial frequencies are necessary to correctly describe the actual one, becomes negligible when checkerboard patterns are used.

As a typical example, Figure 1 shows a strain map measured on a wood specimen containing strong heterogeneities and subjected to a tensile test.

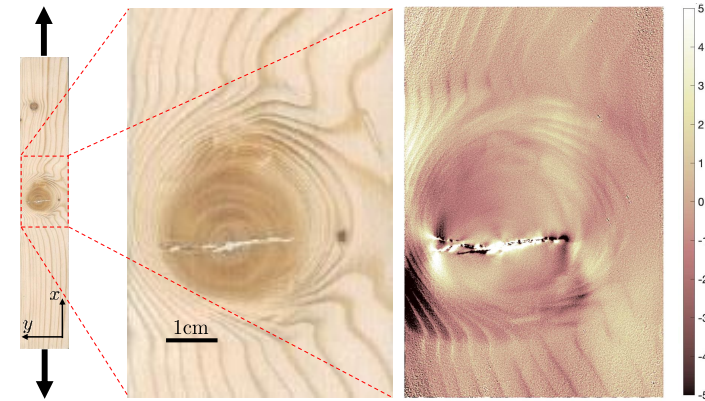


Figure 1: ϵ_{xy} strain map ($\times 10^{-3}$) measured on a wood specimen containing a cracked knot [6]. Number of measuring points forming the map: ≈ 27.5 millions. Computing time on a laptop: 66 s.

The main drawback of checkerboard patterns is the need for a depositing procedure capable of regularly printing dots with only some tens of microns in width. This can be done with a laser engraver, but this tool is expensive, which strongly limits its use. It has been shown recently that checkerboard patterns could also be engraved on the same backing material as that used for electric strain gages. The resulting engraved film can then be bonded and used to measure heterogeneous strain fields on flat specimens. This opens the way for a new type of strain gage [6], which could for instance be used within the framework of Material Testing 2.0 [7].

About the author Michel Grédiac was the founder and head (2003–2010) of the French research network “GDR CNRS 2519: Full-field measurements and identification in solid mechanics” to support the use of full-field measurement techniques in experimental solid mechanics and facilitate collaborative work in this field across France. In 2006, he organized the first international version of the Photomechanics conference in Clermont-Ferrand, France. He is the author/co-author of ≈ 170 papers in international journals and co-authored a book on the Virtual Fields Method. He is a Fellow of the Society for Experimental Mechanics and the recipient of several scientific awards.

References

- [1] G.F. Bomarito, J.D. Hochhalter, T.J. Ruggles, and A.H. Cannon. Increasing accuracy and precision of digital image correlation through pattern optimization. *Optics and Lasers in Engineering*, 91:73–85, 2017.
- [2] M. Grédiac, B. Blaysat, and F. Sur. A robust-to-noise deconvolution algorithm to enhance displacement and strain maps obtained with local DIC and LSA. *Experimental Mechanics*, 59(2):219–243, 2019.
- [3] M. Grédiac, X. Balandraud, B. Blaysat, T. Jailin, R. Langlois, F. Sur, and A. Vinel. Fine-tuning a deconvolution algorithm to restore displacement and strain maps obtained with LSA. *Experimental Mechanics*, 63(9):1509–1537, 2023.
- [4] S. S. Fayad and D. T. Seidl and P. L. Reu. Spatial DIC Errors due to Pattern-Induced Bias and Grey Level Discretization *Experimental Mechanics*, 60:249–263, 2020.
- [5] F. Sur, B. Blaysat, and M. Grédiac. On biases in displacement estimation for image registration, with a focus on photomechanics. *Journal of Mathematical Imaging and Vision*, 63:777–806, 2021.
- [6] A. Vinel, M. Grédiac, X. Balandraud, B. Blaysat, T. Jailin, and F. Sur. Towards strain gauge 2.0. Substituting the electric resistance routinely deposited on polyimide film by the optimal pattern for full-field strain measurement. *Strain*. Online, 2024.
- [7] F. Pierron and M. Grédiac. Towards Material Testing 2.0. A review of test design for identification of constitutive parameters from full-field measurements. *Strain*, 57(1):e12370, 2021.

Understanding the behaviour of a Cu-CuAl functionally-graded alloy using DIC

F.G. Cunha¹, J. Xavier^{1,2}, T.G. Santos^{1,2} and F. Pierron³

¹ UNIDEMI, Department of Mechanical and Industrial Engineering, NOVA School of Science and Technology, Universidade NOVA de Lisboa, 2829-516 Caparica, Portugal;

² LASI, Intelligent Systems Associate Laboratory, 4800-058 Guimarães, Portugal;

³ MatchID NV, Leiekaai 25A, Gent, 9000, Belgium

Abstract — This paper presents a numerical analysis and experimental validation of the behaviour of a Cu-CuAl Functionally Graded Material (FGM). In the inverse identification, the Virtual Fields Method (VFM) was employed to extract material parameters from full-field deformation measurements obtained by Digital Image Correlation (DIC). The FGMs were manufactured using Wire and Arc Additive Manufacturing (WAAM), employing gas tungsten arc welding (GTAW) and gas metal arc welding (GMAW) as heat sources. This study demonstrated the viability of using WAAM for the fabrication of FGMs. The material parameter identification was conducted initially through simulation as a verification process, and subsequently on experimental data. The present research provides the way for the manufacturing and analysis of Cu-CuAl FGM using the WAAM process.

Keywords — FGM, WAAM, DIC, VFM, AM.

Introduction The importance of materials to society has evolved significantly over time [1]. Nowadays, material innovation is increasingly recognised as a key driver of both economic and environmental sustainability [2]. Advanced FGMs are characterised by a gradual variation in composition, microstructure, or properties over their volume, presenting unique features that enhance their performance, durability, and reliability for engineered components and structures [3]. FGMs are created using advanced computational and manufacturing methods, resulting in components with exceptional mechanical properties [4]. This approach, inspired by natural tissues such as bone, teeth, wood, and bamboo, employs a methodology that allows for the creation of gradient patterns [5], facilitating the development of FGMs. Additive manufacturing (AM) represents a revolutionary technology for the production of three-dimensional parts. Some AM processes have been employed to obtain FGM parts in a single step, which represents an advantage over more traditional manufacturing processes [6]. FGM metal components have been manufactured using WAAM in order to identify a manufacturing method that will reduce material costs [7]. In response to the growing prevalence of full-field measurement techniques, such as DIC [8], material parameter identification methods have been proposed. Among the various methodologies, the VFM is an effective approach for the extraction of material parameters from deformation maps [9]. Nevertheless, it is first necessary to define a suitable test configuration [10]. In the case of heterogeneous properties, it is necessary to formulate a suitable parameterisation. This is the subject of the present research.

Numerical Simulation A finite element analysis of the experimental test method was developed to create synthetic data to verify the VFM code and to explore the design space for a suitable test configuration. To describe the material behaviour, a bilinear isotropic hardening plastic model was selected. This elasto-plastic model was built in Ansys Parametric Design Language (APDL). To simulate the heterogeneous elastic constants, two distinct regions were designed in the model. In the transition zone between the two materials, a linear variation of the elastic properties was considered. The numerical data was used to validate the identification procedure. In this analysis, sensitivity-based virtual fields were selected for the VFM. For the elastic constants, the deformation values of the elements were exported

and analysed in a MATLAB software VFM in order to identify the stiffness coefficients. Subsequently, the outcomes were identified and converted to Young's modulus, E , and Poisson's ratio, ν .

Experimental Work The samples were produced through the WAAM process using an inert metal gas (MIG) welding power source PRO MIG 3200 from Kempy and a gas tungsten arc welding (GTAW) power source CITOTIG 315 AC/DC from Oerlikon. The welding parameters, travel speed, wire feed speed, gas flow rate, voltage, electrical current and interpass temperature were defined depending on the material and type of welding used. The FGMs were produced through the deposition of layers on layers. These layers were deposited on an ASTM A36 steel substrate. After some layers had been deposited and cooled, the sample was machined. This machining allowed the production of a sample with a uniform appearance, which could then be applied with a speckle pattern. The wall produced was cut transversally and placed in resin to carry out some characterisation tests of the material. The research involved the study of several FGM specimens with the objective of improving the manufacturing efficiency and accuracy of the current process. In order to overcome specific challenges, such as porosity, defects, cracks and delamination of the layers, it was necessary to develop a solution. Finally, the specimens were tested on an electro-mechanical test machine. In order to acquire images of the specimen during the loading, a setup system for the DIC, comprising cameras, a light source and acquisition software (MatchID), was necessary.

Conclusion This study presents a numerical analysis and experimental validation of the behaviour of a Cu-CuAl FGM. The paper presents the material parameter identification based on simulation first, as verification, then on experimental data. This work reports some initial test results and provides an outlook for the future challenges in this topic.

References

- [1] Ashby, M. *Materials Selection in Mechanical Design*. Butterworth-Heinemann, 2011.
- [2] Naebe, M. and Shirvanimoghaddam, K. Functionally graded materials: A review of fabrication and properties. *Applied Materials Today*, 2016, 5, 223-245.
- [3] Bhavar, V.; Kattire, P.; Thakare, S.; Patil, S.; Singh, R. A Review on Functionally Gradient Materials (FGMs) and Their Applications. 229, 012021, 2017.
- [4] Meng, L. et al. From Topology Optimization Design to Additive Manufacturing: Today's Success and Tomorrow's Roadmap. *Archives of Computational Methods in Engineering*, 27, 805-830, 2020.
- [5] Liu, Z.; Meyers, M.; Zhang, Z.; Ritchie, R. Functional gradients and heterogeneities in biological materials: Design principles, functions, and bioinspired applications. *Progress in Materials Science*, 88, 467-498, 2017.
- [6] Mahamood, R.; Akinlabi, E. *Functionally Graded Materials* 1997.
- [7] Wang, J. et al. Characterization of wire arc additively manufactured titanium aluminide functionally graded material: Microstructure, mechanical properties and oxidation behaviour. *Materials Science and Engineering*, 734, 110-119, 2018.
- [8] Sutton MA, Orteu JJ, Schreier HW Image correlation for shape, motion and deformation measurements: basic concepts, theory and applications. pp 1-321, 2009.
- [9] Pierron F, Grédiac M The Virtual Fields Method. *Springer, Berlin.*, 2012.
- [10] Pierron, F, Grédiac, M. Towards Material Testing 2.0. A review of test design for identification of constitutive parameters from full-field measurements. *Strain*, 57:e12370,2021.

Acknowledgments The authors acknowledge the support of Fundação para a Ciência e a Tecnologia (FCT-MCTES) throughout the project: UNIDEMI – UIDB/00667/2020 and UIDP/00667/2020; TOP&AM4FGM (DOI: 10.54499/2022.06903.PTDC). F.G. Cunha acknowledges the support received under PhD grant 2021.06889.BD (DOI: 10.54499/2021.06889.BD). The authors acknowledge the support of the University of Southampton through the hosting of F.G. Cunha to carry out the experimental tests of this work.

Building simulation models credibility: the role of DIC in a complex structural testing environment

P. Baudoin¹, F. Mathieu¹, N. Swiergiel²

¹ EikoSim, Montrouge, France

² ArianeGroup, Les Mureaux, France

Abstract — Building simulation models credibility is mandatory to justify reducing testing costs and developing innovative structures faster. But increasing model credibility from less test data means building indisputable model validation metrics and toolboxes. This talk will discuss the challenges and benefits of implementing data fusion based on DIC and other measurement devices through the Ariane 6 Dual Launch Structure development.

Keywords — FEA Validation, DIC integration, Structural testing

Introduction

This presentation focuses on the implementation of data fusion techniques to enhance the reliability of building simulation models; particularly, it explores the integration of Digital Image Correlation (DIC) technology for acquiring supplementary test data. The objective is to highlight the application of these techniques through a real-world case study on the large-scale "Dual Launch Structure" (see Figure 1) constructed by ArianeGroup for the Ariane 6 launcher. Through this exploration, we aim to showcase how data fusion and DIC technology can optimize model validation processes, ultimately facilitating the development of reliable simulation models for complex structures.



Figure 1: Ariane 6's Dual Launch Structure (left) and location within the launcher (right)

Methods

In the context of the Dual Launch Structure, data fusion involves amalgamating data from various sources, such as DIC measurements from three separate systems, strain values from approximately 200 strain gauges, strain profiles obtained from fiber optics measurement, as well as force and displacement measurements from dozens of sensors (see Figure 2).

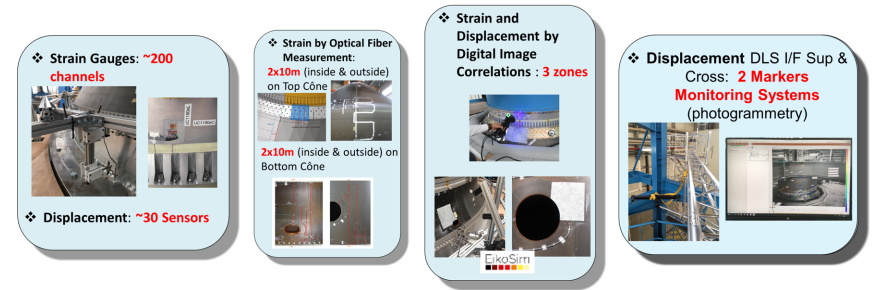


Figure 2: Instrumentation for the Dual Launch Structure test.

The main challenge in assembling these datasets onto the simulation model resided in the fact that these test datasets were not originally well aligned with a 3D model, or synchronized with original simulation predictions. This is the case for DIC data, as well as point-wise or linear data such as strain gauges or fiber optics. FE-based Stereo-DIC [1] was used to facilitate DIC integration to the FEA tool base.

Finally, resource constraints, such as limited time, budget, and computational power, impose challenges in efficiently utilizing available resources for model validation: traditional spreadsheet-based FEA validation can be extremely long to set up in the case of large test datasets, and most of the test data is often discarded.

Results and Conclusion

Through collaborative efforts and a "Smart testing" framework, challenges in validating complex structures were effectively addressed, resulting in an overall validation of the FEA model for future test-less developments.

Having a data fusion framework facilitated the integration of disparate datasets, offering a comprehensive understanding of the structure's behaviour. DIC technology, as well as optical fibers and more traditional sensors, provided detailed insights into structural deformation, validating simulation predictions and identifying areas for optimization.

Key lessons include the importance of robust data preprocessing and convenient tools to aggregate datasets coming from different sources to a 3D model. These insights will guide future endeavours in building simulation models for the DLS, but also ensuring the development of reliable validation methodologies for complex structures in general.

References

- [1] L. Dubreuil, J.-E. Dufour, Y. Quinsat, F. Hild, Mesh-Based Shape Measurements with Stereocorrelation, *Experimental Mechanics*, Volume 56, pages 1231-1242, 2016.

Investigation of the dissipative mechanisms in 3D layer-to-layer woven composite under cyclic loading

V. Le Saux¹, L. Navrátil^{1,2}, N. Carrere¹, S. Leclercq², Y. Marco¹

¹ ENSTA Bretagne – Institut de Recherche Dupuy de Lôme (IRDL), UMR CNRS 6027, Brest, France
² Safran Landing Systems, Vélizy, France

Abstract — This article discusses techniques that aim at facilitating the identification of dissipative mechanisms activated in woven composites under cyclic loadings. The focus is put on the post-processing of thermal measurements performed with a cooled infrared camera. Various effects that may have an influence on the results are discussed and taken into account the processings. Several thermal indicators are proposed that can be used to characterize various phenomena useful for understanding and modelling purposes.

Keywords — infrared thermography, motion compensation, cyclic loadings, 3D woven composite

Introduction The characterization of the thermal effects under cyclic loading is more and more used as it can provide precious information regarding the analysis of the deformation processes [1] or the rapid characterization of the fatigue properties [2]. In the context of fatigue characterization and design, it is necessary to separate the numerous heat sources (viscoelasticity, plasticity, damage, friction, etc.) as they do not all play a role on the fatigue properties. This article presents post-processing techniques that aim at facilitating the identification of these dissipation sources under cyclic loadings. The use of these techniques is illustrated on a layer-to-layer woven composite material.

Methods The temperature measurements were carried out with a cooled InSb InfraTec ImageIR 10300 camera. The Focal Plane Array is a matrix of 1920×1536 detectors sensitive in the $(3.6-4.9) \mu\text{m}$ spectral range. A classic 50 mm lens was used for most of the tests and a Mx1 lens was used for measurements at small scale. For this lens, a compensated pixelwise calibration was used to improve the thermal accuracy of the camera [3]. A high emissivity paint was applied prior to the test over the gauge length of the specimen. Low emissivity markers were applied to delimitate the gauge length of the specimens and were used to track and compensate the motion for each frame using an affine transform. A servo-hydraulic testing machine was used to apply a heat build-up loading protocol applies a set of loading steps of increasing stress amplitude to the tested specimen [4]. This stress amplitude is held constant during each step. The load ratio R_σ was set to 0.05 and the mechanical frequency was so to 2 Hz.

Infrared data processing As a pixel on the infrared image is not a particle of matter due to local displacement, artefacts can be generated during the post-processing stage. It is important to compensate for it prior to the data post-processing. A procedure described in [4] has been used systematically. The data were then analyzed using a homemade software [5] and several indicators were extracted (Figure 1): the first harmonic, which is related to thermoelasticity, the cyclic dissipation, evaluated from the initial slope of the temperature rate $\dot{\theta}_0$ [6], and the second harmonic (also called as the $2 \times f$ component). These maps were evaluated using a pixelwise fit, discrete fourier transform or the lock-in technique [7]. They are related to different heat sources, and their signification will be discussed in the presentation, supported by microstructural observations and numerical simulations.

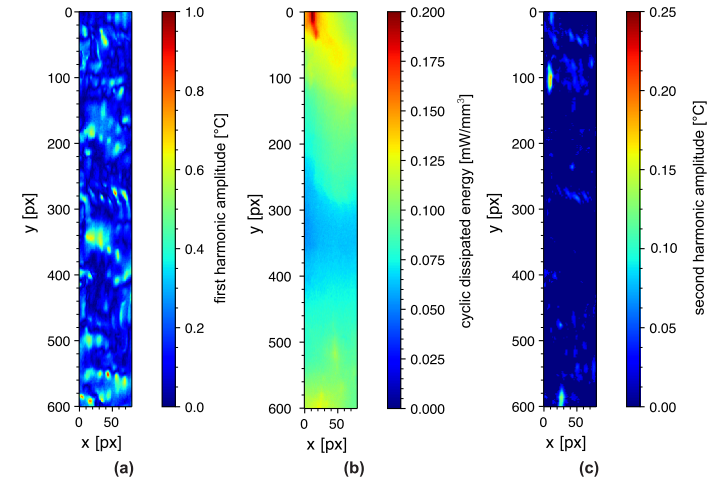


Figure 1: Example of infrared imaging results: (a) first harmonic amplitude, (b) cyclic dissipation and (c) second harmonic amplitude (also called $2 \times f$ amplitude).

Conclusion Infrared thermography appear to be a valuable tool to investigate the thermal effects under cyclic loading of 3D layer-to-layer composite materials. Various post-processings were proposed to extract useful indicators and try to separate the numerous heat sources at stake. Some of these indicators are sensitive to relative motion during the loading and motion compensation techniques were applied to each frame of the records prior to the application of the post-processings. Complex maps can then be obtained on 3D layer-to-layer composite. These maps are precious for understanding and modelling purposes of the studied material.

References

- [1] A. Chrysochoos and A. Louche. An infrared image processing to analyse the calorific effects accompanying strain localisation. *Int. J. Eng. Sci.*, 38:1759–1788, 2000.
- [2] L. Leveuf, Y. Marco, V. Le Saux, L. Navrátil, S. Leclercq and J. Olhagaray. Fast screening of the fatigue properties of thermoplastics reinforced with short carbon fibers based on thermal measurements. *Polymer Testing*, 68:19–26, 2018.
- [3] V. Le Saux and C. Doudard. Proposition of a compensated pixelwise calibration for photonic infrared cameras and comparison to classic calibration procedures: Case of thermoelastic stress analysis. *Infrared Physics & Technology*, 80:83–92, 2017.
- [4] L. Navrátil, V. Le Saux, S. Leclercq, N. Carrere and Y. Marco. Infrared image processing to guide the identification of damage and dissipative mechanisms in 3D layer-to-layer woven composites *Applied Composite Materials*, 29:1449-1477, 2022.
- [5] V. Le Saux Celenos. *Zenodo*, <https://doi.org/10.5281/zenodo.10925713>.
- [6] L. Navrátil, N. Carrere, V. Le Saux, Y. Marco and S. Leclercq. Influence of thermal diffusion on thermoelastic coupling and dissipated energy fields evaluated in the heterogeneous case of a woven composite *Composite Structures*, 308:116711, 2023.
- [7] O. Breitenstein, W. Warta, and M. Langenkamp. *Lock-in Thermography - Basics and Use for Evaluating Electronic Devices and Materials*, Springer, Berlin, 2010.
- [8] L. Navrátil, V. Le Saux, Y. Marco, Z. Aboura, W. Harizi, C. Cuniberti, N. Carrere and S. Leclercq. Understanding the damage mechanisms in 3D layer-to-layer woven composites from thermal and acoustic measurements *Journal of Composites Materials*, 56:1559-1575, 2022.

Localized Deformation and Band Formation in Superelastic Nitinol Wires

P. Shabani Nezhad¹, J.A. Moore¹, D. Erdeniz²

¹Department of Mechanical Engineering, Marquette University, Milwaukee, Wisconsin, United States

²Department of Mechanical and Materials Engineering, University of Cincinnati, Cincinnati, Ohio, United States

Abstract

Martensitic phase transformations in superelastic nitinol are known to be accompanied by the accumulation of microstructural damage. While previous studies have explored the heterogeneous nature of these transformations, the factors influencing the accumulation of the localized permanent damage are not well understood. In this research, a digital image correlation (DIC) technique was employed to analyze localized deformation and residual strain at the macro-scale level. The experimental results revealed that the band formation, annihilation, and coalescence play a significant role in the heterogeneous damage accumulation in superelastic nitinol.

Keywords – Nitinol, superelasticity, martensitic transformation, localized damage, DIC.

Introduction Superelastic nitinol wires are of significant interest in medical, dental, automotive, and aerospace industries due to their reversible martensitic transformation under specific temperature and stress conditions [1]. Though theoretically fully recoverable, cycling leads to superelastic degradation and residual martensite formation [2]. While previous studies have examined martensitic transformation and local defect accumulation, factors affecting localized permanent damage are not well understood [3]. We hypothesize that martensite band formation, annihilation, and interaction affect local residual strain and subsequent transformations. This research analyzes changes in local deformation and residual strain using a 3-D DIC technique to evaluate phase transformation and martensite band behavior.

Methods Medical grade superelastic nitinol wires (1-mm diameter) from Edgetech Industries were tested. The A_r temperature was reported as 0-10°C by the manufacturer. Initial load/unload tests determined the wire's upper and lower plateaus using a Mark10-ESM750 tensile test stand. DIC data was collected using a Leica M-125C microscope with Dantec cameras and analyzed with Istra4D V4.7 software. Wires, approximately 25 mm long, were painted white and speckled with black patterns for DIC measurement. Tested under displacement-controlled conditions at 0.1 Hz, DIC images were collected continuously until the end of the 10th cycle and then at the 30th, 100th, and 500th cycles.

Results Figure 1(a) shows the first cycle of the as-received wire fatigued under displacement-controlled conditions at 0.1 Hz. Figure 1(b) details the progression of the DIC strain field distribution along the wire at points 0-9. Frame 0 shows the initial state of the wire. The first martensite band nucleated at Point 1, causing a drop in load. The band grew in both directions with increasing load, but at the cycle's maximum (Point 4), an area at the bottom did not transform, stopping the A/M interface.

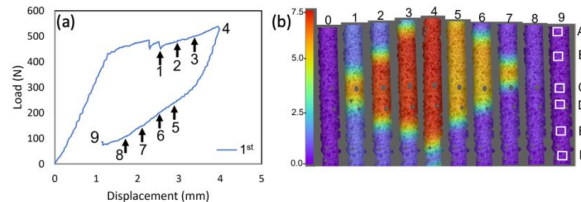


Figure 1: (a) Load vs displacement during the 1st cycle, (b) progression of the strain distribution along the length of wire at the points 0-9 in as labeled in (a)

Figure 2(a) shows the last frame of cycles 1-10. Figure 2(b) exhibits the evolution of residual strain in selected areas at each cycle's end. After the 1st cycle, area "E" (where the A/M interface stopped) had the highest, and area "F" (non-transforming) had the lowest residual strain. By the 2nd cycle, the non-transforming region shifted near area "C," and area "F" began increasing in residual strain. Residual strain accumulation stabilized after initial cycles, with area "C" showing the least strain by the 10th cycle, while other areas approached 0.9%.

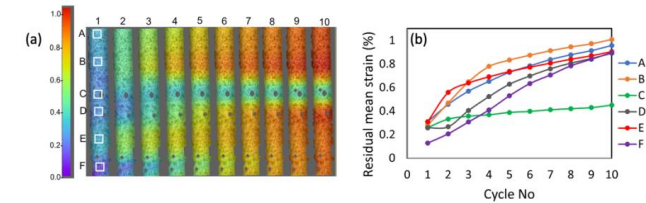


Figure 2: (a) The last frames of the cycles 1-10 and 6 selected areas, (b) the residual mean strain of each area at the end of the cycles 1-10.

Figure 3(a) shows that the coalescence of unsaturated martensite bands didn't result in high residual strain. The 30th cycle left the highest residual strain near areas "A", "B", and "F". Despite A/M interfaces stopping near areas "B" and "D", area "B" had higher defect accumulation. Figure 3(b) represents the band formation pattern for the 30th and 100th cycles. By Cycle 500, Figure 3(c) indicated that residual strain no longer followed the martensite pattern, showing a shift towards plasticity surpassing superelasticity due to defect accumulation.

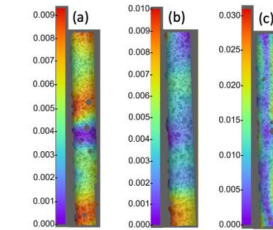


Figure 3: Residual strain of the cycles (a) 30, (b) 100, (c) 500.

Discussion and Conclusion The accumulation of localized defects during the early cycles provided activation energy for further martensite band nucleation. With repeated cycling, the critical strain level required for band nucleation increased while the plateau stress decreased. Areas where the austenite/martensite interface stopped exhibited relatively high residual strain, making them more susceptible to new martensite band formation. The coalescence and annihilation of bands resulted in localized defect accumulation, correlating higher levels of martensite band saturation with increased localized defects. This research investigated localized damage in superelastic nitinol wire during cyclic loading using a 3D DIC system. The study found that macroscopic band patterns stabilize after initial cycles, with localized defects accumulating, providing energy for further martensite band nucleation.

References

- [1] R. Chaudhari, J.J. Vora, D.M. Parikh. A review on applications of nitinol shape memory alloy. In *Proceedings of ICRAM 2020*, pages 123–132, 2021.
- [2] O. Molnárová, P. Šittner, J. Veselý, M. Cieslar. TEM analysis of deformation bands created by tensile deformation of superelastic NiTi wires. *Materials Characterization*, 167: 110470, 2020.
- [3] L. Zheng, Y. He, Z. Moumni. Investigation on fatigue behaviors of NiTi polycrystalline strips under stress-controlled tension via in-situ macro-band observation. *International Journal of Plasticity*, 90: 116–145, 2017.

DIC data integration to achieve multi-measurement system on full-scale wing tests

E. Rolfe

Airbus Operations Ltd., Pegasus House, Aerospace Avenue, Filton, Bristol, BS34 7PA, UK

Abstract – Smarter Testing aims to develop a novel test process for airframe structures where dependence on physical testing is reduced in favour of virtual testing. High quality measurement data, including DIC data, from the physical tests that are retained will be critical for validating virtual simulations. This article summarises two aircraft structural tests where DIC and other measurement techniques have been deployed and integrated to enable informed live decision making, improve the efficiency of physical testing and advance methods for data correlation.

Keywords – DIC, Aerospace, Structures Testing

Introduction

Smarter Testing (an ATI funded project) aims to develop a novel test and certification process for airframe structures to align with future ambitions for new aircraft programmes.

A key project aim is to promote virtual testing as a validated certification means of compliance to reduce dependence on expensive and time-consuming physical testing. To achieve this aim, virtual testing simulations require validation and increased credibility. Capturing high quality measurement data during physical tests that are performed is critical in order to validate simulations and build this required credibility. Typically a variety of measurement techniques are selected to gain the necessary high quality data and to optimise data capture from physical tests. The choice of measurement technique depends on the quantity of interest, component geometry, load profile and other parameters. Digital Image Correlation (DIC) plays a significant role as it is highly adaptable and full-field. However, DIC is just one of the techniques being deployed within Smarter Testing.

Furthermore, measurement techniques are typically perceived as stand-alone. Measurement data is frequently captured in isolation on dedicated software and compared with simulations during post-processing, often only qualitatively. Integration of the DIC data with results from other measurement techniques into a common environment is a key project outcome. When achieved live this will enable informed live decision making, for example to shutdown if a critical threshold is surpassed and identify which region of the specimen surpassed the threshold (test protection and condition led inspection). This will lead to more efficient inspection intervals, reduced shutdown time and ultimately reduce the time and cost associated with physical testing. Post-test, data within a common environment will improve the efficiency of correlation against simulations.

This article summarises two aircraft structural tests (level 4 on the test pyramid), where a suite of measurement systems have been simultaneously deployed and resulting measurement data integrated to the full extent of each system's capability. These trials have been performed in preparation for a full-scale 17 metre static wing test (level 2), where all aspects of the novel test and certification methods being developed within Smarter Testing will be demonstrated.

Methods and Results

The first specimen was a five stringer composite panel from a wing structure that was subjected to compression loading. The goal was to progressively grow damage from a seeded defect within the specimen under increasing loads, whilst preventing catastrophic final failure. The damage size was evaluated using ultrasonic inspection between load cases for comparison with simulations. A 3D DIC system and an Acoustic Emission (AE) system were deployed on the specimen. Both measurement systems were synchronised with the machine control system. During loading, test protection decisions were successfully made based on live AE hits (intensity and location). Ultrasonic inspection confirmed damage initiation, growth and location which correlated with AE location results. A post-processing

method to visualise both measurement data sets within Zeiss Inspect Correlate software was developed. This significantly improved efficiency of data correlation and revealed interdependencies between the AE, DIC and strain second derivatives. The ambition is to enable live overlay of AE and DIC data to provide test operators with a more informed picture from which to make test protection decisions for the full-scale static wing test.

The second specimen is a 5 metre scaled wing demonstrator, shown in Figure 1, specifically designed as a test bench for the Smarter Testing project. Two 3D DIC systems were mounted above the speckled upper surface of the specimen on truss structures at an optimised stand-off distance. DIC reference point markers were positioned around the specimen on rigid structures to enable multi-system post-processing. Laser tracker nests were adhered to datums on the specimen itself to establish the specimen position within the global referencing network and to measure key specimen dimensions. The laser tracker Spherically Mounted Retroreflectors (SMRs) were removed from the nests and replaced with bespoke hemispherical DIC reference point markers. This enabled the DIC systems to track the networked points during dynamic load steps at a rate that the laser tracker was unable to achieve. The displacement of these points and other component regions were streamed live from the DIC system over a local network into the Data Acquisition (DAQ) system. This live stream was monitored on the DAQ system and pushed to the common environment (3DExperience) for live remote viewing and analysis. Live comparisons of DIC displacement versus Linear Variable Differential Transformers (LVDTs) and simulation data were performed. This live data feed revealed a discrepancy between DIC displacement and one LVDT allowing for targeted inspection, and efficient troubleshooting.

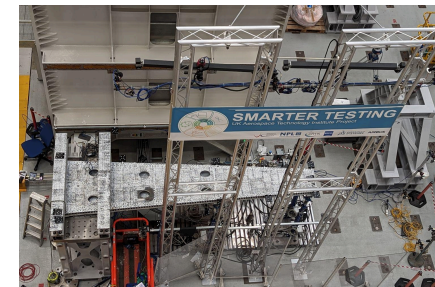


Figure 1: Scaled Wing Demonstrator

Discussion and Conclusion

These lower level tests have helped to identify and overcome limitations associated with integrating multiple measurement techniques. The live data streams have demonstrated the added value of test protection and condition led inspection. Although the scaled wing demonstrator only had 4 LVDTs from which to identify the one with a fault, when scaling up to a full-scale wing test with many more LVDTs the true benefits of this capability will be realised. Furthermore, the tests have been used to challenge the current capabilities of the measurement systems and confirm the most suitable technique to address each measurement requirement.

The scaled wing demonstrator has aided with addressing some of the physical challenges posed by the ambition of capturing the displacement of the entire upper surface of the full-scale 17 metre wing using DIC. The expected deflection of the wing tip during the failure case has led to the design of a remotely operated moving camera system to maintain the surface within an acceptable depth of view. This moving camera system will undergo trials ahead of deployment on the full-scale test.

Acknowledgements

This work was carried out as part of the Smarter Testing project (Innovate UK, Contract: D20016286).

Investigating heterogeneous strain-induced crystallization in natural rubber with infrared thermography based micro-surface calorimetry

J.-B. Le Cam, A. Tayeb, S. Charlès

Institut de Physique de Rennes UMR 6251 CNRS/Université de Rennes, Campus de Beaulieu, Bât. 10B, 35042 Rennes Cedex, France.

Abstract — Infrared thermography based micro-surface calorimetry is used to detect and characterize heterogeneities in the strain-induced crystallinity field in elastomers submitted to homogeneous loadings at the macroscopic scale. The results obtained provide the first evidence of strain-induced crystallization (SIC) heterogeneity under a homogeneous loading, which could be explained by strain/stress concentrations at the macromolecular scale.

Keywords — Infrared thermography, Surface calorimetry, Heterogeneous SIC, Natural rubber.

Introduction The strain-induced crystallization (SIC) is considered as the phenomenon responsible for the extraordinary properties of natural rubber (NR). Up to now, macroscopic heterogeneities in the crystallinity field are assumed to be due to the mechanical state, i.e. the strain state and level, not to other factors. As a consequence, if the strain field is homogeneous, so is considered the macroscopic crystallinity field. Macroscopic SIC heterogeneities as well as memory effects under homogeneous strain states have therefore never been investigated at the macroscopic scale in the literature. This is the aim of the present study.

Determining the strain-induced crystallinity from quantitative surface calorimetry The test conditions enabled us to apply the "OD" formulation of the heat diffusion equation [1]:

$$\rho_0 C \left(\dot{\theta} + \frac{\theta}{\tau} \right) = \hat{S}. \quad (1)$$

with ρ_0 the initial density, C the heat capacity, θ the temperature variation, τ a parameter driven by the heat exchange with the specimen outside. The heat source due to SIC is deduced by subtracting the heat source predicted for the third cycle, which is a thermodynamical cycle, from the total heat source. The equivalent temperature variation T_{cryst} can then be determined from the integration of the heat source due to SIC over time, and assuming that it is equal to 0 before the crystallization starts. The crystallinity χ , which is the volume fraction of crystallites, is deduced from T_{cryst} and the fusion enthalpy ΔH_{cryst} as follows:

$$\chi(t) = \frac{\rho C_p T_{cryst}(t)}{\Delta H_{cryst}} \quad (2)$$

The method has been validated by comparing with the X-ray technique in [3].

Experimental set-up An unfilled natural rubber provided by The "Manufacture Française des pneumatiques Michelin" is considered. The specimens were stretched symmetrically. Three load-unload uniaxial tensile cycles were carried out at a maximum stretch of 7 and a loading rate of 300 mm/min. Temperature measurement was performed by using a cooled high-resolution FLIR X6540sc infrared camera. The surface emissivity was set at 0.94, according to the measurements on a similar material in [4].

Results The crystallinity has been evaluated along profiles at the specimens' middle. The profiles include 14 measurement points (IR pixels), uniformly distributed along the specimen's width. Figure 1

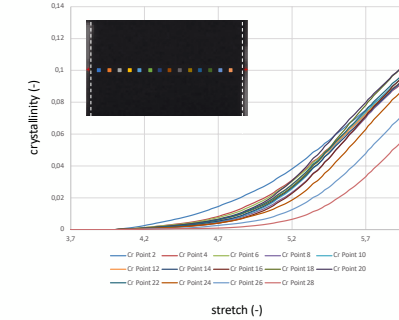


Figure 1: Crystallinity along the profile in the middle section (specimen NR_{1,6}L).

illustrates the crystallinity determined at the 14 measurement points for a given specimen. In order to visualize the distribution of the crystallinity along the profile during the test, the crystallinity profiles have been plotted for each specimen at increasing global stretches. This will be further detailed in the presentation.

Discussion and conclusion For stretches inferior to the SIC onset, the heat sources at each measurement points are almost superimposed for each specimen. Once the SIC onset is exceeded, the heat sources evolve differently from one point to another. In terms of crystallization, either its rate is different, or its onset is different, or both. These results show that heterogeneous SIC can take place while the macroscopic strain field is homogeneous, which obviously justifies taking precautions to analyze the results issued from only one measurement point or averaged over a large zone in a specimen.

References

- [1] A. Chrysochoos. Analyse du comportement des matériaux par thermographie infra rouge. In *Colloque Photomécanique*, volume 95, pages 201–211, 1995.
- [2] Donald E. Roberts and Leo Mandelkern. Thermodynamics of crystallization in high polymers. natural rubber. *Rubber Chemistry and Technology*, 28(3):718–727, 1955.
- [3] J B. Le Cam, P.-A. Albouy, and S. Charlès. Comparison between x-ray diffraction and quantitative surface calorimetry based on ir thermography to evaluate strain-induced crystallinity in natural rubber. *Review of Scientific Instruments*, 91:044902, 2020.
- [4] S. Charlès and J.-B. Le Cam. Inverse identification from heat source fields: a local approach applied to hyperelasticity. *Strain*, <https://doi.org/10.1111/str.12334>, 2020.
- [5] J.-M. Chenal, L. Chazeau, L. Guy, Y. Bomal, and C. Gauthier. Molecular weight between physical entanglements in natural rubber: A critical parameter during strain-induced crystallization. *Polymer*, 48:1042–1046, 2007.
- [6] S. Trabelsi, P.A. Albouy, and J. Rault. Crystallization and melting processes in vulcanized stretched natural rubber. *Macromolecules*, 36(20):7624–7639, 2003.
- [7] J.-B. Le Cam. Energy storage due to strain-induced crystallization in natural rubber: the physical origin of the mechanical hysteresis. *Polymer*, 127:166–173, 2017.

Strength characterisation of Nicrofer—Stellite joint using Digital Image Correlation

Rajat R. Pawar¹, N. Niyan Thiruselvam¹, Kiran D. Mali¹, D. M. Kulkarni¹, Biswajit Das¹, R. Jeyaraam², G. Pavan Kumar³

¹Department of Mechanical Engineering, BITS Pilani, K. K. Birla Goa Campus, Goa 403726, India.
²Diffusion, NAND Technology Integration, Micron Semiconductor Asia Pte Ltd., Singapore.
³Pruna industries Private Limited, Nellore 524121, India.

Abstract — An additive manufacturing technology called Direct Laser Deposition (DLD) powered by laser is commonly used for joining dissimilar materials because it leads to a smaller heat-affected zone than other material joining technologies. In the context of repair welding of expensive parts, it offers cost savings too. Several studies in the literature have used scanning electron microscope (SEM) to characterize DLD bimetal. Nevertheless, less attention has been paid to revealing the deformation heterogeneity in DLD bimetal using full-field deformation measurement techniques. We solve this problem by using Digital Image Correlation (DIC). A bimetal joint is created by fusing Stellite (a Co—Cr alloy) on to Nicrofer (a Ni—Cr—Mo alloy) through DLD. Standard test specimens are prepared and subjected to uniaxial tensile tests upto failure by fracture. Stellite is centered in the gauge area of the test specimens and runs through the specimen thickness. Using SEM, the changes in grain morphology and material composition are traced to identify four distinct domains. They are unaffected Nicrofer (D1), heat-affected Nicrofer (D2), transition zone (D3) and Stellite (D4). Full-field von Mises strain (E_v) maps are superimposed with the domain interfaces. Localized peaks in E_v are observed over D1—D2 interfaces even at the early stages of deformation. At the later stages, there is a steep reduction in the spatial distribution of E_v from D2—D3 to D3—D4 interfaces. D4 deforms less than the other domains. Further investigation is underway to corroborate DIC strain maps with post deformation microstructure.

Keywords — Additive Manufacturing, Tensile test, Full-field deformation, DIC, SEM.

Introduction Over the years, Additive Manufacturing (AM) is used not only for rapid prototyping but also to fabricate end-use parts since it is more suitable for mass customization (i.e. large-scale production of custom-made products) than the conventional manufacturing processes [1, 2]. An AM technology called laser cladding is commonly used for depositing coatings and repairing an existing product in function [4]. In the context of repair welding of expensive parts, laser cladding offers cost savings too. Among all clad metals, a Co-Cr hard-facing alloy called Stellite stands out due to its high strength, hot hardness, and resistance to wear, corrosion, and oxidation [5, 6]. A deformation study conducted using test coupons extracted from clad joints would provide useful insights on the mechanical behavior of the resulting bimetal joint. In this work, we use Digital Image Correlation (DIC) to collect full-field maps of von Mises strain to characterise the strength of Nicrofer—Stellite joint prepared by laser cladding.

Methods First, a bimetal was fabricated through laser cladding by depositing Stellite on to a Nicrofer plate. ASTM standard E8M sub-size dog-bone specimens were cut from the bimetal plate such that Stellite exists only at about the center of the gauge area and spans through the specimen thickness as depicted in Fig. (1). Electron backscatter diffraction (EBSD) and energy dispersive spectroscopy (EDS) scans were performed on the specimen gauge area to characterize the undeformed tensile specimen. Four distinct domains were identified. They are unaffected Nicrofer (D1), heat-affected Nicrofer (D2), transition zone (D3) and Stellite (D4). Next, the tensile specimens were painted to create a speckle pattern, as typically seen in the Digital Image Correlation (DIC) experiments, and subjected to standard

uniaxial tensile test. The images of the speckled test specimen were collected using a DIC system, composed a full-frame DSLR camera (Canon 6D Mark II) coupled to a Canon 50mm macro lens. The images were processed through an inhouse 2D DIC software. Full-field von Mises strain (E_v) maps were superimposed with the domain interfaces to study the evolution of strains in each domain.

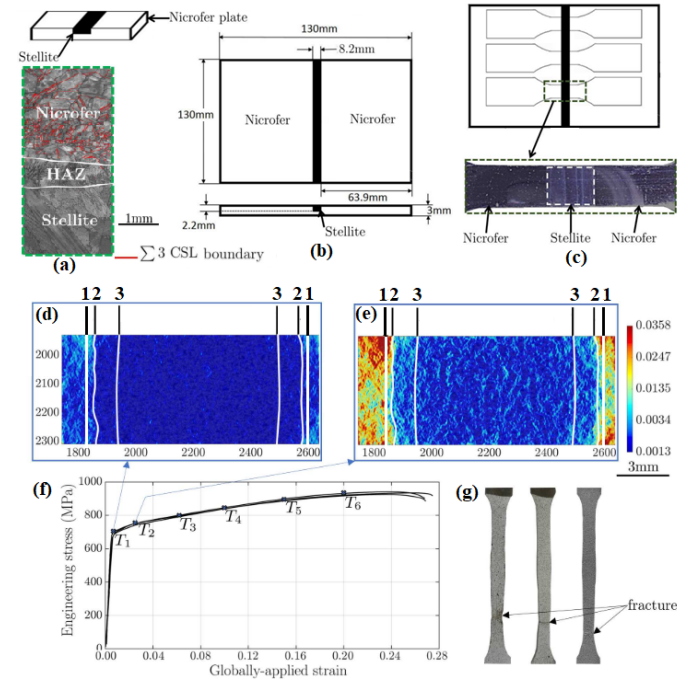


Figure 1: Strength characterisation was done on dog-bone specimens (c) cut from a plate (b) to obtain strain maps (d and e) that correspond to six different stages of deformation $T_1 \dots T_6$ in the tensile curve (f). The failed specimens (g) show ductile fracture far away from the clad region [see EBSD map in (a)].

Results and Conclusion Localized peaks in E_v are observed over D1—D2 interfaces even at the early stages of deformation as depicted in Fig. (1). At the later stages, there is a steep reduction in the spatial distribution of E_v from D2—D3 to D3—D4 interfaces. D4 deforms less than the other domains. Further investigation is underway to corroborate DIC strain maps with post deformation microstructure.

References

- [1] F.S. Fogliatto, J.C. Giovanni (Ed.), *Additive manufacturing for mass customization*, in: *Mass customization*, Springer, New York, NY (USA), 2011.
- [2] R.K. Chen, Y.A. Jin, J. Wensman, A. Shih, Additive manufacturing of custom orthoses and prostheses—A review. *Additive Manufacturing*, 12 (A):77–89, 2016.
- [3] I. Gibson, D. Rosen, B. Stucker, *Additive manufacturing technologies 3D printing, rapid prototyping, and direct digital manufacturing*, Springer, New York, NY (USA), 2015.
- [4] E. Toyserkani, A. Khajepour, S.F. Corbin, *Laser cladding*, CRC Press, 2004.
- [5] R. Kaul, P. Ganesh, M.K. Tiwari, A.K. Singh, P. Tripathi, A. Gupta, A.K. Nath, Laser assisted deposition of graded overlay of Stellite 6 on austenitic stainless steel. *Lasers in Engineering*, 12 (3):207–225, 2002.
- [6] P. Bendeich, N. Alam, M. Brandt, D. Carr, K. Short, R. Blevins, C. Curfs, O. Kirstein, G. Atkinson, T. Holden, R. Rogge, Residual stress measurements in laser clad repaired low pressure turbine blades for the power industry. *Materials Science and Engineering: A*, 437 (1):70–74, 2006.

Full Field Imaging and Data Fusion for Substructural Testing

R. Cappello¹, T. Laux¹, J. S. Callaghan², G. Ólafsson¹, S. W. Boyd³, D. A. Crump³, A. F. Robinson³, O. T. Thomsen¹, J. M. Dulieu-Barton^{1,3}

¹Bristol Composites Institute, Faculty of Engineering, University of Bristol, Queen's Building, University Walk, Bristol, BS8 1TR, UK, ²Bangor University, Bangor, Gwynedd, LL57 2DG, UK, ³School of Engineering, Boldrewood Innovation Campus, University of Southampton, Southampton, UK

Abstract – Digital Image Correlation and Thermoelastic Stress Analysis are used to capture the complex deformation of a Wind Turbine Blade (WTB) subcomponent, tested in a novel multiaxial test set-up. A Finite Element (FE) model of the test is built, and numerical and experimental datasets are combined employing Full-Field Data Fusion, which allows the identification of discrepancies between model and experiment and enables refining of the model and the experiment. This iterative process is demonstrated on a steel specimen prior to the application to the high-value composite WTB subcomponent.

Keywords – Subcomponent testing, Digital Image Correlation (DIC), Thermoelastic Stress Analysis (TSA), Finite Element Analysis (FEA), Full-Field Data Fusion (FFDF)

Introduction Testing large structures for certification and validation presents significant challenges. Conventional methods tend to be both time and cost-intensive, and they may not fully capture all stress states and potential failure modes encountered throughout the in-service life of a structure. Full-field imaging techniques such as Digital Image Correlation (DIC) and Thermoelastic Stress Analysis (TSA) to subcomponent testing can be fused with Finite Element (FE) modelling in a process known as Full-Field Data Fusion (FFDF) [1]. The procedure provides rich datasets that has the potential to reduce the amount of testing required for development and certification by improving confidence in modelling and paving the way to virtual testing. The main challenges are associated with the application of full-field imaging techniques to large structures testing and the correct integration with model results. In this work, the potential of the FFDF in the integrated testing and modelling of a Wind Turbine Blade (WTB) subcomponent is explored, and some best practices identified for the full field imaging of large structures.

Methods The tested subcomponent is a WTB spar cap to web T-joint. Representative load case are defined starting from realistic substructural loads derived from a full-scale FE model of the blade, as shown in Fig. 1 (a). The multiaxial custom testing rig shown in Fig. 1 (b) is employed to apply the representative service load: two vertical actuators apply bending and compression in the flange and the web, while a third horizontal actuator allows the application of shear loading in the web. Tests are conducted using the Structures 2025 facility in the Large Structures Testing Laboratory (LSTL), part of the National Infrastructure Laboratory, at the University of Southampton. The analysed region of interest (ROI) is constituted by the web and flange regions, as shown in Fig. 1 (c). The ROI was prepared applying a white random speckle pattern, through a computer generated laser cut stencil, over a spray-painted black base coat. The final imaging system is shown in Fig. 1 (d). Two DIC stereo pairs were employed to image separately web and flange: the short standoff distance and the large field of view required the use of short focal length lenses (12.5 mm and 25 mm). MatchID [2] software was used for image capturing and processing. A cooled sensor Telops infrared camera was used to capture the stress induced temperature variations for the TSA. Actions to remove the effect thermal distortions caused by convection from heat sources in the measurement space were taken that included, thermal shields, fans and strobe lights synchronised with the DIC triggerbox. Experimental data were fused with a numerical model of the experiment, generated in the commercial FE software Abaqus. The ‘DIC levelling’ approach proposed in [3] has been employed to produce synthetic DIC results from the FE displacements, addressing inconsistencies between the DIC and FE data, and enabling quantitative full-field data comparison. Also, both adiabatic and non-adiabatic [4] thermal numerical solutions are considered for the fusion with the TSA experimental results.

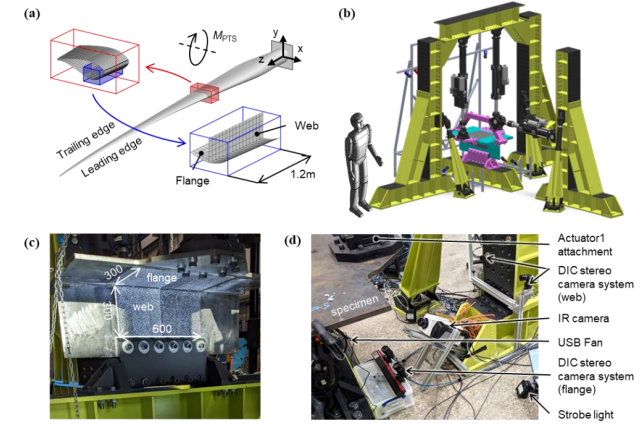


Figure 1: a) Definition of the subcomponent; b) Multiaxial test rig; c) Steel specimen in the testing machine and analysed ROI; d) Imaging equipment. [5]

Discussion and Conclusion The FFDF provides histograms from the pointwise subtraction of the numerical and experimental datasets [1]. The first iteration of the FFDF showed a mismatch between the experimental and FE data, that was attributed to a distortion in the web region of the specimen caused during manufacture that was not included in the initial model. The FFDF with the updated model enabled an assessment and quantification of the improvements resulting from the change of the geometry of the model. Figure 2 shows an example of the initial and updated DIC full-field data fusion histograms.

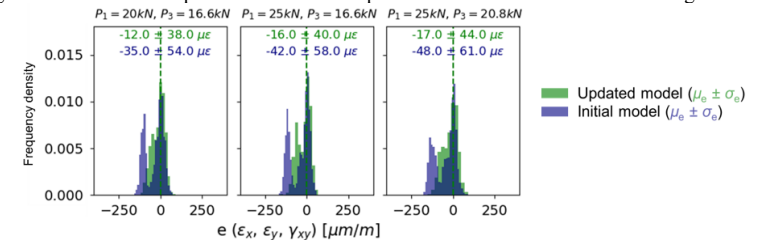


Figure 2: Examples of histograms for quantification of model's improvement for different load cases.

Full-field data fusion constitutes an effective tool in highlighting differences between the experimental and FE datasets, quantifying the impact of improvements made. However, obtaining good quality DIC data in large structural testing poses significant challenges, primarily due to thermal errors resulting from heat convection and the susceptibility of short focal lenses to temperature changes.

References

- [1] J. S. Callaghan, D. Crump, A. S. Nielsen, O. T. Thomsen, and J. M. Dulieu-Barton, “Quantitative Full-Field Data Fusion for Evaluation of Complex Structures,” *Exp Mech*, no. 0123456789, 2023, doi: 10.1007/s11340-023-00973-8.
- [2] “MatchID.” [Online]. Available: <https://www.matchid.eu/>
- [3] P. Lava, E. M. C. Jones, L. Wittevrongel, and F. Pierron, “Validation of finite-element models using full-field experimental data: Levelling finite-element analysis data through a digital image correlation engine,” *Strain*, vol. 56, no. 4, pp. 1–17, 2020, doi: 10.1111/str.12350.
- [4] R. Cappello, G. Pitarresi, and G. Catalanotti, “Thermoelastic Stress Analysis for composite laminates: A numerical investigation,” *Compos Sci Technol*, vol. 241, Aug. 2023, doi: 10.1016/j.compscitech.2023.110103.
- [5] T. Laux et al., “Testing of a wind turbine blade spar cap to web joint subcomponent subjected to multiaxial loading,” in 23rd International Conference on Composite Materials (ICCM23), Belfast, 2023.

Infrared Thermography Applied to In-Situ Fatigue Crack Growth Assessment

L. Bercelli¹, B. Leveuil¹, C. Doudard¹, F. Bridier², S. Calloch¹

¹ ENSTA Bretagne, IRDL – UMR CNRS 6027, Brest, France

² Naval Group Research, Technocampus Océan, Bouguenais, France

Abstract – The fatigue testing of structures is costly and often limited in number of specimens. The use of an adapted instrumentation to get the most information out of a test is then critical. The present study aims at demonstrating the capability of infrared thermography for efficient fatigue characterization of structures. In particular, the proposed experimental techniques allow for failure mechanism identification, *in-situ* surface crack monitoring and fracture mechanics model assessment with consideration of the stress ratio effect.

Keywords – Infrared Thermography, Fatigue, Crack Propagation, Structures, Crack Closure

Introduction In the context of the fatigue testing of structures, an efficient instrumentation is required to make the most of costly and time-consuming tests. In this study, the use of infrared thermography is used to model the fatigue failure of structures based on Linear Elastic Fracture Mechanics (LEFM). The presented experimental technique relies on a fine analysis of the temperature response of the structure linked to its thermoelastic coupling under cyclic loading. First, the theoretical background of the method is reminded and the different experimental precautions are detailed. Then, different case studies are presented, to expose the procedure for a complete assessment of the LEFM model adapted to the structure of interest.

Method Thermoelastic Stress Analysis (TSA) is a mechanical field measurement technique that relies on the measurement of the temperature linked to the thermoelastic coupling of a sample under cyclic loading. The theoretical background of this method is based on the local heat equation

$$\rho c \frac{\partial \theta}{\partial t} = -\text{div}(\vec{q}) + C_{the} + \Delta \quad (1)$$

where θ is the temperature variation, ρ is the mass density, c is the specific heat, \vec{q} is the local heat flux, C_{the} is the thermoelastic coupling heat source and Δ is the dissipation heat source. Let us consider the case of an undamaged linear elastic metallic sample under cyclic sine loading of frequency f_m and under adiabatic conditions with small temperature variations. In such conditions, the sample temperature θ component at mechanical frequency f_m , *i.e.* its first harmonic amplitude θ_1^c , is proportional to the stress tensor's first invariant amplitude I_{1a} . In practice, due to conduction effects, the first harmonic θ_1^c field as measured via infrared thermography is rather a locally averaged image of the field of I_{1a} .

The experimental practice of TSA requires specific precautions. First, the sample must be coated with high emissivity black paint. Then, the highest achievable mechanical frequency is preferred, in order to limit conduction effects and obtain the best possible spatial resolution depending on material's thermal conductivity. Finally, a high-end infrared camera is to be set with suitable integration time and sampling frequency to ensure high-quality field measurement (in the sense of the θ_1^c). Once a satisfying set-up is defined, the sample can be submitted to cyclic loading until fatigue failure. Regular infrared films are recorded throughout the test to allow for failure mechanism identification and crack propagation kinetics assessment when deemed appropriate.

Infrared data post-processing Typical TSA consists in the computation of the field of the temperature's first harmonic θ_1^c , as it is an image of the stress field [1], from infrared films via the lock-in method [2]. The evolution of the θ_1^c field throughout the fatigue test then allows for the *in-situ* observation of surface crack initiation and propagation. The processing of differential measurement with respect to a reference image of θ_1^c then allows for a quantitative assessment of surface crack growth [3]–[5]. However, it has been observed that non-linearities can arise which lead to misleading interpretations of the first harmonic θ_1^c field. Namely the crack closure phenomenon (induced by specific the load ratio

or local compressive residual stresses) deeply affects the local temperature response, for which θ_1^c is no longer a representative indicator. Rather, the second harmonic θ_2^c was found to better exhibit the presence of such closing cracks and allow their monitoring [4]. Moreover, the local temperature response of closing cracks, can be analyzed in more detail to estimate the crack closing time and the corresponding opening rate τ_o that links the nominal applied stress range $\Delta\sigma_{nom}$ to the local effective range $\Delta\sigma_{eff}$ that effectively takes part in the crack propagation. Finally, these infrared data post-processing methods allows for the determination of the number of cycles to crack initiation and fatigue crack growth $\frac{da}{dN}$ with consideration of closure effects due to local stress state (Figure 1).

Conclusion The proposed methodology appears as an efficient technique to assess LEFM models specific to a given structure, considering load ratio as well as residual stresses inherent to the manufacturing process. Moreover, the experimental set-up is suited to the assessment of intrinsic dissipation-based approaches (self-heating), making it a go-to technique in structural fatigue analysis.

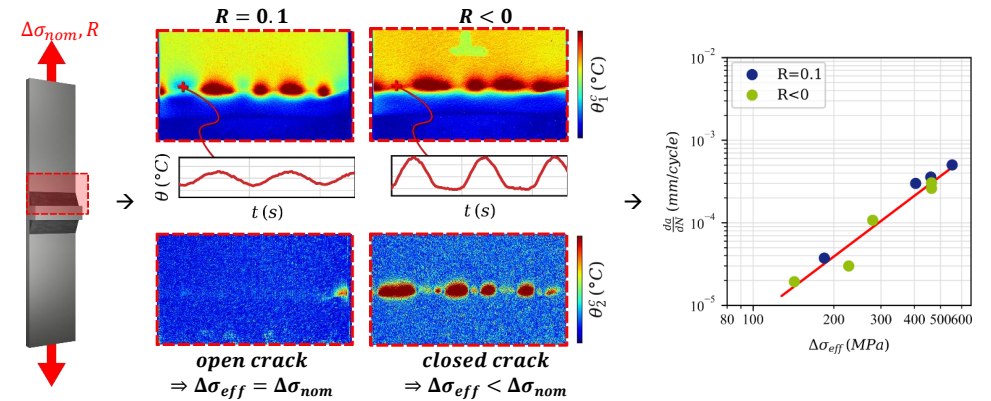


Figure 1: Illustration of the process of crack growth rate assessment via infrared thermography with consideration of the stress ratio R effect for a welded T-joint

References

- [1] P. Florin, C. Doudard, M. L. Facchinetti, and S. Calloch, "Determination of the First Stress Tensor Invariant of a Complex Steel Sheet Structure from Thermoelastic Stress Analysis Determination of the first stress tensor invariant of a complex steel sheet structure from Thermoelastic Stress Analysis," *Procedia Eng.*, vol. 133, no. January 2016, pp. 736–745, 2015, doi: <https://doi.org/10.1016/j.proeng.2015.12.655>.
- [2] O. Breitenstein, W. Warta, and M. Langenkamp, *Lock-in Thermography - Basics and Use for Evaluating Electronic Devices and Materials*. Berlin: Springer, 2010.
- [3] L. Carteron, C. Doudard, S. Calloch, B. Leveuil, J. Beaudet, and F. Bridier, "Naval welded joints local stress assessment and fatigue cracks monitoring with quantitative thermoelastic stress analysis," *Theor. Appl. Fract. Mech.*, vol. 110, no. September, p. 102792, Dec. 2020, doi: [10.1016/j.tafmec.2020.102792](https://doi.org/10.1016/j.tafmec.2020.102792).
- [4] L. Bercelli, B. Leveuil, B. Malek, F. Bridier, and A. Ezanno, "Use of infrared thermography to model the effective stress ratio effect on fatigue crack growth in welded T-joints," *Eng. Fract. Mech.*, vol. 279, no. September 2022, pp. 1–17, 2023, doi: [10.1016/j.engfracmech.2023.109061](https://doi.org/10.1016/j.engfracmech.2023.109061).
- [5] R. De Finis, D. Palumbo, and U. Galietti, "Evaluation of damage in composites by using thermoelastic stress analysis: A promising technique to assess the stiffness degradation," *Fatigue Fract. Eng. Mater. Struct.*, vol. 43, no. 9, pp. 2085–2100, 2020, doi: [10.1111/ffe.13285](https://doi.org/10.1111/ffe.13285).

Experimental Quantification of Ultraslow Slip Rate of Shear Interfaces Using Digital Image Correlation

K. Sidorattanakul¹, V. Rubino^{2,3}, A. Lattanzi^{2,4}, A. J. Rosakis²

¹Seismological Laboratory, California Institute of Technology, Pasadena, CA, USA

²Graduate Aerospace Laboratories, California Institute of Technology, Pasadena, CA, USA

³Nantes Université, Ecole Centrale Nantes, CNRS, Institut de Recherche en Génie Civil et Mécanique (GeM), Nantes, France

⁴Department of Industrial Engineering and Mathematical Sciences, Università Politecnica delle Marche, Ancona, Italy

Abstract – Frictional interfaces subjected to constant non-zero shear stress lower than the shear resistance are expected to continuously slide with decaying slip rate. Here, we develop a new experimental procedure designed to directly capture the slip rate of shear interfaces using digital image correlation method without needing to infer it from far-field measurements at loading point. Uncertainty analyses suggest that we can measure slip to the precision of sub-micron and to capture ultraslow slip rate down to at least 10^{-12} m/s.

Keywords – DIC, Shear Interface, Uncertainty Quantification

Introduction Understanding how shear interfaces start to slide is a fundamental problem relevant to a wide range of geophysics and engineering topics, including earthquakes and landslides, delamination of composites, and automobile brakes. In the classical model of friction, the driving stress must overcome to shear resistance of the interface in order to initiate sliding [1]. In contrast, a more comprehensive empirical model of friction, which describes it as being dependent on slip rate and its sliding history, encoded as the “state” of the interface, predicts that the shear interface under non-zero shear stress is always sliding, even when the driving stress is smaller than the shear resistance [2]. Such phenomenon reflects the “healing” nature of shear interface which constantly modifies the “state” of the interface as the real contact area grows logarithmically with time due to thermally activated creep [3]. While such a small sliding rate, typically on order of 10^{-12} m/s, can be considered stationary in many applications, the state of the interface plays a major role in controlling the nucleation of propagation of subsequent dynamic ruptures [4]. Here, we develop a novel experimental procedure capable of directly measuring ultraslow slip rate of shear interfaces. Such measurements are important as they are needed to quantify and better understand interface healing.

Methods An inclined shear interface at an angle $\alpha = 26^\circ$ is created by placing two quadrilateral plates of Poly Methyl Meth Acrylate (PMMA) in contact. The specimen is then compressed using a vertical load $P = 10$ MPa, resulting in resolved shear and normal stresses of 3.94 and 8.08 MPa, respectively. After the target load is reached, the specimen is left untouched while the load is kept constant using the load-control mode for 18 hours. The 30×22 mm² region in the middle is monitored using optical images, taken every 5 minutes using 32 frames-averaging denoising. Using digital image correlation (DIC) method [5], we can obtain the full-field displacement maps. To treat the displacement discontinuity across the interface, we separate the correlation domains into regions above and below the interface, similar to those done in [6]. The mean accumulated slip for each frame is computed by its spatial average. To ensure the robustness of our measurements, several methods are employed to determine the uncertainties: (1) performing identical experiments but with loaded intact specimen without any interface, (2) analysis of camera noise in motionless images, (3) simulated experiments using the method by [7], (4) misplacement of the interface location.

Results The procedure developed here allows us to measure slip with sub-micron accuracy. In our typical measurements, the accumulated slip over 18 hours is typically several microns, with faster accumulation toward the beginning (Figure 1a). The subset size employed in the DIC analysis influences the spatial distribution of slip. However, upon performing spatially averaging, its effect on the mean slip

is significantly reduced (Figure 1b). The accumulated slip translates to a decaying slip rate from 10^{-8} m/s down to approximately 10^{-12} m/s. Uncertainty analysis, performed by correlating images of a loaded specimen with no interface, reveals of uncertainty from viscoelastic deformation and other measurement errors. Further uncertainty analysis conducted by a various approached, including correlating motionless images, numerically simulated experiments, and mislocating the interface (Figure 1c), indicate an error on the same order of magnitude or lower than $0.16 \mu\text{m}$, which is far below the slip level of interest in the measurements discussed here.

Discussion and Conclusion The novel experimental procedure developed here allows us to capture the local evolution of extremely small slip along a frictional interface over very long timescales from hours to days. These measurements enable us to study the “healing” effects of shear interfaces in details which can be used to enhance our understanding of frictional interfaces. The procedure is also applicable to other scenarios beyond frictional interfaces, such as the slow quasi-static failure and fatigue of composites and other bimaterial interfaces.

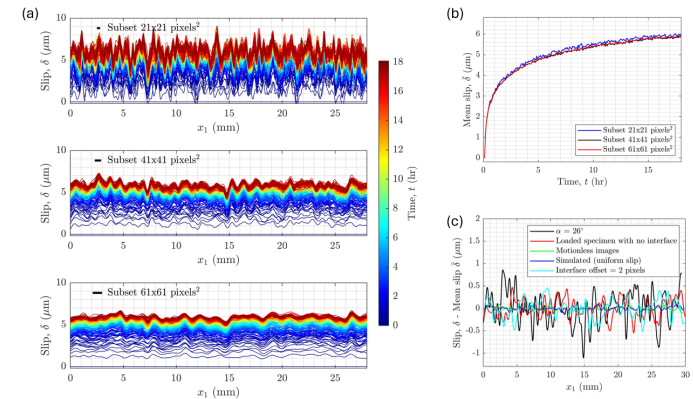


Figure 1: Capturing slip using digital image correlation. (a) Spatial distribution of accumulated slip. (b) Mean accumulated slip vs. time by spatially averaging the slip distribution in (a). (c) Comparison of spatial variation of measured slip with loaded intact specimen, motionless images, simulated experiment with uniform slip, and simulated experiments with misidentification of interface location by 2 pixels. Subset of 41×41 pixels² is employed for (b) and (c).

References

- [1] D. Dowson, *History of Tribology*, Addison-Wesley Longman Group Limited, 1979.
- [2] C. Marone. Laboratory-derived friction laws and their application to seismic faulting. *Annual Review of Earth and Planetary Sciences*, 26:643–696, 1998.
- [3] J. H. Dieterich, B. D. Kilgore. Direct observation of frictional contacts: New insights for state-dependent properties. *Pure and Applied Geophysics*, 143:283–302, 1994.
- [4] N. M. Beeler, T. E. Tullis, J. D. Weeks. The roles of time and displacement in the evolution effect of fock friction. *Geophysical Research Letters*, 21(18):1987–1990, 1998.
- [5] M.A. Sutton, J.-J. Orteu, H. Schreier. *Image correlation for shape, motion and deformation measurements: Basic Concepts, Theory and Applications*. Springer, New York, NY (USA), 2009.
- [6] V. Rubino, A. J. Rosakis, N. Lapusta. Full-field ultrahigh-speed quantification of dynamic shear ruptures using digital image correlation. *Experimental Mechanics*, 55(1):77–94, 2019.
- [7] M. Rossi, P. Lava, F. Pierron, D. Debruyne, M. Sasso. Effects of DIC spatial resolution, noise and interpolation error on identification results with the VFM. *Strain*, 51(3):206–222, 2015.

Using DIC for Full-Field Measurement of Long Slender Structures

Mennu, M.; Gardner, N.

NASA Langley Research Center, Hampton, Virginia

Abstract – High-strain composite deployable structures have been developed for systems such as solar arrays, camera masts or solar sailing propulsion elements. Composite booms in such applications are often flattened and then rolled into a small footprint for low-packaged volume and are then deployed in space. There is a need to obtain deformation for long, slender composite booms on earth through gravity offloading by suspending them vertically and applying distal end (tip) loads. Three-dimensional digital image correlation (3D-DIC), along with other measurement techniques, were used to obtain strain and displacement along the length of a 7.5 m subscale composite Triangular, Rollable, and Collapsible (TRAC) boom in preparation for full scale testing of a 30 m boom. However, incorporating 3D-DIC as a primary measurement tool on long, slender, high-aspect-ratio boom structures presents significant challenges. Challenges include small correlated area due to high aspect ratio, limited standoff distance due to size of test area, coordinate system alignment of multiple camera systems along the length of the boom, nodal mesh extraction for adequate test/analysis correlation, as well as measurement comparison between DIC and other instrumentation used such as fiber optic strain sensing (FOSS) and laser displacement tracking. The contents of the proposed paper will focus on techniques and methods for overcoming the previously mentioned challenges associated with applying 3D-DIC to long, slender boom structures. Results from subscale test along with lessons learned will be discussed.

Keywords – DIC, Composite, Slender Structure, High Aspect-Ratio, Deployable Boom

Introduction As ever-more capable space missions are of interest, long and slender deployable booms provide a viable means for deploying large space structures such as solar arrays and camera masts. Booms can be rolled up for low-packaged volume but need to have sufficient stiffness and strength to withstand loads due to spacecraft operation and deployment. One of the major challenges with boom structures are the slight imperfections due to manufacturing processes. Characterizing the effects of imperfections during deployment in space (i.e., zero gravity) cannot be achieved in a conventional lab setting due to Earth's gravity. One approach to mitigate the effect of gravity is to suspend the composite boom. However, due to the size of boom structures ranging from 7 m to 30 m, limitations on available testing facilities constrain various offloading strategies. Researchers at NASA Langley Research Center (LaRC) plan to develop and conduct experimental characterization methods under the Gravity Offloading and Analysis of Long Imperfection-sensitive Elements (GOALIE) project. To characterize mechanical response of the boom, instrumentation such as fiber optic strain sensing (FOSS) and laser displacement measurement only allow for data to be collected at discrete locations and would therefore not be sufficient on their own to provide the desired data to validate the model. Therefore, 3D-DIC was used to complement the other instrumentation. DIC is a non-contact full-field optical measurement technique capable of tracking a unique speckle pattern throughout deformation with sub-pixel accuracy [1]. This method uses camera pairs in a stereo configuration to obtain in-plane as well as out-of-plane deformations.

Methods A 30-m tall test facility at NASA LaRC known as Thor tower was selected within which a composite boom was suspended vertically to conduct the test campaign. The lower portion of the Thor tower, as shown in Figure 1, has backstops on two sides, as well as multiple floor levels above the portion shown in the figure. A photogrammetry grid consisting of aluminium extrusion was fabricated and mounted on the backstops for convenient mounting of cameras and lighting. The 7.5-m boom subscale test article was mounted on level 4 as seen in Figure 1. Two different types of low-speed camera systems were selected for 3D-DIC based on availability. Three pairs of 6.4-megapixel (MP) cameras were used to capture large segments of the boom for global displacement tracking, while two pairs of 12-MP cameras were used for capturing strain data closer to the root. A technique developed by Correlated Solutions, Inc.¹ known as multi-view registration from rigid motion [3] was implemented to align the local coordinate system of each camera pair to a global coordinate system as defined by analysis. The principle behind using this technique is to calibrate multiple systems separately, use rigid motions of speckle pattern to determine the geometric transformation between each system, and use this transformation to merge data into the same global coordinate system. An additional high-speed camera system

¹ The use of trademarks or names of corporations in this report is for accurate reporting and does not constitute an official endorsement, either expressed or implied, of such products or corporations by the National Aeronautics and Space Administration.

was positioned at the anticipated buckling location, as determined by pre-test analysis, to capture buckling initiation and subsequent collapse.

Results One of the main challenges for implementing DIC systems for the test was the limited standoff distance from the test article to the backstop of the Thor tower. In addition, the aspect ratio of the length of the composite boom to its width was approximately 55:1. To properly capture and measure the data necessary for test-analysis correlation, the number of systems required as well as the lenses used was optimized [2] as shown in Figure 1b. Aside from displacement and rotation of the boom, pre-test analysis showed higher strain value closer to the root which need to be accurately measured by the DIC systems. In addition to the higher-fidelity strain data, boundary conditions and load introduction conditions need to be captured for model validation. Therefore, two pairs of 12 MP cameras using 16 mm lenses will be used in series to capture the response of the test article and fixturing based on their higher spatial resolution. Three pairs of 6.4 MP cameras with 8.5 mm lenses will be used to capture the displacement of the boom, with two pairs in series with 12 MP cameras viewing the boom from root to mid-span, while the third pair will monitor the distal end of the boom. The camera locations were selected based on the anticipated overall boom tip displacement. By placing most of the systems between the root and the midspan of the boom, higher spatial resolution was achieved, and complete view of the top section was maintained throughout loading. Pre-test analysis indicates distal end displacement on the order of 300 mm.

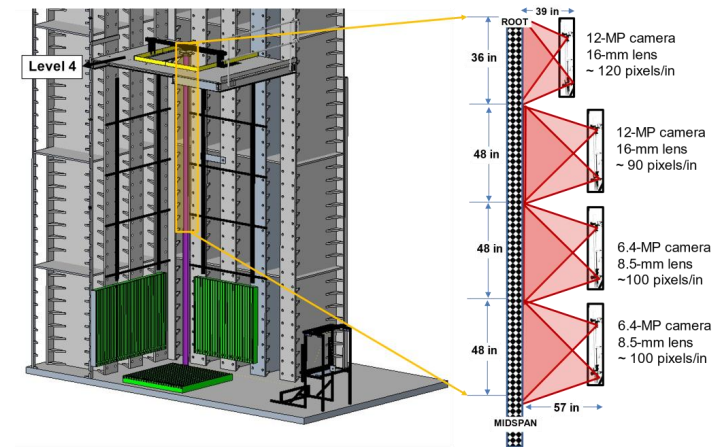


Figure 1: Preliminary setup of 7.5 m subscale test facility (left) and stereo DIC placement (right).

Discussion and Conclusion

A photogrammetry system layout incorporating multiple low-speed 3D-DIC cameras has been designed to capture full-field deformation of a 7-m long, slender composite boom. Numerous challenges associated with implementing DIC on such booms have been identified requiring careful consideration of placement of cameras for testing. Strain measurements were obtained through higher resolution cameras while displacement of longer sections of the boom obtained using lower resolution cameras with short focal length lenses. Results such as displacement and strain contours obtained will be compared to other measurement techniques. In addition, test/analysis correlation will be presented once testing has been conducted.

References

- [1] M.A. Sutton, J.-J. Orteu, H. Schreier, *Image correlation for shape, motion and deformation measurements: Basic Concepts, Theory and Applications*, Springer, New York, NY (USA), 2009.
- [2] International Digital Image Correlation Society, Jones, E.M.C. and Iadicola, M.A. (Eds.) (2018). *A Good Practices Guide for Digital Image Correlation*. DOI: 10.32720/idics/gpg.ed1
- [3] Adkins, I. (2021, March 31). *Application Note: AN-1804 — Multi-View Registration from Rigid Motions*. Correlated Solutions, Inc. <https://correlated.kayako.com/article/73-multi-view-registration-from-rigid-motions> (Accessed: April 26, 2024).

Evaluation of Conduction Thermography for Surface Crack Detection in Titanium Specimens: Preliminary Offline Tests and Initial Online Monitoring During Fatigue Tests

E. D'Accardi¹, R. De Finis², D. Palumbo¹ and U. Galietti¹

¹ Department of Mechanics, Mathematics and Management (DMMM), Polytechnic University of Bari, Via Edoardo Orabona n. 4, 70125 Bari (BA), Italy, ester.daccardi@poliba.it, umberto.galietti@poliba.it, davide.palumbo@poliba.it

² Innovation Engineering Department, University of Salento, Campus Ecotekne build. O-S.P. 6, Via Lecce Monteroni, 73100 Lecce (LE), Italy, rosa.definis@unisalento.it

Abstract – Conduction thermography is a non-destructive testing method employed to detect surface cracks in titanium materials, which are widely used in aerospace and biomedical applications due to their high strength-to-weight ratio and corrosion resistance. This study explores the use of conduction thermography to identify surface cracks in titanium alloys both during and after loading tests. The technique involves heating the specimen and monitoring its thermal response with infrared cameras. By applying suitable algorithms to post-process the thermal data, the method has demonstrated the ability to identify very short fatigue cracks, even during fatigue testing.

Keywords – Conduction thermography, cracks, non-destructive testing

Introduction

Conduction thermography is a non-destructive testing (NDT) method that is based on the principles of heat conduction to detect surface and subsurface defects in various materials [1]-[3]. This technique involves the application of a heat source to the specimen and the subsequent monitoring of the thermal response using infrared cameras. Surface cracks, voids, or inclusions alter the heat flow, creating detectable thermal contrasts that can be captured and analysed to identify and characterize defects.

Conduction thermography offers several advantages over traditional NDT methods [1]-[5], including its ability to inspect complex geometries, rapid inspection times, and the capability to detect both surface and near-surface defects without direct contact with the specimen. These attributes make it particularly suitable for materials such as titanium, widely used in aerospace and biomedical applications due to its high strength-to-weight ratio, excellent corrosion resistance, and biocompatibility [1].

Conduction thermography, beyond its role in defect detection, shows promise as a crucial technique in Structural Health Monitoring (SHM) systems, which continuously or periodically assess structural integrity to ensure safety and reliability. When integrated into SHM, conduction thermography enables real-time monitoring during fatigue tests, allowing for early damage detection and characterization.

This study explores conduction thermography for both preliminary offline tests and initial online monitoring of titanium specimens during fatigue tests. The offline tests use a low-cost setup for heating and thermal response capture, with post-processing to enhance crack detectability. Insights from these tests will guide the online monitoring approach, which aims to observe crack initiation and propagation under cyclic loading. This dual approach seeks to validate conduction thermography as a reliable non-destructive testing method and assess its potential for SHM integration. Thermoelastic stress analysis (TSA) is also used as a reference technique for comparison.

Methods

The setup used to monitor crack growth during fatigue tests is illustrated in Fig. (1). Both pulsed and lock-in thermography tests were conducted offline and online, using a direct current switching power supply (83 A, 12V) and a FLIR A65 camera to capture thermal sequences. The setup included cables, terminals, and copper plates to ensure uniform contact during current flow. The current value was adjustable by placing resistors of varying nominal values in series with the specimen. Pulse duration and the number of cycles were modified using a pulse generator and a solid-state relay to perform the thermography tests.



Figure 1: Experimental set-up adopted during on-line fatigue tests for conduction thermography.

Results

An example of the obtained results is shown in Fig. (2). A post-processing of the acquired thermal sequences has been considered to enhance crack detection and increase the contrast-to-noise ratio in correspondence of the crack tip, based on the analyses of the first frames acquired during the heating and the R^2 algorithm. Considering a thermal profile along the direction of the crack growth, it is possible to observe a typical trend with a very noisy signal that oscillates around low values of R^2 , and then changes sign at the crack tip. The point where the sign change is recorded was chosen to identify the crack tip position, and therefore estimate its length knowing the mm/pixel ratio.

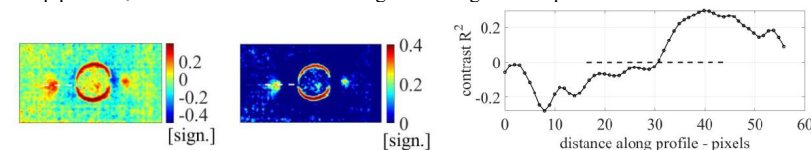


Figure 2: An example of the obtained results after 36000 cycles and a post-processing with R^2 algorithm.

Discussion and Conclusion

In this work, the conduction thermography technique was employed to identify fatigue cracks in thin titanium specimens. An innovative, low-cost setup was proposed, utilizing a low voltage (12 V) direct current switching power supply, ensuring safety during testing. Fatigue cracks approximately 2 mm in length were successfully identified by inspecting uncoated surfaces during offline tests using a microbolometer sensor. The same setup was then applied during fatigue tests, allowing for real-time identification of the crack tip and monitoring of crack growth without halting the tests. The quantitative results obtained through this technique showed good agreement with those from thermoelastic stress analysis (TSA).

References

- [1] D'Accardi, E., Palumbo, D., De Finis, R., & Galietti, U. (2023). *Detection and Characterization of Short Fatigue Cracks by Conduction Thermography*. Engineering Proceedings, 51(1), 23.
- [2] Vrana, J., Goldammer, M., Netzelmann, U. *Induction and Conduction Thermography. A new Surface Inspection Method Suited for the Forging Industry*. Proceedings of the 20th International Forgemasters Meeting; 2017 Sep 11–13; Graz, Austria.
- [3] Sakagami, T., & Ogura, K. *New flaw inspection technique based on infrared thermal images under Joule effect heating*. JSME international journal. Ser. A, Mechanics and material engineering, 1994, 37.4: 380-388.
- [4] Addante, G. D., Dell'Avvocato, G., Bisceglia, F., D'Accardi, E., Palumbo, D., & Galietti, U. (2023). *Laser Thermography: An Investigation of Test Parameters on Detection and Quantitative Assessment in a Finite Crack*. Engineering Proceedings, 51(1), 7.
- [5] Oswald-Tranta, B. *Induction thermography for surface crack detection and depth determination*. Applied Sciences, 2018, 8.2: 257.

Measuring and modelling the elastoplastic transition in engineering alloys at the microstructural scale

J. Quinta da Fonseca, D. Wu, M. Atkinson, S. Engel

Department of Materials, University of Manchester, Oxford Road, Manchester M1 3PL

Abstract — In-situ, automated high (spatial) resolution digital image correlation (HRDIC) was used to study the onset of plasticity in different engineering alloys at the microstructural scale. Different strain paths were studied, including full reversibility and orthogonal path changes. Crystal plasticity modelling was used as a theoretical framework with which to interpret the experimental results. These experiments suggest that the stress within individual grains develops in a non-monotonic way during yielding, in a way that cannot be reproduced by current crystal plasticity models. These findings have implications for the development of new, improved computational models of microplasticity.

Keywords — HRDIC, incipient plasticity, crystal plasticity modelling, path change

Introduction Many damage mechanisms in engineering alloys like cracking and void growth are controlled by the development of local plasticity at the microstructural scale near and often below plastic yield. Despite its importance, this deformation regime is very difficult to study since the microstructural changes produced by incipient plasticity are very subtle and much of the plasticity is reversed on unloading. Here we will present a series of in-situ high (spatial) resolution digital image correlation (HRDIC) studies on microplasticity of advanced engineering alloys, aimed at revealing how slip occurs and develops during the elastoplastic transition, for different strain paths.

Methods We used scanning electron microscope, equipped with an in-situ loading stage, and with fully automated image acquisition, to capture images of the nano-patterned surface of several engineering alloys during yielding. These included Ni superalloys alloys and Ti alloys. Images covering an area containing hundreds of grains, were acquired from stresses as low as 20% of the yield stress. Image acquisition was done for up to 50 increments up to a maximum strain of 5%. Some samples were pre-strained along different directions, in order to study the effect of path changes. These images were then processed using image correlation algorithms to provide total and incremental maps of local strain, at the microstructural scale, and with a spatial resolution better than 0.5 μm . Electron back-scatter diffraction (EBSD) was used to map the crystallographic orientations of the grains in the regions of interest. This data was then correlated and analysed using the open source software DepDap [?], to determine the onset of slip activity and its development during deformation. Crystal plasticity modelling was used as a theoretical framework with which to interpret the experimental results. The modelling framework DAMASK was used to simulate RVEs representing the surface studied, using the EBSD data obtained previously and calibrated using macroscopic stress-strain data.

Results The experiments revealed that the onset of yield is correlated with orientation and the elastic anisotropy of the grains making up the alloy, however these two characteristics cannot fully explain the yield sequence. As yield progresses, the number of slip events increases and very pronounced changes in slip patterns occur within individual grains, as shown in figure 1. The number of slip events continues to increase at a high rate up to strains of about 3% in tension, after which plastic deformation appears almost homogeneous. Slip within individual slip bands also changes with increasing deformation, both in magnitude and character. Initially developing at a high rate, slip activity within each band slows down after a small amount of strain, after which it increases only slowly and often through the activation of different slip systems within the same plane. The slip activity was also found to be strongly influenced by the deformation path, in a way which cannot be fully predicted by crystal plasticity modelling, in which plasticity occurs homogeneously. Direct comparisons between crystal plasticity results and crystal plasticity simulations are limited by the effects of the sub-surface grains on the deformation of the grains at the surface. The magnitude of these effects on the predicted strain at the surface was found to be significant, however the effects on relative slip activity were small.

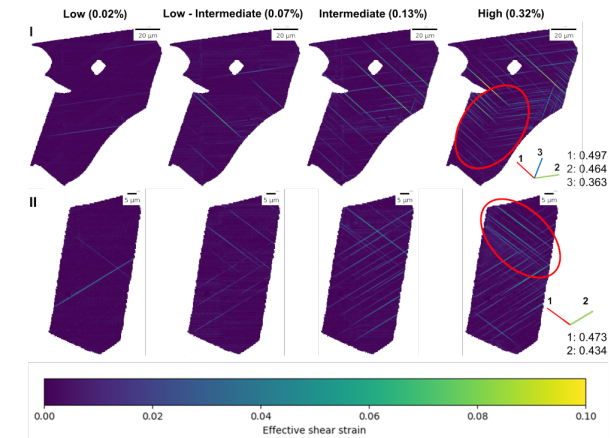


Figure 1: Change of slip character during the onset of plasticity. Slip occurs on very different planes during yielding, forming distinct regions of parallel slip

Discussion and Conclusion The actual yield sequence is clearly affected by grain orientation, elastic anisotropy and the stresses imposed by neighbouring grains. The development of plasticity is even more strongly affected by intergranular effects. The change in slip activity is consistent with a non-monotonic development of the stress in grains during yielding. This implies that plasticity events occur suddenly and lead noticeable stress redistributions within the polycrystal. The effect of pre-strain on the slip activity suggests that slip creates stresses within grains that affect plasticity after a path change. These path effects cannot be predicted by current crystal plasticity finite element models, which assume deformation occurs homogeneously. Comparing crystal plasticity results with HRDIC experiments is challenging. However, studies on the effects of varying the subsurface microstructure show that slip activity analysis at the surface of cubic alloys, is a good representation of that in the bulk.

References

- [1] M.D Atkinson, R. Thomas, A. Harte, P. Crowther, J. Quinta da Fonseca DefDAP: Deformation Data Analysis in Python - v0.92 (Version 0.92). *Zenodo*, 2020.

Automated crack detection in laminated composite materials from optical flow measurements

M. Nicol¹, F. Laurin¹, M. Hirsekorn¹, M. Kaminski¹, S. Feld-Payet¹, P. Paulmier¹, W. Albouy²,

¹ ONERA, DMAS, Université Paris-Saclay, 29 avenue de la Division Leclerc, 92320 Châtillon, France
² Safran Composites, a technology platform of Safran Tech, 33 avenue de la gare, Itteville, France

Abstract — An automated crack detection method for laminated composites of carbon fiber reinforced polymers (CFRP) is presented. An optical flow algorithm (DeepFlow) correlates the micrographs of the unspeckled specimen's edge, taken at increasing applied load, to obtain dense displacement fields. Transverse cracks are then detected from local maxima of the displacement gradient, evaluated along the midline of the plies. The robustness of the method has been validated on 3 different materials and can provide an extensive amount of data that are useful for the identification of damage models for laminates.

Keywords — Crack detection, Optical flow, Laminated composites

Introduction Under tensile loading, transverse cracking in the off-axis plies is the first damage mechanism observed at the ply scale in composite laminates. It is of industrial interest to better understand and quantify damage scenario in laminates, in particular for the identification of advanced damage models based on observable quantities, such as the transverse crack density [1, 2].

Imaging the edge of specimens is often used for *in situ* damage monitoring during tensile tests. Digital Image Correlation (DIC) and Optical Flow (OF) both enable the computation of displacement fields based on images of the pristine and damaged material, and can be used to detect cracks. While the former is commonly used in material mechanics [3], the latter is gaining interest. One such method, namely *DeepFlow* [4], combines an optical flow formulation with a deep matching algorithm and, as results, offers interesting features for crack detection [5].

We present here an experimental procedure for the identification of crack densities in laminates, with a focus on an automated crack detection approach, based on *DeepFlow*. The aim of this method is to detect a large number of cracks in various layups, to standardize the analysis of test data and reduce analysis time and, ultimately, to be transferable for industrial applications.

Methods Multi-level quasi-static tensile tests are carried out to progressively develop damage in the material. The crack initiation is monitored with optical micrography on the polished edge of the specimen. The material is scanned over 80mm to ensure the statistical representativity of the state of damage over the observed region. This scan is performed under load to maintain the cracks open. At each loading step, *DeepFlow* estimates the displacement field $\mathbf{w}(x,y) = u(x,y)\mathbf{e}_x + v(x,y)\mathbf{e}_y$. Material discontinuities translate as displacement jump in the (smooth) displacement field and can be detected in the displacement gradient field. Due to the particular crack morphology, dictated by the microstructure and the tensile loading, it is sufficient to compute the vertical gradient $\partial v/\partial y$ along the midlines of the plies and to search for peaks. The only detection parameter consists in a threshold defined as a multiple of the macroscopic applied strain. Figure 1 illustrates this procedure on a quasi-isotropic laminate.

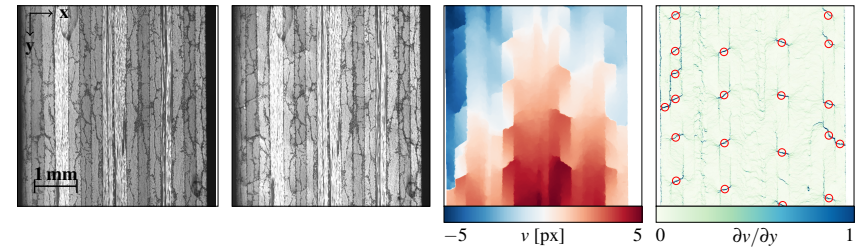


Figure 1: Illustration of the crack detection method on a quasi-isotropic laminate (T700GC/M21). From left to right: (i) pristine material; (ii) damaged material; (iii) vertical displacement field; (iv) vertical displacement gradient with detected cracks in red.

Results Figure 2 presents the results of the crack detection procedure: the crack density evolutions in three different aeronautic materials. The crack density, noted $\bar{\rho}$, depends on the number N of detected cracks, the observed length L and is normalized by the ply thickness t . It is a quantitative representation of the damage state in each ply of the layups as a function of the applied load, and a precious information for the calibration of damage models. The differences in applied strain at damage onset, damage kinetics and saturating values, both in 90° and $\pm 45^\circ$ plies, between the three materials, appear clearly.

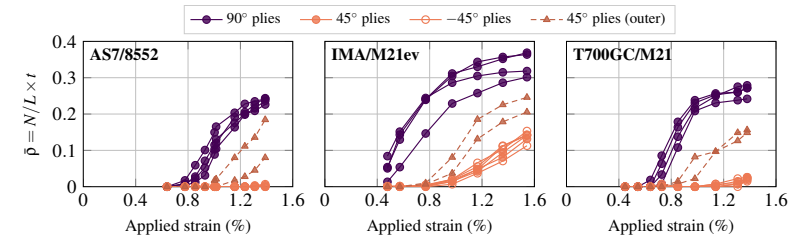


Figure 2: Identified crack densities in quasi-isotropic layups of three aeronautic CFRP materials.

Discussion and Conclusion The proposed method is particularly effective and robust to detect and count cracks in laminates. *DeepFlow* proved to be able to detect material discontinuities with a good spatial accuracy and is robust to local illumination variations that would impair other detection methods. It is possible to accurately detect cracks in 90° plies and even in challenging $\pm 45^\circ$ plies, which is rarely seen in the literature. This detection procedure is largely automated, compatible with any layup and has been validated on several materials. Test data analysis is greatly simplified and the procedure has been transferred for industrial applications. This tool was used to generate an extensive database for the quantitative study of the stacking sequence influence on damage in laminates.

References

- [1] P. Ladeveze and G. Lubineau. On a damage mesomodel for laminates: Micromechanics basis and improvement. *Mechanics of Materials*, 35:763–775, 2003.
- [2] F. Laurin, N. Carrere, C. Huchette, and J.-F. Maire. A multiscale hybrid approach for damage and final failure predictions of composite structures. *Journal of Composite Materials*, 47(20-21):2713–2747, 2013.
- [3] J. Réthoré, F. Hild, and S. Roux. Extended digital image correlation with crack shape optimization. *International Journal for Numerical Methods in Engineering*, 73(2):248–272, 2008.
- [4] P. Weinzaepfel, J. Revaud, Z. Harchaoui, and C. Schmid. DeepFlow: Large displacement optical flow with deep matching. *2013 IEEE International Conference on Computer Vision*, 2013.
- [5] Sylvia Feld-Payet, Guy Le Besnerais, Vincent Bonnard, Didier Pacou, and Léo Thiercelin. Crack path tracking from full field measurements: A novel empirical methodology. *Strain*, 56(2):e12333, 2020.

Stereocorrelation to analyze crack propagation until failure during a shaking table test

J. Grashorn¹, M. Bittner¹, M. Beer¹, X. Chang^{2,3}, A. Fau³, F. Hild³, S. Roux³

¹Leibniz Universität Hannover, Institut für Risiko und Zuverlässigkeit, Hannover, Germany

²University of Science and Technology, Department of Math and Physics, Beijing, China

³Université Paris-Saclay, CentraleSupélec, ENS Paris-Saclay, CNRS LMPS-Laboratoire de Mécanique Paris-Saclay, Gif-sur-Yvette, France

Abstract — An experimental campaign of a chevron-notched L-beam subjected to a stochastic vibration signal generated by a shaking table is presented. Analyzing large displacement amplitudes, mixed mode fracture, and complex kinematics is challenging. A finite element stereocorrelation code using a multiscale “coarse-graining” approach gave access to the full 3D crack mouth opening displacement history, thereby allowing for detailed quantification of damage growth over the entire loading history.

Keywords — Stereo Digital Image Correlation (SDIC), Mixed-Mode Fracture, Vibration, Shaking Table

Introduction Low-frequency seismic loads enable nonlinear dynamic testing to be performed. DIC has been used for structural health monitoring in recent decades thanks to its non-contacting and full-field nature. It appears particularly appealing for assessing the seismic performance of large-scale structures. Among different variants of DIC, stereocorrelation (or 3D DIC) is attractive because of its capacity to measure 3D surface motions for structures of arbitrary shapes [1, 2, 3]. A chevron-notched 3D-printed L-shape specimen was loaded with a shaking table, where the specimen design ensured that the crack could be opened only by vibration loads. A finite element-based stereocorrelation analysis [4, 5] was conducted to measure the kinematics of the notched beam. The 3D crack mouth opening displacement history allows the mixed damage growth to be quantified during vibration loads.

Methods The experimental campaign was based on Namazu, a low-cost tunable shaking table framework for uniaxial vibration experiments [6]. The notched L-beam was mounted on a “wagon” moved by the shaking table following a stochastic signal with frequencies up to 12 Hz. Two high-speed cameras were used to monitor the specimen. Multiscale FE-stereocorrelation was run to measure the corresponding kinematics. The displacements were first assessed by applying a Gauss convolution filter with a kernel size of 2 pixels to the entire image sequences, and the rigid body motions (RBMs) of the upper and lower parts of the specimen were estimated. The full kinematic computation was repeated over the raw image sequence using the previous results as an initial guess.

Results Figure 1 displays the nodal displacements in the x - and z -directions and the crack mouth opening displacement in the y -direction during the loading history. In Figure 2, one snap-shot of the deformed FE mesh is also projected onto the deformed images (time step # 3940). During the static stage $t \in [0, 600]$, the axial displacement was almost zero with (negligible) fluctuations at the level of measurement uncertainties. Despite very large displacement amplitudes (for instance, at time step # 3940, the maximum displacement reached more than 8 mm in the z -direction for a specimen with a total height of 150 mm), the projected deformed mesh matches well with the deformed images. The global multiscale approach was instrumental in successfully reaching such convergence. At the end of the prescribed motion, the displacement amplitude gradually decreased to a stabilized level. The deviation of U_x , U_y , and U_z components implied some permanent strains in the specimen.

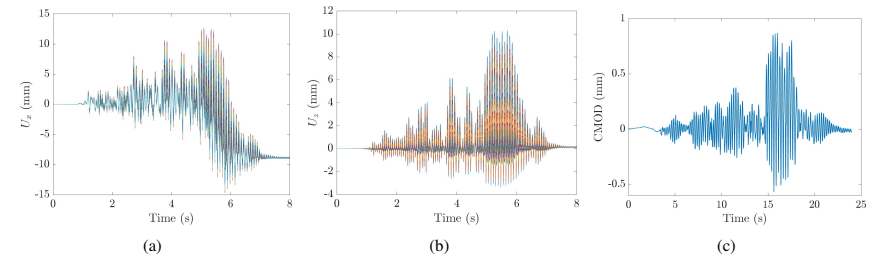


Figure 1: Nodal displacements during the entire loading history. (a) U_x , (b) U_z , (c) y component of the crack mouth opening displacement.

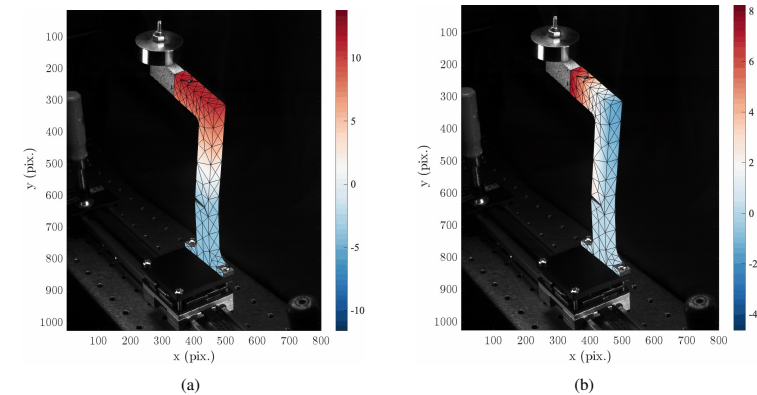


Figure 2: Projected deformed mesh superimposed with deformed images acquired by camera #2 at frame $t = 3940$. (a) U_x , (b) U_z displacement fields (expressed in mm).

Discussion and Conclusion Despite extremely large displacements of the notched specimen, using a multiscale strategy, the FE-stereocorrelation analyses led to successful convergence. The complete history of the 3D crack mouth opening displacement allows quantifying mixed damage growth in the specimen.

References

- [1] M. Helfrick et al. 3D digital image correlation methods for full-field vibration measurement. *Mechanical Systems and Signal Processing*, 25(3):917–927, 2011.
- [2] P. Reu et al. Comparison of DIC and LDV for practical vibration and modal measurements. *Mechanical Systems and Signal Processing*, 86:2–16, 2017.
- [3] W. Kang et al. High-speed multi-camera 3D DIC measurement of the deformation of cassette structure with large shaking table. *Mechanical Systems and Signal Processing*, 177:109273, 2022.
- [4] X. Chang et al. Proper generalized decomposition stereocorrelation to measure kinematic fields for high speed impact on laminated glass. *Computer Methods in Applied Mechanics and Engineering*, 415:116217, 2023.
- [5] X. Chang et al. Brightness and contrast corrections for stereocorrelation: Global and instantaneous formulation with spatial regularization. *Mechanical Systems and Signal Processing*, 208:111057, 2024.
- [6] J. Grashorn et al. Namazu: Low-cost tunable shaking table for vibration experiments under generic signals. *Submitted for publication*.

In-situ 2D-DIC as a crack growth analysis tool for high-cycle fatigue bending tests

L. Gallegos-Mayorga, T. Landron, F. Morel

LAMPA, Arts et Metiers Institute of Technology, 2 boulevard du Ronceray, 49035, Angers, France

Abstract — In the present work, a failure scenario for high-pressure die-cast aluminium specimens submitted to high-cycle fatigue was observed. To this purpose, crack growth was monitored by means of in-situ digital image correlation measurements on an uninterrupted bending fatigue test at 60 Hz. The obtained results were corroborated by post-mortem SEM observations of the failure surfaces.

Keywords — 2D-DIC, fatigue, crack monitoring, resonant fatigue testing machine.

Introduction Schematically, the fatigue life of a given specimen can be described as a two-part sequence of initiation, then propagation, of a crack under cyclic loadings until catastrophic failure appears. Experimentally, however, distinctions between initiation, propagation, and failure can be subtle and the definition of the boundaries of each stage delicate. This is further the case when specimens have defects assimilated to cracks, when multiple cracks can lead to failure, and when the definition of final fracture is not self-evident. This is exemplified by the high-pressure die-cast aluminium (AlSi9Cu3) here by studied [1].

The interest in the identification of the boundaries between the different stages of fatigue life comes from the need to understand the mechanisms behind fatigue damage. In our particular case, the sponge-like networks of gas and shrinkage pores from the casting process is suspected to be the cause of stress concentration leading to premature failure.

Our purpose being to observe cracks and their evolution to determine a failure scenario, Digital Image Correlation in 2D [2] was used to measure the discontinuity on local displacements provoked by each crack. A major advantage of this technique was the possibility, given the proper conditions of lighting and exposure time, to capture high-quality images of the specimen throughout a bending fatigue test at 60 Hz without the need of interruption.

Methods The heterogeneous distribution of defects (in size and location) on our specimens was the feature that oriented the design of our experimental set-up for two main reasons: (i) larger pores (located at the core) are known to be a greater nuisance to fatigue life, and (ii) given the distribution of the pores in the studied volume, an influence of the stress gradient on the fatigue behaviour is to be expected.

Figure 1 shows the way specimens were cut in half in order to expose the most “critical” pores to the surface and how the camera was located in order to capture the images. Cross polarization was used to avoid glare [3]. Finally, an electronic circuit based on a reprogrammable micro-controller was designed to capture a loading signal generated by the RUMUL resonant fatigue machine to generate a trigger signal for both the camera and the lighting fixture. Post-processing of the images included “sanity checks” of time stamps embedded in the first pixels of each image, longitudinal displacement fields were obtained by local digital image correlation (VIC 2D), and crack identification and measurement performed through python scikit-image library functions (mainly for gradient, contour detection and skeletonization calculations) [4].

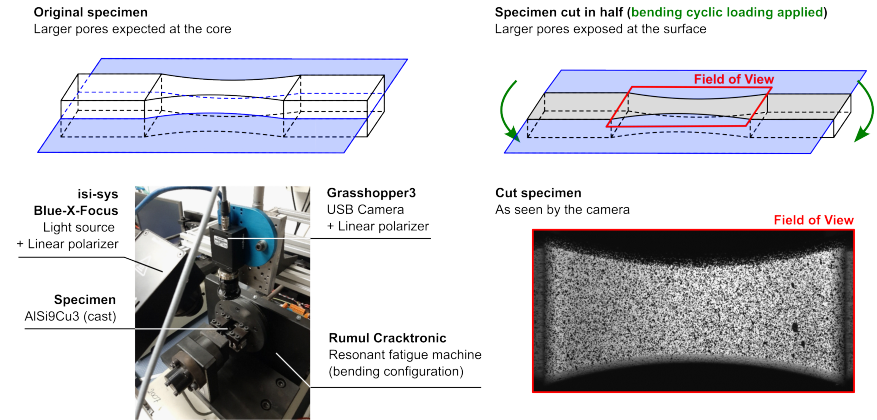


Figure 1: Experimental set-up.

Results and Discussion As seen in figure 2, discontinuities on the longitudinal displacement field of a loaded specimen allowed to detect with ease cracks hardly visible to the naked eye. Conforted by post-mortem SEM measurement porous clusters were proven to be a major source of weakness on the specimen by behaving as one large defect. Progressive interaction between pores as the fatigue damage progressed was also confirmed.

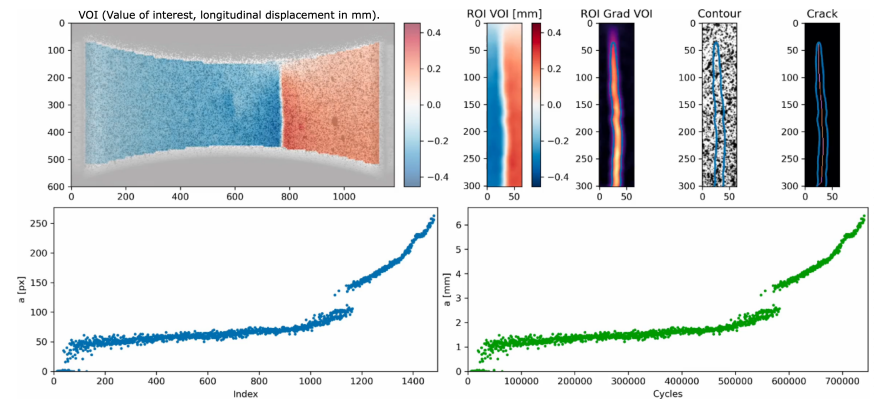


Figure 2: Crack growth results for one of the specimens.

References

- [1] T. Landron, F. Morel, N. Santier, V.D. Le, D. Bellett, P. Osmond and A. Forré. The combined effects of a heterogeneous porosity distribution and stress gradient on the high cycle fatigue behavior of high pressure die cast AlSi9Cu3. *International Journal of Fatigue*, Vol 182, May 2024.
- [2] M.A. Sutton, J.-J. Orteu, H. Schreier. *Image correlation for shape, motion and deformation measurements: Basic Concepts, Theory and Applications*, Springer, New York, NY (USA), 2009.
- [3] W. LePage, S. Daly and J. Shaw, *Cross Polarization for Improved Digital Image Correlation*, Exp Mech 56, 969-985, 2016
- [4] S. van der Walt, J. L. Schonberger, J. Nunez-Iglesias, F. Boulogne, J. D. Warner, N. Yager, E. Gouillart, T. Yu and the scikit-image contributors, *scikit-image: Image processing in Python*, PeerJ 2:e453, 2014.

Enhanced snow fracture toughness estimates through digital image correlation analysis of the elastic behaviour of weak snowpack layers

M. Walet¹, J. Schöttner¹, V. Adam^{1,2}, F. Rheinschmidt², J. Schweizer¹, P. Rosendahl², P. Weißgraeber³, A. Van Herwijnen¹

¹ WSL Institute for Snow and Avalanche Research SLF, Davos Dorf, Switzerland (melin.walet@slf.ch)

² Institute of Structural Mechanics and Design, Technical University of Darmstadt, Darmstadt, Germany

³ Chair of Lightweight Design, University of Rostock, Rostock, Germany

Abstract

Measuring the mechanical properties of snow is essential to improve our understanding and prediction of snow failure. In this context, fracture characteristics of weak snowpack layers are needed to describe the onset of crack propagation and hence to forecast avalanche release. Here, we present the results of fracture mechanical field experiments conducted to obtain fracture toughness values of natural weak layers. By analyzing snow displacement during the experiments through digital image correlation, we retrieve the elastic properties of weak layers and the overlying snow slabs. These elastic properties were then used to obtain more reliable estimates of weak layer fracture toughness values, which ultimately can be used to improve slab avalanche forecasting.

Keywords – DIC, elastic properties, mixed-mode fracture, fracture toughness, weak snowpack layers, dry-snow slab avalanche release

Introduction

Snow avalanches come in many different types and sizes. The deadliest type of avalanche, the dry snow slab avalanche, releases after a crack propagates through a weak layer inside the snowpack. Understanding the fracture characteristics of weak layers is thus essential to improve avalanche prediction. As avalanches only release on slopes steeper than 30 degrees, a crack in a weak layer is always subjected to a combination of shear and normal forces, making crack propagation a mixed-mode fracture problem. However, little is known about the mixed-mode fracture toughness of weak layers, a material property describing the resistance to crack growth under different loading conditions. Measuring fracture toughness in any material generally involves conducting standardized tests under controlled conditions and using a model to interpret the results. However, until the early 2000s, there were neither standardized tests nor appropriate models to estimate fracture toughness values of weak snowpack layers. This paradigm shifted with the advent of the propagation saw test (PST), a fracture mechanical field test developed during that period [1]. Initial estimates of fracture toughness values for weak layers relied on PST results combined with finite element modeling [2]. While this method was very sensitive to the choice of the snow elastic modulus, subsequent developments of more sophisticated fracture mechanical avalanche models [3,4] allowed to derive both elastic properties and fracture toughness values from field measurements [5,6]. Nevertheless, most fracture toughness values derived from field experiments did not distinguish between the different mixed-mode contributions, and the only study that did relied on experiments performed on low-angle terrain where normal forces dominate [6]. In this work, we therefore performed modified PST experiments and used digital image correlation in combination with a closed-form fracture model to derive the elastic properties of weak layers and the overlying snow slab and to obtain the full range interaction between mode I (compression) and mode II (shear) fracture toughness of natural weak layers.

Methods

To investigate the fracture toughness of weak snowpack layers, field experiments were conducted using natural snow samples containing buried weak layers. Each experiment involved extracting a one-meter-long sample from the snowpack, ensuring the inclusion of the target weak layer. The sample was then placed in a tilting device, loaded with weights (metal rods) and tilted to the desired angle. We then used a snow saw to cut into the weak layer until reaching the critical cut length, at which point the crack

propagated across the sample (Fig. 1a). The side wall of the snow samples was speckled with black dye and recorded on video.

From the recorded videos, precise critical cut length values were extracted. We then used digital image correlation (DIC) analysis on the video recordings to assess the displacement within the snow samples (Fig. 1b). These displacement fields served as input to derive the elastic properties of the weak layer and the overlying snow slab using a closed-form model [4]. In a last step, the collected input parameters and the retrieved elastic properties were used to obtain a fracture toughness value and the respective mode I and mode II contribution in each test.

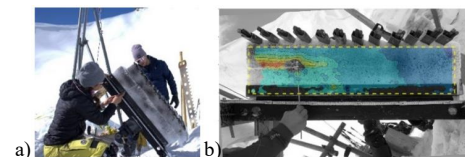


Figure 1: a) The mixed-mode fracture test. b) Example of the displacement field obtained via digital image correlation.

Results

We performed over 150 experiments and obtained fracture toughness envelopes for various weak layers. Fracture toughness values were typically around 2 J/m² in mode II and 0.5 J/m² in mode I. Overall, our results show that the fracture toughness is larger in mode II than in mode I in line with the behaviour observed in other materials. Furthermore, we observed that the fracture envelope expands as the weak layers strengthen over time.

Discussion and Conclusion

With the new experimental setup, we can test the mixed-mode fracture toughness values of weak snowpack layers. Combining our field experiments with DIC and a closed-form model allowed us to obtain more accurate fracture toughness estimates. Our results show that the fracture toughness is larger in mode II than in mode I and that the fracture envelope increases as the weak layer strengthens during the winter season.

Our results provide valuable benchmark data for numerical models and much needed data on mixed-mode fracture toughness values of weak snowpack layers to improve avalanche prediction.

In the future, we will investigate the fracture properties of numerous weak layer microstructures. Since the snow microstructure most likely controls the mechanical properties, a characterization of the microstructure is essential. The connection between weak layer fracture and the microstructure of weak snowpack layers can be used to ultimately improve slab avalanche forecasting.

References

- [1] D. Gauthier and B. Jamieson. Fracture propagation propensity in relation to snow slab avalanche release: Validating the Propagation Saw Test. *Geophysical Research Letters*, 35(13), 2008.
- [2] C. Sigrist and J. Schweizer. Critical energy release rates of weak snowpack layers determined in field experiments. *Geophysical Research Letters*, 34, 2007.
- [3] J. Heierli et al. Anticrack Nucleation as Triggering Mechanism for Snow Slab Avalanches, *Science*, 321:240-243, 2008.
- [4] P. Weißgraeber and P. Rosendahl. A closed-form model for layered snow slabs, *The Cryosphere*, 17:1475-1496, 2023.
- [5] A. Van Herwijnen, J. Gaume, E. H. Bair, B. Reuter, K. W. Birkeland, and J. Schweizer. Estimating the effective elastic modulus and specific fracture energy of snowpack layers from field experiment, *Journal of Glaciology*, 62(236):997–1007, 2016.
- [6] B. Bergfeld, A. Van Herwijnen, B. Reuter, G. Bobillier, J. Dual, and J. Schweizer. Dynamic crack propagation in weak snowpack layers: insights from high-resolution, high-speed photography, *The Cryosphere*, 15(7):3539–3553, 2021.

Study of different DIC approaches to measure crack opening/closing levels in a biaxial crack growth trial with combined HCF/LCF loads

A. Blug¹, A. Zaiat², C. Kontermann², G. Laskin¹, A. Bertz¹, D. Carl¹, M. Oechsner²

¹: Fraunhofer Institute for Physical Measurement Techniques IPM, Georges-Köhler-Allee 301, 79110 Freiburg, Germany

²: Technical University of Darmstadt, Institute for Materials Technology IfW, Grafenstraße 2, 64283 Darmstadt, Germany

Abstract – Crack closing forces are important to determine effective cyclic stress intensity factors ΔK_{eff} in fatigue crack growth trials. By digital image correlation (DIC), the change of stiffness between the open and closed crack can be measured in different ways evaluating stress-strain curves either globally using integral strain perpendicular to crack growth direction or locally measured by virtual extensometers distributed along the crack. Crack opening and crack closing forces obtained by compliance of integral strain and of crack opening profiles measured by virtual extensometers are compared for a biaxial crack growth trial applying HCF and LCF cycles.

Keywords – DIC; Fatigue crack growth; Uni- and biaxial loading; Compliance method

Precise determination of the remaining service life of technical components requires sufficient knowledge of fatigue crack growth behavior and the growth rate of defects. Cracks in real components often experience multiaxial far-field stresses due to their complex geometry and composite loadings acting on it. This paper shows results from a GPU-based high-performance DIC system specifically designed for a planar biaxial test-rig to carry out multiaxial fatigue crack-growth experiments. It provides comprehensive strain data comprising biaxial integral strain on a measurement rate of 850 Hz, like mechanical extensometers, and fast full-field evaluations in selected images selected from the data stream in real-time [1, 2]. Figure 1 shows on the left the DIC measurement head in front of a biaxial testing machine equipped with a cruciform specimen. As can be seen in the camera image on the right, the microstructure of the specimen is used as correlation pattern without need for speckle paint.

To investigate crack closure behavior, the resulting DIC data can be used in three different ways: calibration of fracture mechanical FE models to simulate the influence of T-stress or crack-closure effects like plasticity-induced crack closure [3] or evaluating the strain data directly for the change of specimen stiffness when the crack opens or closes. The latter can be done either in integral strain signal by the compliance method as defined by ASTM E647 [4] or, similarly, by evaluating stress-strain curves from virtual extensometers placed in full-field DIC along the crack [5].

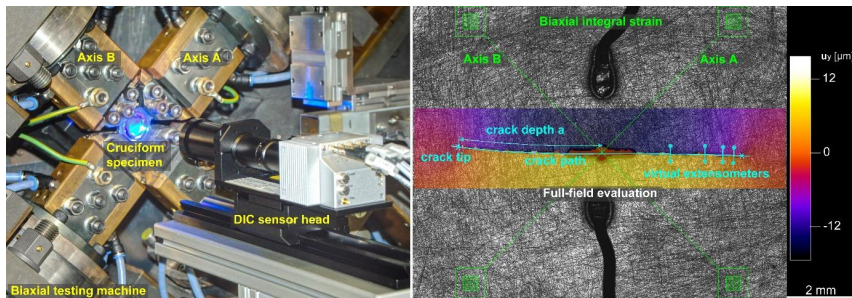


Figure 1: Left: DIC sensor head in front of the biaxial testing machine equipped with a cruciform specimen. Right: camera image of specimen surface superimposed by the four subsets for measuring integral strain or elongation Δl (green) and by the full-field evaluation area with vertical displacement u_y (color scale), i.e., in force direction. Crack evaluation (cyan): crack opening Δu_1 , in mode I direction is measured by virtual extensometers positioned 0.2, 0.5, 1.0, and 2.0 mm behind the crack tip. Crack tip positions are marked by 'x'. Crack depth a is defined as half crack path length between the tips.

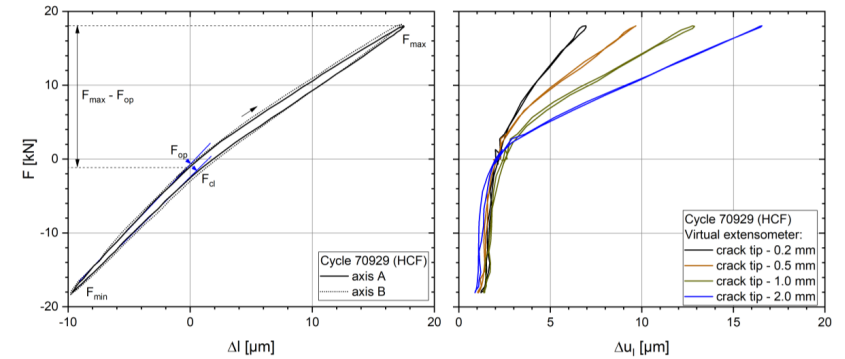


Figure 2: Left: Opening and closing forces F_{op} and F_{cl} from integral strain for an HCF cycle at a crack depth a of 4.164 mm. Right: corresponding curves from virtual extensometers depicted in Figure 1. The load is symmetric to axes A and B, therefore total force is perpendicular to the crack. As the crack appears as a discontinuity in displacement, the elongation Δl and, correspondingly, the crack opening Δu_1 , in mode I direction are drawn instead of strain values.

The crack opening/closing curves from figure 2 were taken from trial mAARTdf5 [2] using a titanium alloy Ti6246 for aero engine applications like blisks. A component near load-collective is mimicked by a fixed sequence where 20 HCF-amplitudes of 18 kN are applied symmetrically to both axes for 20 consecutive cycles, followed by an overload LCF-amplitude of 35.5 kN.

Generally, crack growth rates da/dN in Paris diagrams are often drawn against the effective cyclic stress intensity factor ΔK_{eff} which is calculated from the force range $F_{max} - F_{op}$ instead of $F_{max} - F_{min}$. In that effective range, the crack is open and growing. A common method to measure opening and closing levels, F_{op} and F_{cl} , is based on the offset of the compliance du_1/dF [4 - 6]. On the left in figure 2 it is demonstrated that the stiffness of the specimen changes when the crack opens or closes. On the right of figure 2, similar stiffness curves from the virtual extensometers depicted in figure 1 are drawn which were placed 0.2, 0.5, 1.0, and 2.0 mm behind the crack tip, respectively. This paper studies the consistency of the crack opening/closing levels obtained from these curves under HCF an LCF loading situations.

References

- [1] A. Blug, D.J. Regina, S. Eckmann, M. Senn, A. Bertz, D. Carl, C. Eberl. Real-Time GPU-Based Digital Image Correlation Sensor for Marker-Free Strain-Controlled Fatigue Testing. *Applied Sciences* 9:10-2025, 2019.
- [2] A. Blug, F. Conrad, A. Bertz, C. Kontermann, D. Carl, M. Oechsner. Application of high-performance DIC for a comprehensive evaluation of biaxial fatigue crack growth experiments. *Strain* 59:6-e12455, 2023.
- [3] F. Conrad, C. Kontermann, A. Blug, A. Bertz, D. Carl, M. Oechsner. Influence of multiaxial far field loading on the fatigue crack-growth behaviour by using corner-crack and cruciform specimen. *Proceedings of the ASME Turbo Expo 2022: Turbomachinery Technical Conference and Exposition*. 8A:GT2022-79394, 2022.
- [4] ASTM E647-15: Standard Test Method for Measurement of Fatigue Crack Growth Rates. *ASTM International*, July 2016.
- [5] L. Patriarca, S. Foletti, S. Beretta, G. Hénaff. LCF and crack growth. Recent results obtained by DIC. *MATEC Web Conf.* 165-1001, 2018.
- [6] B. Marques, D. Neto, F. Antunes, J. Vasco-Olmo, F. Díaz. Numerical tool for the analysis of CTOD curves obtained by DIC or FEM. *Fatigue Fract Eng Mat Struct* 43:12, 2984–2997, 2020.

A new methodology exploiting digital image correlation to detect crack initiation

S. Feld-Payet, V. Bonnard, D. Pacou

DMAS, ONERA, Université Paris Saclay, F-92322 Châtillon, France

Abstract — Establishing predictive fatigue damage model requires an accurate detection of crack initiation during tests. To this end, a new empirical methodology is proposed. It is based on the exploitation of a global digital image correlation algorithm of the total variation type. Two new criteria are proposed to detect strain localization, on the one hand, and crack localization, on the other hand. This methodology is applied to analyze biaxial fatigue test images.

Keywords — DIC, strain localization, crack detection

Introduction In order to ensure transport safety, particularly in the aeronautical sector, it is necessary to be able to predict the mechanical behavior of a part when subjected to repetitive stress cycles that could lead to its ruin. In particular, it is important to predict crack initiation. To do this, the first step is to perform fatigue tests that reproduce the mechanical stresses experienced throughout the life of the part. The analyze of the results is then expected to lead to an estimation of the crack initiation moment, which can serve to propose a fatigue damage model. However, existing methods for detecting crack initiation are not entirely satisfactory. Indeed, the method based on potential difference [1] is not sensitive enough. Moreover, the acoustic emission method is not easy to use since it is quite difficult to establish an unequivocal link between the acoustic signals recorded by the sensors and the corresponding damage mechanisms [2]. Dense field measurements are a promising lead but analyses of infrared images or global DIC based on finite elements (without the knowledge of the material behavior) come with a limited resolution. This can delay the moment of crack initiation detection. In this study, we propose a new methodology to exploit the images obtained with a conventional camera and detect not only crack initiation but also strain localization, as early as possible. This empirical approach is meant to be independent of the loading conditions or the material behavior and do not require their knowledge.

Methods The proposed methodology is based on the use of a global digital image correlation algorithm of the total variation type [3] to calculate, for each image, the scalar field corresponding to the maximum component of the displacement gradient at each pixel. This gradient type field then serves to determine the position of the final crack (according to the methodology proposed in [4]). Then, the strain localization moment is determined based on a new criterion: it is the moment the standard deviation of the maximum gradient component begins, at a certain point in the approximation of the final crack, to become significantly greater than the standard deviation in the vicinity of the crack. Once localization has been detected, the authors propose to use a new criterion to define a discretized crack from high-gradient pixels. This criterion involves estimating, for each image, where the points with the strongest gradients are located. The position of these points is compared with their final position. All the points that remain sufficiently close (i.e. within 3 or 5 pixels, depending on the level of uncertainty) to their final position are considered to be part of the crack. However, when the micro-cracks have coalesced and a macro-crack propagates, it becomes necessary to add an additional contiguity criterion.

Results The methodology is applied to estimate crack length and orientation based on images taken at maximum loading during fatigue tests on cruciform specimens made of Inconel 718. The tests were

performed at room temperature with an imposed force at a loading frequency of 1 Hz. Four conditions were tested in five tests, the first of which was doubled. Load ratios were 0.05 for each axis, with only the biaxiality ratio defined by Eq. (1).

$$R_b = \frac{F_1^{\max}}{F_2^{\max}} \quad (1)$$

For the test with $R_b = 0.4$, strain localization is detected at image 156 (see Fig. (1) with a spatial resolution of approximately $17.6\mu\text{m}$ per pixel). From this moment, the methodology enables to distinguish micro-cracks that coalesce to form a macro-crack at image 170. This macro-crack then propagates in two opposite directions from image 180. Similar results were obtained from the images of the test with $R_b = 1$.

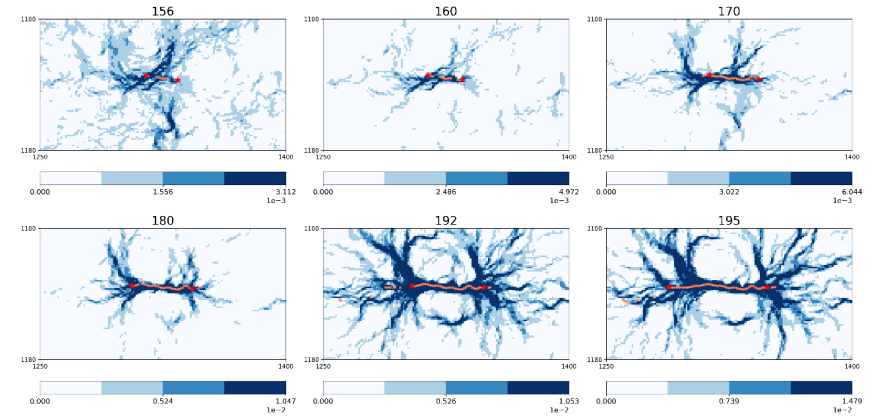


Figure 1: Maximum gradient component maps for 6 images of the $R_b = 0.4$ test. The crack corresponds to the orange points between the two red stars. Image taken from [5].

Discussion and Conclusion The proposed methodology produced very encouraging results for, at least, two analyzed cases ($R_b = 0.4$ and $R_b = 1$). The method is currently being adapted for strain localization and crack detection during the tests.

Acknowledgements The authors would like to thank Safran for its financial support, in particular for the experimental part. The results presented in this work were obtained within the ATLAAS framework, which was funded by the European Union, the French government and the DGAC.

References

- [1] ASTM E647. *Standard Test Method for Measurement of Fatigue Crack Growth Rates*. ASTM International, 2015.
- [2] A. Doitrand, Z. Hamam, N. Godin, P. Reynaud, N. Carrère. Simulation de l'émission acoustique due à la fissuration transverse d'un stratifié époxy-carbone. In *AMAC Infos n°39*, march 2023.
- [3] P. Weinzaepfel, J. Revaud, Z. Harchaoui, C. Schmid. DeepFlow : Large displacement optical flow with deep matching. In *IEEE International Conference on Computer Vision (ICCV)*, 2013.
- [4] S. Feld-Payet, G. Le Besnerais, V. Bonnard, D. Pacou, L. Thiercelin. Crack path tracking from full field measurements : A novel empirical methodology. *Strain*, 56(2), e12333 10.1111/str.12333, 2020.
- [5] S. Feld-Payet, V. Bonnard, D. Pacou. Exploiting Global Digital Image Correlation for Crack Initiation. In *Procedia Structural Integrity*, 52:517–522, 2024.

Preconditioned conjugate gradient solver for the linearized optical flow systems.

Ahmed Chabib, [Pierre Gosselet](#), Jean-François Witz, Vincent Magnier

Univ. Lille, CNRS, Centrale Lille, UMR 9013 - LaMcube - Laboratoire de Mécanique, Multiphysique, Multiéchelle, F-59000 Lille, France

Abstract — We investigate the possibilities offered by combining regularization and preconditioning by the same symmetric positive semi-definite operator when solving the linearized equations of optical flow. We study the question of the stopping criterion, and the possibility offered by Ritz eigen elements to recycle the numerical information, to a posteriori filter the solution and to tune of Tikhonov's weight.

Keywords — Optical flow, Regularization, Preconditioning, Ritz values.

Introduction Among the techniques for the contactless full-field estimation of the displacement u in mechanical testing [1], the methods based on the optical flow [2, 3] combine the conservation of grayscale between two images (f, g) and a regularization term:

$$u = \arg \min \int \left((f(x) - g(x + u(x)))^2 + \lambda |\nabla u|^2 \right) dx \quad (1)$$

$\lambda > 0$ is a parameter that manages to balance between the identification error and the regularity of the displacement. In this work, we use the Euclidean norm of the gradient of the displacement $|\nabla u|$ to measure its lack of regularity. This is the simplest form of the optical flow techniques. Our choice results in linear systems with constant matrix, but it may lead to too much diffusion in the results. Other choices may be more pertinent from a mechanical point of view, see [4] and references therein. The main objective of this work is to derive an efficient computational strategy for Equation (1). Our aim is to combine efficient solving and controlled regularization.

Methods We use a modified Newton method to solve (1). Starting from a guess u , the update $u + du$ is computed by solving the system:

$$(\mathbf{A} + \lambda \mathbf{M})\mathbf{x} = \mathbf{b}_A + \lambda \mathbf{b}_M, \quad (2)$$

with

$$\mathbf{A} = \begin{pmatrix} \mathbf{J}_x & \\ & \mathbf{J}_y \end{pmatrix} \begin{pmatrix} \mathbf{I} & \mathbf{I} \\ \mathbf{I} & \mathbf{I} \end{pmatrix} \begin{pmatrix} \mathbf{J}_x \\ \mathbf{J}_y \end{pmatrix}, \quad \mathbf{M} = \begin{pmatrix} \Delta & \\ & \Delta \end{pmatrix} \quad (3)$$

$$\mathbf{x} = \begin{pmatrix} \text{vec}(du_x) \\ \text{vec}(du_y) \end{pmatrix}, \quad \mathbf{b}_A = \begin{pmatrix} \text{vec}((f - g \circ (I + u))J_x) \\ \text{vec}((f - g \circ (I + u))J_y) \end{pmatrix}, \quad \mathbf{b}_M = \begin{pmatrix} \text{vec}(\Delta u_x) \\ \text{vec}(\Delta u_y) \end{pmatrix}.$$

The vec operator converts images to vectors. For $z \in \{x, y\}$, J_z is the z component of the gradient of f , Δu_z is the (scalar) Laplace operator applied to u_z . \mathbf{J}_z is the diagonal operator containing the values of the gradient J_z , and Δ is the matrix version of Laplace operator (with Neumann boundary conditions). All the operators are in fact obtained by discrete difference on the image. Note that the gradient of f is used to approximate the current Jacobian. As commonly done in image treatment, a median filter is applied to all the computed increments in order to remove outliers caused by the imperfect speckle.

It is extremely simple to work with \mathbf{A} and \mathbf{M} without assembling them, one only needs to compute and store the two images ($\mathbf{J}_x, \mathbf{J}_y$) and use Hadamard product and Laplace function when computing matrix-vector multiplication, so that it is natural to solve (2) with an iterative solver.

We propose to solve (2) with state-of-the-art augmented preconditioned conjugate gradient. Due to the rectangular shape of the images, solving the Laplace equation can be efficiently done with Fourier transform. We thus propose to use the (pseudo)-inverse of \mathbf{M} as a preconditioner. Indeed, the preconditioner can be viewed as a regularization tool when solving ill-posed problems [5]. We also combine the solver with Krylov subspace recycling strategies in order to speed up the resolution. Finally, we use a Ritz analysis to polish the solver and help analyze the ill-posed nature of the system, which permits to tune the weight λ at a very low cost.

Results Due to the restrictions of this proceeding, we are simply presenting the comparison between the proposed preconditioner and a classical Jacobi (diagonal) preconditioner for the identification of a crack in a holed composite plate, see Table 1. We observe that, as expected, the proposed preconditioner enables to obtain much smoother fields even with low regularization weight λ .

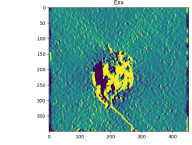
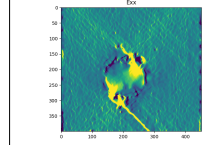
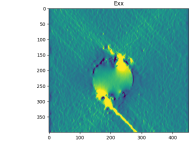
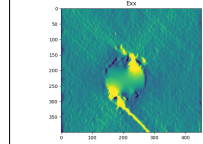
λ	Diagonal Prec.	Regularization Prec.
low (1)		
high (1000)		

Table 1: ϵ_{xx} strain field (range = mean value ± 3 st.dev.). Comparison of the effect of preconditioning by diagonal vs by regularization for different weight λ .

Discussion and Conclusion During the presentation, we will discuss other important features of the solver, like the definition of costless stopping criteria, the recycling techniques to speed up the resolution, the different tools to tune the weight λ and other a posteriori filtering using Ritz analysis.

References

- [1] Stéphane Avril, Marc Bonnet, Anne-Sophie Bretelle, Michel Grediac, François Hild, Patrick Jenny, Felix Latourte, Didier Lemosse, Stéphane Pagano, Emmanuel Pagnacco, et al. Overview of identification methods of mechanical parameters based on full-field measurements. *Experimental Mechanics*, 48(4):381, 2008.
- [2] B.K.P. Horn and G. Schunck. Determining optical flow. *Artificial Intelligence*, 17:185–203, 1981.
- [3] D. Sun, S. Roth, and M. J. Black. Secrets of optical flow estimation and their principles. In *Computer society conference on computer vision and pattern recognition.*, pages 2432–2439. IEEE, 2010.
- [4] Ahmed Chabib, Jean-François Witz, Pierre Gosselet, and Vincent Magnier. The impact of metrics in mechanical imaging. <https://hal.science/hal-04251608>, 2023.
- [5] Renaud Ferrier, Mohamed L. Kadri, and Pierre Gosselet. The Steklov-Poincaré technique for data completion: Preconditioning and filtering. *International Journal for Numerical Methods in Engineering*, 116(4):270–286, 2018.

Large Motion Tracking Regularization with the Finite Strain Formulation of the Discrete Equilibrium Gap Principle

M. Genet

Laboratoire de Mécanique des Solides, École Polytechnique/IPP/CNRS, Palaiseau, France
Équipe M ϵ DISIM, INRIA, Palaiseau, France

Abstract — The equilibrium gap principle offers a good trade-off between robustness and accuracy for regularizing motion tracking, as it simply enforces that the tracked motion corresponds to a body deforming under arbitrary loadings. In this presentation, I will describe an extension of the equilibrium gap principle in the large deformation setting and in the context of finite element motion tracking. I will demonstrate the tracking performance of the proposed method, with displacement resolution down to the pixel size, on synthetic images representing various motions with various signal-to-noise ratios.

Keywords — Motion tracking, Mechanical regularization, Equilibrium gap principle, Finite element method, Inverse problems

Abstract

The presentation will be based on [Genet 2023]. In this work, I use an intensity-based global approach to motion tracking, which is the most natural to integrate the novel regularization term, though other tracking approaches could have been considered as well. One key question in motion tracking is the regularization, *i.e.*, the *a priori* knowledge introduced in the process to improve the quality of the tracking. It is required by the intrinsic ill-posedness of the problem (we are looking for a vector field—the displacement—from an input scalar field—the image—), as well as image finite resolution, noise and bias. As in any inverse or optimization problem, efficient regularization requires a fine trade-off, here between providing enough constraint to help the tracking quality and robustness, while providing enough freedom so as to not interfere with the actual motion. In some sense regularization allows for a control, through penalization, of the function space into which the solution is sought. Many regularization terms have been proposed in the literature, such as Laplacian smoothing [Passieux et al. 2012], fluid-like mechanical regularization [Christensen et al. 1996], incompressibility [Mansi et al. 2011], hyperelastic energy [Veress et al. 2005], *etc.*, some of which will be discussed in details in this paper. An optimal trade-off is arguably reached by the so-called equilibrium gap regularization [Hild et al. 2006; Genet et al. 2018], which puts no direct constraint on the kinematics, while enforcing that the motion is close to a solution of a mechanics problem, in a sense that will be specified later in the paper.

The equilibrium gap principle was originally formulated, at the discrete level and in the linear setting, in the context of material parameter identification based on full-field measurement, in [Claire et al. 2004], and was later used in the context of motion tracking notably in [Leclerc et al. 2010]. An extension to the non linear setting was proposed, at the continuous level, in [Genet et al. 2018; Lee et al. 2019; Berberoğlu et al. 2019], with multiple applications to biomedical images [Xi et al. 2016; Castellanos et al. 2021]. In this presentation, I will describe a new extension [Genet 2023], still in the nonlinear finite strain setting but at the discrete level—hence allowing to better distinguish the equilibrium gaps induced by the motion itself and the finite element discretization, as will be detailed in the presentation—, and show that it performs better than all previous formulations.

As already mentioned, the equilibrium gap regularization consists in enforcing that the obtained dis-

placement is close to a solution of a mechanics problem with generic material behavior and arbitrary imposed surface tractions [Leclerc et al. 2010; Genet et al. 2018; Genet 2023]. To actually obtain some regularization of the problem, this arbitrariness must be handled, and the surface tractions must be somehow controlled independently of the discretization of the displacement field [Leclerc et al. 2010]. A surface Laplacian of the displacement was used as an additional regularization term in [Leclerc et al. 2010], which unfortunately does not generalize to the large motion setting. One option would be to use a separate discretization for the displacement and the tractions, which however would represent a significant technical difficulty. Instead, in this presentation, I will describe a recently introduced regularization term [Genet 2023], based on the surface gradient of the normal and tangential components of the surface tractions, and show that it performs as expected.

References

- Berberoğlu, E., C. T. Stoeck, P. Moireau, S. Kozerke, and M. Genet (2019). “Validation of Finite Element Image Registration-based Cardiac Strain Estimation from Magnetic Resonance Images”. In: *PAMM* 19.1. DOI: 10.1002/pamm.201900418.
- Castellanos, D. A., K. Škardová, A. Bhattaru, E. Berberoğlu, G. Greil, A. Tandon, J. Dillenbeck, B. Burkhardt, T. Hussain, M. Genet, and R. Chabiniok (2021). “Left Ventricular Torsion Obtained Using Equilibrated Warping in Patients with Repaired Tetralogy of Fallot”. In: *Pediatric Cardiology*. DOI: 10.1007/s00246-021-02608-y.
- Christensen, G. E., R. D. Rabbitt, and M. I. Miller (1996). “Deformable Templates Using Large Deformation Kinematics”. In: *IEEE transactions on image processing : a publication of the IEEE Signal Processing Society* 5.10, pp. 1435–47. DOI: 10.1109/83.536892.
- Claire, D., F. Hild, and S. Roux (2004). “A Finite Element Formulation to Identify Damage Fields: The Equilibrium Gap Method”. In: *International Journal for Numerical Methods in Engineering* 61.2, pp. 189–208. DOI: 10.1002/nme.1057.
- Genet, M. (2023). “Finite Strain Formulation of the Discrete Equilibrium Gap Principle: Application to Mechanically Consistent Regularization for Large Motion Tracking”. In: *Comptes Rendus. Mécanique* 351.G2, pp. 429–458. DOI: 10.5802/crmeca.228.
- Genet, M., C. T. Stoeck, C. von Deuster, L. C. Lee, and S. Kozerke (2018). “Equilibrated Warping: Finite Element Image Registration with Finite Strain Equilibrium Gap Regularization”. In: *Medical Image Analysis* 50, pp. 1–22. DOI: 10.1016/j.media.2018.07.007.
- Hild, F. and S. Roux (2006). “Digital Image Correlation: From Displacement Measurement to Identification of Elastic Properties - a Review”. In: *Strain* 42.2, pp. 69–80. DOI: 10.1111/j.1475-1305.2006.00258.x.
- Leclerc, H., J.-N. Périé, S. Roux, and F. Hild (2010). “Voxel-Scale Digital Volume Correlation”. In: *Experimental Mechanics* 51.4, pp. 479–490. DOI: 10.1007/s11340-010-9407-6.
- Lee, L. C. and M. Genet (2019). “Validation of Equilibrated Warping—Image Registration with Mechanical Regularization—On 3D Ultrasound Images”. In: *Functional Imaging and Modeling of the Heart (FIMH)*. Ed. by Y. Coudière, V. Ozenne, E. Vigmond, and N. Zemzemi. Vol. 11504. Cham: Springer International Publishing, pp. 334–341. DOI: 10.1007/978-3-030-21949-9_36.
- Mansi, T., X. Pennec, M. Sermesant, H. Delingette, and N. Ayache (2011). “iLogDemons: A Demons-Based Registration Algorithm for Tracking Incompressible Elastic Biological Tissues”. In: *International Journal of Computer Vision* 92.1, pp. 92–111. DOI: 10.1007/s11263-010-0405-z.
- Passieux, J.-C. and J.-N. Périé (2012). “High Resolution Digital Image Correlation Using Proper Generalized Decomposition: PGD-DIC”. In: *International Journal for Numerical Methods in Engineering* 92.6, pp. 531–550. DOI: 10.1002/nme.4349.
- Veress, A. I., G. T. Gullberg, and J. A. Weiss (2005). “Measurement of Strain in the Left Ventricle during Diastole with Cine-MRI and Deformable Image Registration”. In: *Journal of Biomechanical Engineering* 127.7, pp. 1195–1207. DOI: 10.1115/1.2073677.
- Xi, C., C. Latnie, X. Zhao, J. L. Tan, S. T. Wall, M. Genet, L. Zhong, and L. C. Lee (2016). “Patient-Specific Computational Analysis of Ventricular Mechanics in Pulmonary Arterial Hypertension”. In: *Journal of Biomechanical Engineering* 138.11, p. 111001. DOI: 10.1115/1.4034559.

A Procedure for Global Non-Local Digital Image Correlation (NL-DIC)

Tushar Bhandari and Debasis Deb

Indian Institute of Technology Kharagpur, West Bengal, India-721302

Abstract — Finite element (FE) based displacement measurement for digital image correlation (FE-DIC) is being applied to measure heterogeneous displacement field. The concepts of mechanically based non-local elastic continuum model is also applied in the finite element method. In the present work, a non-local continuum model is implemented in FE-DIC framework to measure non-local displacements. In the proposed model, the displacement of each element in the domain is considered to be mutually interacting with the others. The constitutive relations of the long-range interactions involve the product of the relative displacement of the centroids of elements by a distance-decaying function. The algorithm is tested on numerical images and significant increase in accuracy is obtained compared to FE-DIC.

Keywords — DIC, Non-Local Displacement, Discontinuity, Finite-Element DIC

Introduction The measurement of displacement using DIC around cracks and other discontinuities has been a challenge primarily due to the displacement jump around the vicinity of these discontinuities. Researchers have made attempts to resolve this discontinuous displacement by developing procedures such as Extended DIC (X-DIC) [1, 2], Peridynamics-based DIC [3], and non-local subset-based strain measurement [4]. This study proposes an FE based method for non-local displacement measurement (NL-DIC). In this model, the FE nodal displacement is further enriched with non-local displacement, a distance decaying function of the relative displacement between the element and the neighbour elements.

Methods The reference image ($f(\mathbf{x})$) can be equated to the deformed one ($g(\mathbf{x})$) by adding the displacement \mathbf{u} to every spatial pixel coordinate, also the relation can be expanded by applying First Order Taylor series expansion as,

$$f(\mathbf{x}) = g(\mathbf{x} + \mathbf{u}) = g(\mathbf{x}) + \mathbf{u}(\mathbf{x}) \cdot \nabla f(\mathbf{x}) \quad (1)$$

The non-local displacement \mathbf{u} can be expressed as,

$$\mathbf{u} = \mathbf{u}_{FE} + \mathbf{u}_{Non-Local} = \mathbf{N}_i \mathbf{C}_i \mathbf{d}_i + \sum_{n=1}^N \sum_{p=1}^{P_j} h[\mathbf{N}_i \mathbf{C}_i - \mathbf{N}_{jp}^n \mathbf{C}_j^n] \mathbf{d}_j \quad (2)$$

where, \mathbf{N}_i is the shape function of the element i ; \mathbf{C}_i is the connectivity matrix of the i^{th} element; $\mathbf{d}_i = [d_1 d_2 \dots d_m]^T$ is the degree of freedom of all nodes within the neighbour of the i^{th} element; N is the number of elements neighbour of i^{th} element; P_j is the number of pixel in the j^{th} element, and; $h = Ce^{(-s/l)}$ in which C and l are constants and s is the distance between i^{th} and j^{th} pixels.

Rewriting Eq 2 as $\mathbf{u} = \mathbf{M}_i \mathbf{d}_i$ where \mathbf{M}_i incorporated both the local and non local shape functions and solving for displacement by the procedures given by [1], the following linear system of equations is obtained:

$$\mathbf{M}_i \mathbf{u}_i = \mathbf{b}_i \quad (3)$$

Where matrix \mathbf{M}_i and \mathbf{b}_i are formed by assembly process of l^{th} elemental matrix \mathbf{M}_i and \mathbf{b}_i given in equation 4, respectively (where $\partial \mathbf{G} = [\frac{\partial g}{\partial x} \quad \frac{\partial g}{\partial y}]$).

$$\mathbf{M}_i = \int_{\Omega_e} (\mathbf{M}^T \partial \mathbf{G}) (\partial \mathbf{G}^T \mathbf{M}) d\Omega \quad \mathbf{b}_i = \int_{\Omega_e} [f(\mathbf{x}) - g(\mathbf{x})] (\mathbf{M}^T \partial \mathbf{G}) d\Omega \quad (4)$$

Irwin's analytical solution for near crack tip displacement [5] given by the following equation is applied to generate numerical images of size 200×200 pixels.

$$u_x = \frac{K}{2G} \sqrt{\frac{r}{2\pi}} \cos \frac{\theta}{2} \left[\kappa - 1 + 2 \sin^2 \frac{\theta}{2} \right] \quad u_y = \frac{K}{2G} \sqrt{\frac{r}{2\pi}} \sin \frac{\theta}{2} \left[\kappa + 1 - 2 \cos^2 \frac{\theta}{2} \right] \quad (5)$$

where the Kolosov's constant, $\kappa = 3 - 4\nu$ (Plane strain), K is the stress intensity factor, G is the shear modulus, and r is the radial distance from the crack tip. The value of constants are set as: $\sigma_{\infty} = 15$ MPa, $G = 26$ GPa, $\nu = 0.33$, $a = 12$ pixels where $\text{Pa} = \text{N/pixels}^2$ (Displacement is scaled up by a factor of 100).

Results Fig. (1) shows the analytical, FE-DIC and non-local FE-DIC displacement field.

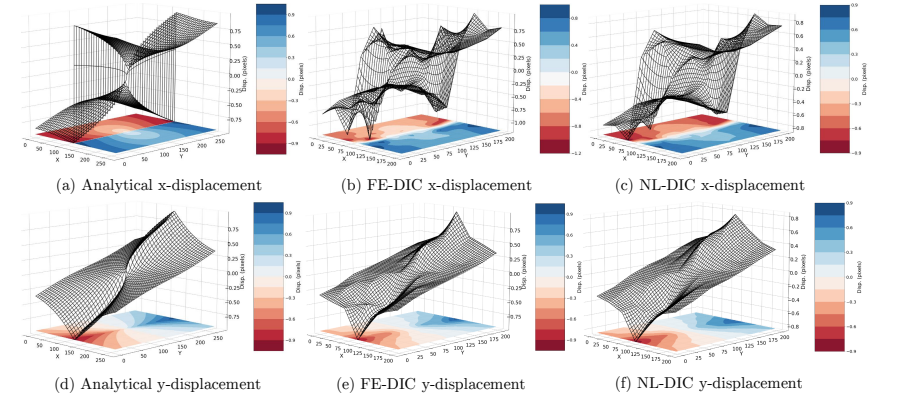


Figure 1: Discontinuous displacement field captured by non-local FE-DIC algorithm

Discussion and Conclusion The developed NL-DIC procedure to capture non-local displacement is applied to capture discontinuous displacement field. The plots in Fig. (1) show that for x displacement, the non-local algorithm can resolve the displacement more accurately than the standard FE-DIC. It is worth noting that no input regarding the discontinuity is required for the proposed algorithm to perform. Compared to the analytical solution for displacement (Eq. 5), the RMSE of nodal displacement is 0.13 pixels and 0.045 pixels for FE-DIC, while it is 0.065 pixels and 0.028 pixels for NL-DIC. The non-local displacement measure is 51% and 37% more accurate than the FE-DIC displacement. The proposed algorithm has demonstrated a significant increase in accuracy for measuring non-linear and discontinuous displacement fields; further implementation of integrated non-local displacement and strain measures is required to make the algorithm more robust.

References

- [1] D. Deb and S. Bhattacharjee. Extended digital image correlation method for analysis of discrete discontinuity. *Optics and Lasers in Engineering*, 74:59–66, 2015.
- [2] J. Rethore, F. Hild and S. Roux. Extended digital image correlation with crack shape optimization. *International journal for numerical methods in engineering*, 73:248–272, 2008.
- [3] D. Z. Turner. Peridynamics-based digital image correlation algorithm suitable for cracks and other discontinuities. *Journal of Engineering Mechanics*, 141.2:04014115, 2015.
- [4] R. B. Lehoucq, P. L. Reu, and D. Z. Turner. A novel class of strain measures for digital image correlation. *Strain*, 51.4: 265-275, 2015.
- [5] G. R. Irwin. Analysis of stresses and strains near the end of a crack traversing a plate. *Journal of applied mechanics*, 24:361-364, 1957.

Development of a virtual DIC approach to improve measurement accuracy and assess experimental setups

O. Tyley, T. Laux, O. T. Thomsen, J. M. Dulieu-Barton

Bristol Composites Institute, School of Civil, Aerospace and Design Engineering, University of Bristol, UK

Abstract — The arrangement of the equipment for Digital Image Correlation (DIC) experiments requires consideration of many competing factors, including standoff distance, camera and lens selection, and stereo angle. The final set-up is often a qualitative process based on experience of the practitioner. A more quantitative means of evaluation is suggested where the equipment set-up is recreated and adjusted virtually to generate accurate synthetic images. The paper explores the use of the computer graphics software package *Blender* as a tool to aid the design of a DIC experiment. A virtual experiment was modelled, corresponding to a physical test on a Brazilian disc. The virtual experiment is shown to accurately reconstruct the strains obtained from the physical test. It is then demonstrated how the virtual experiment can be used to improve the experimental outcome.

Keywords — Digital Image Correlation (DIC), Blender, Virtual Experiment.

Introduction Designing the set-up for a DIC experiment requires a practitioner to balance multiple competing demands. Published guidelines [1] can provide recommendations for parameters like stereo angle, focal length and speckle pattern size. However, in complex, larger-scale tests, the position of cameras and lighting is often restricted by the available space and performance of the set-up may not be known until it is physically built. The outcome is a compromise with a potentially sub-optimal set-up with poorly-understood biases and measurement uncertainties.

In recent years there has been interest in the generation and analysis of synthetic images for assessing the capabilities of DIC Experiments. These include techniques which deform real-world images based on finite element calculations, e.g. [2], as well as techniques which fully model a virtual test environment in the computer graphics software package Blender [3]. The present paper builds upon these findings and demonstrates how a virtual experiment that includes features such as lighting and can be adjusted for different lens distortions, stereo angles, etc., can be used to prescribe an effective experimental set-up.

Methods An aluminium Brazilian disc specimen (diameter 70 mm, thickness 6 mm) with a speckle pattern applied was loaded to 5 kN. The strains were measured using a stereo-DIC system, with a variety of setups which varied in focal length, stereo angle, and f-stop.

A corresponding virtual stereo-DIC system was modelled using the computer graphics software package Blender [4]. A finite-element model was used to predict the 3-dimensional strain field on the disc and the virtual disc was correspondingly deformed. Synthetic images from the virtual DIC system were rendered of the disc in both deformed and undeformed states. An instance of the virtual experiment is shown in Figure 1. Images of a virtual calibration plate were also rendered so that the virtual experiment could be calibrated just as in the physical experiment. For both the physical and virtual experiments, the calibration data and images were correlated using MatchID's *Stereo* package [5].

Results The virtual and physical DIC systems, the synthetic and experimental images, and the resulting strains are all shown in Figure 1. This configuration has a standoff distance of 0.5 m, a stereo angle of 25°, and uses 50 mm lenses but other configurations are possible.

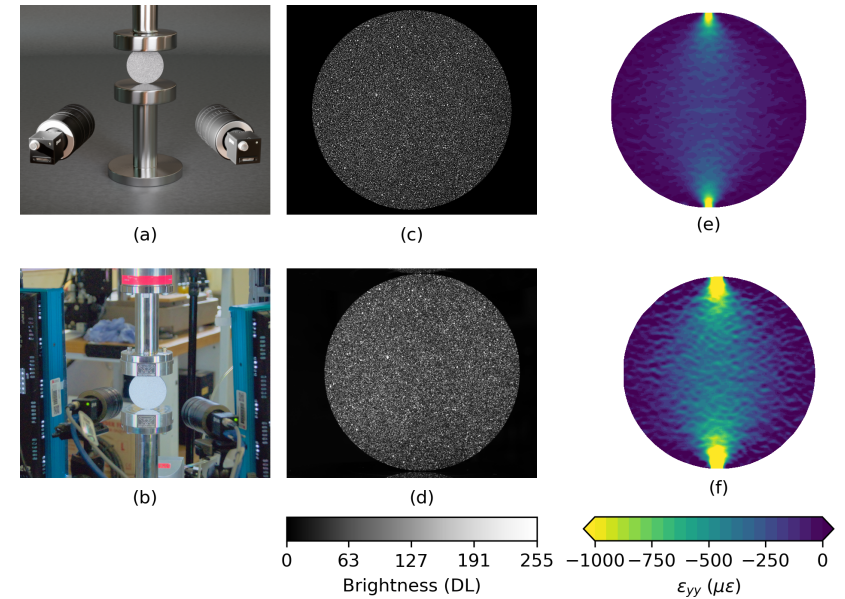


Figure 1: A comparison between a virtual experiment modelled in Blender and the real-world counterpart. (a) a rendering of the virtual system. (b) The physical experimental setup. (c) a synthetically-generated image. (d) an image from the physical experiment. (e) the strain measured from the synthetic images. (f) the strain measured from the physical experiment.

Discussion and Conclusion DIC images synthetically generated using Blender were shown to be able to accurately reconstruct heterogeneous strain fields for a simple test object. A framework has been developed for virtually comparing different DIC measurement systems. This can aid in designing experimental set-ups by allowing a quantitative assessment of measurement performance. In the presentation, the virtual testing procedure will be validated against several different configurations of test set-up. Sources of error can also be quantitatively evaluated with the introduction of known defects in the DIC system such as defocus, image distortion or aliased speckle patterns.

References

- [1] International Digital Image Correlation Society, E. Jones, M. Iadicola, *et al.*, “A Good Practices Guide for Digital Image Correlation,” International Digital Image Correlation Society, Tech. Rep., Oct. 2018. [Online]. Available: <http://idics.org/guide/>.
- [2] R. Balcaen, L. Wittevrongel, P. L. Reu, P. Lava, and D. Debruyne, “Stereo-DIC Calibration and Speckle Image Generator Based on FE Formulations,” *Experimental Mechanics*, vol. 57, no. 5, pp. 703–718, Jun. 2017. [Online]. Available: <https://doi.org/10.1007/s11340-017-0259-1>.
- [3] D. P. Rohe and E. M. C. Jones, “Generation of Synthetic Digital Image Correlation Images Using the Open-Source Blender Software,” *Experimental Techniques*, vol. 46, no. 4, pp. 615–631, Aug. 2022. [Online]. Available: <https://doi.org/10.1007/s40799-021-00491-z>.
- [4] Blender Institute, *Blender*, Mar. 2024. [Online]. Available: <https://www.blender.org/about/>.
- [5] MatchID, *MatchID*, Ghent (Belgium), 2024. [Online]. Available: <https://www.matchid.eu/>.

An efficient approach for identifying the coefficients of thermal expansion of CFRPs

R. Ruiz-Iglesias, R. Cappello, O. T. Thomsen, J. M. Dulieu-Barton

Bristol Composites Institute, School of Civil, Aerospace and Design Engineering, University of Bristol, Queen's Building, University Walk, Bristol, BS8 1TR, UK,

Abstract – In composite materials the Coefficient of Thermal Expansion (CTE) is a difficult parameter to measure using traditional methods, as evidenced by a wide range of values reported in the literature, even for the well-documented IM7/8552 CFRP material. Thermoelastic Stress Analysis (TSA) traditionally assesses surface stresses, however, it has been demonstrated that in CFRPs, surface measurements are affected by heat transfer from underlying plies. In contrast, Digital Image Correlation (DIC) exclusively captures surface strains, and is unaffected by any heat transfer. Hence a new tool is proposed to enable rapid and accurate predictions of CTE based on full-field data fusion (FFDF) of TSA and DIC. The approach uses the experimentally obtained thermoelastic response in combination with a 1D ply-by-ply heat transfer model for multidirectional (MD) CFRP laminates. Utilizing an inverse optimisation methodology, the FFDF tool extracts CTEs for the material.

Keywords – Digital Image Correlation (DIC), Thermoelastic Stress Analysis (TSA), Coefficients of Thermal Expansion (CTEs), Full-Field Data Fusion (FFDF)

Introduction The Coefficients of Thermal Expansion (CTEs) of composite material are important quantities that are required to understand the generation of residual stresses and distortions when designing and manufacturing parts. In many structural applications composites are exposed to a wide range of temperatures. Consequently, the CTEs are required as input parameter in the formulation of many structural and thermal models of CFRP components. Unfortunately, even for well documented materials a wide range of values are reported, e.g. [1]–[4]. The reason is that traditional techniques such as Thermomechanical Mechanical Analyses (TMA) are difficult to perform accurately unless thick specimens of unidirectional material are especially manufactured for the purpose. Hence, a new approach is proposed that can provide both the longitudinal and transverse CTEs for CFRP materials in a simple experiment. The approach applies full-field data fusion (FFDF) from the well-established techniques of Thermoelastic Stress Analysis (TSA) and Digital Image Correlation (DIC), as described in [1], alongside an optimisation based on a 1D heat transfer model to estimate the non-adiabatic thermoelastic response [5].

Methods TSA is a non-contact, full-field infrared imaging technique that provides spatially detailed information to obtain the surface stresses in cyclically loaded components. The temperature change, ΔT , is obtained from an infrared camera and for an orthotropic material is related to the stresses by:

$$\Delta T = \frac{-T_0}{\rho C_p} (\alpha_1 \Delta \sigma_1 + \alpha_2 \Delta \sigma_2) \quad (1)$$

where T_0 is the material mean temperature, ρ is the density, C_p is the specific heat capacity, α_1 and α_2 are the CTEs in the principal material directions and $\Delta \sigma_1$ and $\Delta \sigma_2$ are the stress changes in the principal material directions.

Equation (1) is only valid for orthotropic materials when ΔT occurs under adiabatic conditions. Nonetheless, results in [1] have shown that through thickness heat diffusion occurs at relatively low loading frequencies in laminated CFRP materials. The dependence of ΔT on CTEs is used in an optimization, where the experimentally $\Delta T/T_0$ is obtained over a range of loading frequencies and compared with the output from a 1-D heat transfer model. The 1-D assumption presumes that only the ply-by-ply stresses change, and that the stress in the plane of each ply is uniform, i.e. the test component is in a state of uniaxial tension. The model requires inputs of the global laminate strain, hence the strains are obtained using DIC. The mechanical properties of the laminate, as well as the CTEs, the specific heat, the thermal conductivity and density are also required as inputs for the model.

A pattern search optimization procedure [6] is used that does not rely on gradients, and is suitable for functions that are not continuous or differentiable. The process involves iterative steps, systematically adjusting variables to discover the best match by minimising the following difference:

$$F(\alpha_1, \alpha_2) = \left(\frac{\Delta T}{T_0} \right)_{TSA} - \left(\frac{\Delta T}{T_0} \right)_{Model} \quad (2)$$

Equation (2) requires multiple inputs of pairs of CTE values, however, it is crucial to define the range of α_1 and α_2 within physically plausible limits, so that CTE values are searched by minimizing $F(\alpha_1, \alpha_2)$ within a defined range for each loading frequency. The range was set based on values from the literature. MD CFRP specimens $[0,45,-45,0,0,0]_S$ and $[0,0,0,45,-45,0]_S$ were subjected to non-damaging cyclic loading over a range of frequencies and the thermoelastic response used in conjunction with the heat transfer model to obtain the CTEs. A comparison between the results using the CTEs from the optimisation and the experimental data is shown in Figure 1. The derived CTEs are given in Table 1.

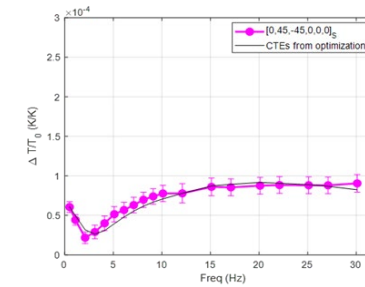


Table 1 Derived CTEs

Configuration	CTE α_1 (10^{-6} K^{-1})	CTE α_2 (10^{-6} K^{-1})
$[0,45,-45,0,0,0]_S$	-0.132605 ± 0.029937	22.500991 ± 1.065008
$[0,0,0,45,-45,0]_S$	-0.120466 ± 0.019197	21.260635 ± 2.622473
AVERAGE	-0.126536	21.880813

Figure 1. Comparison between experimental and optimization results

Discussion and Conclusion An inverse approach based on a 1-D heat transfer model has been developed to obtain the CTEs from TSA. It is shown that the approach offers the possibility of accurately identifying CTEs using simple coupon specimens. Further validation work is required but the results demonstrate the potential of a new tool based on TSA to obtain CTEs in CFRPs.

References

- [1] Jiménez-Fortunato I., Bull DJ., Thomsen OT., Dulieu-Barton JM. On the source of the thermoelastic response from orthotropic fibre reinforced composite laminates. *Comp. Part A*;2021; 149(106515).
- [2] Camanho PP., Maimi P., Dávila CG. Prediction of size effects in notched laminates using continuum damage mechanics. *Comp Sci Tech.* 2007; 67(13): 2715–2727. DOI:10.1016/j.compscitech.2007.02.005
- [3] Stacey JP., O'Donnell MP., Schenk M. Thermal Prestress in Composite Compliant Shell Mechanisms. 42nd Mechanisms and Robotics Conf. ASME; 2018. Available at: DOI:10.1115/DETC2018-85826
- [4] Daynes S., Potter KD., Weaver PM. Bistable prestressed buckled laminates. *Comp Sci Tech.* 2008; 68(15–16): 3431–3437. DOI:10.1016/j.compscitech.2008.09.036
- [5] Wong A. A non-adiabatic thermoelastic theory for composite laminates. *J Phys Chem oSolids.* 1991; 52: 483–494. Available at: DOI:10.1016/0022-3697(91)90180-8
- [6] Hooke R., Jeeves TA. 'Direct Search - Solution of Numerical and Statistical Problems'. *Association for Computing Machinery*; 1961; 8(2): 212–229. Available at: DOI:10.1145/321062.321069

High-Performance Mechanically Regularized Finite-Element Digital Volume Correlation for Complex Architected Materials

L. Person^{1,2,4}, P. Jolivet³, J-C. Passieux¹, R. Bouclier^{1,2}, P. Oumaziz¹

¹Institut Clément Ader, CNRS/INSA/ISAE Supaero/Mines Albi/UT3, Toulouse, France, passieux@insa-toulouse.fr paul.oumaziz@insa-toulouse.fr

²Institut de Mathématiques de Toulouse, INSA/UT1/UT2/UT3, Toulouse, France, bouclier@insa-toulouse.fr

³Sorbonne Université, CNRS, LIP6, Paris, France, pierre.jolivet@lip6.fr

⁴Ecole Normale Supérieure Paris-Saclay, Université Paris-Saclay, Gif-sur-Yvette, France, lucas.person@ens-paris-saclay.fr

Abstract — Measuring kinematic fields at the architecture scale of cellular materials is known to be highly challenging in experimental mechanics, in particular because of the geometric complexity of the specimen and the poor texture at this scale. To overcome this obstacle, a solution consists in assisting Digital Volume Correlation (DVC) with a FE-based mechanical regularization. However, such approaches entail a substantial computational burden when considering complex architected materials along with large volume images. To address this issue, this study proposes a scalable domain decomposition algorithm to efficiently estimate subcellular kinematic fields across large regions of cellular materials.

Keywords — DVC, HPC, Mechanical Regularization, Domain Decomposition, Parallel computing

Introduction Architected materials are excellent candidates for the design of multifunctional structures with outstanding specific properties. However, due to the coexistence of two very different scales, the prediction of the mechanical behavior of such materials remains an issue. This is especially true for synthetic materials such as foams because of their random architecture. Their mechanical characterization requires conducting *in-situ* experiments on real and representative cellular material samples. In this context, X-ray Computed Tomography (CT) scans provide a three-dimensional insight into specimens, which enables the analyses of such structures at different loading stages. Then, Digital Volume Correlation (DVC) enables the quantitative analysis of these series of volume images and the consequent extraction of relevant displacement fields.

These volume images contain a huge amount of data, enabling detailed observation of the geometric complexity of cellular material architecture. Yet, the inherent texture of the material at this scale is too poor to measure subcellular kinematic fields with DVC. To overcome this obstacle, a solution consists in considering FE-based DVC and complementing it with a finely-tuned mechanical regularization [1] to assist the correlation below the cell scale. However, such FE-DVC approaches come with a high numerical complexity compared to subset-DVC, as the former entail solving multiple (sparse but) global linear systems, while the latter involve smaller and independent systems of equations formulated on each subset which are parallelizable. Hence, numerous CPU and GPU parallel computing techniques have been employed to accelerate subset DVC methods due to their inherent parallel nature [2]. Much less work has been done on the parallelization of FE-DVC (using GPU for instance in [3, 4]).

This work focuses on developing and implementing a scalable algorithm for solving a mechanically regularized FE-DVC problem using domain decomposition [5] to parallelize the solution.

Methods The DVC problem is based on the gray level conservation equation. The displacement field is discretized using a FE mesh of the architecture of the specimen built on the image (see [1] for more details). To simplify the formulation of the domain decomposition method, we consider the mechanical regularization based on the potential FE energy as introduced in [6]:

$$\mathbf{u}^* = \arg \min \phi_{cor}(\mathbf{u}) + \alpha \left(\frac{1}{2} \mathbf{u}^T \mathbf{K} \mathbf{u} - \mathbf{u}^T \bar{\mathbf{f}} \right),$$

where ϕ_{cor} represents the classical DVC functional, \mathbf{K} the FE stiffness matrix and $\bar{\mathbf{f}}$ an approximation of distribution forces at the boundaries. This force distribution is calculated based on an *a priori* assumption

about the displacement field, which is obtained by initially solving the DVC problem with standard Tikhonov regularization.

The Cartesian partitioning employed for domain decomposition produces conforming and non-overlapping submeshes. To ensure that the submesh locally deformed by the computed solution \mathbf{u}^* remains fully contained within its corresponding subimage, we introduced a slight overlap in the volume image partitioning. The algorithm was constructed in 3 steps and implemented in Python for parallel solution with distributed memory. PETSc (`petsc4py`) is used for iterative and direct solving and domain decomposition management [7]. The first solution is computed in parallel with local solve on each subdomain. This step serves as an initialization for a global parallel solution with standard Tikhonov regularization. The obtained result initializes the distribution forces $\bar{\mathbf{f}}$ used for the mechanical regularization and then solves the global problem.

Results The proposed algorithm is used to solve the problem on $(827 \times 757 \times 761)$ voxels 8-bit 3D CT scans of an *in-situ* compression of a polyurethane foam cylinder (see, again, [1]). The tested sample has a diameter of 9 mm and a height of 10 mm. The considered stage of loading corresponds to a 3.4 %-overall strain in order. The voxel size is about $13.34 \mu\text{m}$. The mesh, shown on figure 1a, has 2 976 000 nodes and 8 928 009 elements. The average element size is 2.6 voxels. The convergence of a solution towards a displacement field at architecture scale and under little texture is demonstrated on figure 1b. The strong scalability of the proposed algorithm is illustrated on figure 1c. The sequential resolution on ISAE-Supaero cluster takes 34 min 25 s whereas the resolution with 32 processors takes 1 min 20 s.

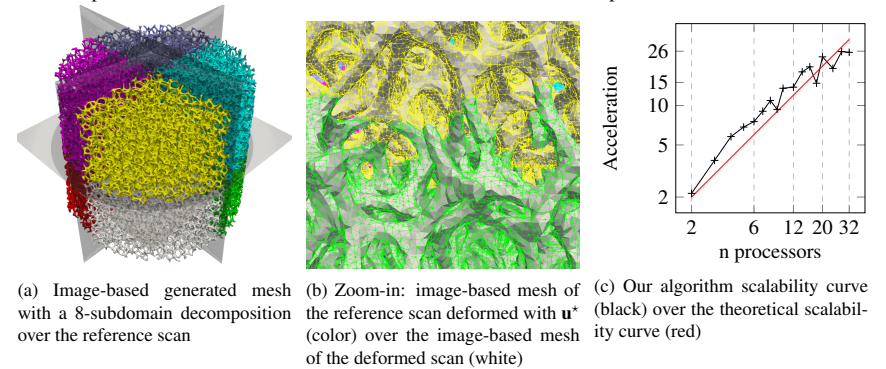


Figure 1: Mechanical and computational results of the proposed algorithm on a polyurethane foam.

Conclusion This study proposed a domain decomposition mechanically regularized FE-DVC algorithm for a parallel solution with distributed memory. The strong scalability of the implemented algorithm is demonstrated, opening the door for addressing highly complex applications starting by analyzing the other scans at higher deformation levels.

References

- [1] Rouwane, Doumalin, Bouclier and al. Architecture-Driven Digital Volume Correlation: Application to the Analysis of In-Situ Crushing of a Polyurethane Foam Experimental Mechanics, 63:897–913, 2023.
- [2] Wang and Kemao. Parallel computing in experimental mechanics and optical measurement: A review (II) Optics and Lasers in Engineering, 104:181–191, 2018.
- [3] Leclerc, Périé, Hild and Roux. Digital volume correlation: what are the limits to the spatial resolution? Mechanics & Industry, 13(6):361–371, 2012.
- [4] Couty, Witz, Lecomte-Grosbras, Berthe, Deletombe, Brieu. GPUCorrel: A GPU accelerated Digital Image Correlation software written in Python SoftwareX, 16:100815, 2021.
- [5] Bouclier and Passieux. A domain coupling method for finite element digital image correlation with mechanical regularization: Application to multiscale measurements and parallel IJNME, 111:123–143, 2017.
- [6] Réthoré, Muhibullah, Elguedj, Coret, Chaudet and Combescure Robust identification of elasto-plastic constitutive law parameters from digital images using 3D kinematics IJSS, 50:73–85, 2013
- [7] Balay, S., et al. PETSc/TAO Users Manual Argonne National Laboratory, 2024.

Image-based data pipeline for fusion engineering qualification and model validation

A. Tayeb, L. Fletcher, C. Hamelin

UK Atomic Energy Authority, Culham Science Centre, Abingdon, OX14 3DB, United Kingdom

Abstract – Our work focuses on gathering high fidelity data for model validation in fusion engineering. To this end, we carried out a full kinematic and thermal fields characterisation experiment of a heatsink mock-up design candidate to be deployed in future fusion powerplants. We used Digital Image Correlation (DIC) and Infra-Red Thermography (IRT) for kinematic and thermal fields measurements, respectively, as well as thermocouple measurements. We performed a thorough uncertainty quantification from an experimental point of view so that the data can be used for model validation.

Keywords – DIC, Model Validation, Extreme Environments, Uncertainty Quantification

Introduction

Qualification in fusion engineering is reliant on simulation of component performance under the extreme multi-physics fusion environment. It is therefore crucial to validate simulations under combined testable environments and extrapolate model predictions only for the untestable fusion neutron damage. This includes validation under high temperature, strong magnetic fields, and vacuum conditions. This can be achieved by designing data-rich experiments under combined thermo-mechanical loads coupled with the use of image-based diagnostics. DIC and IRT are among imaging techniques that are used extensively in experimental mechanics for material characterisation. In the recent years, the use of these techniques was extended to the framework of model validation in solid mechanics [1], [2].

In this work, we conducted a full kinematic and thermal field characterisation of a water-cooled heat sink mock-up under high heat flux and vacuum conditions. We performed a thorough uncertainty quantification for both the kinematic and thermal fields. We then used our uncertainty analysis to perform a quantitative comparison to our model.

Methods

The mock-up was made with 316L material and was tested in the Heating by Induction to Verify Extremes facility (HIVE) [3] at UKAEA. The sample geometry is a monolithic equivalent of the so-called thermal break design [4]. The heat flux was applied by induction heating of the top surface of the sample as a set of pulses of a duration of around 60s. Before the test, the sample surface was sprayed with a random black and white speckle pattern using high temperature paint that can resist up to 1000° C. The DIC set-up included two 24 MPx cameras coupled with pass-band blue filters to mitigate loss of contrast at elevated temperature. We used a 640 x 480 IR bolometer to monitor temperature fields in the same region of interest as the DIC. To this end, we carried out a combined DIC-IRT calibration procedure using a MatchID calibration target to have good contrast with both DIC and IR cameras. The advantage of such a calibration procedure is to gather both displacement and temperature data at the same locations with movement compensation for the thermal data based on the DIC displacements. We firstly performed a non-combined kinematic-thermal fields characterisation with the more complicated thermal break design.

Results

Fig. (1) shows the experimental set-up and the quantitative comparison between experimental and FE model results following image deformation validation procedure [1]. Then, we carried out the combined kinematic-thermal fields characterisation with the simple case of lab scale benchtop experiment of induction heating of a metallic plate in ambient air. The set-up for this experiment is depicted in Fig. (2) along with preliminary results in terms of displacement and temperature fields at one of the highest achieved temperatures. Finally, we carried out the combination of the two experiments with the 316L heat sink mock-up. The results for the mock-up will be presented at the conference.

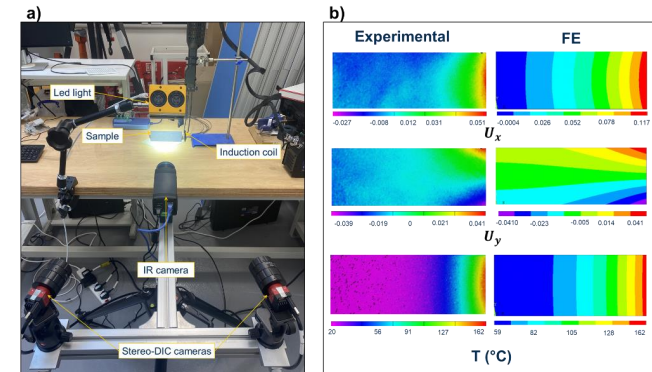


Figure 1: experimental set-up (a) and preliminary results from the combined DIC-Thermal benchtop experiment

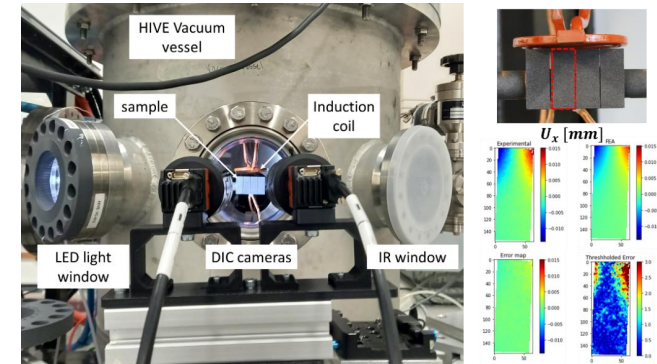


Figure 2: HIVE experimental set-up with preliminary quantitative validation for the horizontal displacement field

Discussion and Conclusion In this work we presented two different experiments using image-based data fusion engineering workflow. We obtained high fidelity data from the combined kinematic-thermal fields characterisation that will be used in the validation of both electro-magnetic thermal and thermal-structural FE models considering experimental uncertainties.

References

- [1] P., Lava and E. M., Jones and L., Wittevrongel and F., Pierron. (2020). Validation of finite-element models using full-field experimental data: Levelling finite-element analysis data through a digital image correlation engine. *Strain*, 56(4), e12350..
- [2] C., Sebastian and E., Hack and E., Patterson. An approach to the validation of computational solid mechanics models for strain analysis. *The Journal of Strain Analysis for Engineering Design* 2013;48(1):36–47.
- [3] D., Hancock and D., Homfray and M., Porton and B., Iain Todd and R., Bamber and K., Flinders, Testing advanced divertor concepts for fusion power plants using a small high heat flux facility. *JOTE*; 2018.
- [4] A., Lukenskas and T., Barrett and M., Fursdon and F., Domptail and F., Schoofs and H., Greuner et al. High heat flux test results for a thermal break DEMO divertor target and subsequent design and manufacture development. *Fusion Engineering and Design* 2019; 146:1657–1660.

Study of Non-Adiabatic Thermoelastic Effect in Face-sheet/Core Debonded Composite Sandwich Structures by Mean of Full Field Imaging

H.L. Emily Leung, R. Cappello, J.M. Dulieu-Barton and O.T. Thomsen

Bristol Composites Institute, School of Aerospace, and Mechanical Engineering, University of Bristol, Bristol BS8 1TR, UK

Abstract – An investigation of the non-adiabatic thermoelastic response from composite sandwich structures is presented, with a focus on a face-sheet/core interfacial debond. Sandwich structure beam specimens are tested in a 3-point bending configuration. Thermoelastic Stress Analysis is used on a region of interest that contains the a ‘through-thickness’ view of the sandwich beams. The overarching aim is to combine finite element numerical predictions with experimental findings to discern the severity of defects. The experimental results are shown to validate finite element numerical predictions, which, in turn, facilitate the exploration of surface and interface thermoelastic responses through the face-sheet of debonded sandwich structures.

Keywords – Thermography, Thermoelastic Stress Analysis, Finite Element Analysis

Introduction

Face-sheet/core debonding in composite sandwich structures can significantly reduce the stiffness and strength of the structure. A previous study [1] showed that the combined use of Finite Element (FE) analysis and full-field imaging techniques, including Digital Image Correlation (DIC) and Thermoelastic Stress Analysis (TSA), can identify the crack tip at the face-sheet/core interface and track subsequent damage propagation by viewing a sandwich beam specimen in the through-thickness direction. TSA is a non-contact full-field technique that employs infrared (IR) detectors to capture small temperature changes (ΔT) resulting from the thermoelastic effect within a structure. A general assumption is that a sufficiently high loading frequencies ensure adiabatic conditions and avoid heat transfer. Research [2] has shown that discontinuities at the interface of core and face-sheet of sandwich structures will result in stress concentrations and large gradients in ΔT . These embedded stress concentrations drive heat transfer through the face-sheet of the sandwich structure and can be detected on the surface of the specimen. When high thermal conductivity material are used, such as carbon fibre reinforced polymers (CFRP), the heat conduction is facilitated. Laminated CFRP composites have been the subject of prior investigations [3, 4], which showed that subsurface plies can influence the temperature retrieved at the surface. It has been shown that the non-adiabatic thermoelastic response can be used to reveal the location hidden debonded regions at the face-sheet/core interface through the CFRP face sheets [5]. In the present work, a FE model is validated to demonstrate that it can accurately predict the thermoelastic response at debonds in sandwich structures and then can be used to aid in characterisation of hidden defects in sandwich structures.

Materials and Methods

Sandwich specimens were manufactured using PVC foam core (Divinycell H100 manufactured by DIAB, Sweden) and pre-preg carbon fibre reinforced polymer face-sheets (IM7/8552). A 20 mm length of PTFE film was inserted between the face-sheet and core to create an artificial debond. The face-sheet was bonded to the core using a secondary bonding process with adhesive film. The sandwich specimens were loaded cyclically via a 3-point bending (3PB) setup, with frequencies ranging from 1.1 Hz to 10.1 Hz. An infrared (IR) camera was used for the region of interest was a through-thickness view of the specimens that included the debonded regions. Experimental results are compared with FE models constructed using Abaqus 2018. A Fortran user subroutine [4] was used to simulate the thermoelastic effect.

Discussion and Conclusion

Both experimental and numerical results show two areas of high ΔT at the bottom of the core, as illustrated in Figure 1(a) and (b). These high ΔT are caused by the discontinuity introduced by the debond, supported by their being location approximately 20 mm apart, which corresponds to the size of the debonding areas. Figure 2 shows the maximum ΔT observed on the left side of the core across

different frequencies. Both experiment and FE results give similar trends: a slight decrease in ΔT when the frequency is below 5 Hz, followed by an increase in ΔT between 5 Hz to 10 Hz. However, it is observed that the FE results generally are greater than the experimental results. This discrepancy may arise from uncertainties in material properties, or from the attenuation of the measured signal due to motion in the IR images underlining the need to compensate for the motion. In conclusion, there is general agreement between experimental and FE results. Future research will focus on accounting for the motion in the IR images using DIC experimental data. Furthermore, FE models will be used to explore the heat transfer at the fact-sheet/core interface.

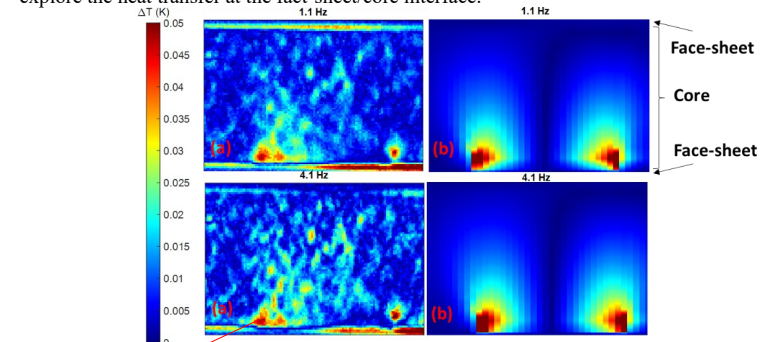


Figure 1: Thermoelastic responses (a) Experimental (b) FE

Max. ΔT on the left side of the core

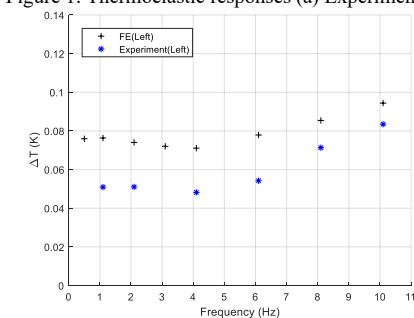


Figure 2: Thermoelastic responses at different frequencies

References

- [1] Wang, W., Martakos, G., Dulieu-Barton, J.M., Andreasen, J.H., Thomsen, O.T.: Fracture behaviour at tri-material junctions of crack stoppers in sandwich structures. *Compos Struct.* 133, 818–833 (2015). <https://doi.org/10.1016/j.compstruct.2015.07.060>
- [2] Johannes, M., Dulieu-Barton, J.M., Bozhevolnaya, E., Thomsen, O.T.: Characterization of local effects at core junctions in sandwich structures using thermoelastic stress analysis. *Journal of Strain Analysis for Engineering Design.* 43, 469–491 (2008). <https://doi.org/10.1243/03093247JSA389>
- [3] Wong, A.K.: A NON-ADIABATIC THERMOELASTIC THEORY FOR COMPOSITE LAMINATES. (1991)
- [4] Cappello, R., Pitarresi, G., Catalanotti, G.: Thermoelastic Stress Analysis for composite laminates: A numerical investigation. *Compos Sci Technol.* 241, 110103 (2023). <https://doi.org/10.1016/J.COMPSCITECH.2023.110103>
- [5] Leung H. L., Dulieu-Barton J.M. and Thomsen O.T. [Detecting debonded regions through the face sheets of sandwich structures using mirror assisted imaging techniques](https://www.icmcentral.org/Proceedings/ICCM23proceedings/papers/ICCM23_PPT_523.pdf), ICCM23, https://www.icmcentral.org/Proceedings/ICCM23proceedings/papers/ICCM23_PPT_523.pdf

Beyond Nyquist Theorem: Reconstruction algorithms of down-sampled signals for vision-based vibration measurements

D. Mastrodicasa^{1,2}, E. Di Lorenzo¹, B. Peeters¹, P. Guillaume²

¹ Siemens Industry Software NV, Interleuvenlaan 68, 3001, Leuven, Belgium

² Vrije Universiteit Brussel, Pleinlaan 2, 1050, Brussels, Belgium

Abstract

Mechanical products in industries such as automotive and aerospace are tested for validation using vibration measurements and experimental modal analysis. These tests are usually carried out using pointwise sensors connected to the structure. Image processing techniques like Digital Image Correlation (DIC) are developed to perform modal analysis. One area where DIC is of interest is in the use of cheap, light, and low-speed cameras for detecting the high-frequency behaviour of structures. This work focuses on the use of signal reconstruction algorithms for bandlimited signals, which makes it possible to go beyond the Nyquist Shannon frequency limit even without the use of high-speed cameras. The approach involves exciting a structure using a band-limited signal, reconstructing the output, and performing modal analysis. A numerical validation of the approach has been conducted on a simple simulated MDOF system. An experimental validation has been conducted on a simple cantilever beam.

Keywords – DIC, Modal Analysis, Vibration Analysis, Low-speed cameras, Down sampling

Introduction

Experimental Modal Analysis (EMA) is an important technology used to study structural dynamics. It breaks down complex phenomena into separate modes, which reveal natural frequencies, modal damping, and mode shapes [1]. These modes provide insights into the dynamic properties of structures and are derived from controlled forced vibrations and natural ambient vibrations [2-4]. Together, these modal parameters form a Modal Model that is crucial for various applications, from automotive to aerospace industries. It helps in the design, optimization, and validation of Finite Element (FE) models. Traditionally, EMA requires measuring system responses through point-wise sensors like accelerometers. However, this can be labor-intensive and introduce electrical noise [5]. Vision-based methods, such as Digital Image Correlation (DIC), are becoming increasingly popular because they enable full-field 3D measurements with high accuracy. DIC was traditionally used for static measurements but has now expanded into dynamic analysis. Phase-based Motion Magnification (PMM) and Lucas-Kanade (LK) optical flow offer similar approaches. Additionally, deep learning techniques are employed to predict displacements and strains, which outperform traditional methods in terms of computational time. These non-contact vision-based methods are useful in Structural Health Monitoring (SHM) in various fields, from aeroelasticity to wind energy and aerospace.

However, measuring high-frequency displacements presents challenges due to camera speed and resolution limitations. Recent advancements extend the use of low-speed cameras and down-sampling methods to accommodate the use of low-speed cameras for high-frequency measurements [6]. This paper presents a novel data acquisition and post-processing strategy to reconstruct high-frequency measurement responses without the need for single harmonic excitation.

This approach is numerically validated on a simple MDOF system. After, the methodology is applied on a simple cantilever beam, and validated against accelerometer data.

Methods

A bandlimited continuous-time signal, with the highest frequency (bandwidth) B Hertz, can be uniquely recovered from its samples provided that the sampling rate $F_s \geq 2B$ samples per second. $x_a(t)$ is the analogic signal, and it can be recovered in the time domain from its samples $x_a(nT)$:

$$x_a(t) = \sum_{n=-\infty}^{\infty} x_a(nT) \cdot \frac{\sin(\pi B(t - nT))}{\pi B(t - nT)} \cos(2\pi F_c(t - nT))$$

Results

Numerical validations have been conducted on a multi-degree of freedom system, shown in figure 2.9 The model is built with the following data: $k_1 = k_2 = k_3 = k_4 = 900 \text{ kN/m}$; $m_1 = m_2 = 50 \text{ kg}$; $m_3 = 20 \text{ kg}$; $c_{v1} = 25 \text{ Ns/m}$; $c_{v2} = 10 \text{ Ns/m}$; $f_1 = f_2 = 0$; $f_3 = \text{Chirp}$. The excitation is only in the m_3 mass and it is a windowed chirp defined in the range [50 – 75] Hz.

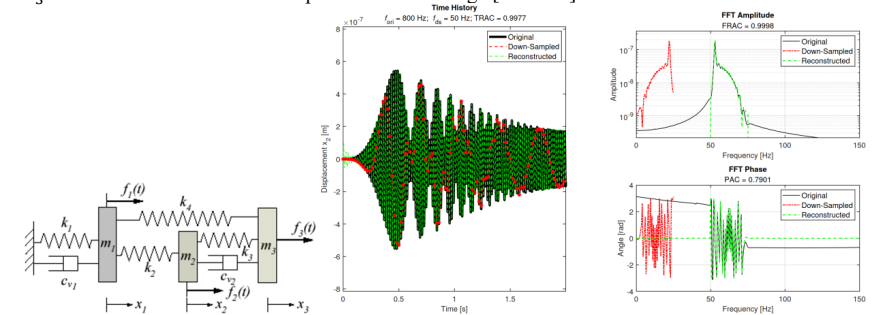


Figure 1 : MDOF Validation. a) MDOF model. b) Original-Down sampled-Reconstructed Signal in Time and Frequency domain.

To validate the methodology, the response x_2 is computed and considered (black signal). The x_2 signal is downsampled (red signal). Finally, the approach in Equation 1 is used to reconstruct the original signal and to compare the reconstruction with it (green signal). The reconstruction approach show high fidelity of the reconstructed data, showing a TRAC/FRAC values higher than 99% and a PAC value of 79%. The experimental validation is carried out on a cantilever beam excited by using an electrodynamic shaker in multiple sub-bands in the frequency range [0 – 800]Hz. The different sub-bands are reconstructed using Equation 1 and the FRF for each band is calculated. The results of the modal analysis procedure on 4 of the 40 sub-bands are shown in Figure 2 together with a comparison with the accelerometers.

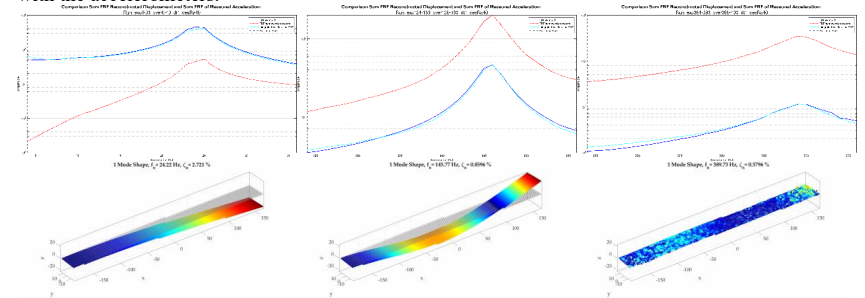


Figure 2 : Experimental Validation in the frequency bands a) 4-36 Hz b) 124-156 Hz c) 364-396 Hz.

References

[1] B. Peeters, H. Van der Auweraer, P. Guillaume, J. Leuridan, The polymax frequency-domain method: A new standard for modal parameter estimation?, Shock and Vibration 11 (2004) 395–409.

Practical assessment of DIC uncertainties in view of FE model validation

A. Peshave, P. Lava, F. Pierron

MatchID NV, Leikaai 25A, 9000 Ghent, Belgium

Abstract – The validation of structural models using Digital Image Correlation (DIC) is an emerging field. Using a DIC Digital Twin of the DIC experiments to create validation maps, it is possible to account for most of the systematic errors like limited spatial resolution or interpolation bias. The validation residuals then need to be compared to the random errors of the DIC set-up to decide whether or not there is still a model error present. This paper proposes a practical assessment of DIC errors and illustrates the remaining challenges, particularly for small elastic strains.

Keywords – DIC, Uncertainty quantification, Model validation

Introduction Digital Image Correlation (DIC) is an experimental technique used to measure full-field surface deformation using digital cameras. The data-rich nature of the resulting deformation fields makes it an ideal tool for detailed experimental validation of structural mechanical models, most often obtained with the finite element (FE) method. There is however limited literature on this topic. A recent approach has been recently proposed, the so-called 'DIC-levelling' method, which uses the model displacements to create a Digital Twin (DT) by numerically deforming the speckle images [1]. These images can then be processed with the same DIC parameters as the experiment to allow for a direct comparison in the form of a validation map. DIC uncertainties have been extensively studied in detail in the past [2], but not with a view to finite element model validation. The objective of the present paper is to propose a practical methodology to address DIC uncertainties in the context of FE model validation with DIC measurements.

Methods Table 1 lists the main uncertainties associated with DIC. The digital twin approach deals with interpolation bias, pattern induced bias and limited spatial resolution [1]. Therefore, this will not be studied here. We will concentrate on the remaining errors. Most of these are random errors that can be evaluated using stationary images, namely: Camera noise (CN), Noise induced bias (NIB) and Intensity digitization bias (IDB). CN arises from the random grey level noise at each pixel which creates a random deformation noise when processed through DIC [3]. NIB is generated by the interplay between camera noise and interpolation [3]. Digitization bias [2] arises from the digitization of the camera signal and depends on the bit depth used. The calibration errors have not been studied here and will be the object of a separate study. The remaining ones (7, 8 and 10) are errors that can only be minimized at setup stage. To study the above, a series of 100 stationary images were experimentally recorded on a glass/epoxy specimen with two asymmetric notches, using or not using cross-polarization to specifically study the effect of specular reflection. Displacement and strains were computed using the first image as reference and all others as deformed. The same was repeated by using the average of the 100 images as reference. This average was also used to simulate camera noise.

Results First, it was found that there existed a temporal bias caused by the fact that the noise copy of the reference image is present on all maps. Figure (1) shows a comparison between the simulation and the experimental noise on strain. The temporal bias is of the same order of magnitude as the standard deviation (noise floor) and has to be considered in the validation maps. Also, both random and bias errors are spatially dependent because of local changes of contrast and/or NIB. The experimental maps are well reproduced by the simulation, showing that we have captured the main sources of errors in this example. The paper will present more results on the effects of IDB, specular reflection, discuss heat haze and show the benefits of using an averaged image as reference.

Ref.	Name	Nature	Covered by
1	Camera noise	Random	Stationary images
2	Noise induced bias	Random*	Stationary images
3	Interpolation bias	Random*	Digital twin
4	Pattern induced bias	Random*	Digital twin
5	Intensity digitization bias	Random	Stationary images
6	Spatial filtering	Systematic	Digital twin
7	Specular reflection	Random*	Polarized light
8	Heat haze	Random*	Nothing
9	Calibration errors	Systematic	Rigid body movements
10	Camera heating	Systematic	Nothing (let camera heat up before test)

* deterministic but too complex, treated as random in practice

Table 1: Main sources of DIC uncertainties

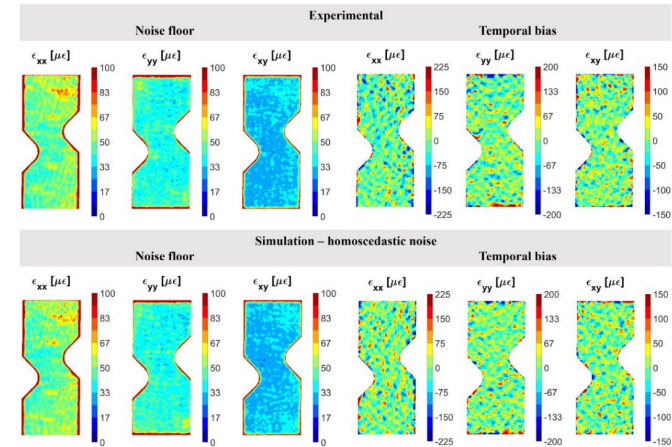


Figure 1: Comparison between experimental and simulated DIC errors

Discussion and Conclusion The paper will present additional results on the effect of specular reflection and heat haze. Conclusions will be drawn about practical establishment of noise floor values for model validation.

References

[1] Lava, P., et al., Validation of finite-element models using full-field experimental data: Levelling finite-element analysis data through a digital image correlation engine. *Strain*, **56**(4): pages. e12350, 2020.

[2] Fayad, S.S., D.T. Seidl, and P.L. Reu, Spatial DIC Errors due to Pattern-Induced Bias and Grey Level Discretization. *Experimental Mechanics*, **60**(2): pages. 249-263, 2020.

[3] Wang, Y.Q., et al., Quantitative Error Assessment in Pattern Matching: Effects of Intensity Pattern Noise, Interpolation, Strain and Image Contrast on Motion Measurements. *Strain*, **45**(2): pages. 160-178, 2009.

Characterization of deformation behaviour in metallic alloys using high-temperature digital image correlation analysis

Seung-Yong Lee, Junbeom Kwon

Materials Characterization Center, Korea Institute of Materials Science, 797, Changwon-daero, Seongsan-gu, Changwon-si, Gyeongsangnam-do, 51508, Republic of Korea

Abstract – Deformation behaviour accompanied with plastic instability, the Portevin-Le Chatelier (PLC) effect, was investigated by high-temperature tensile testing equipped with Digital Image Correlation (DIC) system at various temperatures and strain rates. With the help of the DIC analysis, high-temperature localized deformation bands, so-called PLC bands, in a gauge part were successfully characterized, and the nucleation and propagation behaviour of the PLC band varied depending on temperature and strain rate, which leads to the variation of serrated flow on stress-strain curve. Further, it was confirmed that the global strain behaviour of a gauge part is concentrated to the local strain in a PLC band, and consequently the local strain rate becomes remarkably high within a PLC band.

Keywords – Tensile property, Plastic instability, DIC, Local strain distribution

Introduction

High-temperature mechanical properties of metallic alloys are very sensitive to aspects such as the alloying elements and concentration, temperature and strain rate. Among many alloys, austenitic stainless steel (γ -STS) has been actively used at an elevated temperature for various applications. But, the stress-strain curve of γ -STSs shows serrated flow, which is known as the Portevin-LeChatelier (PLC) effect, in specific conditions, and this could affect its properties in positive or negative way. In order to control the mechanical properties of γ -STS, therefore, it is necessary to understand deformation behavior under the PLC effect. As motivated by this background, we applied DIC analysis for high-temperature tensile testing under various testing conditions using γ -STS to investigate the PLC effect from macroscopic and microscopic viewpoints.

Methods

The stable γ -STS, Fe-19Cr-13Ni-0.2C in mass%, was used in this study. For tensile testing, a plate-shaped test-piece with a gauge part of $50^l \times 10^w \times 2^t \text{ mm}^3$ in volume was prepared. Next, high-temperature tensile testing was carried out using an Instron-type tensile testing machine equipped with a heating furnace at temperatures from 723 K to 823 K under varying applied strain rates from 10^{-4} s^{-1} to 10^{-2} s^{-1} . The tensile deformation behavior was captured digitally with 2752×2200 pixels with sufficient high-time resolution using a three-dimensional camera system, ARAMIS 3D, developed by GOM. Next, the strain distribution and strain rate were analyzed by the GOM Correlate Professional. The gauge part of the tensile test piece was decorated by heat-resistant black-and-white sprays before the testing to form speckle pattern. The positional relations between the tensile testing machine, test piece and DIC camera system, and the decorated tensile test piece are shown in Fig. 1.

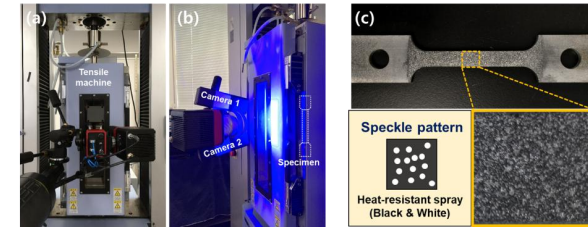


Figure 1 : High-temperature digital image correlation (DIC) analysis system ; (a) Front view and (b) side view showing the positional relationship between the DIC camera system and tensile testing machine ; (c) A tensile test piece decorated by heat-resistant black-and-white sprays.

Results and Discussion

The magnified image of stress-strain curves obtained by high-temperature tensile testing under various temperatures at an applied strain rate of 10^{-4} s^{-1} are shown in Fig. 2(a). A serrated flow associated with the PLC effect was observed in all stress-strain curves. The series of DIC images corresponding to the black arrows in Fig. 2(a) are indicated in Fig. 2(b). It is noteworthy that deformation of the gauge part of test piece proceeds with a localized deformation band, so-called PLC band; a PLC band nucleated at an edge of the gauge part and then propagated toward the opposite edge. Accordingly, the deformation of the gauge part is highly localized at the PLC band with a steep gradient of local strain, as shown in Fig. 2(b). It was found that the local strain rate inside the PLC bands is consistently much higher than the applied strain rate and gradually increases as the global strain increases, and finally the highly localized deformation behavior under the PLC effect results in the occurrence of necking deformation inside the PLC band. Therefore, in order to increase uniform elongation, it is important to control the local strain rate in PLC bands by careful control of the temperature and applied strain rate. (Detailed discussion will be presented in oral presentation)

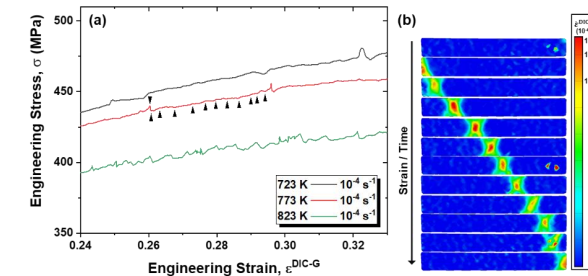


Figure 2 : Strain rate distribution map showing A-type PLC band propagation in the gauge part of a test piece deformed at 773 K/ 10^{-4} s^{-1} . Each image in (b) was acquired at the strain represented by the black triangles in the stress-strain curve in(a).

References

[1] Seung-Yong Lee, Chikako Takushima, Jun-Ichi Hamada and Nobuo Nakada, Macroscopic and microscopic characterizations of Portevin-LeChatelier effect in austenitic stainless steel using high-temperature digital image correlation analysis. *Acta Materialia*, 205:116560, 2021.

IBIS : Imaging bifurcations in 2D periodic metamaterials

M. Poncelet¹, C. Combescure², F. Amiot³

¹ Université Paris-Saclay, CentraleSupélec, ENS Paris-Saclay, CNRS LMPS - Laboratoire de Mécanique Paris-Saclay, 91190 Gif-sur-Yvette, France
² Saint-Cyr Coetquidan Military Academy, CRcC Saint-Cyr, 56380 Guer, France University Bretagne Sud, UMR CNRS 6027, IRDL, F-56100 Lorient, France
³ FEMTO-ST Institute, CNRS-UMR 6174 / UBFC, 24 chemin de l'Épitaphe, F-25030 Besançon, France

Abstract — Architected materials are often used for their high strength-to-weight ratio. For this matter, they are designed with high porosity which makes them sensitive to buckling under compressive loading. This buckling is usually predicted by numerical computations but very few experiments are available to confront these numerical results. Experimentally, the onset of instabilities is usually determined by following the global force applied onto the sample. However, this detection might be hindered by the presence of various defects which may locally trigger the instabilities. A very simple technique is proposed herein to detect instabilities in periodic architected materials using standard imaging techniques. It is shown to be applicable at a local scale, thereby allowing for a local instability detection. The method is implemented as an Octave/Matlab code which is freely available.

Keywords — Metamaterials, Bifurcations, Imaging

Introduction Architected materials are composite materials in which the macroscopic properties mainly emerge from the local organization of constitutive materials in space at the mesoscopic scale. When optimised to improve the stiffness-to-weight ratio, buckling at the mesoscopic scale becomes a possible mode of deformation of these materials[1]. While many studies are focused on the numerical prediction of this buckling[2], there are fewer experimental studies available to validate these numerical results[1]. The comparison criterion between numerical and experimental results is the onset of instability [3] traditionally identified using the global loading force maximum. However, this detection might be hindered, experimentally, by various defects in real systems which may locally trigger the instabilities[1]. The use of full-field kinematic measurements - e.g. Digital Image Correlation (DIC) - for architected materials is not new. Many different techniques have been developed to consider the fact that a large portion of the observed area, in these highly porous materials, is void and hence doesn't contain kinematic information. For DIC, one may for example circumvent the problem by adding a stiffness-free matter[4], use multiscale approaches[5], choose relevant element types (like beam in the case of lattice materials[6]), use high resolution cameras and a mesh based on the mesoarchitecture[7], etc. However all these techniques while providing many information, require non-negligible expertise and do not detect buckling, thus implying a secondary data-processing. This contribution focuses on a simpler way to exploit images to detect buckling.

Methods The specimen is a parallelepiped rectangle of hexagonal honeycomb. Displacement-controlled equiaxial bicompression tests are performed, with a setup which is instrumented with 8 load sensors to assess the force applied by each platens. The measured normal and tangential loadings are globally denoted as $T(s, n)$, with s spanning the $\{1 \dots 8\}$ range, and n denoting the image index. In the following, the results are displayed as a function of a global loading parameter $g(n)$ defined such that $T(s, n) \simeq g(n) \times f(s)$. The images $P(x, y, n)$ are obtained with a Digital Single Lens Reflex camera (70D, Canon) equipped with a 60-mm fixed focal lens (Canon), and are 3648×5472 pixels in size. x and y denote the position in the image's plane.

Denoting $\hat{P}(\xi, \eta, n)$ the Fourier transform of the windowed $\hat{P}(x, y, n)$, a global bifurcation indicator I_{AB} is defined based on $\hat{P}(\xi, \eta, n)$ [8] and implemented in the IBIS software [9].

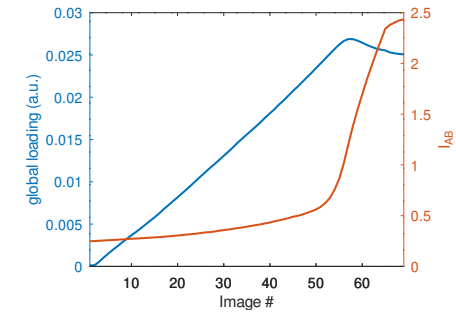


Figure 1: Global bifurcation indicator for the AB zone $I_{AB}(n)$ and the global loading parameter $g(n)$ as a function of the image index n .

Results This indicator is displayed together with the global loading parameter as a function of the image index in Fig. 1. The I_{AB} indicator remains almost constant throughout the specimen loading and suddenly increases when approaching the instability, as it is detected from the global loading maximum. The excellent agreement between the two indicators validates the proposed image-based indicator for the detection of the onset of instabilities in periodic architected materials. The same approach has been applied by subdividing the initial region of interest into subregions. This allows to reveal that buckling does not appear in a uniform manner across the sample.

Discussion and Conclusion The proposed technique, based on an image processing indicator, has been validated with respect to classical global loading maximum criterion. This image processing technique is only based on images obtained using a widespread camera. As a consequence, it could be used to provide feedback to the machine. It can also provide additional information on a possible non-uniform or premature buckling in the specimen that would not necessarily lead to a drastic change in the global loading indicator. Used as such or combined with a global loading measurement, our proposed technique is a new tool to better understand the local-to-global buckling transition in architected materials.

References

- [1] D.D. Papka and S. Kyriakides Biaxial crushing of honeycombs: - Part 1: Experiments. *Int. J. Solids Struct.*, 36, 4367-4396, 1999.
- [2] N. Triantafyllidis and M.W. Schraad Onset of failure in aluminum honeycombs under general in-plane loading *J. Mech. Phys. Solids*, 46, 1089-1124, 1998.
- [3] C. Combescure et al. Deformation Patterns and their Stability in Finitely Strained Circular Cell Honeycombs. *J. Mech. Phys. Solids* 142, 103976, 2020.
- [4] M. Poncelet et al. An experimental evidence of the failure of Cauchy elasticity for the overall modeling of a non-centro-symmetric lattice under static loading *Int. J. Solids Struct.* 147, 223-237, 2018.
- [5] F. Hild et al. Multiscale DIC applied to Pantographic Structures *Exp. Mech.* 61, 431-443, 2021.
- [6] A. Somera On the effective elasticity of quasi-periodic lattice materials : From microscopic foundations to experimental validation PhD thesis, Ecole centrale de Nantes, 2022.
- [7] A. Rouwane et al. Architecture-Driven Digital Image Correlation Technique (ADDICT) for the measurement of sub-cellular kinematic fields in speckle-free cellular materials *Int. J. Solids Struct.*, 234-235, 111223, 2022.
- [8] M. Poncelet, C. Combescure, F. Amiot Detecting bifurcations in 2D periodic metamaterials from images. *Materials Letters* 353, 135307, 2023.
- [9] F. Amiot, M. Poncelet, C. Combescure IBIS : Imaging BifurcationS <https://zenodo.org/records/8252796>

FE validation from DIC data: a practical case study in bending

V. Firouzbakht, A. Peshave, P. Lava, F. Pierron

MatchID NV, 25A Leiekaai, 9000 Ghent, Belgium

Abstract — The validation of structural models using Digital Image Correlation (DIC) is an emerging field. A very important aspect of this process is to be able to read the maps of strain differences between model and experiments, to isolate the sources of discrepancies. This paper provides a case study for a perforated blade in bending and reviews the different challenges associated with the validation.

Keywords — Model validation, Uncertainty quantification, Digital Twin

Introduction Digital Image Correlation (DIC) is an experimental technique used to measure full-field surface deformation using digital cameras. The data-rich nature of the resulting deformation fields makes it an ideal tool for detailed experimental validation of structural mechanical models, most often obtained with the finite element (FE) method. There is however limited literature on this topic. A corpus of work was published by the research group led by E. Patterson [1] using low pass filtering in the form of so-called shape descriptors (polynomials of different sorts). The DIC uncertainties are simply approached through a bending test on a beam. This suffers from the fact that it does not include the complex uncertainty quantification (UQ) arising from the highly nonlinear correlation algorithm. In particular, by using a bending test that leads to linear displacement distributions through the width, it ignores the interplay between the spatial frequencies in the model and the limited spatial resolution of DIC. A more advanced approach has been recently proposed, the so-called 'DIC-levelling' method, which uses the model displacements to create a Digital Twin (DT) by numerically deforming the speckle images [2]. These images can then be processed with the same DIC parameters as the experiment to allow for a direct comparison in the form of a validation map. Although very recent, this approach has already been confirmed as an essential tool for model validation by a few studies [3, 4]. However, an underexplored area is the process to use maps of differences between model and measurements to isolate the different sources of model errors. Here, a practical case study is presented.

Methods Measurements were carried out on a PMMA blade with a notch and a hole, clamped at the bottom and loaded in bending using a point load at the top. The load was measured as well as the deformation field using a stereo-DIC system. A finite element (FE) model was built-up, using the elastic properties measured during a monotonic tensile test. Perfect boundary conditions were also applied: clamp at the bottom, point load at the top. The model was then used to deform the experimental reference images, which were then processed with the same DIC parameters as the experiments, creating a one-to-one digital twin of the experiment [2]. This was done using the FEDEF module of the commercial software MatchID. The FEDEF maps could then be subtracted from the DIC maps to create error maps. A full validation is achieved when these maps only contain high frequency random errors within the bounds of the uncertainty evaluated on stationary images. Fig. (1) shows the longitudinal strain for the experiment, model (FEDEF) and the difference. One sees clearly that there is an error distribution that mimics the actual strain distribution. This suggests that the stiffness is incorrect. Indeed, because of the viscoelastic nature of PMMA, the monotonic loading Young's modulus E is higher than the long-term one activated in the experiment when load relaxation is left to happen before recording the deformed

images. Updating E to its long-term value, 3 GPa, this error vanishes (Fig. (2)). However, one can see a residual error at the bottom of the blade. This is caused by the fact that a perfect clamp does not reflect reality and in practice, a small rotation is always present. Measured boundary conditions were then applied to the bottom of the blade and this solved that problem. However, some errors still persisted and discussions about Poisson's ratio and how to obtain a realistic noise floor will be addressed in the presentation.

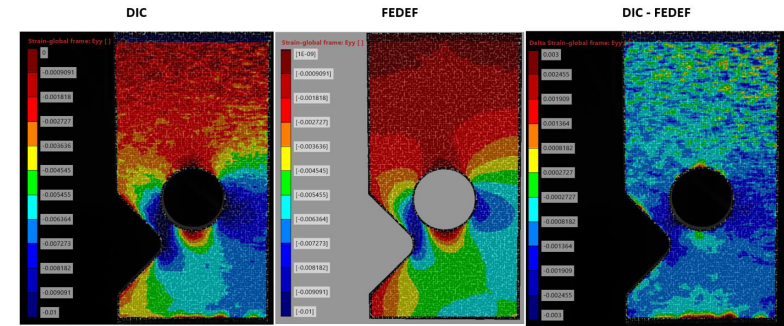


Figure 1: Comparison between experiment and model (FEDEF), longitudinal strain. Illustration of Young's modulus error (3.7 GPa instead of 3 GPa).

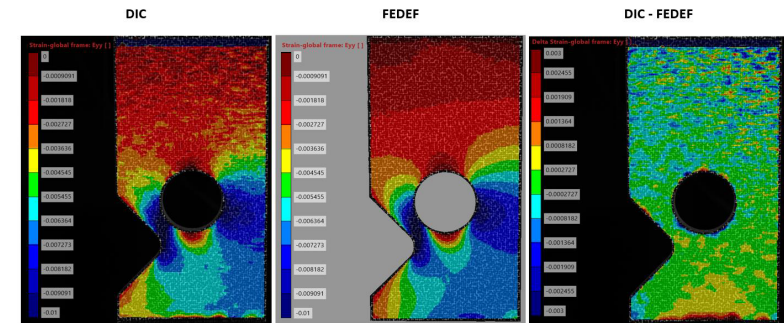


Figure 2: Comparison between experiment and model (FEDEF), longitudinal strain. Illustration of error on boundary conditions (perfect clamping at the bottom).

References

- [1] C. Sebastian, E. Hack, and E. Patterson. An approach to the validation of computational solid mechanics models for strain analysis. *The Journal of Strain Analysis for Engineering Design*, 48 (1):36–47, 2013.
- [2] P. Lava, E. M. C. Jones, L. Wittevrongel, and F. Pierron. Validation of finite-element models using full-field experimental data: Levelling finite-element analysis data through a digital image correlation engine. *Strain*, 56 (4):e 12350, 2020.
- [3] E. M. C. Jones, E. Corona, A.R. Jones, W.M. Scherzinger, and S.L.B. Kramer. Anisotropic plasticity model forms for extruded Al 7079: Part II, validation. *International Journal of Solids and Structures*, 213:148–166, 2021.
- [4] S. Gothivarekar, S. Coppieters, A. Van de Velde, and D. Debruyne. Advanced FE model validation of cold-forming process using DIC: Air bending of high strength steel. *International Journal of Material Forming*, 13 (3):e 409–421, 2020.

Thermal investigations of supercritical CO₂ jet impingement and jet structure influence on its cooling ability

M.El Nahas^{a,c}, T.Pottier^{a,*}, J.-J.Letourneau^b, M.Sauceau^b, Y.Landon^c

^aInstitut Clement Ader, University of Toulouse, CNRS, IMT Mines Albi, INSA, ISAE-SUPAERO, UPS, F-81013, France
^bLaboratoire Rapsodee, RAPSODEE, IMT Mines Albi, CNRS, University of Toulouse, 81013 Albi, France
^cInstitut Clement Ader, University of Toulouse, CNRS, IMT Mines Albi, INSA, ISAE-SUPAERO, UPS, F-31000, France

Abstract — This study intends to address thermal characteristics of supercritical CO₂ free jet impingement on a hot plate as well as the jet structure and characteristic parameters in order to know the evolution of in process parameters on the jet cooling ability. A first experimental approach has been chosen to assess the heat transfer coefficient (HTC) in various experimental conditions. Infrared thermography along with high-speed imaging are setup in order to access the cooling of a titanium plate. Another experimental approach is used to visualize and investigate jet structures and relies on a Schlieren Z-type imaging setup. Nozzle-to-plate distance critically impacts jet cooling, while mass flow rate dominates over initial pressure and temperature, with far-field turbulence offering prospects for optical flow velocity analysis.

Keywords — Thermography, jet impingement, high-speed imaging, heat transfer coefficient, extremely under-expanded jet.

Introduction In a context of safer, more cost-effective, and environmentally friendly machining processes, supercritical carbon dioxide (sCO₂) emerges as an alternative to the use of cutting fluids [1], particularly in drilling operations involving hard material with low thermal conductivity like titanium alloys (Ti-6Al-4V). The dual role of sCO₂ jet needed in this type of machining assistance has been the focus of interest, where enhancing chip removal through lubrication and improving cooling efficiency underscore its potential to extend tool life and reduce cutting forces [2]. However, a consolidated understanding of the optimal sCO₂ jet parameters for drilling remains unavailable and difficult to determine. Experimental work is here conducted to determine the cooling ability of this jet, first a thermal transfer study was conducted, and to better focus on the jet’s cooling ability, an in-depth analysis of the jet’s complex structure was carried out.

Methods This study proposes an experimental methodology to explore the thermal dynamics of sCO₂ jet exiting a nozzle of 250 μm inner diameter d_c and impinging a heated titanium thin plate. The cooling ability of the jet is determined through the space distribution of the heat transfer coefficient (HTC). Utilizing infrared thermography and high-speed imaging as shown in figure 1.a, the cooling process and the behavior of the sCO₂ jet were documented. In-process parameters such as nozzle-to-plate distance, jet angle of incidence, and sCO₂ initial temperature and pressure were systematically investigated to quantify their impact on the cooling efficiency. To explain the jet’s complex structure, an additional experimental study was conducted in a sealed transparent enclosure with a Z-type Schlieren setup (figure 1.b), using high-speed imaging to analyze the jet supersonic structures and parameters under varying pressures and temperatures in both near and far fields. Using this setup various jet parameters for extremely under expanded jets were determined, such as the mach disk diameter D_m , maximum barrel diameter D_{max} and mach disk location Z_m . The jet structure is studied for different initial pressures and temperatures and thus varying flow rates.

Results and Discussion The obtained results show that nozzle-to-plate distance is the key contributor to the cooling process. It is observed from figure 2.a that the HTC decreases non linearly with distance z . Additionally, the total power exchanged over a disk with radius $r = 35\text{ mm} = 140d_c$ (denoted H35 in figure 2.a) also decreases, leading to a longer cooling time from a specified temperature. Indeed, the HTC values rapidly drop when the jet is moved away from the plate, highlighting the importance of



Figure 1: a) Thermography of jet impingement on titanium heated plate imaging setup b) Schlieren experimental setup

understanding the complex nature of the jet at very short ranges as shown in figure 2.b. The results indicate that increasing the initial pressure leads to increase the overall size of the barrel shock. Its length Z_m and diameters D_m and D_{max} linearly increase with pressure. Bigger barrel shock, in turns leads to increase the jet momentum and seems responsible for the increase of the jet cooling ability, but at a cost of higher mass flow rate and thus CO₂ consumption.

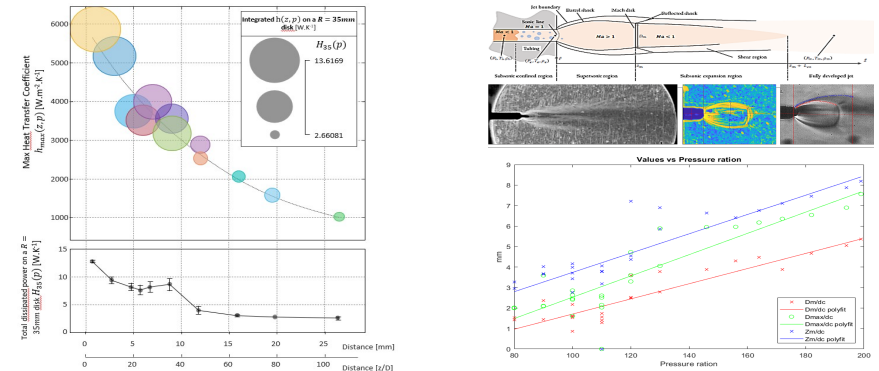


Figure 2: a) Evolution of the maximum HTC value and the overall cooling with respect to the nozzle-plate distance z of the impingement. b) Evolution of jet near field structure dimensions as a function of the pressure ratio using Schlieren optical technique

Conclusion The presented results show that the nozzle to plate distance plays a key and non linear role in the cooling ability of the jet. Initial pressure and temperature appears to be highly correlated through the influence of the mass flow rate. However both parameters do not seem to have any influence independently of their action on the mass flow rate. This latter parameter should therefore be regarded as another factor acting on the jet cooling ability. Velocities and temperature assessment from the near field imaging appears difficult because of the laminar nature of the jet in this region. However at lower magnification (far field), turbulence arise and may allow velocity assessment through optical flow algorithm. This latter approach constitutes the main perspective of the present work.

References

[1] L. Proud, N. Tapoglou, et T. Slatter, ' A Review of CO₂ Coolants for Sustainable Machining ' In *Proceedings of Imaging Understanding Workshop*, vol. 12, no 2, p. 283, fA©vr. 2022, doi: 10.3390/met12020283.
[2] T. Mulyana, E. A. Rahim, et S. N. Md Yahaya, " The influence of cryogenic supercritical carbon dioxide cooling on tool wear during machining high thermal conductivity steel ", *Journal of Cleaner Production*, vol. 164, p. 950-962, oct. 2017, doi: 10.1016/j.jclepro.2017.07.019.

The impact of metrics in mechanical imaging

Ahmed Chabib, Jean-François Witz, Pierre Gosselet, Vincent Magnier

Univ. Lille, CNRS, Centrale Lille, UMR9013 - LaMeube - Laboratoire de Mécanique, Multiphysique, Multi-échelle, F-59000, Lille, France

Abstract – Optical Flow (OF) is an alternative technique to the more classical digital image correlation methods (DIC), able to measure the motion between two images. It is a pixel-wise method, in the sense that the displacement is defined at each pixel and its computation does not require overpixel grids. This paper examines the impact on the identified strain field, the main quantity of interest for solid mechanics, of the metrics used to quantify the conservation of the optical flow and to impose the regularity of the displacement. The Charbonnier and Lorentzian loss functions are inspected in this work. A new regularization approach is used to locally vary the Tikhonov parameter using a mask in order to preserve the discontinuities and encourage the appearance of local phenomena while smoothing the computed fields elsewhere.

Keywords – DIC, PhotoMechanics, Optical Flow

Introduction Digital Image Correlation (DIC) and Optical Flow (OF) are pivotal techniques for analysing deformation and movement from image sequences in materials under stress which was done by the pioneering work of Horn and Schunck (HS) [1,2]. DIC, recognized for its high-resolution, full-field strain measurements, compares pre- and post-deformation images of materials to gauge displacement fields. Optical Flow, traditionally used in computer vision, measures pixel-level motion without physical contact with the object, suitable for delicate or heat-sensitive materials. Both techniques are based on the grey value constancy assumption, essential for calculating displacement fields. Optical Flow has seen significant advancements over the last four decades, improving in accuracy and robustness, particularly with the introduction of robust penalty functions that enhance outlier handling and detail preservation in dynamic scenes. This paper examines the impact of various metrics, especially robust ones, on the strain fields identified in solid mechanics, highlighting the advancements in Optical Flow for mechanical imaging applications.

Methods Optical flow techniques are based on the conservation of grey levels by transforming the image using a displacement field, as presented by Horn [1] and recalled here in equation 1.

$$E(u) = \int_{\Omega} \left(I_1(x) - I_2(x + u_h(x)) \right)^2 dx. \quad (1)$$

Our work takes up the classical method developed by D. Sun [3], the most important point of which is equation 2, which moves from quadratic metric to robust metrics by introducing the ρ function and analysing the impact on fields from mechanics.

$$E(u) = \int_{\Omega} \left\{ \rho \left(I_1(x) - I_2(x + u(x)) \right) + \lambda \left(\rho \left(\nabla_x u \right) + \rho \left(\nabla_y u \right) \right) \right\} dx. \quad (2)$$

Here, I_1 is the reference image, I_2 the distorted image, u the displacement at each pixel, ρ the metric, and λ the regularisation parameter.

The solving process is the same as that presented in [3], but accelerated by GPU and matrix-free methods. This method is therefore an improvement and a generalisation of the HS method. To find the improved HS method, simply take $\rho(x) = x^2$. The Lorentzian metric ($\rho(x) = \log(1 + \frac{x^2}{2\sigma^2})$, $\sigma > 0$) is presented here using the quadratic metric as a reference.

It is important to note that to arrive at a converged solution with robust metrics, a number of steps are required, which are detailed in [2]. Modern code written in Python that allows these methods to be used on modern camera sensors using matrix-free methods is available [here](#).

Results A synthetic isotropic elastic cracking displacement field and a simple one-pixel vertical shift were applied to a synthetic image in order to compare the performance of the two metrics, as shown in Figure 1.

A natural measure of quality in this context is the Average Endpoint Error ($AEE^2 = (\|u - \hat{u}\|^2 + \|v - \hat{v}\|^2) / N^2$) which corresponds to the average (over N pixels) of the Euclidean distance between the calculated horizontal and vertical displacements (u, v) and the ground truth.

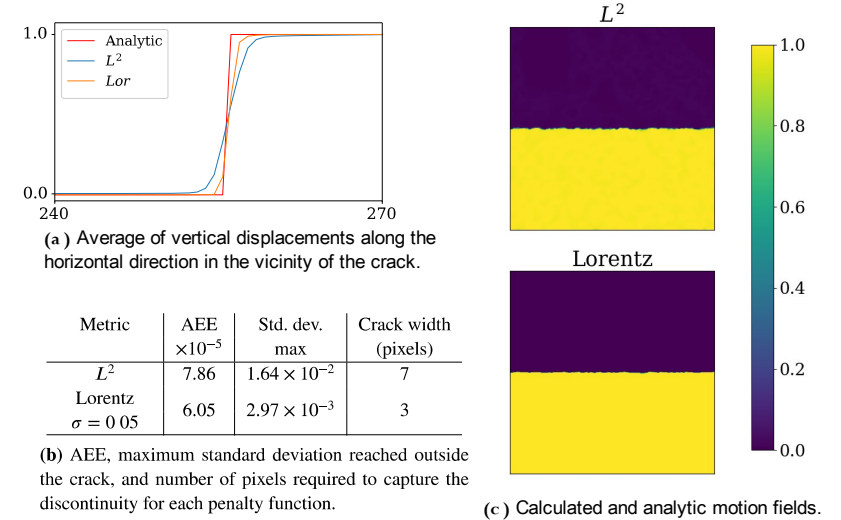


Figure 1: Results of the methods on virtual crack.

Figure 1 (a) clearly shows that the results are much more diffuse with the use of the L^2 metric, which is also illustrated in Figure 1 (c). The table in Figure 1 (b) also shows that the AAE and standard deviation are much higher for the L^2 metric, demonstrating the superiority of this method for this type of test.

Discussion and Conclusion The use of pixel-level optical flow methods in the context of mechanical testing with robust metrics reduces measurement uncertainties and also increases the resolution of measurement since it is conducted at the pixel level. Thus, with a standard L^2 norm and an acceptable level of noise, it is possible to capture discontinuities in 7 pixels, and the introduction of a robust metric, like the Lorentzian one, reduces this to 3 pixels in test images while decreasing the measurement uncertainties. These methods have also been tested on mechanical tests involving heterogeneities, requiring new learning and presenting new challenges that will be discussed at the conference.

References

- [1] B.K.P. Horn, G. Schunck., Artificial Intelligence 1981, 17, 185–203.
- [2] A. Chabib *et al*, GPCU_OpticalFlow: A GPU accelerated Python software for strain measurement, SoftwareX,
- [3] Sun, D. *et al*. Secrets of Optical Flow Estimation and Their Principles. *CVPR 2010*

Vibration Measurements: Effect of Varying Exposure Time on Digital Image Correlation

Hubert Schreier^{1*}, Nadine Koehler²

¹Correlated Solutions Inc., 121 Dutchman Blvd., Irmo, 29063, SC, USA. ² isi-sys GmbH, Wasserweg 8, Kassel, 34131, Hessen, Germany.
 * Corresponding author(s): E-mail:schreier@correlatedsolutions.com; Contributing authors: nk@isi-sys.com

Abstract — Digital image correlation (DIC) in combination with high-speed cameras has found many applications in vibration analysis. This article investigates how the exposure time used for image acquisition influences the measurement results. A simple experiment to measure the amplitude attenuation and phase shift as a function of exposure time is described and used to verify the assumption that a moving average filter applied to the image intensities indeed corresponds to a moving average filter applied to the measured displacement amplitudes. A normalized filter transfer function is presented to estimate and correct errors in vibration amplitudes measured with DIC. Furthermore, the suitability of using long exposure times to suppress aliasing artifacts is discussed.

Keywords — DIC, vibration measurement, exposure time, temporal aliasing, filter transfer function, phase shifted image acquisition

Introduction Digital image correlation [1] can be used for vibration analysis by transforming a time sequence of full-field displacements into the Fourier domain. This has been used to study a variety of vibration phenomena with excellent results, first time applied with the VIC-3D FFT module on diesel engine components in 2011 [2]. High speed cameras are typically used for these applications to acquire images at a rate sufficiently faster than the vibration frequencies of interest. With phase shifted recording in relation to a periodic, reproducible excitation signal in combination with synchronized stroboscopic illumination, high acquisition rates could be simulated with a low-speed system [3]. Cameras integrate incoming light that is incident on their pixels over an adjustable exposure time. Depending on available light, the exposure time required to produce an image of sufficient contrast and brightness for image correlation can be a significant fraction of the sampling interval, particularly in high-speed applications. It is intuitively clear that averaging of light intensities over a given time period produces a low-pass filtered intensity signal, and that it should similarly produce a low-pass filtering effect for the displacement signal extracted from the images. However, it is not immediately obvious whether the low-pass filter response of the displacement signal matches that of the intensity or gray value signal. The effect of long exposure times on vibration measurements has been described in [4], where the authors measured an intentionally aliased spectrum with a short and long exposure time and observed nominal antialiasing for the longer exposure time. Properties of the low-pass filter were not described in detail in their study.

Methods A stereo image correlation system was used to measure the vibration response of a loud-speaker to a sinusoidal drive signal generated by a function generator. The cameras were triggered at known phase offsets to the excitation signal by means of an ATB-V trigger device from Correlated Solutions, Inc. To obtain an approximation of the actual vibration amplitude, a reference sequence was obtained at very short exposure time. Then, multiple sequences at increasingly longer exposure times were obtained to measure the amplitude attenuation as a function of exposure time for a fixed frequency. In a separate measurement, the amplitude attenuation for a fixed exposure time was measured as a function of frequency. In a third measurement, the speaker was driven from a PC sound card through an amplifier with a signal containing two sine waves of different frequencies, and the image data was recorded with

a medium speed camera system at a fixed acquisition rate. For the first two experiments, the amplitude attenuation and phase shift were measured by least-squares fitting of the displacement data in the time domain, whereas for the third experiment, the attenuation was computed using Fourier analysis.

Results The experimental results demonstrate that the amplitude attenuation as a function of exposure time and frequency corresponds to that of a running average filter with a transfer function of

$$H(f) = \text{sinc}(t_e f) = \frac{\sin(\pi t_e f)}{\pi t_e f}, \quad (1)$$

where t_e is the exposure time and f is the frequency. The response function was characterized up to the fourth zero-crossing of the sinc-function and showed excellent agreement with the theoretical values.

Discussion and Conclusion To discuss the implications of the experimental results, a normalized version of the transfer function is shown in Figure 1. Here, the frequencies on the abscissa are normalized by the Nyquist frequency, and transfer functions are shown for varying fractions of the maximum exposure time possible, which corresponds to the reciprocal of the sampling frequency. For the maximum normalized exposure of 100%, the attenuation at the Nyquist frequency is about 63.7%. The filter passes substantial amplitudes above the Nyquist frequency and goes to zero at twice the Nyquist frequency. The first side-lobe passes over 20% of the signal, which would appear as an alias. Given those characteristics, using long exposure times does not appear to be a promising approach to mitigating aliasing artifacts. The plot on the right of Figure 1 shows only the 5% error band on the y-axis for frequencies up to the Nyquist frequency. If one aims to keep the amplitude errors due to the averaging effect of the exposure time below 1%, the exposure should be kept below approximately 15% of the interval between frames. If longer exposure times are required, Eq. 1 can be used to compute an inverse filter to correct the measured amplitudes. This was applied to the third experiment conducted in this study, where the speaker was driven with two superimposed sine waves, with excellent results.

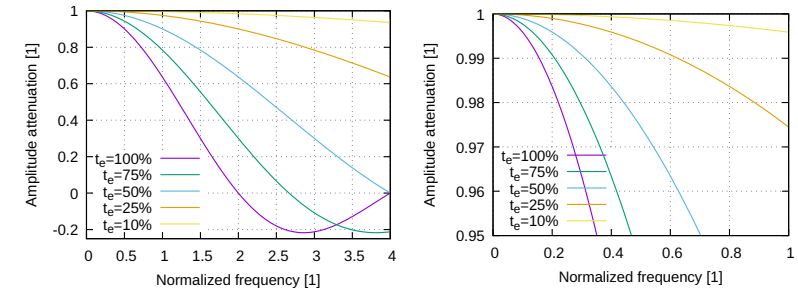


Figure 1: Amplitude attenuation for normalized exposure times versus normalized frequency. Left: full-scale version up to four times the Nyquist frequency. Right: Detail showing the 5% error band up to the Nyquist frequency.

References

- [1] M.A. Sutton, J.-J. Orteu, H. Schreier, *Image correlation for shape, motion and deformation measurements: Basic Concepts, Theory and Applications*, Springer, New York, NY (USA), 2009.
- [2] Dr.-Ing. P. Maeckel *Ganzflächige 3D Betriebsschwingungsanalyse mit der Stereobildkorrelation beim Hochlauf eines Dieselmotors* Technical report, isi-sys GmbH, 2011/12. <http://www.isi-sys.com/download/Betriebschwingungsmessung-Daimler.pdf>
- [3] H.W. Schreier, Peter Maeckel, *Visualization, measurement and analysis of vibration objects.*, United states patent application publication, December 2005.
- [4] P. Reu, D. Rohe, L. Jacobs, *Comparison of DIC and LDV for practical vibration and modal measurements*, Mechanical Systems and Signal Processing 86, 2016 <https://doi.org/10.1016/j.ymssp.2016.02.006>

Multi-physic calibration for coupled IR Thermography - Stereo DIC sensor: from target to software

T. Sentagne^{1,2}, C. Simond¹, J.E. Dufour², R.Fouque¹, J.N. Périé²
 sentagne@insa-toulouse.fr

1. **Direction Générale de l'Armement (DGA)**, Balma, France
 2. **Institut Clément Ader (ICA)**, Université de Toulouse, CNRS/INSA/Mines Albi/UPS/ISAE, Toulouse, France

Abstract — Acquiring rich multi-physics data is becoming essential for characterising thermo-mechanical constitutive relations. Stereo Digital Images Correlation and Infra-Red Thermography sensors can be coupled for this purpose but need to be calibrated. This paper presents a multi-physics calibration method. It is based on a laser marked bi-spectral target pattern and uses a (2+1) calibration algorithm to characterise the parameters of the camera model.

Keywords — Bi-spectral measurement, Uncertainty quantification, Global methods

Introduction The growing complexity of constitutive relations, together with the costs associated with mechanical tests, drives the need for advanced test/calculation dialogue methods based on dense measurement data. To address this challenge, full field measurements such as (Stereo) Digital Images Correlation ((S)DIC) for kinematic measurements, Infra-Red Thermography (IRT) for thermal measurements, or even the coupling of both [3] are therefore good candidates to satisfy the growing need for large amounts of data.

Facilitating the thermo-mechanical test-simulation dialogue by measuring the thermal and kinematic field on the same basis as simulation thanks to an analysis-suitable IRT-SDIC coupling is a topic which we would like to address. Achieving this first requires the development of a coupled calibration method for a multi-physics sensor system (IRT + DIC). This paper presents a multi-physics calibration methodology based on a bi-spectral target pattern and a (2 SDIC cameras + 1 IRT camera) calibration algorithm.

Methods The multi-physics calibration method consists in characterizing the parameters of a camera model, noted \underline{P} , for each camera [1]. The parameters of this model are divided into two families: (1) intrinsic parameters, denoted \underline{p}_{int} , which represent the physics of the sensor; and (2) extrinsic parameters, denoted \underline{p}_{ext} , which represent the position of the sensors in a physical space. Both parameters type is concatenated into $\underline{p} = (\underline{p}_{int}, \underline{p}_{ext})$. This camera model can be used to project from a 3D physical space to a 2D image space, such as:

$$\underline{P}(X, Y, Z) = [u, v]^T. \quad (1)$$

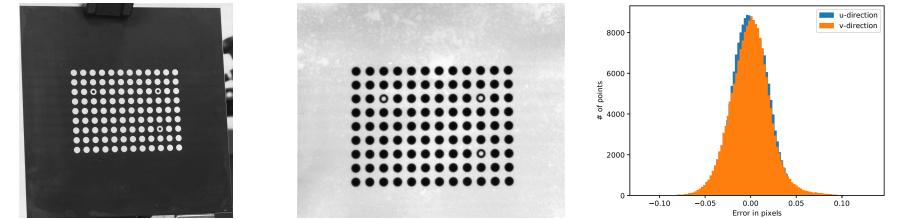
In a first step, the set of parameters \underline{p}_{int} is determined for the SDIC and IRT cameras independently. In a second step, the stereo-rig's \underline{p}_{ext} parameters are obtained and the IRT camera position is then registered in the visible camera frame. This approach, called in this paper (2+1) calibration algorithm, is therefore adopted to characterise the parameters of the camera model \underline{P} during calibration. For each camera, to achieve the parameters characterisation, a Levenberg-Marquardt algorithm is used to minimise (2) :

$$F(\underline{X}, \underline{Y}, \underline{Z}, \underline{p}) = \frac{\sum_i \sum_j \left\| \underline{P}_i(X_j, Y_j, Z_j) - (\hat{u}_{i,j}, \hat{v}_{i,j})^T \right\|_2^2}{\sigma_d^2}, \quad (2)$$

where i and j are respectively the image and point indices, (u, v) the projected coordinates of the target pattern, (\hat{u}, \hat{v}) the detected coordinates and σ_d the random error associated to the point detection algorithm. The latter makes it possible to take into account the greater uncertainty associated with point detection by the IRT sensor in extrinsics parameter identification.

To do this, a bi-spectral target exhibiting suitable digital level gradients in both visible (Fig.1a) and IR wavelengths (Fig.1b) is developed using a laser marking technology. A laser is used to create a reaction on the surface of the sample, changing the emissivity of the material at the targeted location. The advantage of this method is that it makes it fast and simple to manufacture a target.

Results Series of 100 images were taken for different target pattern positions. For each position, a point detection is performed on an image averaged over the 100 images and used as a reference (free noise assumption). A detection is then performed on the 100 images and an absolute error is calculated. Histogram of these error is plot on Fig.1c. It can be seen that the detection error distribution is Gaussian and centred around 0 (by comparison to the standard deviation). This noise is propagated in the algorithm to characterise the parameter identification uncertainties of the camera model.



(a) Left visible image of the target pattern (2048 × 2048) pixels

(b) Thermal image of the target pattern (640 × 512) pixels

(c) Error of center point detection for IRT ($\sigma_d = 0.02$ pixel)

Discussion and Conclusion This work therefore proposes a robust multi-physics sensor calibration method based on a bi-spectral target pattern and a (2 SDIC cameras + 1 IRT camera) calibration algorithm. An evolution of this method would be to develop an algorithm based on the simultaneous calibration of the three cameras that make up the multi-physics sensor, allowing a better mitigation of calibration uncertainties.

References

- [1] Cholewa, N. and Summers, P.T. and Feih, S. and Mouritz, A.P. and Lattimer, B.Y. and Case, S.W., *A Technique for Coupled Thermomechanical Response Measurement Using Infrared Thermography and Digital Image Correlation (TDIC)*, Experimental Mechanics, 2015.
- [2] D. Garcia, *Mesure de formes et de champs de déplacements tridimensionnels par stéréo-corrélation d'images*. Institut National Polytechnique de Toulouse - INPT, 2001.
- [3] L. Li, J.-M. Muracciole, L. Waltz, L. Sabatier, F. Barou, B. Wattrisse, *Local experimental investigations of the thermomechanical behavior of a coarse-grained aluminum multicrystal using combined DIC and IRT methods*. Optics and Lasers in Engineering, 2016.
- [4] T. Pottier, F. Toussaint, H. Louche, P. Vacher, *Inelastic heat fraction estimation from two successive mechanical and thermal analyses and full-field measurements.*, European Journal of Mechanics - A/Solids, 2013

Isogeometric surface fitting from tomographic images

D. Bichet^{1,2}, R. Bouclier^{1,2}, J-C. Passieux², J-N Perié²

¹ Institut de Mathématiques de Toulouse, INSA/UT1/UT2/UT3, Toulouse, France, dbichet@insa-toulouse.fr, bouclier@insa-toulouse.fr
² Institut Clément Ader, INSA/ISAE Supaéro/Mines Albi/UT3, Toulouse, France, passieux@insa-toulouse.fr, jean-noel.perie@iut-tlse3.fr

Abstract — Manufactured lattice structures often deviate from their original *as-designed* CAD models, which can greatly affect their mechanical response. In this work, a method is proposed to adjust an existing CAD model so that it matches *as-manufactured* defects using image-based techniques within a B-spline framework. By regularizing a Virtual Image Correlation method with a membrane strain energy and a high regularity multipatch interconnection, our approach achieves accurate shape measurement with pixel accuracy.

Keywords — Active Contours, Virtual Image Correlation, Multipatch B-spline, Lattice structure

Introduction Additive Manufacturing (AM) processes open the door to the creation of increasingly complex structures. Lattices are cellular architected structures known for their ability to achieve high specific characteristics. When manufactured, lattice structures exhibit geometrical defects that can be revealed by X-ray computed tomography reconstructed volume images (3D CT). The Marching Cubes algorithm is then typically used to extract a triangular surface mesh from the 3D CT. This mesh can contain a very large number of nodes, depending on the size of the image. From it, a volume mesh can be built and used to compute the mechanical response of the structure, showing that the defects may strongly impact the mechanical properties [1]. However, such methods based on finite elements are notoriously expensive to compute. Besides, because the mesh is in a different format than the initial *as-designed* CAD model, characterizing the geometrical transformation is challenging.

This work focuses on constructing an explicit CAD description of a real *as-manufactured* lattice part. This process uses a theoretical *as-designed* CAD geometry and an implicit description of the real part as a 3D gray-level image. Lattices are complex geometric objects that require a multipatch B-spline representation [2]. The proposed method conforms to the Active Contours framework [3], where the gray-level metric is inspired by the Virtual Image Correlation method [4, 5]. The regularization is divided into two parts : inside a B-spline patch, a membrane elasticity constraint [6] is weakly prescribed, while another method is used to impose a high regularity multipatch continuity between patches.

Methods The multipatch B-spline surface geometry depends on the position of its control points. To deform this geometry, each control point undergoes a displacement \mathbf{U} . These displacements are the degrees of freedom of the problem. They are computed by minimizing a sum of cost functions, also called energies:

$$\min_{\mathbf{U}} (E_{image}(\mathbf{U}) + \alpha E_{intra}(\mathbf{U}) + \beta E_{inter}(\mathbf{U})) \quad (1)$$

- E_{image} : This energy is used to attract the geometry to the good location in the image. Given the amount of data contained in a 3D CT, performing calculations on the entire image would be very costly. Therefore, the virtual image correlation is used as the image energy.
- E_{intra} : This energy is used to regularize the problem within a B-spline patch. The intrinsic regularization of B-splines makes Virtual Image Correlation work well with relatively coarse meshes. However, as the spline mesh is refined, tangential deformations that preserve the geometry degrade the conditioning of the problem. An additional regularization is therefore needed. Here, bi-laplacian or gradient-based regularizations, which are commonly used in the literature, appear

to degrade the results by also penalizing out-of-plane displacements. As a remedy, the regularization term proposed in this work is based on the membrane strain energy. This energy increases when the surface is subjected to tangential strains, such as in-plane shear and stretching. This regularizes the in-plane deformation while leaving the out-of-plane modes unaffected.

- E_{inter} : This final energy regularizes the inter-patch problem. It takes the form of a penalization term that ensures higher regularity (C^1) at the interfaces between the patches.

Results The problem was solved using the Gauss-Newton algorithm on a $267 \times 327 \times 327$ voxels binned 3D CT of a nylon lattice strut, measuring approximately 13 mm long and 4 mm in diameter. The multipatch B-spline geometry shown in Fig.1b consists of 6 patches, each forming $\frac{1}{6}$ of a tube containing 2×4 B-spline elements. With degree 2 basis functions, the mesh contains 144 nodes, reduced to 108 after eliminating duplicate nodes at patch edges, resulting in a sparse problem with 324 degrees of freedom. This is a significant improvement over the Marching Cubes mesh of Fig.1a. Virtual Image Correlation, spanning 10 voxels above and below the B-spline surface, explores the image with approximately 8 integration points per voxel. Fig.1b demonstrates the ability of the method to detect complex defects. A distance field estimator to the actual surface in the *as-manufactured* 3D CT is presented in Fig.1c. This estimator illustrates the ability of the method to correct defects from approximately six voxels to less than one voxel.

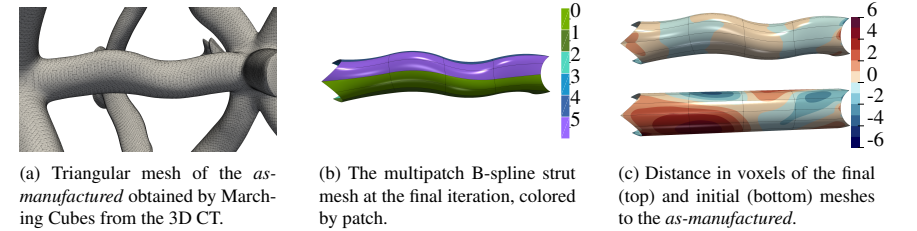


Figure 1: Example of applying the developed surface fitting method to the strut of a lattice structure.

Discussion and Conclusion In summary, the accuracy of the image resolution is achieved with the proposed method, highlighting the efficacy of the regularization techniques. The explicit representation of the *as-manufactured* geometry, along with the introduction of a morphing field, will facilitate quantitative assessment of geometric defects and enable the development of more cost-effective numerical simulations [7].

Acknowledgements This research was supported by the French Agence nationale de la recherche under grant ANR-22-CE46-0007 (AVATAR).

References

- [1] Lu Liu, Paul Kamm, Francisco García-Moreno, John Banhart, and Damiano Pasini. Elastic and failure response of imperfect three-dimensional metallic lattices: the role of geometric defects induced by Selective Laser Melting. *Journal of the Mechanics and Physics of Solids*, 107:160–184, October 2017.
- [2] L.A. Piegl and W. Tiller. *The NURBS Book*. Monographs in visual communication. Springer, 1995.
- [3] Michael Kass, Andrew Witkin, and Demetri Terzopoulos. Snakes: Active contour models. *International Journal of Computer Vision*, 1(4):321–331, January 1988.
- [4] Marc L.M. François, Benoit Semin, and Harold Auradou. Identification of the Shape of Curvilinear Beams and Fibers. *Applied Mechanics and Materials*, 24-25:359–364, June 2010.
- [5] Jean-Charles Passieux, Robin Bouclier, and Oliver Weeger. Image-based isogeometric twins of lattices with virtual image correlation for varying cross-section beams. *International Journal for Numerical Methods in Engineering*, 2023. Publisher: Wiley.
- [6] J. Kiendl, K. U. Bletzinger, J. Linhard, and R. Wüchner. Isogeometric shell analysis with Kirchhoff–Love elements. *Computer Methods in Applied Mechanics and Engineering*, 198(49):3902–3914, November 2009.
- [7] Robin Bouclier and Thibault Hirschler. *IGA: Non-conforming Coupling and Shape Optimization of Complex Multipatch Structures*. Wiley, 1 edition, June 2022.

A Verification Method for Stereo-DIC for Use in the Forming Limit Standard Test

Method

M.A. Iadicola

National Institute of Standards and Technology, Gaithersburg, Maryland, USA

Abstract

To develop a verification procedure for use in the ASTM International E2218 Standard Test Method for Determining Forming Limit Curves, a series of assessments are made on a typical stereo digital image correlation (DIC) system set up for this purpose. The assessments include those used in other standard methods chosen to ensure the system meets all the needs for the intended use. This combined assessment is based on the iDICs Measurement Uncertainty Guide for DIC currently in development. By testing both a well-designed and calibrated system, as well as systems with inferior calibration, the required pass/fail limits are determined for this intended use.

Keywords – DIC, Standards, Forming Limit Test

Introduction

DIC has been extensively used in mechanical testing research; however, use in standardized testing has been limited. The majority of DIC use in standards has been as replacement of two-point mechanical extensometers with virtual extensometers (i.e. in ASTM E83 [1] and ISO 9513 [2]) at gauge lengths of 10 mm or larger. These standards use a process of traceable verification and classification to assess the measurement accuracy limits of a given extensometer system. The verification process interrogates the predominant forces of measurement error (bias and uncertainty from a traceable reference), while the classification sets envelopes of expected performance. Other documentary standards and specifications specify the class of extensometer required for a given measurement based on consensus opinion and testing experience. Less common are standards that use DIC on an *ad hoc* basis for specific standard tests where DIC has substantial advantage over more traditional methods of measurement (e.g. forming limit testing ASTM E2218 [3] and ISO 12004-2 [4]) when a field of strain measurements is needed. The *ad hoc* use is typically less broadly applicable unlike the extensometer usage, and this limited application space leads to limited, or no, traceable verification requirements. The justification is a matter of necessity for tests where a mechanical contacting extensometer can make testing nearly impossible, e.g. thin foil testing to miniature uniaxial test specimens.

The ASTM E28.01 subcommittee on Calibration of Mechanical Testing Machines and Apparatus has a task group looking into expanding the use of DIC with traceable verification and system check requirements for DIC at much smaller length scales. This work is in support of a proposed change to E2218 [3] forming limit test standard to make its use of DIC more rigorous and the measurements more trustworthy. This test takes a clamped flat sheet metal specimen and stretches it with a 100 mm diameter dome shaped punch until necking or failure, which typically occurs with 15 mm to 30 mm of punch displacement. Obviously, 2D-DIC is insufficient due to the out of plane motion and dome shape, thus stereo-DIC is used. For stereo-DIC in these tests, the cameras are typically at a small stereo angle to look down into the clamping die. The DIC system typically has a stand-off distance between 35 cm to 90 cm depending on the test machine design. These limitations, requirements, and specimen motion make the selection of the field-of-view with the necessary depth-of-field challenging.

Methods

In this work, a combination of stereo-DIC system assessments is considered that covers the most prevalent measurement artifacts for use of DIC at gauge lengths ≤ 2.5 mm during the forming limit test

E2218 [3]. The combination of various verifications to meet a specific measurement need is the basic framework of the iDICs Measurement Uncertainty Guide for DIC which is under development. The proposed approach here is also intended to meet the post calibration assessment requirements of the iDICs Good Practices Guide for DIC [5], although the out-of-plane motion during the forming limit test is beyond the scope of the guide.

The assessments for this test application include a static and extended noise floor for both the main verification and daily spot checks. These are used to assess strain resolution, lens distortion correction, and long-term stability of the system. For the traceable strain verification in the focal volume, an approach similar to VDI/VDE 2626 [6] and the ASTM E83 [1] Annex A1. Optical Extensometer Systems is used. The proposed approach does not require a traceable gauge length making it more conducive for DIC as opposed to dot-line tracker style optical extensometers. The approach also uses commonly available equipment to make the process more tractable for industrial application. By interrogating the focal volume over a wide range of spatial locations of strains a superset of data is developed. This superset is then down sampled multiple ways to assess the basal requirements for a complete verification of the DIC system for the intended purpose.

Validation that the verification method will reject systems that are not properly measuring is done through assessment using DIC systems with a series of common short comings. Noise, vibrations, or heat currents are added to demonstrate how the system would fail a spot check should any of these effects be substantially present. To assess the effects of poor calibration or poor resolution. The same set of images is interrogated using calibrations performed with insufficient data and/or incorrect lens distortions. These calibrations demonstrate that the verification will fail under poor calibration. Similarly, a binned version of the images is used to demonstrate that without sufficient camera resolution the verification requirements would not be met.

Conclusion

In this work a combination of various methods for assessing the measurement uncertainty of a stereo-DIC system are used to determine the requirements for traceable verification of the DIC system. The intended use is for verifying a DIC system for measuring localized strain during a forming limit test [3,4]. By purposefully performing poor measurements (i.e. added noise or poor calibration) or measurements with environmental artifacts (i.e. vibrations or heat currents) it is demonstrated that the verification will fail if there is insufficient measurement accuracy.

References

- [1] ASTM International. *E83-23 Standard Practice for Verification and Classification of Extensometer Systems*, 2023.
- [2] International Organization for Standardization. *ISO 9513:2012 Metallic materials – Calibration of extensometer systems used in uniaxial testing*, 2012.
- [3] ASTM International. *E2218-23 Standard Test Method for Determining Forming Limit Curves*, 2023.
- [4] International Organization for Standardization. *ISO 12004-2:2021 Metallic materials – Determination of forming-limit curves for sheet and strip: Part 2: Determination of forming-limit curves in the laboratory*, 2021.
- [5] International Digital Image Correlation Society, Jones, E.M.C. and Iadicola, M.A. (Eds.). *A Good Practices Guide for Digital Image Correlation*, 2018. <https://doi.org/10.32720/idics/gpg.ed1/print.format>
- [6] VDI/VDE 2626 *Optical measuring procedures, Digital image correlation: Basics, acceptance test, and interim check*, 2019.

Fourier Synthesis of Patterns Optimized for DIC

S. Bossuyt

Department of Mechanical Engineering, School of Engineering, Aalto University, Helsinki, Finland

Abstract – Synthesis of greyscale patterns via Fourier transforms allows precise control of the spatial frequencies contained in the pattern. This contribution discusses the performance of such patterns for digital image correlation (DIC) measurements, and modifications to the patterns that improve that performance. From this analysis, we derive an algorithm to generate high-contrast random patterns with prescribed feature sizes, that avoid the most prominent issues with previous versions of this algorithm.

Keywords – DIC, pattern, feature size, resolution, spatial frequency, autocorrelation

Introduction A previously published method to generate optimized patterns for DIC, inspired by the relation between high resolution transmission electron microscopy images and electron diffraction patterns of metallic glass [1], described “optimally sharp” isotropic patterns with a narrow spatial frequency content, and proposed adding a component with longer wavelengths, to suppress oscillations of the autocorrelation peak obtained with these patterns. In practice, it is rare that both the background and the application of the pattern are so uniform that this additional component is needed. Nevertheless, the dependence of the performance of DIC measurements on the quality of the pattern is a drawback of DIC, and generating synthetic patterns with features optimised for the intended measurements can significantly improve the accuracy, precision, and robustness of DIC measurements.

Methods The Fast Fourier Transform (FFT) algorithm provides a convenient means of converting between the spatial representation of an image and its spatial frequency content. In particular, it allows to specify the frequency content of a pattern, and generate random patterns with that frequency content by randomising the phase of the frequency components [2]. However, analysis of the measurement uncertainty and noise-induced bias in DIC measurements indicates that these are reduced when the contrast of the pattern is increased [3]. Increasing the contrast with a limited intensity range ultimately results in clipping of the intensity range. This introduces higher spatial frequencies in the image, but it should be noted that the phase of these high-frequency components is determined by that of the band-limited components, and it may therefore in principle be possible to analyse such images in ways that avoid aliasing effects without discarding the information carried in the high-frequency components. Even when analysing high-contrast patterns as if they were band-limited, the increased contrast at least partly offsets the loss of displacement accuracy induced by interpolation error.

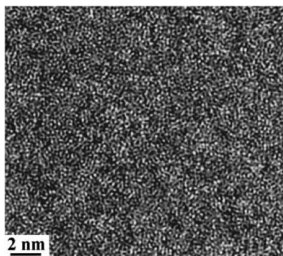


Figure 1: High-Resolution Transmission Electron Microscopy image of annealed metallic glass [1].

As a consequence of clipping the intensity range, some features may be much smaller than in the original band-limited pattern, or disappear entirely. In previous work, this was addressed with morphological operations to detect small features or large featureless areas [2]. An alternative method, less computationally expensive, consists of finding local minima and maxima in the greyscale pattern intensity that are on the wrong side of the threshold for clipping or close to it. This method can also easily detect saddle points in the greyscale pattern intensity that are close to the threshold for clipping, which result in “checkerboard” corners in the high-contrast pattern. Even if those are not necessarily problematic for the DIC algorithm, they may cause difficulties with some methods of applying the pattern and it may therefore be desirable to eliminate them from the pattern.

Results Starting with a nearly “optimally sharp” pattern, and iteratively adjusting the level of any stationary points in the greyscale pattern away from the threshold used to convert it to a black and white pattern, results in a pattern with “worm-like” features with nearly uniform size and spacing. Whereas the pattern has a high density of high-contrast edges, the edges are smooth in the sense that the radius of curvature is everywhere as large as is compatible with the minimum size of the features.

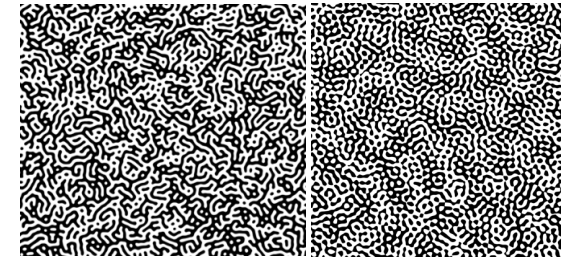


Figure 2: Comparison of the worm-like features with the optimized patterns made earlier [2].

Discussion and Conclusion The worm-like features are in some locations close to a pattern of parallel lines, which causes relatively large uncertainty at those locations in the DIC results for the displacement component parallel to those lines. Whereas it is possible to identify and correct these manually, future work could detect and correct these automatically.

References

- [1] E. Pekarskaya, J.F. Löffler, and W.L. Johnson. Microstructural studies of crystallization of a Zr-based bulk metallic glass. *Acta Materialia* 51(14) 4045–4057, 2003.
- [2] S. Bossuyt. Optimized Patterns for Digital Image Correlation. In *Imaging Methods for Novel Materials and Challenging Applications, Volume 3. Conference Proceedings of the Society for Experimental Mechanics*. DOI:10.1007/978-1-4614-4235-6_34, 2013.
- [3] Y.Q. Wang, M.A. Sutton, H.A. Bruck, and H.W. Schreier. Quantitative Error Assessment in Pattern Matching: Effects of Intensity Pattern Noise, Interpolation, Strain and Image Contrast on Motion Measurements. *Strain* 45(2) 160–178, 2009.

A pseudo-DIC algorithm based on Convolutional Neural Networks

M. Rossi, G. Tanoni, E. Principi

Università Politecnica delle Marche, Faculty of Engineering, 60131 Ancona, Italy

Abstract — In this paper a machine learning algorithm, i.e. a Convolutional Neural Network (CNN), is used to evaluate the deformation of patterns when the reference image is not available. The CNN is trained using simulated images and the level of deformation is expressed in terms of principal strains and principal axes orientation. The method was applied to measure the deformation in a specimen subjected to severe plastic deformation starting from micrographs of the deformed microstructure.

Keywords — DIC, Convolutional Neural Network, Plastic deformation

Introduction Digital image correlation (DIC) is nowadays probably the most used method to measure the strain field along the surface of solids [1]. It has numerous applications, especially in material characterization [2], see for instance the Material Testing 2.0 approach [3]. DIC is based on the correlation between a reference and a deformed image, however, not always the reference image is available. For instance, in order to assess the deformation of a solid from micrographs of the microstructure, only the images of the deformed material are available. The idea, here, is using machine learning (ML) to evaluate the level of deformation from an image without performing a correlation with a reference one. Indeed, ML is becoming a cutting-edge tool in engineering and applications to DIC have been already presented [4]. Among different architectures, Convolutional Neural Networks (CNN) are particularly well-suited for image analysis, especially for classification and object recognition.

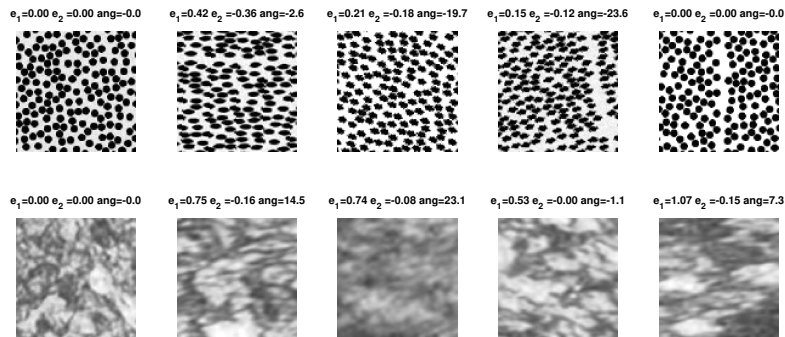


Figure 1: Example of generated synthetic images using a dotted pattern and the microstructure of a steel.

Methods A proof of concept of such approach was demonstrated using synthetic images. A CNN is trained with images that have a known level of deformation, then it is used to predict the deformation of a new set of images. The images are generated using a simulator able to reproduce realistic deformed

images which include experimental uncertainties (noise, change of illumination, etc.) [5]. Two sets of synthetic images are generated, one with a dotted pattern and one using as reference the microstructure of a X-grade steel. Figure 1 illustrates examples of such images, above each image there is the level of deformation applied in terms of principal strain (e_1 , e_2) and orientation (ang).

A VGG16 architecture was used, where the last layer was replaced with a regression layer to have a continuous response. The net was implemented in Python using Keras and Adam optimizer, with a learning rate of 10^{-4} .

Results and Discussion The accuracy of the prediction is assessed on a test set that is obviously different from the training and validation sets. The evaluation is performed in terms of the coefficient of determination R^2 . Using the dotted pattern, an excellent correlation is obtained both using images of 49×49 and 99×99 pixels, with a R^2 above 99% (Table 1). A training set of 5000 images is sufficient to obtain such accuracy.

Size of imm. pixel	Train. set # of images	Valid. set # of images	Test set # of images	R^2 on the test set			
				ϵ_1	ϵ_2	θ	avg.
49×49	5000	1000	1000	0.9964	0.9933	0.9936	0.9944
99×99	5000	1000	1000	0.9951	0.9939	0.9942	0.9944

Table 1: Results on the dotted pattern

Size of imm. pixel	Train. set # of images	Valid. set # of images	Test set # of images	R^2 on the test set			
				ϵ_1	ϵ_2	θ	avg.
49×49	5000	1000	1000	0.9006	0.5591	0.8530	0.7709
99×99	5000	1000	1000	0.9484	0.7067	0.9768	0.8773
199×199	5000	1000	1000	0.9402	0.7501	0.8862	0.8589
99×99	30000	10000	10000	0.9440	0.9598	0.9676	0.9571
99×99	25000	10000	10000	0.9545	0.9515	0.9651	0.9570
99×99	20000	10000	10000	0.9642	0.9534	0.9664	0.9613
99×99	15000	10000	10000	0.9641	0.9439	0.9661	0.9580
99×99	10000	10000	10000	0.9595	0.8349	0.9172	0.9039
99×99	5000	10000	10000	0.9520	0.7647	0.8782	0.8650

Table 2: Results using the microstructure as pattern, with different training sets

Employing the microstructure as reference pattern, instead, poor results are obtained especially for the component ϵ_2 (Table 2). A significant improvement is obtained going from 49×49 to 99×99 pixel, while a further increase of the image size does not impact the outcome. The accuracy, instead, can be substantially improved augmenting the training set, the results stabilizes at around 20000 images.

Conclusion In this work, a CNN is used to measure the deformation over a surface without having a reference image. The net is trained using synthetic images. It is necessary that the surface has a pattern, which, however, can also be not regular. It has shown that, using a suitable number of training images, a reasonably good accuracy can be retrieved using a microstructure as reference pattern.

References

- [1] M.A. Sutton, J.-J. Orteu, H. Schreier, *Image correlation for shape, motion and deformation measurements: Basic Concepts, Theory and Applications*, Springer, New York, NY (USA), 2009.
- [2] S. Avril et al. Overview of identification methods of mechanical parameters based on full-field measurements. *Experimental Mechanics*, 48:381–402, 2008.
- [3] F. Pierron and M. Grédiac. Towards Material Testing 2.0. A review of test design for identification of constitutive parameters from full-field measurements. *Strain*, 57:e12370, 2021.
- [4] X. Duan et al. Digital image correlation based on convolutional neural networks. *Optics and Lasers in Engineering*, 160:107234, 2023.
- [5] Badaloni et al. Impact of experimental uncertainties on the identification of mechanical material properties using DIC. *Experimental Mechanics*, 55:1411-1426, 2015.

Tradeoffs in Lighting when applying Digital Image Correlation to Vibration-based Fatigue Testing

R.B. Berke, J.R. Rigby, B.A. Furman, J.M. Wagner, J.B. Heninger, S.C. Mulhall

Utah State University, Mechanical and Aerospace Engineering, Logan, UT 84322, USA

Abstract – When performing DIC, it is generally recommended to use the brightest lights that are safely available, and to select aperture and exposure time based on the needs of the experiment, but Gain is to be generally avoided. In the case of vibration-based testing, small apertures are needed to ensure sufficient depth-of-field, and short exposure times are needed to reduce motion blur. This raises the question: once other brightening methods are exhausted, could Gain be the least-worst option?

Keywords – DIC, Vibration-based Fatigue Testing, Design of Experiments

Introduction High Cycle Fatigue (HCF) tests are notoriously time-consuming. In order to reduce testing times, vibration-based methods become favorable because they can be performed at rates on the order of kHz and complete cycles more quickly. While performing such tests, one must carefully monitor the excitation to ensure that loading occurs at a desired strain level. However, strain gauges have fatigue lives of their own and often fail before the specimen. Thus, to continue to monitor vibration-based specimens after the strain gauge fails, Hill et. al [1] recently implemented stereo Digital Image Correlation (DIC) to reduce dependence on strain gauges.

To reduce the noise in his DIC-based measurements, Hill fit the analytical solution for a cantilevered plate to the out-of-plane displacements, $W(x,y)$, as measured from his vibrating plate. He then took derivatives on the curve-fitted displacements to compute strains using plate theory. After performing a robust uncertainty quantification, Hill showed that his DIC-based measurement agreed within 1% of the value reported by strain gauges, and could continue to monitor the plate well after the strain gauge failed.

Methods This paper introduces two key improvements relative to Hill's work. First is the introduction of a carrier-insert assembly that reduces material waste by securing a small, expendable specimen into a reusable carrier plate [2], as shown in Figure 1. Because this assembly is no longer a solid rectangular plate as was characterized by Hill, the plate-theory solution is replaced by the analytical solution for an Euler-Bernoulli beam as applied to the insert specimen.

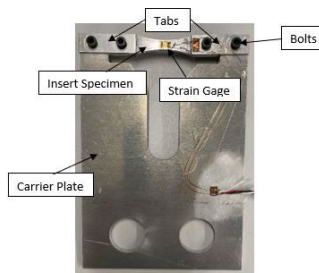


Figure 1: Carrier-insert assembly with a strain gauge mounted to it to monitor strains

The second improvement is a statistical consideration of varying sources of brightness in the DIC images. A Design of Experiments (DOE) statistical analysis is performed using Minitab. Two light sources are considered: a pair of LED ring lights which are relatively dim for vibration-based testing, and a much brighter strobe light which is synchronized to the triggering of the cameras. For each light source, three discrete values of aperture are selected, representing a relatively wide, moderate, and

narrow depth of field. For each of these 6 combinations, a series of 13 experiments are performed using varying exposure time and Gain values, resulting in 78 total measurements of strain.

Results A response surface of the percent relative error between the DIC-derived strain and a strain gauge is given in Figure 2:

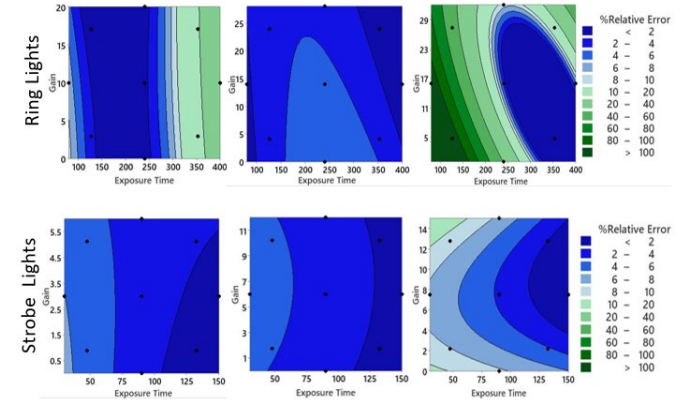


Figure 2: Response surfaces of the percent relative error between DIC and strain gauges for each combination of light source and aperture. (Left to right: widest aperture, moderate aperture and narrowest aperture.)

Discussion and Conclusion Overall: the relative error between DIC versus the strain gauge is lowest when using moderate apertures (middle column in the figure). If the aperture is too broad (left column), the increased error is assumed to be due to poor depth of field. If the aperture is too narrow (right column), the increased error is assumed to be due to poor contrast as a result of insufficient brightness.

It is interesting to note that many of the contours are roughly vertical, with Gain on the vertical axis. This indicates that Gain appears to be relatively harmless, which runs counter to the common wisdom that it should be generally avoided in DIC [3]. In some extreme cases, the right column shows that for certain combinations of narrow aperture and long exposure time, increased Gain can produce lower errors than leaving the Gain at zero. However, there are also counter-examples for which increased Gain can produce worse outcomes, so DIC users should be cautioned not to over-rely on Gain without careful consideration of other lighting methods.

References

- [1] B. D. Hill, B. A. Furman, E. E. German, and R. B. Berke, "Non-contact Strain Measurement to Eliminate Strain Gauges in Vibration-based Fatigue Testing," *J. Strain Anal. Eng. Des.*, in prep 2021.
- [2] J. Bruns, A. Zearley, T. George, O. Scott-Emuakpor, and C. Holycross, "Vibration-Based Bending Fatigue of a Hybrid Insert-Plate System," *Exp. Mech.*, vol. 55, no. 6, Art. no. 6, Jul. 2015, doi: 10.1007/s11340-015-0004-6.
- [3] E. M. C. Jones and M. A. Iadicola, Eds., "A Good Practices Guide for Digital Image Correlation." International DIC Society (iDICs), 2017. [Online]. Available: <https://idics.org/guide/>

DIC monitoring of a half-scale masonry building subjected to cyclic quasi-static loading

 N. Savalle^{1,2}, A. Aşıkoğlu^{2,3}, G. Vasconcelos², P. B. Lourenço²
¹Université Clermont Auvergne, Clermont Auvergne INP, CNRS, Institut Pascal, Clermont-Ferrand, France

²University of Minho, ISISE, ARISE, Department of Civil Engineering, Guimarães, Portugal

³Delft University of Technology, Stevinweg 1, 2628 CN Delft, The Netherlands

Abstract – DIC measurements are gaining popularity among all engineering fields. Thanks to the recognition of black and white random pattern, they provide full-field displacement measurements of the external surfaces of a specimen subjected to a given loading. Often, DIC measurements are conducted on small samples or specific reduced areas of larger samples. The application of such techniques on larger specimens remains scarce, yet it provides full information on the damage evolution of the samples. The present document describes the application of DIC measurements on a masonry façade of a half-scale building tested to failure. The total field of view is 3x2.6 m and the article details the creation of the DIC pattern, the exploitation of the data and discusses the obtained experimental results and the advantage of such tools for full-scale specimens.

Keywords – DIC, half-scale experiments, masonry, black and white speckle.

Introduction As far as the numerical power of computer together with the resolution of cameras increased, it has opened new perspectives for the visual monitoring of samples in research laboratories. Different pictures of a sample taken at different time can be compared and numerically analysed to obtain the displacement map of the monitored face of the sample. In brief, a numerical algorithm first selects a facet composed of several pixels of the picture in the original (undeformed) state and tries to find it in the next (deformed) picture. The contrast and the randomness of the pattern of the monitored face is crucial in order to help the detection algorithm to recognise the facet in the subsequent [1]. For small specimens, either the natural contrast of the sample is enough [2] or spray of black painting on a white background is very popular [3]. Once the displacement map is evaluated, one can derive the strain map, that can be written in the global or principal frame.

Such experimental techniques have been used in different scientific field to monitor the displacement map of specimens subjected to different type of loading (e.g. mechanical, thermal, ...). In the masonry field, it is gaining popularity as confirmed by the literature [2], [4], [5]. However, many tests focused on small scale specimens, while full scale specimens are only rarely being monitored through DIC systems [5], [6]. Since the precision of the measurements is intrinsically linked to the resolution of the camera, large samples typically lead to smaller precision compared to small specimens, and especially classical local measurements such LVDTs. Yet, it provides full field measurements and damage evolution while LVDTs only give very punctual information. The main drawback of such applications lies in the definition of an appropriate pattern on large samples. For instance [5] used perforated sheets with holes of 19mm diameter and [6] used diameters of speckle of 3.2mm. As demonstrated through these rare examples, the documentation of application of DIC on large structures still remain an open topic in the field. In addition, there is still a lack of comparison of such measures on large samples together with other classical techniques.

The present work describes the monitoring of a masonry façade of 3x2.6m through a DIC system. It aims at detailing the protocol followed for the monitoring. It then opens the way for comparison between DIC measurements and local measurements. The following sections respectively present the experimental methods, the obtained results and the conclusions of this work.

Methods The experimental prototype consists in a masonry half scale building (Figure 1). One of the façades is monitored through 2 digital image correlation (DIC) systems. The first one is composed of a single camera of 20MP taking picture of the whole façade, while the other one uses two cameras of 2MP and monitors only the bottom right corner (Figure 1). In addition, several local LVDTs are positioned all around the structure [7].

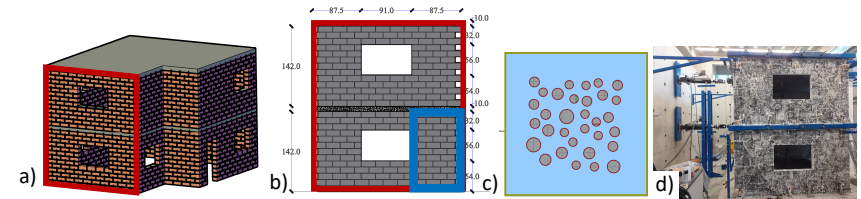


Figure 1: experimental setup (a). The north façade (red) is monitored with the one-camera DIC, while only a small portion (blue) is monitored through the two-cameras DIC (b). Example of a perforated sheet (c) and applied speckle on the façade (d)

Overall, the 3 cameras of the 2 DIC systems have a pixel size of approximately 1mm and therefore dedicated perforated plates with circular holes of 5mm diameter have been designed. The plates have been numerically generated through a grasshopper component that can create randomly distributed circles of random diameters (Figure 1c and d). Then, a CNC machine drills five 4mm-thick plexiglass sheets that are then placed on the white façade of the building and filled with black painting to produce the random pattern. The specimen is then subjected to horizontal cyclic loads through the two hydraulic jacks, while the amplitude of the cycles increases through the time.

Results The one-camera DIC system is analysed through the matlab “ncorr” DIC package [8], while the two-cameras DIC uses a commercial software provided by DANTEC company. Overall, Figure 2 displays the results at the end of the initiation of cracks and at the final stage of the loading, just before failure.

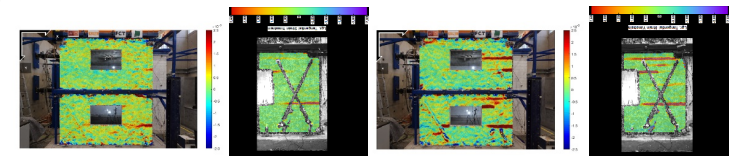


Figure 2: vertical strain obtained at the initiation of the cracks (left) and at the last cycle before failure (right)

Discussion and Conclusion Overall, the agreement between the two DIC systems is satisfactory and paves the way for a deep comparison with local LVDT measurements. In general, it also demonstrates that such experimental tools are now unavoidable as they can monitor unexpected cracks, they can provide crack width evolution, without fearing to damage any contact equipment.

References

- [1] S. Mguil-Touchal, F. Morestin, et M. Brunei, « Various experimental applications of digital image correlation method », *WIT Trans. Model. Simul.*, vol. 17, 1970,
- [2] S. Allaoui, A. Rekik, A. Gasser, E. Blond, et K. Andreev, « Digital Image Correlation measurements of mortarless joint closure in refractory masonries », *Constr. Build. Mater.*, vol. 162, p. 334-344, 2018.
- [3] J. Rocha, J. Sena-Cruz, et E. Pereira, « Tensile behaviour of CFRP-glass adhesively bonded connections: double-lap joint tests and numerical modelling », *Eng. Struct.*, vol. 260, p. 114212, 2022.
- [4] R. L. Oliveira, J. P. C. Rodrigues, J. M. Pereira, P. B. Lourenço, et H. U. Marschall, « Normal and tangential behaviour of dry joints in refractory masonry », *Eng. Struct.*, vol. 243, p. 112600, 2021.
- [5] S. Rajaram *et al.*, « Full-field deformation measurements during seismic loading of masonry buildings », *Struct. Control Health Monit.*, vol. 24, n° 4, p. e1903, 2017.
- [6] R. Ghorbani, F. Matta, et M. A. Sutton, « Full-field deformation measurement and crack mapping on confined masonry walls using digital image correlation », *Exp. Mech.*, vol. 55, n° 1, p. 227-243, 2015.
- [7] A. Aşıkoğlu, A. Barontini, N. Savalle, G. Vasconcelos, et P. B. Lourenço, « Experimental Analysis of Unreinforced Masonry Buildings Through the Quasi-Static Test: A Half-Scale Two-Story Modern Masonry Building », in *North American Masonry Conference*, 2023.
- [8] J. Blaber, B. Adair, et A. Antoniou, « Ncorr: open-source 2D digital image correlation matlab software », *Exp. Mech.*, vol. 55, n° 6, p. 1105-1122, 2015.

Training an AI hyperelastic constitutive model with experimental data

C. Jailin, A. Benady and E. Baranger

Université Paris-Saclay, CentraleSupélec, ENS Paris-Saclay, CNRS,
 LMPS – Laboratoire de Mécanique Paris-Saclay, 91190, Gif-sur-Yvette, France.

Abstract — A Physics-Augmented Neural network is trained to model a hyperelastic behavior. The dataset used for the training, validation, and test are displacement-force couples obtained from two experiments on a rubber-like material. One experiment was dedicated for the test, to assess the capacity of the model to generalize on unseen loadings and geometries. The trained AI model outperforms a standard Neo Hookean model identified on the same data. Particular attention is paid to the mechanical data information contained in the different datasets.

Keywords — Artificial Intelligence, Physics-augmented AI, Data-driven, Constitutive modeling, PANN, DIC

Introduction Recent advancements in artificial intelligence and experimental mechanics have paved the way for innovative approaches to model material behaviors. By enforcing physics and mechanical information in the neural network, their efficiency has greatly improved, allowing them to learn complex behaviors while requiring a reduced number of data. Those mechanically AI-informed constitutive models are called Physics-Augmented Neural Networks (PANN) [1]. Showing promising results from synthetic (yet realistic) experiments, obtained from an initial FEA simulation, those physics-augmented constitutive models have not been trained on real experimental data. Being real data, the true material behavior is unknown (which complexifies the model design), the data are affected by experimental noise/uncertainties, and the final evaluation cannot be challenged to ground truth. It is here presented the optimization and training of a hyperelastic PANN model from DIC and force measurement data.

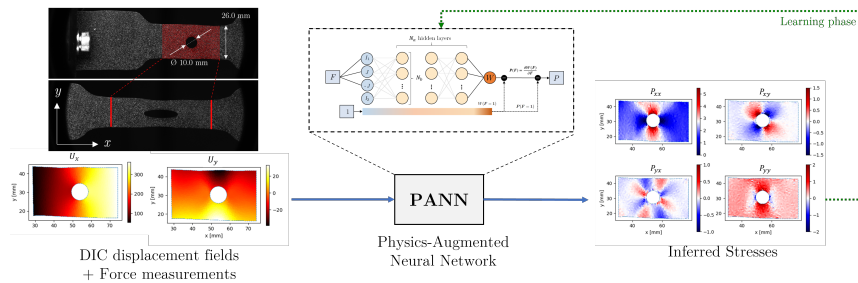


Figure 1: Constitutive model based on a Physics-Augmented Neural Network

Methods *PANN constitutive model*: The constitutive model used in this study [2] is based on a Physics-Augmented Neural Network. Multiple physical constraints are enforced on the neural network (e.g., convexity and positivity of the free energy) to ensure a thermodynamically relevant strain (\mathbf{F}) to stress (\mathbf{P}) mapping (Figure 1). The model $\mathcal{M}_{\text{PANN}}$ is trained in an unsupervised framework (so-called NN-

EUCLID [3]), minimizing a loss function $\mathcal{L}[\mathcal{M}(\mathbf{F}), \mathbf{R}]$ ensuring the whole sample is balanced considering the measured reaction forces \mathbf{R} . The network weights p are finally optimized using gradient-based techniques: $\hat{p} = \underset{p}{\text{Argmin}} \mathcal{L}[\mathcal{M}_{\text{PANN}}(p, \mathbf{F}), \mathbf{R}]$.

Because the true behavior is unknown, 10 different model architectures, comprising 145 up to 17,217 trainable parameters, were evaluated to select the most accurate. Finally, the PANN model is compared with a standard Neo-Hookean law.

Dataset: The study uses two distinct uni-axial experiments on a rubber-like material, achieving local deformations over 200% and exhibiting a highly non-linear behavior. Full-field measurements were extracted using global DIC approaches with brightness-contrast corrections [4]. Together with axial force measurements, this constitutes a dataset of 661 deformation fields/force couples $\{\mathbf{F}, \mathbf{R}\}$ for each loading step and geometry. Data from these experiments were carefully split into 20 training steps (to learn the model weights), 6 validation steps (to monitor the model performances, and optimize the model architecture), and 635 test steps (for the final evaluation and metrics computation).

Results The different model architectures are compared on the validation dataset and evaluated through the equilibrium gap loss, allowing for the identification of the best model hyperparameters (number of layers, number of neurons). The chosen model is then compared to a Neo Hookean model identified using a similar process. Based on the results of different metrics (inner and boundary equilibrium), the PANN model performs in the same range if not better than the Neo Hookean model. On the experiment dedicated to the test, the PANN model outperforms the Neo-Hookean law. The PANN model does not show discontinuities at the trained loading steps and provides accurate results beyond the trained steps. Although its mechanical content may be low informative in the unseen experiment, the PANN model performs better than the Neo Hookean model, showing its generalization capacity.

Discussion and Conclusion The PANN model showed its capacity to learn the material's hyperelastic behavior, outperforming traditional Neo-Hookean models. It demonstrated robustness not only within the range of trained loads but also in unseen loadings, illustrating a capacity for both interpolation and extrapolation (at least on the evaluated states).

The results underscore the importance of carefully controlling the datasets used for the training, validation, and test. The mechanical content in those subsets has to be informative enough for the training to learn the constitutive model from a large range of mechanical states, and challenging enough for the test to provide an accurate evaluation. Although performed with two geometries and large deformations, the two experiments used in the analysis do not exhibit complex stress/strain multi-axial states, thus limiting the potential for learning.

Collecting vast amounts of data from simple mechanical tests alone is not enough; instead, emphasizing the informative mechanical content of that data is crucial for the effective training of the network. Quantifying, comparing, visualizing, and even optimizing the data contained in mechanical tests hence remains a crucial challenge.

References

- [1] L Linden, D K Klein, K A Kalina, J Brummund, O Weeger, and M Kästner. Neural networks meet hyperelasticity: A guide to enforcing physics. *Journal of the Mechanics and Physics of Solids*, page 105363, 2023.
- [2] C Jailin, A Benady, R Legroux, and E Baranger. Experimental learning of a hyperelastic behavior with a physics augmented neural network. *submitted to Experimental Mechanics*, 2024.
- [3] P Thakolkaran, A Joshi, Y Zheng, M Flaschel, L De Lorenzis, and S Kumar. NN-EUCLID: Deep-learning hyperelasticity without stress data. *Journal of the Mechanics and Physics of Solids*, 169:105076, 2022.
- [4] VF Sciuti, RB Canto, J Neggens, and F Hild. On the benefits of correcting brightness and contrast in global digital image correlation: Monitoring cracks during curing and drying of a refractory castable. *Optics and Lasers in Engineering*, 136:106316, 2021.

Improvement of Measurement Uncertainty Using Multi-camera DIC system and Its Benefits in Actual Applications

LiKang Luan

Dantec Dynamics GmbH Ulm, Germany; likang.luan@dantecdynamics.com

Abstract – A cluster-approach-based multi-camera DIC system was applied to measure the same FoVs of one test specimen from different camera viewing angles to study its optimization of measurement uncertainty. An out-of-plane rigid body motion of the specimen was applied, and same DIC evaluation parameters were used from the same image series taken in the test but with various camera group combinations, i.e., from standard two-camera DIC system up to four or more multi-camera DIC system. Test results as contour and displacement error as well as strain noise level show that more cameras lead to a better measurement uncertainty. The upper limit of optimization with camera numbers, influence of reference camera selection, and actual application cases will be discussed in this study.

Keywords – DIC, Multi-camera DIC system, measurement uncertainty

Introduction Multi-camera DIC system is an optimal technical solution for large size specimen for example in civil engineering applications where measurement surface can be divided into multiple smaller FoVs to remain local spatial resolution. For specimens with complex surface shape such as 3D printed material, an improvement of specimen surface coverage can be achieved because multiple cameras can measure specimen at difference viewing angles. Additionally, it is found in our previous study [1] that a three-camera DIC system provides an increasing measurement accuracy if all cameras are viewing the same FoV. In this study, multi-camera DIC system with camera number up to four or more will be used to measure the same FoV of one test specimen in rigid body motion. Measurement uncertainty will be analysed to determine the optimization upper limit on measurement accuracy.

Methods One flat test specimen was prepared with a printed speckle pattern and assembled via screws on a sliding table, which provides an out-of-plane motion relative to the DIC system. A four-camera DIC system was applied in preliminary test, where all four industrial 5 MPx USB3 cameras are measuring the same FoV of the specimen but with different viewing angles as shown in Figure 1 (b). With lens of 25 mm, a FoV of approximately 200 mm×167 mm can be achieved based on a camera pixel resolution of 2448×2048 pixels and a working distance around 580 mm. One checkerboard like calibration target as shown in Figure 1(a) was used for the DIC system calibration. During the calibration process, the calibration target was viewed from four cameras simultaneously to determine all intrinsic and extrinsic parameters of DIC system by using Zhang’s calibration method [2]. After the calibration process, all data points (i.e., facets) on the specimen surface can be mapped into one common global coordinate system as shown in Figure 1(c) in the DIC correlation by using the algorithm from Chen et al. [3].

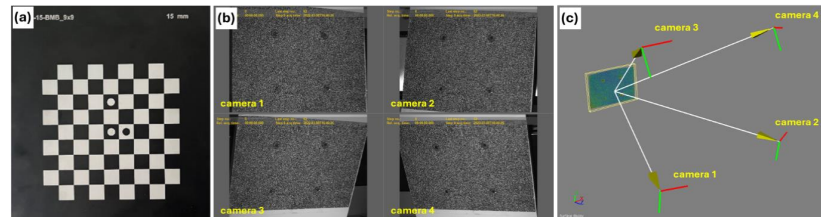


Figure 1: (a) Calibration target; (b) FoVs of four cameras measuring the flat test specimen from different viewing angles; (c) data points from specimen surface evaluated in one common coordinate system and their relative position to cameras.

The DIC results can be evaluated and compared with different camera combinations, i.e., the images from four, three, and two cameras as input for DIC calculation with the identical evaluation parameters.

Results Figure 2 shows the contour error plots of the DIC result from different camera combinations at the reference images. With increasing camera numbers, a smaller and more homogenous distribution of contour error can be observed, especially at the corners of the FoVs where a larger influence of lens distortion exists. Additionally, Eng. Principal Strain 1 maps at max out-of-plane (1 mm for the preliminary testing) were plot, which indicate also an improvement of strain noise level with more cameras used in a DIC evaluation.

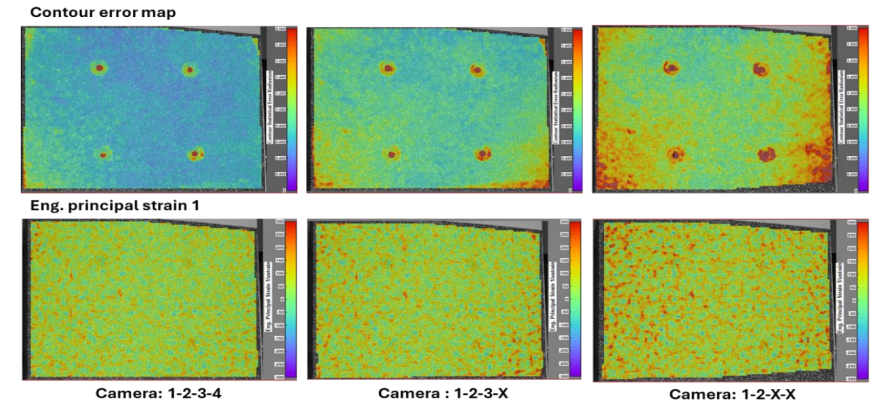


Figure 2: (top) Contour error map plots of four, three, and two camera combinations at reference step with a colorbar range set from 0 to 2 μm ; (bottom) Eng. Principal strain 1 map plots at max out-of-plane displacement based on different camera combinations with a colorbar range set from -300 to 300 μstrain .

Discussion and Conclusion

DIC evaluations based on the same image series but with different camera combinations indicate that a smaller measurement uncertainty can be achieved by applying multiple cameras measuring the same specimen area. But there is less improvement between four-camera and three-camera results compared to two camera result indicating an upper limit of optimization with camera numbers. Discussion about other influence factors such as reference camera selection and actual application cases will be shown in the conference.

References

- [1] L.K. Luan and L. Crosbie. A three-camera Digital Image Correlation System for full-field 3D shape and motion measurement. *Materials Evaluation*, 80(11): 34-41, 2022.
- [2] Z. Zhang. A flexible new technique for camera calibration. *IEEE Transactions on Pattern Analysis and Machine Intelligence*, 22(11): 1330-1334, 2000.
- [3] FX. Chen, X. Chen, X. Xie, X. Feng, and LX. Yang. Full-field 3D measurement using multi-camera digital image correlation system. *Optics and Lasers in Engineering*, 51:1044–1052, 2013.

3D Deformation measurement on a rifle using Multi-Camera High-Speed DIC

T. Siebert, L. Fiedler

LaVision GmbH, Göttingen, Germany

Abstract – In the following article we present a 3D deformation measurement on a rifle barrel during firing. The recording was made with a multi-camera high-speed DIC system in combination with photogenic patterning. The deformation behaviour of the barrel with muzzle brake and with suppressor was compared. Before the bullet leaves the barrel, the deformation behaviour is almost identical, after the bullet leaves the barrel with muzzle brake oscillates considerably more than the barrel with suppressor.

Keywords – DIC, Multi Camera, High-Speed, Photogenic Pattern

Introduction The deformation of the gun barrel during the firing of a shot is an important parameter that significantly influences the accuracy of the weapon. To illustrate how such a measurement can be realised and which deformations can be recorded, the measurements on a rifle barrel with muzzle brake and suppressor are shown here as an example.

Methods The experiment was conducted on a shooting range. The weapon was recorded by three high-speed cameras (Phantom T4040) during the firing of the shot. An LED 300, which emits light in the blue spectrum and is synchronised with the recording of the cameras, serves as the lighting. In order to achieve optimum contrast of the speckle pattern applied to the weapon, the principle of Photogenic Patterning was used. A fluorescent colour is used for patterning and only this part of the light spectrum is imaged onto the camera sensor using suitable filters. The outer two cameras are fitted with a filter that blocks the direct light from the illumination source and only allows the light from the photogenic speckle to pass through. The centre camera has no filter and therefore not only sees the speckle pattern, but also the weapon.

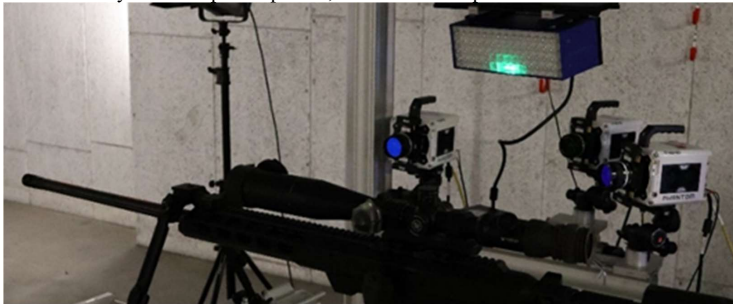


Figure 1: Setup of the 3 Camera High-Speed DIC system and rifle at the shooting range

The measurements were carried out with a reduced ROI (2560x768px) at a recording frequency of 20KHz. The exposure time was 6.1µs and all three cameras were calibrated in a common coordinate system.

The trigger for the shots was activated manually and the image sequence was downloaded with the shot. As the barrel length with muzzle brake and suppressor are not the same length, the time of bullet ignition was selected to synchronise the measurements. This was defined as the time at which the first displacement in the direction of the shot was measured.

As the weapon undergoes a whole-body movement in addition to the deformation, a part of the housing was measured alongside the weapon barrel and its movement subtracted.

Results For the evaluation, four areas along the gun barrel and one area on the housing were marked and their vertical deformation was plotted over time (see Fig. 2, right). It can be seen that approx. 6.5 ms after ignition ($t = 0$) there is a deformation in the rear area of the barrel, which moves forwards at a later time. When the bullet leaves the barrel, it has deformed by less than 0.1mm at the end and 0.3mm at rear area.

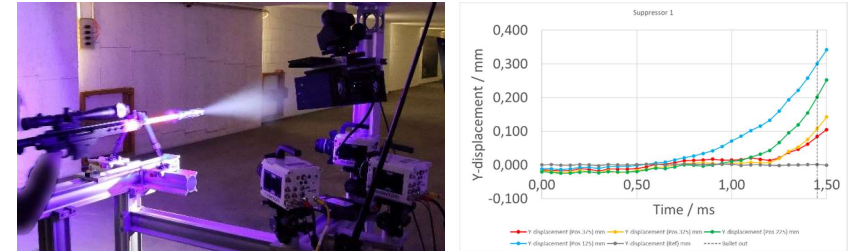


Figure 2: Image of the rifle during the shot (left) and vertical deformation of selected areas along the barrel over time (right)

The following figures 3 show a direct comparison of the vertical deformations of the weapon with muzzle brake (top) and with suppressor (bottom) at two points in time.

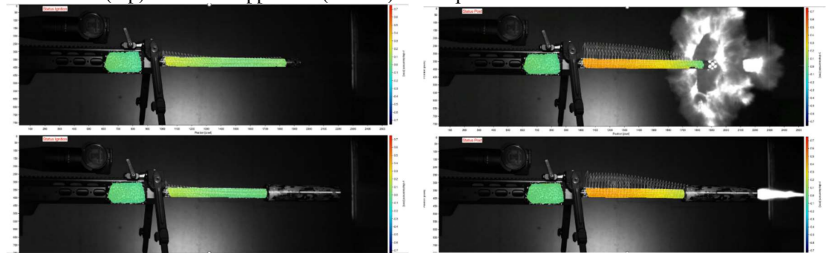


Figure 3: Vertical deformation of barrel with muzzle brake (top) and with suppressor (bottom) before (left) and just after (right) the bullet left the barrel

In addition to the vertical deformation, the deformation in the direction of observation was also measured, but no significant deformations were found here. Therefore, only the vertical deformations are discussed.

Discussion and Conclusion The tests show that a high-speed DIC system can be used to measure small deformations superimposed by whole-body movements with high temporal and spatial resolution. The combination of high-speed and photogenic patterning also achieves a very high image quality and can therefore achieve excellent measurement resolutions. The results show that the differences between the muzzle brake and the suppressor in this configuration are only visible after the bullet has left the barrel.

		Tuesday		Wednesday		Thursday	
08:00	8h00	First floor Welcome	8h30	A002 Small scales	8h30	A002 Fracture	08:00
09:00	9h00	A002 Welcome speech	9h30	A002 Alec van Henwijnen "Chasing anticracks - How PTV and DIC revolutionized snow avalanche research"	10h10	A002 then first floor Poster session	09:00
10:00	10h20	First floor Break	10h20	First floor Break	10h30	First floor Break	10:00
11:00	10h50	A002 Extrem	11h40	A002 Vendor's presentation speeches	11h00	A002 Keynote Pierre Gosselet "Preconditioned conjugate gradient solver for the linearized optical flow systems"	11:00
12:00	11h50	A002 Monosession	11h40	A002 Keynote "From random speckles to checkerboard patterns"	11h50	A002 Monosession Mini symposium: Math & Algorithms	12:00
13:00	Lunch Last floor						13:00
14:00	13h50	109 Volume measurements	13h15	110 DIC Challenge	13h15	110 Committee meeting Standardization	14:00
15:00	14h00	110 Inverse and identification	14h00	109 Materials	14h00	109 Uncertainty quantification	15:00
16:00	15h30	First floor Break	14h00	110 Aerospace	14h00	110 Thermography	16:00
17:00	16h00	109 Volume measurements	15h30	In front of the building Social event Insidie a Volcano	15h40	First floor Break	17:00
18:00	16h00	110 Inverse and identification methods	16h00	109 Software	16h10	109 Uncertainty quantification	18:00
19:00	18h00	In front of the building Social event City tour	18h10	A002 Keynote João Quinta da Fonseca "Measuring and modelling the elastoplastic transition in engineering alloys at the microstructural scale"	17h20	A002 Closure speech	19:00
20:00	19h00	Town hall Social event Town hall reception	19h30	Gala dinner		19h30	20:00
21:00	20:00	to be defined Downtown dinner				21:00	21:00